

**Contribution of road traffic emissions
to tropospheric ozone in Europe and
Germany**

Mariano Burkhard Mertens

Deutsches Zentrum für Luft- und Raumfahrt
Institut für Physik der Atmosphäre
Oberpfaffenhofen

Dissertation
der Fakultät für Physik
der Ludwig-Maximilians-Universität
München

ISRN DLR-FB--2017-13

M. B. Mertens

ISSN 1434-8454

ISRN DLR-FB--2017-13



DLR Deutsches Zentrum
für Luft- und Raumfahrt



Herausgeber Deutsches Zentrum
für Luft- und Raumfahrt e. V.
Bibliotheks- und
Informationswesen
D-51170 Köln
Porz-Wahnheide
Linder Höhe
D-51147 Köln

Telefon (0 22 03) 6 01 - 44 44
Telefax (0 22 03) 6 01 - 47 47

Als Manuskript gedruckt.
Abdruck oder sonstige Verwendung
nur nach Absprache mit dem DLR gestattet.

ISSN 1434-8454

Forschungsbericht 2017-13

Contribution of road traffic emissions to tropospheric ozone in Europe and Germany

Mariano Burkhard Mertens

Deutsches Zentrum für Luft- und Raumfahrt
Institut für Physik der Atmosphäre
Oberpfaffenhofen

Dissertation
der Fakultät für Physik
der Ludwig-Maximilians-Universität
München

215 Seiten
84 Bilder
37 Tabellen
196 Literaturstellen



DLR Deutsches Zentrum
für Luft- und Raumfahrt

Erstgutachter: Prof. Dr. Robert Sausen
Zweitgutachter: Prof. Dr. George Craig
Datum der Abgabe: 19.12.2016
Tag der mündlichen Prüfung: 13.3.2017

Contribution of road traffic emissions to tropospheric ozone in Europe and Germany

Mariano Burkhard Mertens

Dissertation
der Fakultät für Physik
der Ludwig-Maximilians-Universität
München

vorgelegt von
Mariano Burkhard Mertens
aus Tönisvorst

München, im April 2017

Contents

Zusammenfassung	vii
Abstract	ix
1 Introduction	1
1.1 Motivation	1
1.2 Scientific Questions	2
1.3 Investigation Strategy	3
2 Background	5
2.1 Tropospheric and stratospheric ozone	5
2.2 Ozone budget of the troposphere	7
2.3 Chemical production and destruction of ozone	8
2.3.1 Oxidation of carbon monoxide and methane	10
2.3.2 Simplified oxidation of other hydrocarbons	11
2.3.3 Atmospheric reservoir species	11
2.3.4 Non-linearity of ozone production	12
2.4 Dry and wet deposition of ozone	15
2.5 Long range transport of ozone	17
2.6 Natural and anthropogenic origins of ozone precursors	18
2.7 Units used in air quality studies	21
2.8 Modelling the contribution of road traffic emissions to tropospheric O ₃	21
3 Methods	27
3.1 Description of the models	28
3.1.1 ECHAM5	28
3.1.2 COSMO	28
3.1.3 MESSy infrastructure	29
3.1.4 MECO(n) model system	30
3.1.5 Investigation of small chemical changes	34
3.1.6 Estimating the impact of emissions from different sectors	34
3.1.7 The TAGGING submodel	36
3.2 Description of the model set-up	39
3.2.1 Computational domains and on-line coupling	39
3.2.2 Details of the model set-up	40
3.2.3 Description of used emission inventories	41
3.2.4 Comparison of the used emissions inventories	42

3.2.5	Seasonal cycles of emissions	46
3.3	Experimental Design	47
4	Evaluation of the MECO(n) system	51
4.1	Meteorological evaluation	51
4.2	Evaluation of the TAGGING method	53
4.3	Chemical evaluation	55
4.3.1	Observation data	55
4.3.2	Comparison with satellite observations	56
4.3.3	Comparison with ground level measurements	59
4.3.4	Vertical O ₃ profiles	66
4.3.5	Tropospheric oxidation capacity	68
4.4	Discussion on deviations from observations	70
5	Contribution of road traffic emissions in Europe for 2008	75
5.1	Differences between EMAC and COSMO	78
5.1.1	Comparison of the simulated contributions to O ₃	79
5.1.2	Comparison of the O ₃ production	83
5.2	Differences between both COSMO instances	87
5.3	Influence of anthropogenic emission inventories	91
5.3.1	Resolution of anthropogenic emission inventory	91
5.3.2	Differences between the MACCity and the VEU inventory	94
5.3.3	Local O ₃ production rates	98
5.3.4	Emission categories contributing most to the O ₃ production	100
5.4	Sensitivity to changes of biogenic emissions	101
5.5	Intercomparison of the results from the different simulations	105
5.6	Temporal and spatial variations of the contributions	107
5.6.1	Seasonal cycle of the contributions	107
5.6.2	Small scale fluctuations of the contribution	108
5.7	Discussion	110
5.8	Conclusions	113
6	Contribution of road traffic emissions in Europe projected for 2030	115
6.1	Projected differences for the 2030 emission inventory	117
6.2	Influence of changed global boundary conditions	121
6.3	Changes in the O ₃ production efficiency	126
6.4	Implications for the radiative forcing and the methane lifetime	127
6.5	Discussion	129
6.6	Conclusion	133
7	Concluding remarks	135
7.1	Summary	135
7.2	Conclusions and Outlook	137

A Appendix	141
A.1 Description of additional sensitivity studies	141
A.2 Pasing COSMO fields to EMAC for radiation calculations	143
A.3 Detailed list of used MESSy submodels	144
A.4 Mechanism of the gas phase chemistry	146
A.5 Definition of the PRUDENCE subdomains	166
A.6 Details about applied emissions	167
A.7 Additional figures	178
Bibliography	193
Acronyms and specie names	211

Zusammenfassung

Troposphärisches Ozon (O_3) wirkt als Treibhausgas und ist ein Vorläuferstoff des Hydroxyl Radikals (OH), einer wichtigen Substanz für die Selbstreinigung der Troposphäre. Hohe Konzentrationen von O_3 schädigen jedoch die Vegetation und sind schädlich für die menschliche Gesundheit. Quellen für troposphärisches Ozon sind der Abwärtstransport aus der Stratosphäre sowie die photochemische In-Situ Produktion. An dieser Produktion sind vor allem Stickoxide (NO_x), Kohlenstoffmonoxid (CO) sowie leichtflüchtige organische Verbindungen (VOCs) beteiligt, für die eine wichtige Quelle Emissionen aus dem Straßenverkehr sind. Aufgrund der Nichtlinearität der Ozonchemie ist es allerdings nicht möglich, die Menge an O_3 , die von Emissionen aus dem Straßenverkehr erzeugt wird, direkt zu berechnen. Dies ist nur mit Hilfe umfangreicher Simulationen mit Klima-Chemie Modellen möglich.

In dieser Dissertation untersuche ich den Beitrag der Straßenverkehrsemissionen zum troposphärischen O_3 in Europa und Deutschland für gegenwärtige Bedingungen sowie für eine Zukunftsprojektion. Hierfür wende ich in dieser Studie erstmals ein neu entwickeltes Modellsystem an, das es ermöglicht, ein grob aufgelöstes globales Modell in bestimmten Regionen konsistent zu verfeinern. Das Modell wurde um eine Tagging-Technik erweitert. Dadurch lassen sich die Reaktionswege der von unterschiedlichen Quellen emittierten Spezies nachverfolgen. Die Simulationsergebnisse wurden im Hinblick auf die troposphärische Gasphasenchemie evaluiert, indem sie mit Beobachtungsdaten von Satelliteninstrumenten, bodengebunden Messungen sowie von Ozonsonden verglichen wurden.

Für die Emissionen des Straßenverkehrs wurde ein mittlerer Beitrag von 11 ± 1 % zur troposphärischen Ozonsäule bis 850 hPa für Bedingungen des Jahres 2008 in Europa ermittelt. Im Winter wird der Beitrag vor allem durch den Ferntransport bestimmt, während im Sommer die Bedeutung der lokalen Produktion zunimmt. Das globale und das regionale Modell simulieren vergleichbare Werte für das europäische Gebiet. Auf der regionalen Skala (z.B. in der Po Ebene) weichen die Modelle jedoch deutlich voneinander ab. Regionale Modelle sind daher für die Darstellung von extremen O_3 Werten wichtig. Diese Modelle ermöglichen außerdem quantitative Aussagen über den regionalen Beitrag verschiedener Quellen zu O_3 . Die größte Sensitivität der Ergebnisse dieser Analyse zeigt sich für die Unsicherheiten über die Kenntnis der natürlichen und anthropogenen NO_x -Quellen.

Die Analysen der Zukunftsprojektion für das Jahr 2030 deutet eine Abnahme des Beitrags der Straßenverkehrsemissionen von 2–3 Prozentpunkten im Sommer an. Aufgrund der Bedeutung des Ferntransports von Ozon und dessen Vorläuferstoffen wird der Effekt von regionalen Minderungsstrategien jedoch stark durch die globalen Bedingungen bestimmt. Die regionale Abnahme der NO_x Emissionen für Deutschland, projiziert für das Jahr 2030, führt in vielen deutschen Städten zu einer Zunahme von bodennahen Ozon, da VOC Emissionen nicht ebenso stark reduziert werden wie die NO_x Emissionen.

Abstract

Tropospheric ozone (O_3) acts as greenhouse gas and is a precursor of the hydroxyl radical (OH), the self-cleansing agent of the troposphere. Large concentrations of O_3 , however, can damage the vegetation and are harmful for human health. Sources of tropospheric O_3 are the downward transport from the stratosphere and in situ photochemical production, mostly involving nitrogen oxides (NO_x), carbon monoxide (CO) and volatile organic compounds (VOCs). An important source of these precursors are road traffic emissions. As the production of O_3 is highly non-linear, it is not possible to derive the amount of O_3 produced through road traffic emissions directly. Instead, simulations with comprehensive chemistry-climate models are necessary to investigate the contribution of road traffic emissions to tropospheric O_3 .

In this thesis I analyse the contribution of road traffic emissions to tropospheric O_3 over Europe and Germany for present day conditions and a future projection. Therefore, I applied for the first time a newly developed global-regional model for consistent zooming into particular areas from a coarsely resolved global chemistry-climate model. The model has been equipped with a tagging technique, i.e. an accounting system following the reaction pathways from the individual emission sources. Simulation results have been evaluated with respect to tropospheric gas phase chemistry by comparison with observations from satellite instruments, ground based in situ measurements and O_3 sonde data.

The road traffic source attribution revealed an average contribution to the tropospheric O_3 column up to 850 hPa in Europe of $11 \pm 1\%$ for year 2008 conditions. During winter the contribution is mainly influenced by long range transport, while local production is more important during summer. The global and regional models simulate comparable continentally averaged values. On the regional scale (e.g. Po basin), however, differences between global and regional models are considerable. In particular, for the representation of extreme O_3 values, finer resolved models are indispensable for quantitative regional source attributions. The sensitivity of the source attribution are mainly governed by uncertainties of the estimates of natural and anthropogenic NO_x emissions.

The analysis applied to a future projection for the year 2030 suggests a decrease of the contribution from road traffic emissions during summer by 2–3 percentage points. However, the effects of regional emission mitigation are affected by global conditions due to the important role of long range transport of O_3 and its precursors. The projected regional decrease of NO_x emissions in Germany leads to an increase of surface O_3 levels in most German cities, unless VOC emissions are not likewise reduced.

Chapter 1

Introduction

1.1 Motivation

Stratospheric ozone (O_3) is important for life on earth, as it absorbs high energetic radiation in the ultra violet range. In contrast to this, tropospheric O_3 has several negative aspects. First, O_3 is a greenhouse gas and contributes to global warming (e.g. Myhre et al., 2013). Second, O_3 is a strong oxidant and cause health problems (e.g. respiratory problems, headache) to humans and animals (e.g. World Health Organization, 2003, Royal Society, 2008). In addition, plants are damaged by long term exposure to O_3 (e.g. Fowler et al., 2009), which can lead to decreased yield rates of several crops (e.g. Mauzerall et al., 2001, Teixeira et al., 2011).

Further, O_3 is an important source of the hydroxyl radical (OH), which controls the self-cleansing capacity of the atmosphere. Accordingly, concentrations of OH control the lifetime of different other pollutants (as carbon monoxide, CO) and greenhouse gases (as methane (CH_4); e.g. Levy, 1971, Logan et al., 1981, Monks, 2005).

In the troposphere two important O_3 sources exist: the downward transport from the stratosphere, where O_3 is formed by photolysis of oxygen, and photochemical production in the troposphere. This photochemical production involves different precursors (Crutzen, 1974) such as nitrogen oxides (NO_x , including nitrogen oxide (NO) and nitrogen dioxide (NO_2)), CO and volatile organic compounds (VOCs). The production of O_3 is highly non-linear and depends on the ratio of NO_x/VOC (e.g. Royal Society, 2008). Under conditions with large NO_x but low VOC concentrations the production rates of O_3 are rather low. Large concentrations of both precursors, however, lead to large production rates of O_3 .

The production of O_3 is not only governed by the available precursors, but depend also on the meteorological conditions (e.g. Logan, 1985). Especially under stagnant weather conditions during summer very large O_3 concentrations can occur in regions with large amounts of precursors (so called summer smog). Even if the number of these summer smog events decreased considerably since the 1990s, the limits of the World Health Organisation (WHO) of a maximum concentration of $100 \mu\text{g m}^{-3}$ (World Health Organization, 2006) are exceeded regularly in Germany. Moreover, also the thresholds for damages to vegetation are exceeded often (Minkos et al., 2016). One reason for this is that O_3 in the troposphere has a lifetime of about one month (e.g. Seinfeld and Pandis, 2006). Accordingly, increasing emissions of precursors in Asia or America can increase the O_3 concentrations in Europe (e.g. HTAP, 2010a). Therefore, even if maximum O_3 values are decreasing, a profound

understanding of the sources, contributing to the tropospheric O₃ levels, is very important (e.g. Monks et al., 2015). Especially, because O₃ is also important for the global radiation budget and the self-cleansing capacity of the troposphere.

Sources of O₃ precursors in the troposphere are numerous. These sources are natural, such as NO_x emissions from soils or lightning (e.g. Vinken et al., 2014, Schumann and Huntrieser, 2007) or VOC emissions from plants (e.g. Guenther et al., 1995, 2006), as well as anthropogenic. Anthropogenic source of NO_x emissions are combustion processes, including emissions from industrial processes and emissions from the transport sector. A very important source, in particular in densely populated regions, are road traffic emissions.

Because of the non-linearity of the O₃ production the contribution of these precursors to O₃ can not be calculated directly from the amount of emissions. Further, measurements of the amount of O₃ produced by a specific source such as road traffic are not possible. Analyses of the contribution of emissions to O₃ are only possible using complex model simulations with chemistry-climate models (e.g. Grewe, 2004, Eyring et al., 2007, Dahlmann et al., 2011, Emmons et al., 2012).

The importance of the road traffic emissions for the tropospheric O₃ budget has been emphasised by different previous studies (e.g. Granier and Brasseur, 2003, Niemeier et al., 2006, Matthes et al., 2007). These studies, however, used the so-called perturbation method, which compares results from two different simulations; one simulation including all emissions and one simulation with reduced road traffic emissions. Due to the non-linearity of the O₃ chemistry this approach likely underestimates the actual contribution (e.g. Grewe et al., 2012). An alternative approach to investigate the contribution is the so-called tagging method (e.g. Lelieveld and Dentener, 2000, Emmons et al., 2012, Gromov et al., 2010, Grewe, 2013). These tagging methods use additional diagnostic species, which follow the reaction pathways of the different trace gases emitted from different source sectors.

In addition, all previous studies used global models with coarse resolutions. Due to this coarse resolution, O₃ production in the troposphere is overestimated (e.g. Wild and Prather, 2006), which can lead to an erroneous estimation of the contribution of certain source sectors. Besides this, global models provide only limited regional information about the contribution of different source sectors. Especially the emissions of the road traffic sector are very localised near the densely populated regions, rendering regional information about the contributions of emissions from the road traffic sector is crucial.

These limitations provide the motivation for the present thesis, in which I investigate the contribution of road traffic emissions on tropospheric O₃ in Europe and Germany in detail by using a tagging method within a sophisticated global-regional model chain.

1.2 Scientific Questions

The scientific questions which motivated this thesis are stated in detail as follows:

- Q₁: What is the contribution of the road traffic emissions to tropospheric O₃ in Europe for present day conditions? How do long-range transport and local production influence the contribution?

Q₂: How sensitive are the results with respect to uncertainties of anthropogenic and natural emission estimates?

Q₃: How does the contribution of road traffic emissions to tropospheric O₃ change for a future projection and how are these results affected by global changes of the emissions?

Besides these three questions, one further question focuses on the methodological error made by the coarse resolution global chemistry-climate models:

Q₄: Do the results of the contribution depend on the resolution of the model and/or the emissions?

1.3 Investigation Strategy

To answer the scientific questions of the present thesis I applied for the first time the newly developed model system MECO(n) (MESSy-fied ECHAM and COSMO models nested n-times, Kerkweg and Jöckel, 2012a,b) with a set-up involving complex tropospheric and stratospheric chemistry. The MECO(n) model system allows for a nesting of the regional chemistry-climate model COSMO-CLM/MESSy into the global chemistry-climate model EMAC and into itself. I use MECO(n) with three instances¹: EMAC and two COSMO-CLM/MESSy refinements, one covering Europe with 50 km resolution and a second covering Germany with 12 km resolution. Accordingly, the simulated contributions for Europe and Germany can be compared for different resolutions.

First, preparatory work was necessary, before the scientific questions could be answered. This preparatory work is described in Chap. 3 and included mainly the implementation of the tagging method into the MECO(n) model system (Sect. 3.1.7). In a next step, the simulation results of the MECO(n) model system were evaluated (Sect. 4.3). As an evaluation of the meteorology simulated by MECO(n) has been conducted by Hofmann et al. (2012), the focus of the evaluation was on the tropospheric chemistry. The simulation results were compared to satellite observations (Sect. 4.3.2), ground level observations (Sect. 4.3.3) and O₃ sonde measurements (Sect. 4.3.4).

Next, different simulations were conducted to answer the scientific questions Q₁, Q₂ and Q₄. First a reference simulation applying the same emission in all model instances were performed to quantify the contribution of the road traffic emissions for present day conditions and to compare the results simulated by EMAC and COSMO, respectively. Further a simulation were performed in which the resolution of the emissions used by COSMO were artificially decreased to investigate the impact of a coarse emission resolution. As the estimates of natural and anthropogenic emissions are uncertain, several further sensitivity simulations were performed. In these simulations the anthropogenic emissions as well as emission of NO_x from soils and biogenic isoprene emissions were modified systematically in COSMO to estimate how sensitive the results are on uncertainties of the emission estimates.

¹In computer science the word 'instance' describes a specific realisation of an object. The term is used throughout the present thesis to describe a specific realisation of EMAC/COSMO.

Finally three simulations for a projected future scenario of the year 2030, but with different global boundary conditions, were performed and analysed in Chap. 6 to tackle question Q₃ in detail.

The Appendix of this thesis gives further technical details about the performed simulations as well as further information (e.g. the total amounts of emissions). These details are important for the reproducibility.

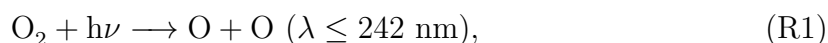
Chapter 2

Background

This chapter summarises the most important background information for this study, focusing on the (chemical) sources and sinks of tropospheric ozone. The information of this chapter is mainly based on Jacob (1999), Monks (2005), Seinfeld and Pandis (2006), and Royal Society (2008).

2.1 Tropospheric and stratospheric ozone

Ozone (O_3) in the stratosphere is essential for life on Earth as it absorbs ultraviolet (UV) radiation, mainly in the UV-B range (280–315 nm), which otherwise can cause skin cancer or damage plants. Within the stratosphere O_3 is formed by a mechanism proposed by S. Chapman in 1930 (called Chapman cycle):



The mechanism is initiated by the photodissociation of molecular oxygen (O_2) to two oxygen atoms (R1). The energy needed to break the O_2 double bond is large, therefore the dissociation requires light with a wavelength of less than 242 nm. In the presence of a third molecule (denoted as M in (R2), e.g. O_2 or N_2), which is needed to transport the excess energy away, the oxygen atom can react with O_2 to form O_3 . Ozone is photodissociated to an oxygen atom and O_2 at wavelengths smaller than 319 nm (R3). The larger maximum wavelength for the photodissociation of O_3 compared to the dissociation of O_2 is caused by the lower binding energy of O_3 compared to O_2 . The oxygen atom, produced by the dissociation of O_3 can further react with O_3 , producing two O_2 molecules (R4). The Chapman cycle leads to larger O_3 mixing ratios than observed in the stratosphere, because reactions of O_3 with other substances like nitrogen oxides or chlorine species are not considered by the Chapman cycle.

Ozone is not only radiative active in the shortwave, but also in the longwave. Therefore O_3 is a greenhouse gas. In the recent assessment report 5 (AR5) of the Intergovernmental

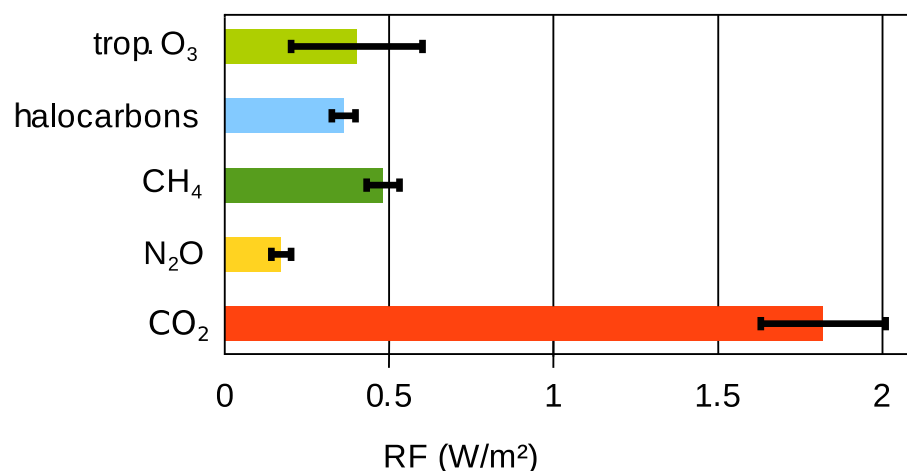


Figure 2.1: Global RF since 1750 (in W m^{-2}) of CO_2 , N_2O , CH_4 , all halocarbons and tropospheric O_3 (trop. O_3) as estimated by Myhre et al. (2013). The error bars indicate the 5–95 % confidence range.

Panel on Climate Change (IPCC, Myhre et al., 2013) the radiative forcing (RF) of O_3 since pre-industrial times (the year 1750) is estimated to $(0.35 \pm 0.20) \text{ W m}^{-2}$.

The RF of stratospheric O_3 is estimated to be $(-0.05 \pm 0.10) \text{ W m}^{-2}$, caused primarily from ozone depletion by halocarbons in the stratosphere, resulting in a positive RF in the shortwave and a negative RF in the longwave. In contrast to this, the RF of tropospheric O_3 is estimated to $(0.40 \pm 0.20) \text{ W m}^{-2}$, caused mainly by the increase of O_3 in the troposphere due to emissions of O_3 precursors.

Figure 2.1 summarises the RFs of the most important greenhouse gases (of anthropogenic origin). The RF of tropospheric O_3 is not as large as for carbon dioxide (CO_2 , $(1.82 \pm 0.19) \text{ W m}^{-2}$), but after methane (CH_4 , $(0.48 \pm 0.05) \text{ W m}^{-2}$) it is the greenhouse gas with the third largest forcing.

Besides the RF, tropospheric O_3 has negative impacts on life. Two important examples are the impact of O_3 on human health and on plants.

Large level of O_3 can cause headaches. Most health problems, however, are related to effects on the respiratory system. In contrast to highly water-soluble gases like sulphur dioxide (SO_2), O_3 is not removed in the upper respiratory tract. Instead O_3 is transported deeper into the lungs, where O_3 can damage tissues in the lower respiratory system (e.g. Royal Society, 2008, Filippidou and Koukoulia, 2011). Therefore outdoor athletic activities are not advisable during events with large ground level O_3 . The World Health Organisation (WHO, World Health Organization, 2006) suggests an upper limit for the O_3 concentration averaged over eight hours of $100 \mu\text{g m}^{-3}$. In Europe the standard defined by the European Commission sets a limit for the maximum eight hour mean concentration of $120 \mu\text{g m}^{-3}$, which should not be exceeded on more than 25 days per year¹.

One important effect of O_3 on plants is the uptake of O_3 by the plants stomata, which can damage the plant tissues. As a consequence, large O_3 levels can lead to reduced crop yields. An example is given in Fig. 2.2 which shows the yield loss rates for different O_3

¹ Averaged over three years, see <http://ec.europa.eu/environment/air/quality/standards.htm>, last access 07.12.2016

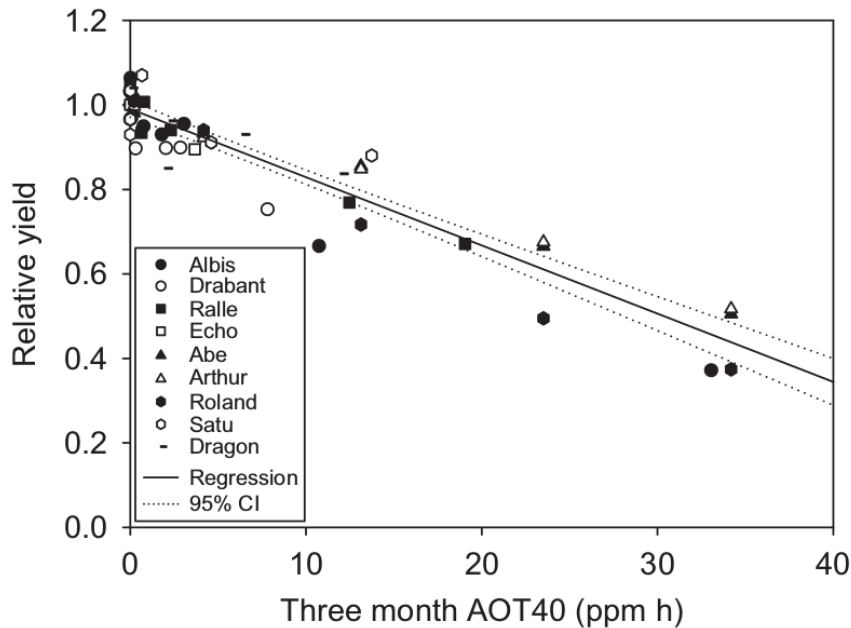


Figure 2.2: Dependency between the decrease of the relative yield of wheat with increasing O_3 concentrations. Summarised are results from different publications (denoted by the different symbols). As a measure of O_3 exposure the AOT40 standard was chosen, which is defined as the accumulated O_3 exposure over a threshold value (hourly mean O_3 mixing ratios above 40 nmol mol^{-1}) during daylight hours (in $\mu\text{mol mol}^{-1} \text{ h}$). Diagram reprinted with permission from Mills et al. (2007).

exposures of wheat, summarised from different studies by Mills et al. (2007). All studies indicate a decrease of the yield rate with increasing O_3 exposure, but the effect differs for different plants. As an example, the decrease of the yield rate with increasing O_3 exposure for maize is according to Mills et al. (2007) lower than for wheat. As the uptake by plants is also an important sink for O_3 a more detailed discussion follows in Sect. 2.4.

2.2 Ozone budget of the troposphere

Ozone in the troposphere has several sources and sinks, which are discussed here. The tropospheric O_3 burden has been estimated by Young et al. (2013) to be $(337 \pm 23) \text{ Tg}$ for present day conditions. Similar values are found by various model studies and calculations based on observations (as summarised in Table 8.1 of Myhre et al., 2013). The values reported by Young et al. (2013) are based on simulation results from different models. Only for a subset of the models information about production and loss processes to the tropospheric O_3 burden were provided. These values are summarised in Fig. 2.3. Tropospheric O_3 on the one hand originates from downward transport from the stratosphere (Sect. 2.1), on the other hand tropospheric O_3 can be produced in situ from anthropogenic and biogenic precursors (as it will be discussed in Sect. 2.3). As given by Young et al. (2013) $(477 \pm 96) \text{ Tg a}^{-1}$ of O_3 are transported downward from the stratosphere,

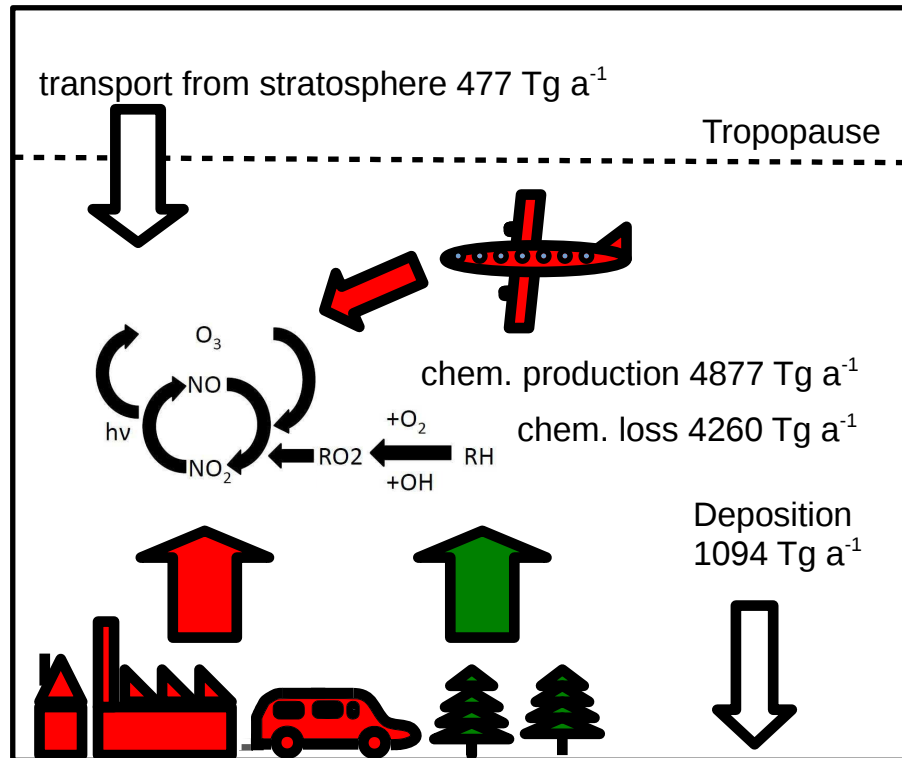


Figure 2.3: Illustration of the tropospheric O_3 budget. The coloured arrows indicate emissions of precursors from which O_3 is formed (more details follow in Sect. 2.3) from anthropogenic (red) or natural (green) sources. Numbers are according to Young et al. (2013). Details about the uncertainties are given in the text.

while $(4877 \pm 853) \text{ Tg a}^{-1}$ are produced in situ (the given uncertainties are the standard deviation with respect to the participating models).

Ozone has two sinks in the troposphere. The most important sink is chemical destruction (Sect. 2.3), which accounts for an O_3 loss of $(4260 \pm 645) \text{ Tg a}^{-1}$. Dry deposition is the second sink of O_3 . As this process takes place at the Earth's surface, near-surface O_3 concentrations are heavily influenced by this process. In general, dry deposition accounts for an annual O_3 loss of $(1094 \pm 264) \text{ Tg a}^{-1}$. A more detailed discussion of this dry deposition process follows in Sect. 2.4. These numbers, however, should be taken with some care, as the different models calculate O_3 loss and production not in a consistent manner (details are given by Young et al., 2013).

2.3 Chemical production and destruction of ozone

Chemical production of O_3 in the troposphere takes place via a photochemical cycle:



The atomic oxygen which is formed through the photodissociation of NO_2 (at wavelengths smaller than $\lambda = 424$ nm, R5) quickly recombines with O_2 to form O_3 (R6). Once O_3 is formed it reacts with NO to form NO_2 (R7). Due to this quick cycling between NO and NO_2 they are usually treated as chemical family $\text{NO}_x = \text{NO} + \text{NO}_2$.

As long as no other reactions than R5–R7 take place, the chemical system reaches a steady state. The mixing ratios of O_3 , NO and NO_2 in this steady state depend on the initial conditions as well as on the photolysis rate of NO_2 and the reaction rate coefficient of reaction R7 (Seinfeld and Pandis, 2006).

The Leighton ratio (Φ , Leighton, 1961) is common to investigate, if chemical O_3 production is within this steady state. It is defined as:

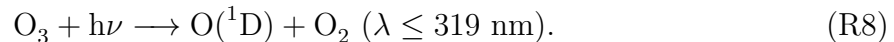
$$\Phi = \frac{J_{\text{NO}_2}[\text{NO}_2]}{k_7[\text{NO}][\text{O}_3]}. \quad (2.1)$$

Here, J_{NO_2} is the photolysis frequency of NO_2 and k_7 the reaction rate coefficient of reaction R7². A Leighton ratio around 1 indicates a photostationary state and is usually found in polluted regions (e.g. Carpenter et al., 1998, Thornton et al., 2002). In regions with low NO and NO_2 mixing ratios, Leighton ratios above 1 are found often (e.g. Hauglustaine et al., 1999, Hosaynali Beygi et al., 2011, Trebs et al., 2012). In these cases reactions of NO to NO_2 involving HO_2 and RO_2 radicals play an important role (details about HO_2 , RO_2 and these reaction pathways are discussed in Sect. 2.3.1 and 2.3.2).

It is important to note that the cycle R5–R7 is catalytic and does not consume any NO_x molecules. Therefore several O_3 molecules can be produced by one NO_x molecule before this molecule is removed from the atmosphere by other reactions (Sect. 2.3.4) or by deposition (Sect. 2.4).

The amount of O_3 , which is produced by this cycle is too low compared to the O_3 values found in the troposphere. As discussed below, oxidation products from the oxidation of carbon monoxide (CO), methane (CH_4) (Sect. 2.3.1) or from oxidation of other hydrocarbons (Sect. 2.3.2) can react with NO . These reactions lead to the formation of NO_2 without involving reactions of O_3 with NO which destroy O_3 . The NO_2 molecules which are formed additionally can be dissociated to form O_3 , leading to O_3 mixing ratios which are larger than produced solely by the cycle R5–R7.

Ozone is not only destroyed chemically by the reaction of NO and O_3 , but also by direct photolysis of O_3 (at wavelength smaller than 319 nm):



The produced excited $\text{O}({}^1\text{D})$ atom (R8) has two possible fates. It can collide with other molecules (M) to transfer its excess energy, forming ground state atomic oxygen. This ground state atomic oxygen reacts with O_2 to form O_3 . Consequently, no O_3 is destroyed by this path. A second reaction path of the excited $\text{O}({}^1\text{D})$ atom is the reaction with water vapour forming the OH radical:



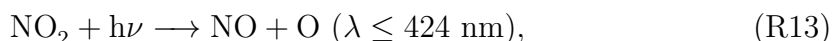
²In the present thesis concentrations are always written in squared brackets, otherwise mixing ratios are considered.

As the probability that the excited $O(^1D)$ atom reacts with water vapour increases with increasing amount of water vapour, more OH is formed in humid than in dry air. OH is the primary oxidizing species within the troposphere. The lifetime of OH is only several seconds, with a global mean concentration in the order of 10^6 molecules cm^{-3} (Seinfeld and Pandis, 2006). Two examples of the oxidation by OH – for CO and CH_4 – are provided in the next section.

Besides the destruction of O_3 by reactions with NO and by photolysis of O_3 also other chemical sinks of O_3 exist, which are not discussed here in detail (e.g. Monks, 2005, Seinfeld and Pandis, 2006). Important loss processes of O_3 include reactions with HO_2 or reactions with VOCs (cf. Sect. 3.1.7).

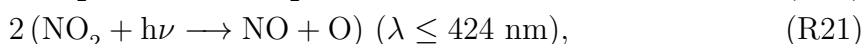
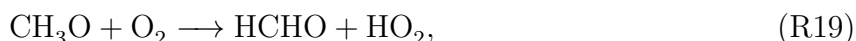
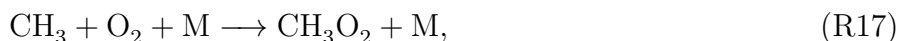
2.3.1 Oxidation of carbon monoxide and methane

The oxidation pathway of CO is:



This chain is initiated by the oxidation of CO by OH (R10), forming one hydrogen atom, which quickly reacts with molecular oxygen to form the hydroperoxyl radical (HO_2 , R11). In the presence of NO, HO_2 reacts with NO to form NO_2 and OH (R12), which can then initiate a new oxidation chain of CO. Through the formation of NO_2 , O_3 can be formed by photolysis as described in Sect. 2.3 (R13 and R14). The overall net reaction (R15) consumes one CO and two O_2 molecules and produces one O_3 and one CO_2 molecule.

The CH_4 oxidation chain is:



The oxidation of CH_4 by OH leads to the formation of the methyl radical (CH_3 , R16), which reacts very fast with O_2 to form the methyl peroxy radical (CH_3O_2 , R17). Reactions of the methyl peroxy radical with NO lead to the formation of NO_2 and the methoxy

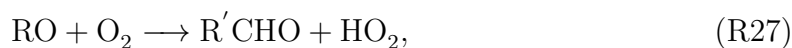
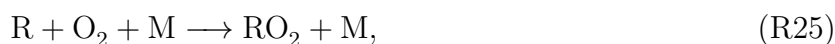
radical (CH_3O , R18). The methoxy radical itself reacts with O_2 forming formaldehyde (HCHO) and HO_2 (R19).

The reactions R18 and R20 lead to the production of two NO_2 molecules, from which O_3 can be produced (R21 and R22, and Sect. 2.3). Overall one CH_4 and four O_2 molecules are consumed by the reaction chain, leading to the production of two O_3 molecules, one HCHO and one H_2O molecules, respectively (R23).

Formaldehyde can further photolyse or react with OH . The lifetime against photolysis is several hours, while the lifetime against oxidation with OH is more than a day. Both reaction pathways lead to the formation of CO , therefore the reaction chain of CO is linked to the reaction chain of CH_4 . Therefore, HCHO is a reservoir specie of CO (discussion follows in Sect. 2.3.3)

2.3.2 Simplified oxidation of other hydrocarbons

Many hydrocarbons are oxidised in a way which is very similar to the oxidation of CH_4 . Depending on the length of the CH -chain the oxidation is much more complex than for CH_4 . Therefore, a simplified oxidation chain as presented by Seinfeld and Pandis (2006) is discussed here. This simplified view holds in general for many hydrocarbons (denoted as RH with R being a not further defined carbon-hydrogen molecule):



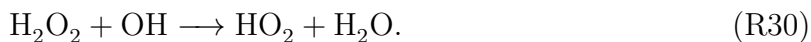
In analogies to the reactions involving CH_3O_2 (R17 and R18) the oxidation of higher hydrocarbons (R24) leads to the formation of the alkyl peroxy radical (RO_2 , R25), which can react with NO to form NO_2 (R26). The alkoxy radical RO reacts rapidly with O_2 forming higher carbonyl products ($\text{R}'\text{CHO}$, R27), which can further be oxidized as described for HCHO . This includes reactions of NO with these oxidation products forming NO_2 . Alkoxy radicals with long CH -chains can undergo more complex reactions, which will not be discussed here.

Throughout the present thesis these hydrocarbons are summarised as VOCs. No differentiation is performed between the terms non methane hydrocarbons (NMHCs) and volatile organic compounds (VOCs) for reasons of simplicity. The definition of VOCs contains not only the NMHCs but also oxygenated NMHCs (e.g. alcohols, aldehydes and organic acids). NMHCs are a subgroup of the VOCs.

2.3.3 Atmospheric reservoir species

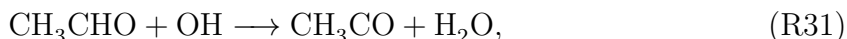
Reservoir species are an important group of species of the tropospheric chemistry. These species bind atoms or molecules, preventing them from reacting with other molecules. Depending on the lifetime of these species, they can be transported over long distances.

Besides HCHO (Sect. 2.3.1) some other important reservoir species are discussed briefly. The first is hydrogen peroxide (H_2O_2), which is formed by reactions of HO_2 with HO_2 . This results in the formation of O_2 and H_2O_2 , which is a temporary reservoir for HO_2 and OH (combined as HO_x). Hydrogen peroxide has two possible fates:



The first reaction (R29) leads to a cycling from HO_2 to OH , because initially H_2O_2 is formed by the reaction of two HO_2 molecules and R29 forms two OH molecules. The second reaction (R30), however, leads to a loss of HO_x . The initial amount of two HO_2 molecules and one OH molecule are reduced to one HO_2 molecule.

A very important reservoir species is the family of peroxyacetyl nitrates (PANs), from which the first compound is usually called PAN³ ($\text{CH}_3\text{C}(\text{O})\text{O}_2\text{NO}_2$). One way for the formation of PAN is:



In the first step acetaldehyde⁴ (CH_3CHO) reacts with OH forming CH_3CO (R31) which reacts quickly with O_2 to form the peroxyacetyl radical $\text{CH}_3\text{C}(\text{O})\text{O}_2$ (R32). In a subsequent step the peroxyacetyl radical can either react with NO forming NO_2 (not shown) or with NO_2 forming PAN (R33).

The most important sinks of PAN are thermal decomposition and photolysis. In the lower troposphere the lifetime is dominated by thermal decomposition, with lifetimes of about 3 h near surface. At a temperature of 250 K the lifetime against thermal decomposition increases to ≈ 5 months (Singh, 1987). Under these conditions the lifetime is limited by photolysis to around 3 month (e.g. Tereszchuk et al., 2013). If PAN is formed in a polluted environment and transported upwards (e.g. through convection) into the upper troposphere, PAN can be transported over long distances. When transported downwards again, PAN decomposes thermally back to NO_2 and the peroxyacetyl radical. This process can transport O_3 precursors over long distances.

2.3.4 Non-linearity of ozone production

In Sect. 2.3 the production of O_3 by the photochemical cycle (reactions R5–R7) has been discussed. The amount of O_3 present in the troposphere cannot be explained solely by this photochemical cycle. As have been discussed in Sect. 2.3.1 and Sect. 2.3.2, O_3 can also be produced by reactions of NO with HO_2 or RO_2 . These reactions lead to the generation of NO_2 , and subsequent formation of O_3 . This complex interplay of different reactions leads

³The parenthesis in the notation depicts a double bond between the carbon atom and the oxygen atom.

⁴Among others acetaldehyde is an oxidation product of hydrocarbons.

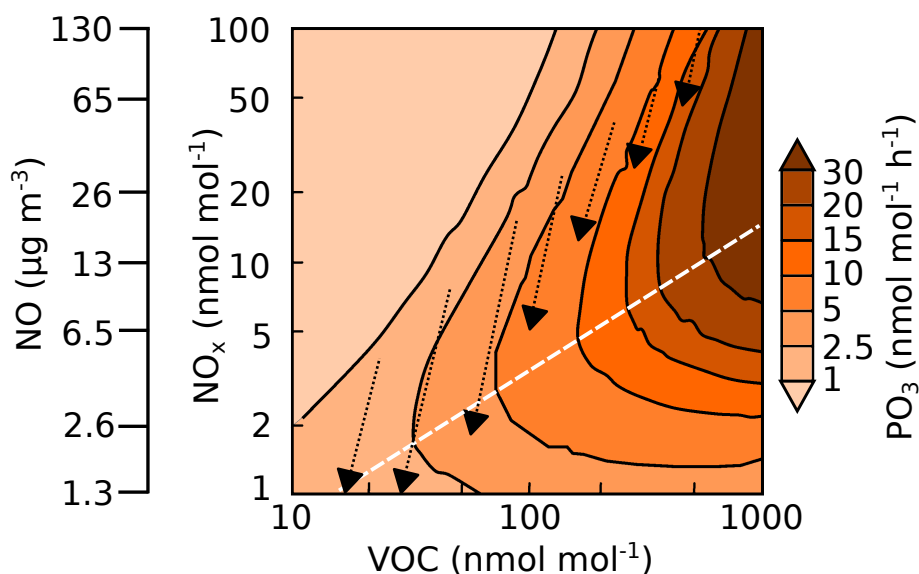


Figure 2.4: Isopleth showing the net O_3 production (PO_3 in $\text{nmol mol}^{-1} \text{h}^{-1}$) as function of mixing ratios of VOCs (as amount of carbon in nmol mol^{-1} and NO_x in nmol mol^{-1}). The underlying calculations were performed for clear sky mean summer daytime conditions. The white dashed line indicates the threshold from 'NO $_x$ '- to 'VOC-limited' (details see text). The arrows indicate the development of the NO_x and VOC mixing ratios for air parcels due to chemical ageing over an 8 hour period (during daytime). The second y-axis depicts the NO_x concentration (in abundance of NO) at 288.5 K and 1023.15 hPa (Sect. 2.7). Adopted from Sillman (1999).

to a non-linear behaviour of the O_3 production. To illustrate this, Fig. 2.4 shows the O_3 production as a function of NO_x and VOC mixing ratios.

First of all the dependency of the O_3 production is analysed for fixed, but sufficiently large, values of VOCs. An increase of NO_x leads to an increase of the O_3 production for small values of NO_x . A further increase of NO_x leads to a slowing down of the increase of the O_3 production. Eventually, the production of O_3 reaches a local maximum and finally decreases with increasing NO_x values. The line connecting these local maxima is called the ridge line. The ridge line separates two regimes, called 'NO $_x$ -limited' and 'VOC-limited'. In the 'NO $_x$ -limited' regime the production of O_3 is mainly limited by the amount NO_x . In the 'VOC-limited' regime, however, enough NO_x is available and the production is limited by the amount of VOCs.

The non-linearity of the O_3 chemistry has important implications for mitigation strategies. Only in 'NO $_x$ -limited' areas a reduction of NO_x emissions leads to a direct decrease of the O_3 production. In 'VOC-limited' areas a decrease of NO_x can lead to an increased O_3 production. In such areas, it is crucial to limit not only the NO_x emissions, but also the emissions of VOCs. Both precursors, however, have not only anthropogenic but also natural origins which must be considered for mitigation options. More details about the sources follow in Sect. 2.6.

Further the non-linearities affect the production of O_3 downwind of large cities. This is indicated by the dashed arrows shown in Fig. 2.4. These arrows indicate the chemical ageing of air parcels during 8 hours (details given by Milford et al., 1994) for different initial

amounts of NO_x and VOCs. During the chemical ageing of the air masses the VOC/NO_x ratio increases, the O_3 production might transits from 'VOC-limited' to ' NO_x -limited'. Depending on the initial conditions of the air parcel the production of O_3 increases during the chemical ageing. In addition to the chemical ageing of the air masses, mixing can alter the composition during the transport away from the cities (or other large sources like power plants). As the NO_x mixing ratios outside the cities are usually lower than inside the cities, the NO_x mixing ratio of the airmass is reduced by mixing during transport. This reduction of the NO_x mixing ratio might increases the O_3 production within the airmass. In addition, large biogenic sources of VOC (e.g. forests) can further enhance the O_3 production outside of cities (e.g. Ehlers et al., 2016).

To provide an example of measured NO_2 concentrations, the average values for the year 2014 as reported from the 'Bayerisches Landesamt für Umwelt' at the station in Munich Stachus (city centre) and Andechs (a rural station near the Ammersee, around 40 km away from Munich Stachus) are compared (LfU, 2015): for Munich Stachus daily average concentrations of more than $50 \mu\text{g m}^{-3}$ are reported throughout most time of the year. Accordingly, the O_3 chemistry is clearly 'VOC-limited'. Compared to this daily average concentrations below $10 \mu\text{g m}^{-3}$ are usually reported at Andechs. Especially during summer, the values drop mostly below $5 \mu\text{g m}^{-3}$, leading to an O_3 chemistry, which is very likely ' NO_x -limited'.

To discuss the reason for the non-linearity of the O_3 production, Fig. 2.5a depicts a simplified overview of the tropospheric O_3 chemistry. In very clean pristine regions (e.g. in the South Pacific) with very low NO_x values oxidation of CO and CH_4 is initiated by OH (Sect. 2.3.1). OH itself is produced by photolysis of O_3 . At low NO_x values in the troposphere virtually no O_3 production occurs through the NO_x -cycle (reactions R5–R7). Therefore, a net loss of O_3 is present, as HO_2 reacts mainly with itself (forming H_2O_2) or with CH_3O_2 (forming methyl hydroperoxide, CH_3OOH) but not with NO.

In the ' NO_x -limited' regime the NO_x mixing ratios are sufficiently large, so that O_3 can be formed by cycles of NO_x as part of the CO or CH_4 oxidation chain. The reactions forming H_2O_2 and CH_3OOH are still the most important radical sinks for HO_2 and CH_3O_2 . These reactions, however, compete with the reactions of NO (forming NO_2) for HO_2 and CH_3OOH . Increasing the NO_x mixing ratio in this regime therefore leads to more reactions of NO with HO_2 or CH_3O_2 , thus increasing the O_3 production.

With further increasing NO_x mixing ratios the reaction:



forming nitric acid (HNO_3) becomes important. This reaction removes both, the OH radical and NO_x from the atmosphere and is a major removal pathway of NO_x during daytime. Nitric acid is very effectively removed from the atmosphere by wet deposition (Sec. 2.4). As the O_3 production cycle is driven by the OH radical, which subsequently oxidises CO, CH_4 or VOCs (not shown in Fig. 2.5a, see Sect. 2.3.2), increasing amounts of NO_x lead to more reactions of OH with NO_2 and subsequently less production of O_3 . Increasing instead the amount of CO, CH_4 or VOCs, the oxidation cycles of these species can compete more effectively with NO_2 for OH. Larger concentrations of CO, CH_4 or VOCs increase the O_3 production in the 'VOC-limited' case.

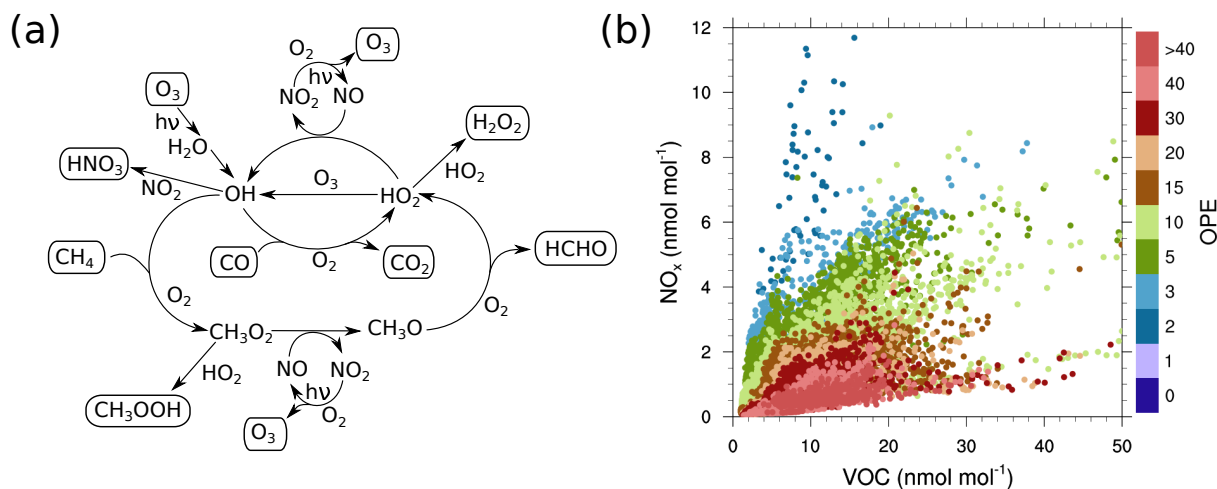


Figure 2.5: (a) Simplified overview of the tropospheric O_3 chemistry involving oxidation of CO , CH_4 and the NO_x cycles (adapted from Royal Society, 2008). (b) Dependency between the O_3 production efficiency (OPE) and mixing ratios of NO_x (in nmol mol^{-1}) and VOCs (weighted by the amount of carbon atoms of the respective species which are summarised as VOC, in nmol mol^{-1}). The values represent monthly average ground-level values in Europe for June–August 2008 and are taken from the *REF* simulation (Sect. 3.3).

It is important to note that only for two conditions a chemical net O_3 loss in the troposphere occurs. This is the case in very clean pristine regions and in very polluted regions, where titration of O_3 via reaction R7 prevails.

Several measures exist to estimate, if O_3 production takes place in the 'NO $_x$ -limited' or the 'VOC-limited' regime. In the present thesis the O_3 production efficiency (OPE) concept is used. The OPE measures the number of O_3 producing cycles of a NO_x molecule before it is removed by chemical loss. Assuming steady state for NO_x and the reaction R34 to be the only chemical loss of NO_2 , the OPE can be defined as (Jacob, 1999):

$$\text{OPE} = \frac{2k_a[HO_2][NO]}{k_b[NO_2][OH]}, \quad (\text{R35})$$

with k_a and k_b being the reaction rate coefficients of the corresponding reactions.

Figure 2.5b shows OPE values at ground level in Europe for different NO_x and VOC mixing ratios. Regions with large amounts of NO_x but low amounts of VOC are indicated by low values of the OPE. In this regions NO_x is effectively removed by reaction R34. With decreasing mixing ratios of NO_x the OPE increases (as long as the VOC levels are sufficiently large). For fixed values of NO_x also an increase of VOC increase the OPE, as OH reacts more effectively with the VOCs as with NO_2 .

2.4 Dry and wet deposition of ozone

In general two pathways exist for the final removal of trace gases from the atmosphere: dry and wet deposition. The term dry deposition describes the transport of trace gases down

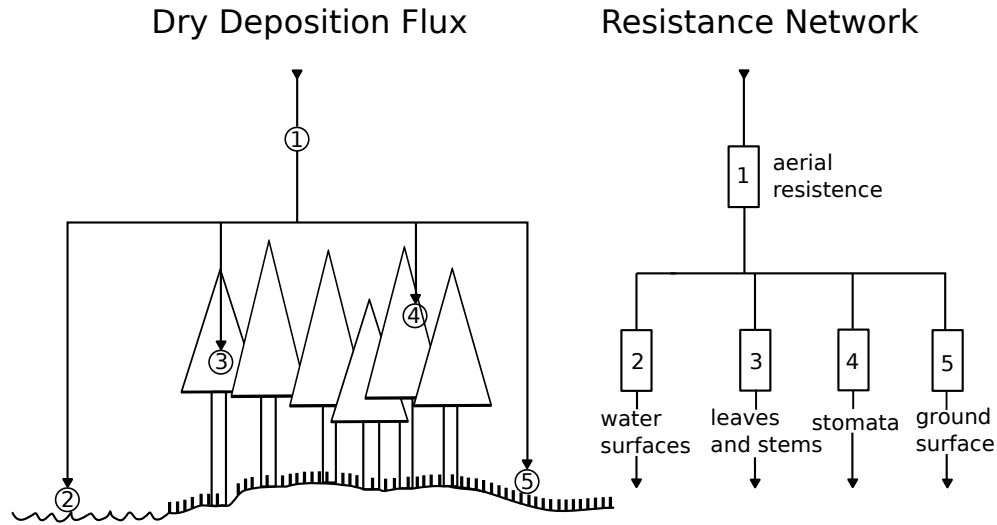


Figure 2.6: Schematic illustration of the processes involved in dry deposition of trace gasses and the analogy of a resistance network in the representation of these processes. Adapted from Zellner (1999).

to the surface through turbulence, where the trace gases are deposited on the surface or are taken up by the biota. Wet deposition describes the uptake of species by cloud water or precipitation (scavenging) and its subsequent downward transport to the surface. As O_3 is not very soluble, it is removed mainly by dry deposition. Wet deposition, however, is mainly important for different O_3 precursors and reservoir species. Therefore this process is discussed only briefly at the end of this section.

The dry deposition mass flux (F) is usually (e.g. Wesely and Hicks, 2000) calculated as

$$F = -v_d \cdot C \quad (2.2)$$

with the concentration C of a given trace gas and the dry deposition velocity v_d . The minus sign indicates by definition a downward flux. The dry deposition velocity depends on different factors, which are summarised in Fig. 2.6. First of all, the trace gases are transported downward to a thin layer above the surface by turbulent motions. The strength of this turbulent motions are controlled by the meteorological conditions. From this laminar thin layer diffusive transport takes place (both processes are summarised as aerial resistance in Fig. 2.6). Finally, different receptors take up the trace gases. These receptors are the plants stomata, the ground surface, leaves and stems, as well as water surfaces. The later, however, plays only a minor role for O_3 . Besides the stomata and non-stomatal uptake, in-canopy chemistry plays a role. In this process e.g. O_3 can directly react with trace gases like NO or $VOCs$ emitted by the plants. This process is not covered here (e.g. Lathièrè et al., 2015).

Both processes, the stomatal and non-stomatal uptake, depend on the vegetation and the surface type, respectively. As an example Table 2.1 lists measured dry deposition velocities of O_3 for four different vegetation types, showing the largest dry deposition velocities for a deciduous forest (1.0 cm s^{-1}) and the lowest dry deposition velocities over grassland (0.2 cm s^{-1}). The dry deposition velocities of O_3 depend not only on the vegetation type, but also on the daytime and season (e.g. Pio et al., 2000). As an example

Table 2.1: Typical dry deposition velocities for O₃ from Padro (1996) during summer for different land-use types.

	v_d early afternoon (cm s ⁻¹)	v_d night (cm s ⁻¹)
deciduous forest	1.0	0.2
vineyard	0.5	0.2
cotton	0.8	0.2
grass (senescent)	0.2	0.05

the dry deposition velocities during night shown in Table 2.1 are notably smaller than during daytime. In addition also the meteorological condition play, especially for the aerial resistance, an important role.

Over vegetated surfaces between $1/3$ and $2/3$ of the dry deposition is due to stomatal uptake (Fowler et al., 2009). As suggested by Coyle et al. (2009) three different regimes exist for the non-stomatal uptake. In the first regime dry deposition velocities for dry surfaces are governed by the temperature and solar radiation of the surface as O₃ is decomposed thermally. In the second regime, on slightly wet surfaces the O₃ dry deposition rate decreases, because O₃ is not very soluble in water, as the dry deposition is blocked by a thin film of water. In the third regime, on wet surfaces the O₃ dry deposition process increases again as O₃ is removed by aqueous phase chemistry.

In models the dry deposition velocity v_d is usually calculated by the reciprocal sum of the involved resistances (compare right side of Fig. 2.6). In a simplified model the velocity can be calculated as:

$$v_d = (R_{air} + R_{surf})^{-1} \quad (2.3)$$

with R_{air} and R_{surf} being the resistances of the air and surface, respectively.

As mentioned, wet deposition is mainly important for nitrogen species, acting as O₃ precursors (e.g. HNO₃). As shown by Tost et al. (2007a) the O₃ mixing ratios are only reduced by around 10 % when considering wet deposition in global models. This decrease of O₃ is caused mainly by scavenging and wet deposition of nitrogen species acting as O₃ precursors. The species which are affected mainly are HNO₃ and the reservoir species H₂O₂ and HCHO (see Sect. 2.3.3).

2.5 Long range transport of ozone

So far, four sources and sinks of O₃ have been discussed: downward transport from the stratosphere, chemical production from precursors, chemical destruction and dry deposition. Locally, the O₃ values are also influenced by another important factor, namely – long range transport.

The lifetime of O₃ near polluted urban regions is in the order of hours (e.g. Monks et al., 2015). In contrast, lifetime of O₃ in the troposphere is around 3 weeks (e.g. Young et al., 2013). In addition, also O₃ precursors or reservoir species of these precursors can be

transported over long distances. As an example NO_x , has a lifetime of 1–2 days at the boundary layer, increasing to 2 weeks near the tropopause (Seinfeld and Pandis, 2006). Crucial is especially PAN (with lifetime up to month, Sect. 2.3.3), which is a reservoir species for both, NO_x and VOCs.

This long lifetime of O_3 (and of the relevant precursors and reservoir species) allows a transport over long distances. Therefore, O_3 is not only a regional, but also a global pollutant. Accordingly, the O_3 values at surface of a given point is controlled by O_3 transported over long range, as well as local production and destruction of O_3 . The local production and destruction can further be influenced by the long range transport of precursors.

The process of long range transport of O_3 (and relevant precursors) involves the transport away from the polluted boundary layer in the source region (for example by convection), the transport in the free troposphere over long distances and the downward transport in the receptor region for example by anticyclones (e.g. HTAP, 2010a).

The O_3 levels caused by long-range transport can be understood as background levels (e.g. Vingarzan, 2004). These background levels (hereafter denoted as background O_3) set the lower limits of O_3 at a given point. The local production and destruction of O_3 interacts with the background O_3 . Accordingly, the background levels control how much O_3 can be produced locally before air quality standards are exceeded. An increase of background O_3 can lead to an exceeding of the air quality standard, if the local emissions are not reduced accordingly (e.g. HTAP, 2007).

A detailed knowledge of the amount of O_3 produced in Europe by regional emissions, produced in Europe by precursors from long-range transport and, transported over long range is therefore important for mitigation options. The Task Force on Hemispheric Transport of Air Pollution (TF HTAP) established by the UNCE⁵ therefore has investigated the impact of long range transport on O_3 (HTAP, 2010a). Further studies has focused especially on the impact of long range transport on O_3 in Europe (e.g. Auvray and Bey, 2005, Derwent, 2008, Derwent et al., 2015).

These studies reported an fraction of background O_3 in the boundary layer in Europe during summer of around 40–60 %. During winter the fraction is larger as local production plays only a minor role, since the photolysis rates during this time are low. The impact of long-range transport on O_3 is most important during medium pollution levels, while during extreme events local production is most important. Under these extreme events usually stagnant weather conditions prevail, where local emissions are 'trapped' for a long time near the source regions leading to very high precursor mixing ratios, favouring high O_3 production rates (HTAP, 2010b).

2.6 Natural and anthropogenic origins of ozone precursors

Precursors of O_3 (CO , NO_x and VOCs) are produced by different natural and anthropogenic processes, summarised in Table 2.2. Natural emission estimates are based on literature values. Anthropogenic emissions (excluding aviation) stem from the ACCMIP

⁵United Nations Economic Commission for Europe

Table 2.2: Overview of anthropogenic and natural sources of O₃ precursors. The NO_x emissions are given in amount of nitrogen, the VOC emissions are given in amount of carbon. The VOC emissions of the ACCMIP inventory are scaled with 161/210 (Jöckel et al., 2016, supplement) to convert the lumped VOC emissions to the amount of carbon.

Sector	NO _x (Tg a ⁻¹)	CO (Tg a ⁻¹)	VOCs (Tg a ⁻¹)	Reference
Aviation	0.66			Gauss et al. (2006)
Transport	11	220	24	Lamarque et al. (2010)
Energy	7.0	19	23	Lamarque et al. (2010)
Solvents		0.69	15	Lamarque et al. (2010)
Waste	0.089	4.3	1.1	Lamarque et al. (2010)
Industries	4.7	96	6.8	Lamarque et al. (2010)
Residential	2.8	250	28	Lamarque et al. (2010)
Agricultural waste burning	0.19	19	2.0	Lamarque et al. (2010)
Agriculture	0.19	0.01	0.64	Lamarque et al. (2010)
Ship	5.6	1.2	2.4	Lamarque et al. (2010)
Biomass burning	5.6	460	76	Lamarque et al. (2010)
Biogenic			440 – 660	Guenther et al. (2006)
Soil	4 – 15			Vinken et al. (2014)
Lightning	2 – 8			Schumann and Huntrieser (2007)

scenario (Lamarque et al., 2010) for the year 2000. Aviation emissions originate from the TRADEOFF inventory (REF case by Gauss et al., 2006). Of course, all these estimates are uncertain. The values here are given mainly to provide an approximate global source strength to the reader. More details on the emissions used in the present study are given in Sect. 3.2.3.

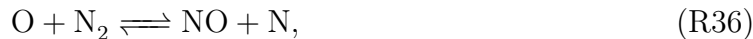
This overview shows that the most important sources of NO_x are the sectors transport (11 Tg a⁻¹), energy (7 Tg a⁻¹), lightning (2–8 Tg a⁻¹), ship traffic (6 Tg a⁻¹), and NO emissions from soil (4–15 Tg a⁻¹). The main sources of CO are biomass burning (460 Tg a⁻¹), the residential sector (250 Tg a⁻¹, e.g. firing or cooking in households), and transport (220 Tg a⁻¹). Finally, the main source of VOCs are biogenic emissions (440–660 Tg a⁻¹), biomass burning (76 Tg a⁻¹), and the residential sector (28 Tg a⁻¹).

Most source of the anthropogenic emissions involve combustion processes. In these processes CO₂ and H₂O are produced by an oxidation process. Besides these products of complete combustion, products of incomplete combustion processes are released to the air, causing CO and VOC emissions.

Nitrogen oxides can be produced by different pathways. The most important are:

1. thermal production at very high temperatures where N₂ is dissociated,
2. prompt production by reactions of hydrocarbons with N₂, and
3. production through nitrogen containing components of the fuel.

The thermal production of NO_x (thermal NO_x , pathway 1) is described by the extended Zeldovich mechanism (Zeldovich, 1946, Lavoie et al., 1970):

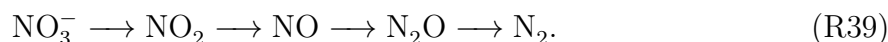


This mechanism converts atmospheric N_2 into NO . Especially the first two possible reaction pathways are strongly temperature-dependent, as a lot of energy is needed to weaken the N_2 and O_2 double-bonds. Therefore, combustion processes usually involve the formation of NO_x . Also lightning- NO_x is generated by this mechanism, as very high temperatures up to 30000 K are present in the lightning channel (e.g. Orville, 1968, Stark et al., 1996, Schumann and Huntrieser, 2007).

The second pathway, the prompt pathway, corresponds to a direct reaction between hydrocarbon radicals and atmospheric N_2 . These reactions lead to the production of an atomic nitrogen molecule, which can lead to NO through the extended Zeldovich mechanism. Further a hydrocarbon-nitrogen molecule is formed, from which additional NO_x can be formed (more detail in Chapter 3 of Flagan and Seinfeld, 1988). Compared to the thermal NO_x process, this pathway is of minor importance for most applications.

The importance of the third, the fuel nitrogen pathway, depends on the combustibile. Very refined combustibles like gasoline have only minor nitrogen compounds. Therefore, this process is of special importance for the combustion of coal or for biomass burning.

The most important source for the production of NO_x emitted from soil are bacteria within the soil (e.g. Hall et al., 1996). These bacteria gain energy from the nitrification of ammonium (NH_4^+) to nitrite (NO_2^-) and nitrate (NO_3^-). In addition NO can be produced by a different sort of bacteria under anaerobic conditions as an intermediate product during a denitrification process:



While the emissions from the soil are an important source for NO_x , many plants are important VOC emitters. Most of the biogenic emissions are emitted in form of isoprene (C_5H_8) by different plants. Reasons for the emissions of C_5H_8 which are discussed in the literature (e.g. Sharkey et al., 2008) are :

- C_5H_8 may act as a protection for heat stress in some plants,
- C_5H_8 is emitted by some plants as a protection against O_3 , as C_5H_8 can directly react with O_3 and prevent the plant from O_3 damage.

The productivity of C_5H_8 , however, heavily changes from plant to plant. In general, most C_5H_8 is emitted in Europe from forests than from agricultural land (Karl et al., 2009).

The oxidation chain of C_5H_8 follows in general the very simplified chain sketched in Sect. 2.3.2. In detail, however, C_5H_8 oxidation is more complex and is not discussed here. Because of this large complexity most atmospheric chemistry models represent oxidation of C_5H_8 only in a simplified manner (e.g. von Kuhlmann et al., 2004, Squire et al., 2015).

Table 2.3: Factors for the conversion of mixing ratios (in nmol mol⁻¹) to concentrations (µg m⁻³) under standard conditions at ground-level.

	M_X (kg mol ⁻¹)	F_X (kg m ⁻³)
O ₃	0.048	2.0
NO	0.030	1.3
NO ₂	0.046	1.9

2.7 Units used in air quality studies

Air quality standards are usually set in terms of concentrations (often µg m⁻³). These concentrations, however, are not conserved if temperature (T) or pressure (p) changes. Therefore the values given in the present thesis are not given as concentrations but as volume mixing ratios⁶, which are commonly used in atmospheric chemistry. This mixing ratio defines the ratio of the moles from a specie X per mole of air.

The volume mixing ratios (C_x) can be converted to mass concentrations (ρ_x) by a simple relation (details see e.g. Jacob, 1999):

$$\rho_X = \frac{p \cdot M_X}{RT} \cdot C_X = F_X \cdot C_X, \quad (2.4)$$

with R being the gas constant ($R = 8.3144598$ J mol⁻¹ K⁻¹), p the pressure, T the temperature, M_X the molar mass of specie X , C_X the mixing ratio of X and F_X the abbreviation for the conversion factor.

Here, the conversion factors are exemplary calculated for standard conditions at ground level ($p = 1013.25$ hPa, $T = 288.15$ K). The factors for O₃, NO and NO₂ are given in Table 2.3. By applying these conversion factors the mixing ratios of NO, NO₂ and O₃, which are given in nmol mol⁻¹ in the present thesis, can be transformed to concentrations of µg m⁻³.

2.8 Modelling the contribution of road traffic emissions to tropospheric O₃

So far this section focussed on the processes influencing the tropospheric O₃ levels. However, the implementation of these processes in numerical models has not yet been discussed. Therefore, this section ends with a brief discussion about the state of the art of the implementation of chemistry related processes in models, as well as previous estimates of the contribution of road traffic emissions to tropospheric ozone⁷. As discussed, ozone abundance (and abundances of many other trace gases) are primarily controlled by four factors: the emissions, the reaction kinetics, physical processes in the atmosphere (especially transport), and sink processes (dry- and wet deposition). These processes must be adequately represented by the models.

⁶Possible exceptions are noted separately.

⁷Please note that here a general discussion is presented, details about the specific setup for the simulations I performed for this thesis are given in Sect. 3.2.

In principle, most models used for atmospheric chemistry studies show a positive bias of tropospheric O₃ at least in the Northern Hemisphere (e.g. Young et al., 2013, Parrish et al., 2014, Righi et al., 2015). Different reasons for this overestimation have been discussed in the literature. One important contributor to this positive bias are the precursor emissions (e.g. Wild, 2007, Righi et al., 2015). The precursor emissions are highly uncertain, officially reported values of the anthropogenic emissions by the different countries might be wrong. Also natural emission estimates are rather uncertain. Especially, NO_x emissions from lightning, emissions of NO_x from soils and biogenic VOC emissions are poorly constrained. Two different methods exist to describe these emissions in models: either by prescribing climatologies (which might stem from previous model calculations), or the emissions are self consistently calculated by the model using parametrisations, depending on the actual meteorological conditions.

Different parametrisations exist for each of these processes. As an example lightning-NO_x is considered. Most of the lightning-NO_x parametrisations depend on quantities calculated by the convection parametrisation, for example convective cloud top height (Price and Rind, 1992), convective precipitation (Allen and Pickering, 2002), or convective mass flux (Grewe et al., 2001). Accordingly, these parametrisations depend on the results of parametrisations, which of course are subject to assumptions and approximations (Tost et al., 2007b). Therefore, only few parametrisations show a good agreement with observations (Lopez, 2016). Especially, the total emission rates are rather uncertain (2–8 Tg(N) a⁻¹, Schumann and Huntrieser, 2007).

Similar is true for the NO_x emissions from soils. Estimates from satellite observations and models are in the range of 4–15 Tg(N) a⁻¹ (Vinken et al., 2014). Most models use parametrisations based on the work by Yienger and Levy (1995), estimating emissions from temperature, precipitation, vegetation classes and fertilizer application. These parametrisations estimate total emissions which are usually at the lower end of estimates from Vinken et al. (2014). More recent parametrisations introduce several improvements (e.g. Hudman et al., 2012), leading to results, better corresponding to satellite observations. These parametrisations still rely heavily on external factors like the fertilizer usage which globally is rather uncertain. Especially future predictions are delicate.

The calculation of biogenic isoprene (C₅H₈) emissions⁸ are most often based on parametrisations from Guenther et al. (1995) or Guenther et al. (2006). These parametrisations use meteorological variables (e.g. temperature, radiation) and external data sources like leaf area index. Observations of C₅H₈ are rather sparse and the lifetime of C₅H₈ is short. Therefore, direct evaluation of the simulated C₅H₈ with observations is challenging (Guenther et al., 2006). Instead C₅H₈ estimates derived from satellite products of formaldehyde are used (e.g. Palmer et al., 2006, Pacifico et al., 2011) or other parameters like O₃ are evaluated (e.g. Zare et al., 2012). Again, the input parameters are rather uncertain.

Focusing on the simulation of O₃, deficits in the representation of these processes (and the processes which are further discussed) can influence each other. For example, if too large soil-NO_x but too low lightning-NO_x are simulated the O₃ values might compare well to observations. On the other side, positive biases of emissions can increase the overall bias.

Biases of the O₃ concentrations might also be caused by the applied chemical mechanism. Different mechanisms with different degrees of complexity exist. More basic mechanisms

⁸The discussion here focuses on the calculation of biogenic isoprene, because isoprene is the only VOC which is calculated by the used model.

2.8 Modelling the contribution of road traffic emissions to tropospheric O₃ 23

consider mainly the NO_x–HO_x–CH₄–CO–O₃ chemistry (e.g. Lauer et al., 2007), while more complex mechanisms consider the organic chemistry in much more detail. Here, mechanisms range from some ten organic species up to more than 1000 organic species (Chen et al., 2010, Coates and Butler, 2015). In the simplified schemes, usually different VOCs are lumped together. The demand for computational memory and the required computational costs limit the complexity of the chemical mechanisms, which can be used in three dimensional models (e.g. Stockwell et al., 2012). Knote et al. (2015) showed that for O₃ the differences between chosen mechanisms are in the range of several percent, while differences of other species (especially short-lived species) can be much larger.

Many models use parametrisations for dry deposition, which are based on (more or less) modified versions from Wesely (1989), using the resistance analogies which have been discussed in Sect. 2.4. A comparison of simulated dry deposition velocities of some state-of-the-art models with observations performed by Hardacre et al. (2015), showed that the models do not have systematic biases, but differences up to a factor of 2 between simulated and observed dry deposition velocities were found. Wesely and Hicks (2000) stated that differences of 30 % are common between different dry deposition models and that these models heavily rely on empirical data. Some improved scheme exist (e.g. Zhang et al., 2003) but to my knowledge no detailed model intercomparisons using these schemes have been published.

The knowledge about the dynamical processes influencing O₃ is in general high, but the detailed quantification of the impact of long range transport compared to locally produced O₃ is still challenging (Monks et al., 2015). Most crucial for this are, on the one hand the resolution of the used models, as with coarser resolution the emissions are diluted over larger areas. On the other hand the representation of convection, which can not be resolved explicitly with resolutions typically used in global and regional model (in the order of 10–100 km). Instead, convection is parametrised. Different schemes have been developed (e.g. Tiedtke, 1989, Bechtold et al., 2004, Plant and Craig, 2008). As shown by Tost et al. (2010) differences for O₃ of up to 25 % between simulated and observed vertical profiles applying different convection schemes can result. Short lived trace gases might be even more influenced. Especially when increasing the level of detail of such models (e.g. including diurnal cycles of emissions) the right timing of convection might become even more important. In many models, however, the diurnal cycle of the convection is not represented well (e.g. Bechtold et al., 2004, Rio et al., 2009).

Because of the uncertainties which arise from emission estimates, simplification of the chemical kinetics, and from parametrisations of physical and chemical processes, the evaluation of such models is very important. This holds in particular, because these models are the only available scientifically based tools to investigate, how the chemistry and/or climate might change in the future under different projections. Especially investigations of the impact of different emission sectors on the present (or for future projections) state of the chemical composition of the atmosphere (and associated radiative feedbacks) are only possible with model simulations.

In the past, simulations have been used to investigate the impact⁹ of different emission sectors on tropospheric O₃, such as aviation (e.g. Brasseur et al., 1998, Grewe et al., 2002), shipping (e.g. Eyring et al., 2007, Hoor et al., 2009) or biomass burning (e.g. Galanter

⁹In this thesis the term 'impact' is used for results of perturbation studies, while the term 'contribution' is used when discussing results from studies using tagging methods (see discussion in Sect. 3.1.6).

et al., 2000, Pacifico et al., 2015). Often, these studies compared two different simulations, one simulation with all emissions and a second simulation with changed emissions from the sector of interest (called perturbation approach). As has been discussed in this section, the O_3 chemistry is non-linear. Accordingly, the response of O_3 on the reduction of emissions might not be linear. This can lead to erroneous attribution estimates for different sectors. Better suited to investigate the impact of emission sectors of O_3 are so-called tagging methods, which use additional diagnostic to follow the reaction pathways of different emissions (e.g. Lelieveld and Dentener, 2000, Grewe, 2004, Emmons et al., 2012, Wu et al., 2009, Grewe et al., 2010). The development of such tagging methods, however, is not straightforward and requires a implementation of complex diagnostics into the used model. A detailed discussion about the difference between the tagging and the perturbation approach follows in Sect. 3.1.6. The methodological error made by contribution analyses using the perturbation approach compared to the tagging method cannot be quantified in general. The error largely depends on the chemical state, in which the O_3 chemistry is perturbed. Accordingly, different factors of the underestimation of the contribution by the perturbation approach compared to the tagging method have been reported. For example, Grewe et al. (2012) found an underestimation of a factor of 5 by the perturbation approach, while Emmons et al. (2012) found a factor of 3, and Grewe et al. (2016) a factor of 2.

Of interest for the present study are in particular previous studies of the impact of road traffic emissions. Granier and Brasseur (2003) investigated the impact of road traffic emissions by removing the road traffic emissions completely (from now on called 100 % perturbation), but considering only NO_x emissions from road traffic. They reported an impact in Europe during summer of 15 % on surface O_3 . Similar studies were performed by Niemeier et al. (2006) (100 % perturbation) but with different emissions, claiming an impact of road traffic emissions on O_3 in Europe of 10–25 %. Similar values were reported by Matthes et al. (2007) (100 % perturbation) with a near surface impact of road traffic emissions in Europe of more than 15 %.

More recent studies used a 5 % reduction of road traffic emissions (Hoor et al., 2009, Koffi et al., 2010). These studies in general report lower impacts of ≈ 4 % (upscaled to 100 %, average 30° – 60° N, 1000–850 hPa, Hoor et al., 2009) and 5–10 % (for zonal mean O_3 near surface as roughly estimated from Fig. 2 and Fig. 5 of Koffi et al., 2010). The differences compared to the 100 % perturbations can be accounted by the different perturbations as well as emissions inventories. Koffi et al. (2010) additionally provided results from a 100 % perturbation and concluded that the differences compared to the 100 % perturbations mentioned above are due to different emissions inventories.

As discussed, the perturbation method of these studies might underestimate the real contribution of road traffic emissions. But only few studies exist investigating the impact of road traffic emissions using a tagging method (Dahlmann et al., 2011, Grewe et al., 2012). These studies report global tropospheric contributions of around 12 % (Grewe et al., 2012) and around 15–20 % for the tropospheric O_3 column over Europe.

All of these studies applied coarsely resolved global chemistry climate models. These models provide only limited regional information. In addition, the coarse resolution can lead to an overestimation of the O_3 production (as will be discussed at the beginning of the chapter 3). To overcome these limitations finer resolved regional models can be

2.8 Modelling the contribution of road traffic emissions to tropospheric O₃ 25

used. Such models were applied for many studies, mainly focusing on air quality issues on different parts of the world.

Studies investigating the impact of road traffic emissions on O₃ focused mainly on emission control scenarios of road traffic emissions (e.g. Saikawa et al., 2011, Roustan et al., 2011, Collet et al., 2014). Only limited studies are available investigating the impact of road traffic emissions in Europe to O₃. Reis et al. (2000), Tagaris et al. (2015) performed such investigations, but by applying a 100 % perturbation and focusing on air quality relevant metrics. Reis et al. (2000) claimed an impact of around 20 % on the AOT40 values¹⁰. Tagaris et al. (2015) found an impact of around 10 % in most parts in Europe on the daily average maximum 8 hour ozone values.

Some regional models have been equipped with some kind of tagging methods (e.g. Li et al., 2012, Kwok et al., 2015) delivering information about the contribution of road traffic emissions. In these approaches, however, the handling of the boundary conditions is problematic. The tagging methods are only applied within the regional domains. Ozone stemming from across the lateral boundaries is usually tagged as 'boundary ozone'. Only very few studies exist using such methods for Europe and focus on the effect of road traffic emission. As an example, Valverde et al. (2016) investigated the contribution of road traffic emissions for Spain, claiming a maximum contribution of less than 25 % of urban road traffic emissions and a large importance of the inflow. This thesis therefore investigate the contribution of road traffic emissions on tropospheric O₃ in more detail, applying a tagging method which is used consistently on global and regional scale.

¹⁰Accumulated Ozone Exposure over a threshold of 40 nmol mol⁻¹.

Chapter 3

Methods

The investigation of the contribution of road traffic emissions to tropospheric O_3 requires the use of complex chemistry-climate models. This requirement arises for two different reasons: First, it is not possible to directly measure O_3 solely produced from road traffic emissions. Second, the contribution can not be interfered directly from the amount of emissions as the production of O_3 is highly non-linear (Sect. 2.3.4). Due to this non-linearity the choice of the resolution of the models affects the results of this assessment. As an example, consider a large city surrounded by rural areas as shown in Fig. 3.1. This city is a large source of NO_x emissions. A model with a fine resolution is able to reproduce the gradient of the emissions between the city and the surroundings correctly. In a coarse model, however, the emissions of the city are instantaneously diluted over large parts. This leads to lower NO_x mixing ratios in the city and larger mixing ratios outside, compared to the coarse resolution. Due to this instantaneous mixing the O_3 production can artificially be increased (e.g. Wild and Prather, 2006).

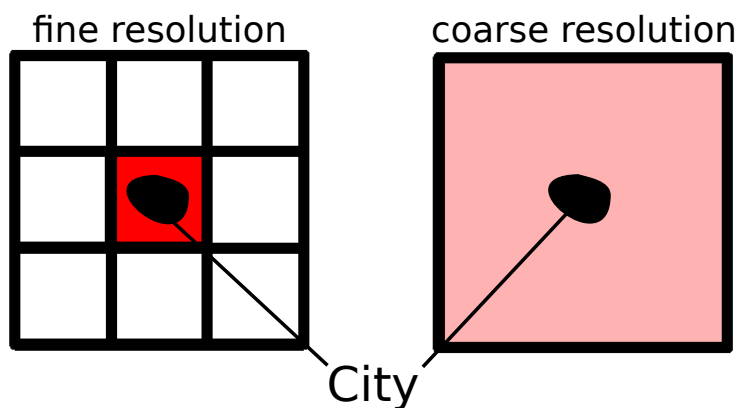


Figure 3.1: Illustration of the influence of a coarse resolution with respect to the NO_x mixing ratio in and outside a city, which is a large source of NO_x emissions (red) and surrounded by rural areas. More details are given in the text.

To overcome this methodological problem of the resolution I used a model chain including a coarsely resolved global model and finer resolved regional refinements (so called nests). This model chain and the used methods are discussed in the present chapter. The structure is as follows. In Sect. 3.1 the applied global and regional atmospheric circulation

models as well as the resulting model chain are introduced. This includes also a discussion about the methods applied to investigate the contribution of road traffic emissions. In Sect. 3.2 an overview about the model configurations used for this thesis follows. This includes an overview about the applied emissions inventories. Finally, Sect. 3.3 summarises the design of the numerical experiments performed in the scope of this thesis.

3.1 Description of the models

This section focuses on the description of the models applied in the present thesis. First of all the atmospheric circulation models ECHAM5 (global) and COSMO (regional) are introduced very briefly. Further, the Modular Earth Submodel System (MESSy), a modular concept for earth system models (ESMs), is introduced. After this, a more detailed description of the MECO(n) model system is presented, including a short comparison with other model systems. At the end of this section a more detailed discussion about the applied methods follows. This includes a general discussion about the investigation of small chemical perturbations (such as slightly changed emissions) and the methods to investigate the contribution of emissions of a given source.

3.1.1 ECHAM5

ECHAM5 is a global circulation model (GCM). It consists of a dynamical core developed at the European Centre for Medium-Range Weather Forecasts (**ECMWF**) together with a package of physical parametrisations developed at the Max-Planck Institute for Meteorology in **HAMBURG**. The primitive equations are solved for the hydrostatic approximation. The four prognostic variables temperature, vorticity, divergence and the logarithm of the surface pressure are defined in spectral space by a truncated series of spherical harmonics. The mixing ratios for the prognostic water species (vapour, liquid and ice) are defined in the grid space on the corresponding Gaussian grid. Also the tendencies due to the physical parametrisations are calculated and applied in the grid space. In the vertical a terrain following hybrid-pressure coordinate is used. The time integration is performed by a leapfrog scheme with time filter (Asselin, 1972). The transport of tracers and water species is calculated by a flux-form semi-Lagrangian scheme (Lin and Rood, 1996).

3.1.2 COSMO

The COSMO model solves the full compressible hydro-thermodynamical equations. As prognostic quantities the horizontal and vertical wind components, the perturbations of pressure and temperature from a reference state, the specific humidity and the cloud water content are considered. All computations are performed on a staggered Arakawa C-Grid (Arakawa and Lamb, 1977), meaning that pressure and temperature are defined in the middle of every grid box, while the velocities are defined on the grid-box boundaries.

At the four lateral boundaries COSMO is relaxed towards the driving model/data by overwriting the three outer (for the Runge-Kutta scheme) grid boxes with the values of the driving model. In addition to this, a Davies-relaxation (Davies, 1976) is performed for a set of grid-boxes in each direction. The size of this relaxation area is controlled by

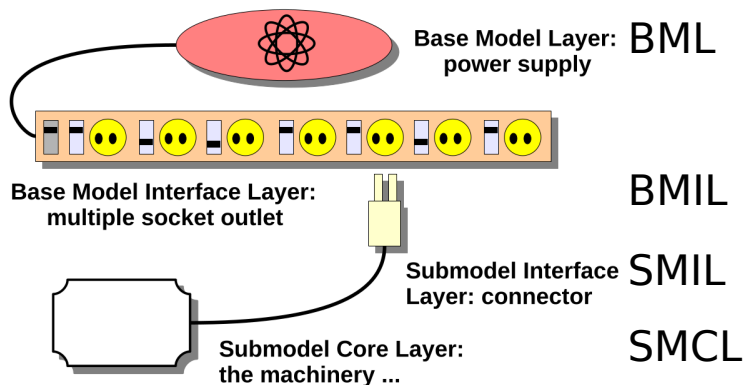


Figure 3.2: Illustration of the MESSy concept. The individual layers are described in the text. Graphics adapted from Kerkweg and Jöckel (2012a).

the user. Details about the values chosen for the simulation performed in the scope of this thesis are given in Sect. 3.2.2.

In addition to the relaxation at the lateral boundaries a Rayleigh damping starting (for the configuration used in the present thesis) at 11 km height is implemented. Both, the Rayleigh damping and the Davies-relaxation do not only influence the meteorological fields, but also all chemical species and diagnostic tracers. The relaxation areas are important to avoid unwanted reflections of outgoing waves at the boundaries, but at the moment no possibility exists to budget the influence of these areas on the chemical species. Therefore, this relaxation causes an unaccounted source/sink within the lateral and vertical relaxation area.

3.1.3 MESSy infrastructure

MESSy (Jöckel et al., 2005) is a concept for a modular ESM and consists of different so-called submodels. These submodels are infrastructure components, process descriptions, or diagnostics. Examples of such processes and diagnostic are the calculation of the chemical kinetics, the calculation of dry deposition, or the diagnosis of the height of the tropopause.

Technically the MESSy concept distinguishes four layer (see Fig. 3.2); the base model layer (BML), the base model interface layer (BMIL), the submodel interface layer (SMIL), and the submodel core layer (SMCL). The base models (e.g. ECHAM5 or COSMO, as described in Sect. 3.1.1 and 3.1.2, respectively) are the BML. The different processes are described in the SMCL. The BMIL can be described as a socket, where the SMILs of the individual submodels are plugged in. Due to this layer system the same process descriptions/diagnostics, which are coded in the SMCL, can be used in connection to different basemodels.

A central part of MESSy are the generic submodels. These submodels provide the infrastructure components. One example is the submodel CHANNEL (Jöckel et al., 2010), which provides an interface for the generation and access to data objects (called 'channel-objects'). Using these channel-objects different submodels can access easily to variables generated by other submodels. This simplifies the programming of additional submodels

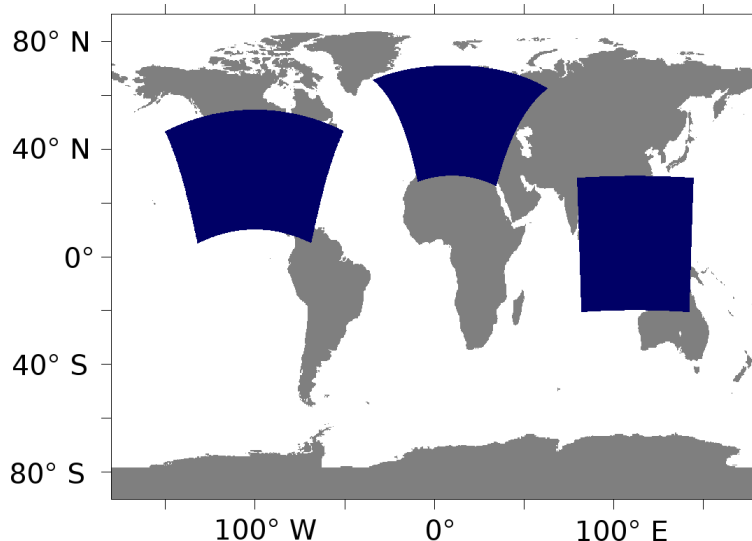


Figure 3.3: Illustration of a MECO(3) set-up with one global EMAC instance and three regional COSMO/MESSy instances (coloured blue).

describing processes (e.g. a submodel, which describes a process that alters the temperature) or diagnostics (e.g. a submodel, which needs the temperature for a certain diagnostic).

Besides these generic submodels 68 submodels¹ describing different processes and diagnostics are part of MESSy. An overview over all these submodels is given on the MESSy-website² or can be found in various articles (e.g. Jöckel et al., 2006, 2010, 2016). An overview of the submodels used in the present study is provided in Sect. 3.2.2.

The combination of the MESSy infrastructure and ECHAM5 is called EMAC (ECHAM5/MESSy for Atmospheric Chemistry, Jöckel et al., 2006, 2010). The combination of the regional model COSMO-CLM and MESSy is called COSMO-CLM/MESSy (hereafter COSMO/MESSy, Kerkweg and Jöckel, 2012a).

3.1.4 MECO(n) model system

The framework allowing a downscaling of EMAC with COSMO/MESSy is the MESSy-fied ECHAM and COSMO models nested n-times (MECO(n)) model system. Figure. 3.3 depicts the idea of MECO(n), showing regional refinements covering North America, Europa and South Asia. EMAC is used as global model, calculating the chemical processes (and dynamics) on a coarsely resolved global grid and providing the necessary initial and boundary conditions for the finer resolved regional domains (called nesting).

This nesting can be performed in two different ways: One way is to calculate the necessary information first with a global model and store these data to a harddisk and read these data during runtime of the regional model (called off-line nesting). In the second way the necessary information are exchanged directly during runtime of both models, without storing and reading to/from harddisks (called on-line nesting).

¹as counted on 26.01.2016 on the MESSy-website

²<http://www.messy-interface.org>

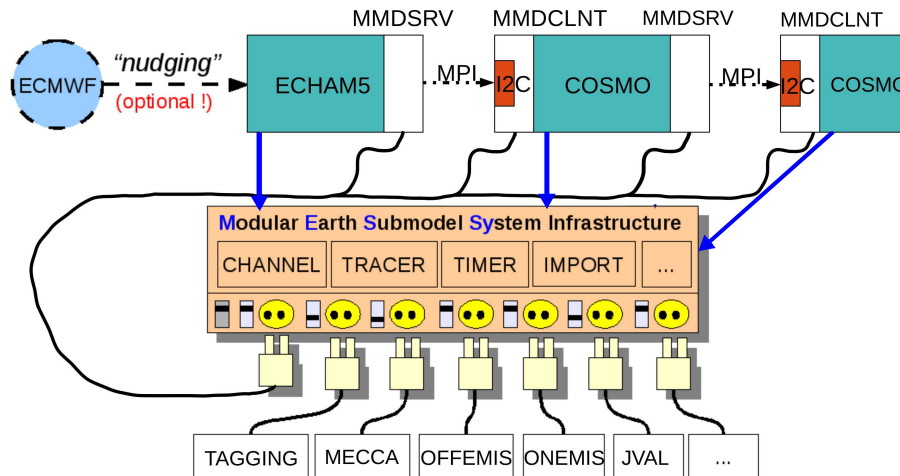


Figure 3.4: Sketch of the MECO(n) model system. A detailed explanation is given in the text. Modified version of a original sketch from P. Jöckel.

In MECO(n) the nesting is performed on-line, realised by the utilisation of the tool INT2LM (provided by the Deutscher Wetterdienst (DWD)) as MESSy sub-submodel (named INT2COSMO, Kerkweg and Jöckel, 2012b). This tool handles the interpolation steps from the coarse grid of the driving model (EMAC) to the finer grid of the regional model (COSMO). For atmospheric chemistry applications not only the meteorological fields are interpolated, but also all chemical species and additional diagnostic tracers. A regional instance can be driven by a global EMAC instance or by a coarser resolved COSMO/MESSy instance.

Due to the use of the Multi Model Driver library (MMD, Kerkweg and Jöckel, 2012b) and corresponding submodels the global and the regional model domains are running in the same Message Passing Interface (MPI) environment. So far the number of regional refinements is only limited by the computational resources, meaning that one EMAC instance could in general provide the boundary data for an arbitrary number of COSMO/MESSy instances, which itself could provide the boundary data for finer resolved COSMO/MESSy instances. The exchange of the initial and boundary fields between the different instances is implemented in MMD as point-to-point, single-sided, non-blocking MPI communication.

This general idea of the MECO(n) system is sketched in more detail in Fig. 3.4. The key compound is the MESSy infrastructure with the generic submodels and the submodels describing different processes/diagnostics (e.g. TAGGING, MECCA, OFFEMIS). ECHAM5 as well as COSMO are extended by the MESSy infrastructure (indicated by the blue arrows). The ECHAM5 instance provides the boundary and initial conditions for one (or more) COSMO instance(s). These data are prepared by the MESSy submodel MMD-SRV and exchanged using MPI communication between MMDSRV and MMDCLNT. INT2COSMO (denoted as I2C) is integrated into MMDCLNT and performs the interpolation for the transformation from the coarse to the fine model grid. This transformation is done for both, the initial and the boundary conditions. The COSMO instance itself can serve as data provider for one (or more) finer resolved COSMO instance(s).

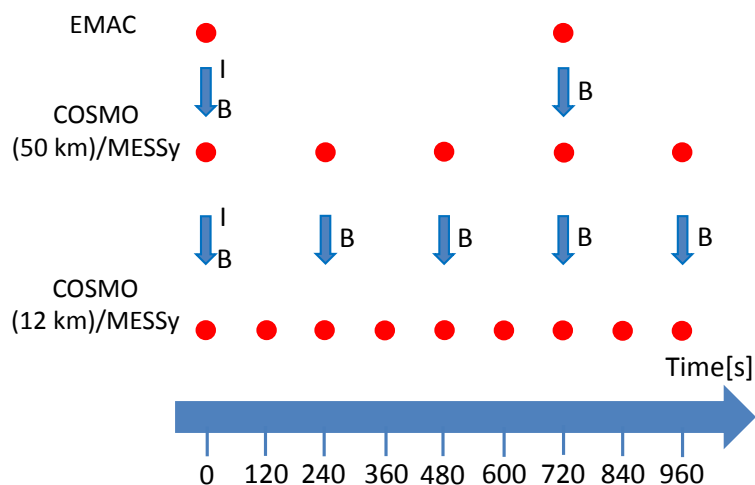


Figure 3.5: Illustration of the MECO(2) data exchange used in this study. The red circles indicate the time steps, the blue arrows indicate the data exchange. The exchange of initial data is marked with I, the exchange of boundary data with B. Taken from Mertens et al. (2016).

Figure 3.5 gives an example of the coupling procedure involving one EMAC and two COSMO/MESSy instances (details follow in Sect. 3.2.1). EMAC provides the necessary data for the first COSMO/MESSy instance, which itself provides the necessary data for the second, finer resolved, COSMO/MESSy instance. At the first time step EMAC provides the initial data for the finer resolved COSMO instance. This instance itself provides the initial data for an finer resolved COSMO instance. After every time-step, EMAC provides new boundary conditions to the first COSMO/MESSy instance. The first COSMO/MESSy instance itself also provides new boundary conditions to the second COSMO/MESSy instance after every time step.

The application of fine resolved limited area models including chemical processes for detailed regional studies is not new. In general two types of regional models exist: (regional) chemistry-transport models (CTMs) and chemistry-climate models (CCMs). The former are (by definition) not calculating any dynamics. Instead they are using precalculated information of the meteorology as input (calculated by other models or from re-analysis data like ERA-Interim, Dee et al., 2011). CTMs solve the continuity equation to account for a mass balance, i.e. transport processes of gaseous and (if included) aerosols, the gas-phase chemistry and aerosol microphysics. The processes acting as sources (emissions) and sinks (dry- and wet deposition) are included in these models as well.

Many CTMs exist for the global scale, for example TM5 (Transport Model, version 5, Krol et al., 2005), the GEOS-Chem model (Goddard Earth Observing System, Bey et al., 2001) or MOZART-4 (Emmons et al., 2010). Some of these models already feature regional nesting capabilities (both excluding (one-way) or including (two-way) feedback on the global scale). Other CTMs are focussing on the regional scale like the CHIMRE model (Menuet et al., 2013), CAMx (developed by ENVI-RON Int. Corp.) or CMAQ (Community Multi-scale Air Quality, e.g. Canty et al., 2015). The application of regional

CTMs mainly focus on the investigation of air quality issues and therefore feature fine spatial resolutions. However, the model top is often located within the troposphere as the focus of such models are ground level concentrations of pollutants. This leads to the problem that the downward transport of O_3 from the stratosphere is not resolved by the model itself, but is only specified by the upper boundary conditions.

In comparison to CTMs, CCMs are including the calculation of dynamics. Usually the dynamics and chemistry or aerosol microphysics are coupled, meaning that the chemistry (e.g. by radiation) or the aerosols (e.g. by radiation or cloud properties) feed back on the dynamics. Besides global CCMs, e.g. EMAC, also regional CCMs exist, for example WRF/Chem (Grell et al., 2005) or COSMO-ART (Knote et al., 2011). In comparison to MECO(n) these models are off-line coupled to global calculations (by a CCM or by a CTM). Compared to the off-line coupling the on-line coupling of MECO(n) has several advantages:

- The meteorological and chemical boundaries are consistent with respect to each other, e.g. weather dependent chemical fluctuations are resolved by the boundary conditions. In many off-line applications the chemical and meteorological boundary conditions stem from different models; this might cause inconsistencies.
- As the global EMAC and the regional COSMO/MESSy instances use the same chemical solver and chemical speciations, the chemical boundary conditions are highly consistent. In the off-line case the chemical speciation between driving and regional model might be different, which introduces additional inconsistencies.
- No disk storage for boundary conditions is necessary. This allows for a much higher update frequency of the boundary conditions compared to the off-line coupling, as it is not feasible to store boundary conditions for more than 200 chemical species after every time-step of the driving model. This is of special importance for chemical species with short lifetimes. In addition the on-line exchange via the memory is also more efficient, as the I/O³-performance is the current bottleneck in HPC⁴.

Due to these advantages MECO(n) is an ideal tool for the investigation of atmospheric chemical processes from the global to the regional scale, because it allows a highly consistent model chain with consistent chemical boundary conditions.

Compared to the regional CCMs (like WRF/Chem or COSMO-ART), which are usually driven by meteorological information from reanalysis data, MECO(n) is driven by meteorological fields from a (coarsely resolved) CCM, which might cause additional biases. To investigate this issue, Hofmann et al. (2012) has compared results from the classical off-line nested version of the COSMO model (using ECMWF analysis data) to results from the on-line nested set-up with EMAC 'nudged' towards the same analysis data. It was shown that for all three cases (a cold front, a convective frontal event and a winter storm) both approaches lead to similar results.

³Input-Output, meaning writing and reading of data to/from hard-disks.

⁴High performance computing

3.1.5 Investigation of small chemical changes

In the present thesis I investigate the impact of small chemical perturbations (e.g. changed road traffic emissions). CCMs like EMAC feature a coupling between dynamics and chemistry, meaning that even small changes in the chemical state of the atmosphere lead to changes in the dynamics (which in turn feed back to the chemistry). When comparing two simulations with slightly changed emissions, the coupling between dynamics and chemistry lead to a diverging meteorology in both simulation, even if both simulations are initialised identically. This diverging meteorology (meaning different weather patterns at a certain time and location) is caused by the inherent chaotic nature of the system, usually known as 'butterfly effect'.

To overcome this problem Deckert et al. (2011) proposed a Quasi Chemistry Transport Model (QCTM) mode for EMAC. This includes a decoupling of chemistry and dynamics by prescribing climatologies of the radiative active species⁵ for the radiation calculations. Further, climatologies of HNO₃ for the calculation of the stratospheric heterogeneous chemistry (submodel MSBM (Multiphase Stratospheric Box Model)) as well as climatologies of OH, O¹D and Cl are needed for the calculation of the CH₄ oxidation in the stratosphere (submodel CH4).

In contrast to EMAC, the radiation routine of COSMO uses internal climatologies and no coupling between the calculated trace gas concentrations and the radiation is present. A coupling between the dynamics, more precisely the hydrological cycle, and the chemistry exists through the stratospheric heterogeneous chemistry, which is calculated by the submodel MSBM. This submodel alters the partitioning between water in the vapour, liquid, and ice phase and feeds back on the hydrological cycle. Therefore the same HNO₃ climatologies as in EMAC were used for MSBM in COSMO. To improve the consistency between EMAC and COSMO/MESSy, it would be desirable to use the same climatologies for the radiative active species in EMAC and COSMO, respectively. With the current COSMO version, this is, however, not possible, but it might be implemented for future versions.

Due to the use of the QCTM mode in EMAC and in COSMO the dynamics within every specific instance is identical in all simulations performed in the present study. This allows to identify small chemical perturbations, even if the simulation period is only very short, or the changes are small compared to the natural variability. In turn this also means, that all differences, which are found between different simulations can be directly related to the change of the emissions.

3.1.6 Estimating the impact of emissions from different sectors

The main goal of the present study is the quantification of the contribution of road traffic emissions to tropospheric O₃. Usually two different methods are used to investigate the impact of specific emission sectors. These methods are the perturbation and the tagging approach, which are described briefly.

3.1.6.1 Perturbation approach

In the perturbation approach usually two (or more) simulations are compared: one simulation with all emissions (base) and one simulation with modified emissions (e.g. with

⁵These species are CO₂, CH₄, O₃, N₂O as well as the halocarbons CF₂Cl₂ and CFC₃.

five percent decreased road traffic emissions, perturbation). Mathematically, this method is based on a Taylor approach to approximate the derivative of a function $f(x)$ around the base state called e_0 (details given by Grewe et al., 2010). Accordingly the first two terms of the Taylor series are:

$$f(e_0 + \alpha e_c) \approx f(e_0) + \alpha e_c f'(e_0), \quad (3.1)$$

where α is the strength of the perturbation of the emission category e_c and f' the first derivative from f . The contribution (δf) of a certain category can be estimated as

$$\delta f \approx e_c f'(e_0). \quad (3.2)$$

By comparing the results of both simulations, the derivative f' around the base state (e_0) can be estimated and the contribution can be calculated as:

$$\delta^\alpha f = -\frac{\Delta^\alpha f}{\alpha}, \quad (3.3)$$

with $\Delta^\alpha f$ being the difference of the quantity f between both simulations.

In a linear system the perturbation method can be applied with arbitrary strength of the perturbation (α). In case of the O₃ chemistry, which is non-linear (Sect. 2.3.4), the results depend on the strength of the perturbation. Two problems are apparent:

- The result depends on the magnitude of the perturbation. Only for small perturbations non-linear effects of the system can be neglected.
- The result depends on the base state (e_0) where the system is analysed.

Therefore the perturbation approach is not well suited to investigate the contribution of a certain emission category to the O₃ chemistry (e.g. Wu et al., 2009, Grewe et al., 2010). Further, these problems lead to a principal issue of the method (Grewe et al., 2010), namely a non closed budget, which means that the sum of the contributions from all emission sources (e.g. road traffic, aviation) to O₃ is not necessarily equal to the total O₃ sum. Additionally, many simulations must be performed for the perturbation approach leading to large needs of computational resources. A study in which the O₃ budget should be disentangled into ten sectors, for example, requires eleven simulations (one base, ten perturbation simulations). In addition, the dynamics and the chemistry of all simulations should be decoupled (Sect. 3.1.5), otherwise the different meteorological conditions would add an additional error to the calculation of the contribution. Well suited is the perturbation approach for the investigation of potential mitigation strategies, i.e. answering questions like: 'Does a reduction of the road traffic emissions in Europe by five percent reduce the amount of tropospheric O₃?'

3.1.6.2 Tagging approach

The word 'tagging' is a coinage, describing a method where certain objects are marked with a tag. In applications focussing on atmospheric chemistry usually trace gases from different emitters (e.g. sectors like road traffic, or geographical regions) are tagged according to their origin. Different tagging approaches exist (e.g. Lelieveld and Dentener,

2000, Grewe, 2004, Emmons et al., 2012, Gromov et al., 2010, Grewe, 2013, Coates and Butler, 2015). The technical realisations of all these approaches differ, but the general idea is identical. The chemical system is extended by additional diagnostic species for the emission sectors of interest. Exemplary for a system where NO_x emissions from road traffic (rt), and aviation (air) should be tagged the effective NO_x loss reaction (neglecting the necessary third molecule, Sect. 2.3.4),



is extended by additional diagnostic reactions:



As the reaction pathways of the emitted trace gases from the different emission sectors and their reactions are traced, this approach is in general well suited to investigate the contribution of the different emission sectors to different species. This approach investigates only the contribution of different sources for a given emission inventory. Sensitivity simulations to test different mitigation strategies are not replaced by using the tagging method, because with changed emissions, the O_3 production efficiency (Sect. 2.3.4) of different emission sectors might change. In these cases the tagging approach gives additional information to assess the given mitigation scenario.

Compared to the perturbation approach, the demands of one simulation with respect to the computation time and especially to the needed memory increase because of the required additional diagnostic species. Through the reduction of needed simulations the overall demand regarding the computational costs is, however, reduced dramatically compared to the perturbation approach.

3.1.7 The TAGGING submodel

The TAGGING submodel is the technical realisation of a tagging method described below, which is used in the present thesis to analyse the road traffic emissions to tropospheric O_3 . The development of the submodel is described by Tsati (2014) and Grewe et al. (2016), the method is described by Grewe et al. (2010) and Grewe (2013). Here, only the most important details are presented.

As an example of the method, the effective NO_x loss reaction is considered:



which can in mathematical formulation be written as:

$$\frac{\partial[\text{HNO}_3]}{\partial t} = \kappa \cdot [\text{OH}] \cdot [\text{NO}_2] = P_{\text{HNO}_3}. \quad (3.7)$$

The production of HNO_3 (P_{HNO_3}) depends on the reaction rate coefficient (κ) and the concentrations⁶ of NO_2 and OH . P_{HNO_3} is calculated by the chemical solver of the model

⁶As long as concentrations are considered, these are written in squared brackets, otherwise mixing ratios are considered.

Table 3.1: Description of seven production (P) and loss (D) channels considered by the TAGGING submodel. The last column gives the corresponding name of the variable in chemical mechanism applied in the present thesis (Sect A.4, page 146).

channel name	corresponding reaction(s)	corresponding diagnostic production rate
$P_{O_3}(\text{HO}_2)$	$\text{NO} + \text{HO}_2 \longrightarrow \text{NO}_2 + \text{OH}$	o3prodho2
$P_{O_3}(\text{RO}_2)$	$\text{NO} + \text{RO}_2 \longrightarrow \text{NO}_2 + \text{RO}$	o3prodro2
$D_{O_3}(\text{OH})$	$\text{O}_3 + \text{OH} \longrightarrow \text{O}_2 + \text{HO}_2$	o3lossoh
$D_{O_3}(\text{HO}_2)$	$\text{O}_3 + \text{HO}_2 \longrightarrow \text{OH} + 2 \text{O}_2$	o3lossho2
$D_{O_3}(\text{NO})$	Reactions of O_3 with NO_y	o3lossno
$D_{O_3}(\text{RO})$	Reactions of O_3 with NMHCs	o3lossro
$D_{O_3}(\text{XO})$	Reactions of O_3 with untagged species	o3lossxo

system (the submodel MECCA, Sander et al., 2011). The TAGGING submodel distributes the calculated production rates among the different tagged categories⁷. This is done by a combinatorial approach, which takes into account all possible combinations between NO_2 and OH molecules from different categories (denoted as j):

$$\frac{\partial HNO_3^j}{\partial t} = \frac{1}{2} P_{HNO_3} \left(\frac{OH^j}{OH} + \frac{NO_2^j}{NO_2} \right). \quad (3.8)$$

This means that the production rates considered by the TAGGING submodel are scaled with the fraction of OH and NO_2 from the category j over the total OH and NO_2 mixing ratios, respectively.

The TAGGING submodel uses the concept of effective production- and loss rates of O_3 (Crutzen and Schmailzl, 1983), meaning that O_3 is considered as family including O_3 and fast exchange processes between other chemical species. This family of effective O_3 is called O_3 for convenience and because O_3 is the most important specie of this family.

The submodel distinguishes two O_3 production and five O_3 destruction channels. Therefore, the chemical mechanism is extended by seven diagnostic production and loss rates. Table 3.1 gives an overview about these seven channels with the corresponding reaction(s). In addition, the names of the corresponding variables in the model system are listed. More details about the tagged reactions are given in the applied chemical mechanism as part of the Appendix (Sect. A.4, page 146). This chemical mechanism includes the diagnostic production and loss rates.

Further details about these production and loss channels are given by Grewe et al. (2016), containing also information about the production and loss rates of the other tagged species, which are not shown here, as the present study focuses on O_3 .

In the TAGGING submodel seven species are tagged: NO_y , NMHC⁸, CO , O_3 , PAN, HO_2 , and OH . The species NO_y and NMHC are so called families, containing all odd

⁷In the context of the TAGGING method and the results from this method the term category is used instead of the term sector from now on. The reason for this is that some of the categories which are used by the TAGGING scheme do not correspond to emission sectors, e.g. downward transport from the stratosphere. Table 3.2 gives an overview about the categories and the associated emission sectors.

⁸In this section the term NMHC is used instead of VOC in order to avoid confusion with existing documentation of the TAGGING submodel.

Table 3.2: Description of the different categories as used by the TAGGING submodel.

tagging categories	description
road traffic	emissions from road traffic
anthropogenic non-traffic	all anthropogenic emissions without agricultural waste burning (AWB) and traffic (road, shipping, aviation) emissions
ship	emissions from ships
aviation	emissions from airplanes
lightning	lightning NO_x emissions
biogenic	on-line calculated isoprene and soil- NO_x emissions, off-line emissions from biogenic sources and AWB
biomass burning	biomass burning emissions
CH_4	degradation of CH_4
N_2O	degradation of N_2O
stratosphere	downward transport from the stratosphere

nitrogen compounds (NO_y) and all volatile organic compounds (NMHC), respectively. This approach is chosen to reduce the demands for computational time and memory (details given by Grewe et al., 2016). Due to the short lifetime, HO_2 and OH are considered in a steady state approach. Additionally, the relevant emission sources (both, on-line calculated and prescribed) and the chemical sinks are considered for the tagged species. The sink processes (dry deposition and scavenging) are treated as bulk process.

Ten categories are considered by the TAGGING submodel, which are summarised in Table 3.2. The category CH_4 is important as in EMAC/MECO(n) so far no emissions of CH_4 are used, instead the near-surface mixing-ratios are prescribed. Therefore, degradation products of the CH_4 oxidation are tagged as NMHC from CH_4 . A similar approach is implemented for N_2O , which is not tagged but serves as source of NO in the stratosphere (by reaction with $\text{O}(^1\text{D})$). The degradation products of N_2O are treated as NO_y from N_2O .

The TAGGING submodel described by Tsati (2014) was at that time implemented as submodel for MESSy1 (Jöckel et al., 2005) and it was not usable for the current EMAC and MECO(n) version of the MESSy development cycle 2 (Jöckel et al., 2010). Therefore I have adopted the TAGGING submodel to MESSy2 (Jöckel et al., 2010) and to MECO(n). Within this scope, I have completely re-written large part of the SMIL (Sect. 3.1.3). The most important modifications I have performed are:

Adaptation to the new TRACER infrastructure

The original version of the TAGGING submodel used the old `new_tracer` routine to define the tracers, which is obsolete in MESSy2. Therefore all corresponding calls were changed to `new_tracer` (definition of the tracer) and `tracer_set` (set tracer properties).

Changing STREAM to CHANNEL interface

All calls to the obsolete STREAM interface for the memory management were replaced by calls to the new CHANNEL interface (Jöckel et al., 2010).

Improved initialisation of the tropopause

In the initialisation phase all O₃ above the tropopause is tagged as stratospheric O₃. Previously the initialisation was performed using a fixed vertical layer, which is not working correctly if different resolutions/models are used. This has been replaced by a climatological tropopause definition.

Implementation of RANK Identifiers

The RANK identifiers are preprocessor-directives which consider different orders of the horizontal and vertical directions in the memory management of the basemodels (details are given by Kerkweg and Jöckel, 2012a). The implementation was important to be able to use this submodel with both, EMAC and COSMO.

3.2 Description of the model set-up ⁹

This section is dedicated to the description of the general model set-up for the simulations I performed in the scope of this thesis. In this description two simulation sets are distinguished, the *REF* and the *GLOB* sets. The *REF* set (and corresponding sensitivity studies defined in Sect. 3.3) involves a MECO(n) set-up with two nested domains described in Sect. 3.2.1. The second set, named *GLOB*, is a global simulation without any nested domains described in Sect. 3.2.2.1. Further, from Sect. 3.2.3 onwards the emissions inventories applied in these simulations are discussed in detail.

3.2.1 Computational domains and on-line coupling

I applied a MECO(2) set-up consisting of EMAC as global driving model and two COSMO/MESSy instances. EMAC was applied with a spectral resolution of T42 and a time step of 720 s. The T-value indicates the triangular spectral truncation. T42 corresponds to a Gaussian grid of $\approx 2.8^\circ \times 2.8^\circ$ in latitude and longitude, corresponding approximately to 280 km. The first COSMO/MESSy instance covered the European area with a resolution of 0.44° (≈ 50 km) and integrated with a time step of 240 s. This instance is called COSMO(50km)/MESSy (CM50).

The second COSMO/MESSy instance covered the German area with a resolution of 0.1° (≈ 12 km) and integrated with a time step of 120 s and is called COSMO(12km)/MESSy (CM12). This results in a MECO(2) model cascade EMAC \rightarrow CM50 \rightarrow CM12. The regions covered by the two COSMO/MESSy instances are shown in Fig. 3.6.

The coupling sequence of this set-up has been discussed in Sect. 3.1.4 and is shortly recapped here. In the first time step the driving model EMAC provides the necessary initial and boundary conditions for CM50. This CM50 instance provides the initial and boundary data for the CM12 instance. For the subsequent time steps new boundary data are provided after every time step of the driving model for the finer resolved instances. Consequently, CM50 is receiving new boundary data every three time steps, while CM12 is receiving updated data every two time steps.

⁹Parts of this subsection are published in: The 1-way on-line coupled model system MECO(n) – Part 4: Chemical evaluation (based on MESSy v2.52) (Mertens et al., 2016).

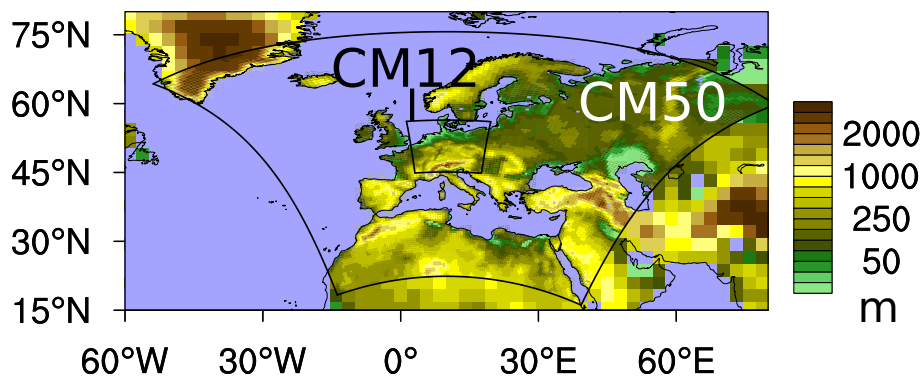


Figure 3.6: Computational domain of the CM50 and CM12 instances. Depicted is the topography of the continents (in m) at the resolution of the corresponding instance. Outside the CM50 domain the values of EMAC are displayed. In both cases, the entire computational domains, including the boundary zones, are shown.

3.2.2 Details of the model set-up

The description of the applied set-up briefly focuses on the most important details. Readers, which are interested in more details are referred to the Appendix. A detailed list of all submodels (meaning processes and diagnostics) is given in Table A2 (page 144). Further, the chemical mechanism which were employed in MECCA (gas phase and heterogeneous chemistry) is given in Sect. A.4 (page 146). More details of the mechanism, as well as the set-up of the reference simulation including all namelist-files are part of the supplement of Mertens et al. (2016).

Both, EMAC and COSMO/MESSy were applied with complex tropospheric and stratospheric chemistry. This involved gas-phase chemistry of O_3 , CH_4 and odd nitrogen. Alkanes and alkenes up to C_4 were considered. The oxidation of some NMHCs as well as C_5H_8 was based on the Mainz Isoprene Mechanism (MIM) in version 1 (based on Pöschl et al., 2000). Further, halogen chemistry involving bromine and chlorine was considered. Some heterogeneous reactions and aqueous phase chemistry were considered as well (for more details see Jöckel et al., 2016). The gas phase mechanism consists of 164 species and 218 reactions. The model set-up further includes sinks of trace gases by dry deposition (based on Wesely, 1989), wet deposition and scavenging (Tost et al., 2006a), as well as anthropogenic, natural (Yienger and Levy, 1995, for soil NO_x), and biogenic emissions (Guenther et al., 1995, for isoprene). The TAGGING method was used in EMAC and COSMO/MESSy, respectively. The further details of the configuration of EMAC and COSMO/MESSy differs slightly and is discussed separately for each model.

3.2.2.1 EMAC

As discussed (Sect. 3.2.1) EMAC was applied at a spectral resolution of T42. The simulations of the *REF* series were conducted with 31 vertical hybrid pressure levels reaching up to 10 hPa (called T42L31ECMWF). In contrast to this, 90 vertical levels, reaching up to 0.01 hPa, were chosen for the *GLOB* simulation series (called T42L90MA). Further differences exist regarding the chosen lightning NO_x parametrisations; the *REF* series used the parametrisation based on Price and Rind (1992) and the *GLOB* series used the

parametrisation described by Grewe et al. (2001). Convection was parametrized after Tiedtke (1989) with the closure approach from Nordeng (1994). The convective transport of tracers was handled with an additional approach based on the diagnosed up- and downdrafts as well as de- and entrainment rates from the convection parametrisation (Tost et al., 2010).

EMAC was operated in the (QCTM mode, Deckert et al., 2011), as described in Sect. 3.1.5. The necessary climatologies for the QCTM mode were taken as monthly mean values from the *RC1SD-base-10a* simulation (a global simulation conducted by Jöckel et al. (2016) using the same emissions as in the present thesis).

To facilitate a comparison with observations EMAC were 'nudged' by Newtonian relaxation of temperature, divergence, vorticity and the logarithm of surface pressure (Jöckel et al., 2006) towards ERA-Interim (Dee et al., 2011) reanalysis data. The time-scales of the relaxation were 48 h for divergence, 6 h for vorticity and 12 h for temperature and surface pressure. Sea surface temperature and sea ice coverage were prescribed as boundary conditions for the simulation set-up from this data source, too.

3.2.2.2 COSMO/MESSy

I applied a similar set-up for both COSMO/MESSy instances (Sect. 3.2.1). The only differences are the chosen computational domains, the time-step as well as necessary changes of the width of the relaxation area (details see Supplement of Mertens et al., 2016). A vertical resolution of 40 levels ranging up to approx 24 km height (20 hPa) were chosen. In the present study a Runge-Kutta scheme of third order with advection terms of fifth order were chosen. The horizontal advection was calculated using a second order Bott scheme (Bott, 1989). Convection was parametrised following Tiedtke (1989), as in EMAC the convective tracer transport is handled according to Tost et al. (2010).

In COSMO no nudging of the dynamics was applied, instead the dynamics were relaxed towards EMAC at the five boundaries (four lateral boundaries and damping layer above 11 km). Accordingly, COSMO can develop its own dynamics within the domain. The coupling between chemistry and dynamics were suppressed (Sect. 3.1.5).

3.2.3 Description of used emission inventories

In the scope of this thesis two different global emission inventories were used – the MACCity inventory (Granier et al., 2011) and the ACCMIP inventory (Lamarque et al., 2010). Both inventories provide historical information about the emissions only up to the year 2000. After this year the MACCity inventory follows the Representative Concentration Pathways (RCP) 8.5 inventory of the IPCC until the year 2100. The ACCMIP inventory follows the RCP 6.0 inventory until the year 2100. The historical part of the MACCity emissions are based on the ACCMIP emissions, but additional source specific annual cycles were added. In addition, also the biomass burning emissions of this dataset differ from the ACCMIP emissions. Both datasets have a monthly resolution and are available at $0.5^\circ \times 0.5^\circ$ grid resolution.

In addition to the global emission inventories a regional inventory were used, which had been created in the scope of the DLR project "Verkehrsentwicklung und Umwelt" (VEU). This dataset covers the European domain with a resolution of $0.0625^\circ \times 0.0625^\circ$.

The emissions for the year 2008 and 2030 were used in the present thesis. The original dataset consists of yearly total emissions for every grid box and additional time dependent modulation functions including the hourly shares of the annual total emissions.

The description of the generation of the emission data set was, at the time handing in this thesis¹⁰, only available as project report, which is not available to the public (Kugler et al., 2013). Therefore more details about the details of this emission data set are given in Sect. A.6 (page 167). Here, only some important details are given.

The VEU emission data set is based on a bottom up approach for emissions of traffic on roads, rails and inland navigation for Germany. Based on modelled activity data for the three transportation sectors emissions of these sectors for Germany were calculated using emission factors. A top-down approach was chosen for the emissions of all other sectors in Germany, as well as for all emission sectors in Europe. In this approach given total emissions (mostly officially reported by the governments) are distributed within the country. This approach leads to an inconsistency as only the traffic emissions in Germany are modelled in detail.

The emissions for the year 2030 were calculated with separate activity data and corresponding emission factors, assuming increasing travelled kilometres of passenger cars and heavy duty vehicles. The emissions of the other sectors for Germany and of all sectors for Europe were calculated using an energy modelling approach, assuming a „current legislation“ state. This means that, if the politics decide stronger emission reductions in the next years, compared to the present state, the emissions are overestimated.

The application of the VEU emission data set in the MECO(n) model set-up was not straightforward, as the regional emissions were tailor made for an other model system. Therefore I performed extensive post processing, described in detail in Sect. A.6 (page 168).

3.2.4 Comparison of the used emissions inventories

Before the contribution of road traffic emissions based on the three emission inventories are compared in detail in Chapter 5 and 6, first the emission inventories itself are compared.

Figure 3.7 shows the road traffic emission of NO_x, CO and VOC for the three emission inventories which are used in this study. The total NO_x emissions¹¹ for the year 2008 of the MACCity (hereafter denoted as MAC08) and the VEU inventories (hereafter denoted as VEU08 and VEU30 for 2008 and 2030, respectively) are similar (5.2 Tg MAC08, 5.4 Tg VEU08), but the geographical distributions differ. In the VEU08 inventory the emissions in the hot-spot regions (e.g. Northern England, Paris, Po-basin, Rhine-Ruhr area) are more pronounced than in MAC08. As the total emissions are similar, VEU08 features lower emissions in Northern- and Eastern Europe compared to MAC08. In comparison to the year 2008 VEU30 assumes a reduction of the total NO_x emissions of the road traffic sector to 4.1 Tg. The most prominent reductions are assumed to take place in Germany and the Po basin. Additional reductions are mainly assumed in Eastern Europe.

¹⁰A publication containing more information about the project is submitted by Hendricks et al., 2016 to Transportation Research Part D.

¹¹All totals given in this section are expressed in totals of NO for NO_x, totals of C for VOCs, and in totals of species for all other emissions. The emissions are given for the whole computational domain of the CM50 instance and are computed based on the emissions transformed onto the computational grids.

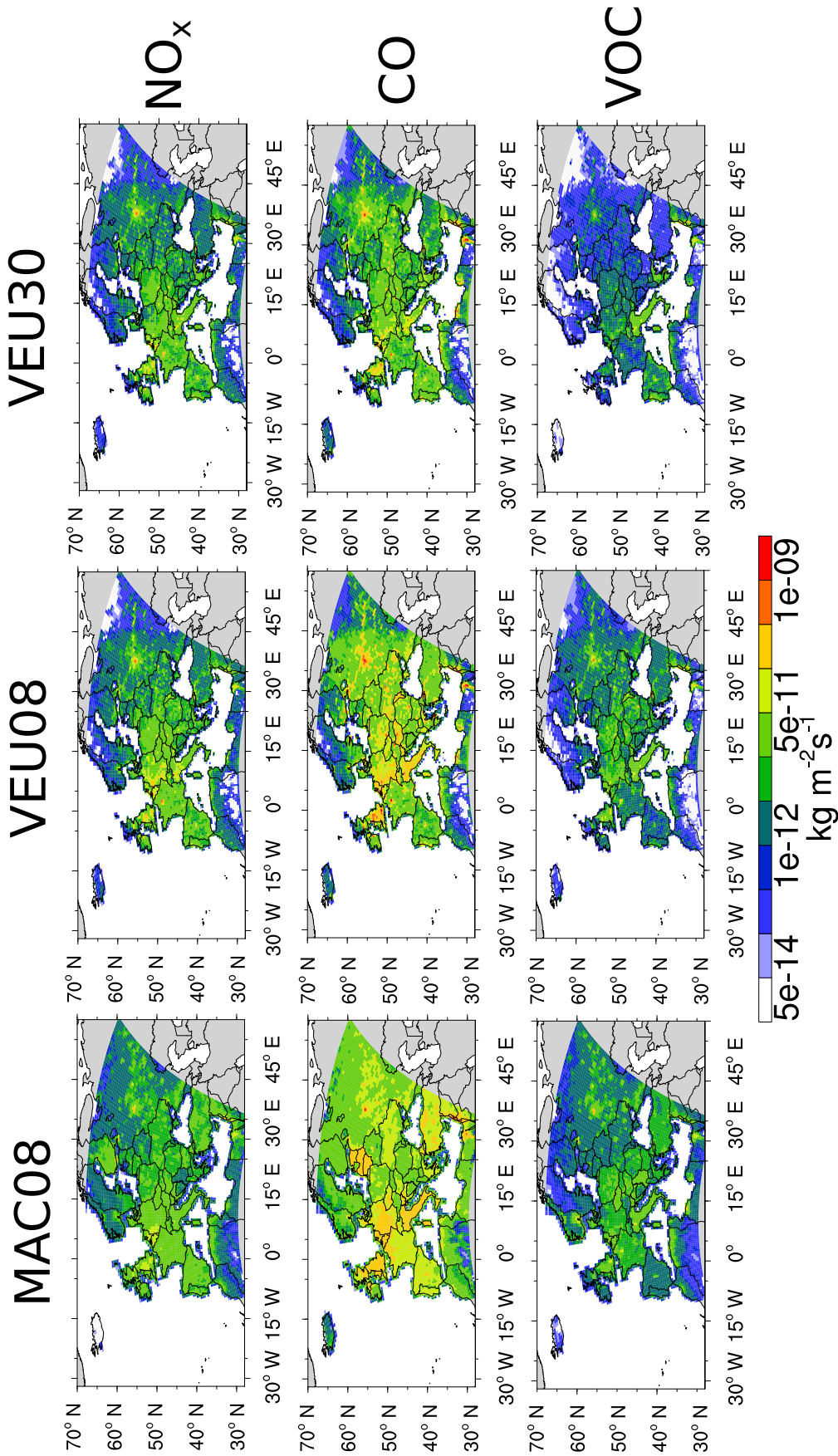


Figure 3.7: Comparison of the annually averaged emission fluxes from the road sector (in $\text{kg m}^{-2}\text{s}^{-1}$) between the MAC08 (left), VEU08 (middle) and VEU30 (right) inventories. Compared are the emissions of NO_x (in kg NO), CO (in kg CO); and VOC (in kg C). Only the part of the CM50 domain without the relaxation area is shown.

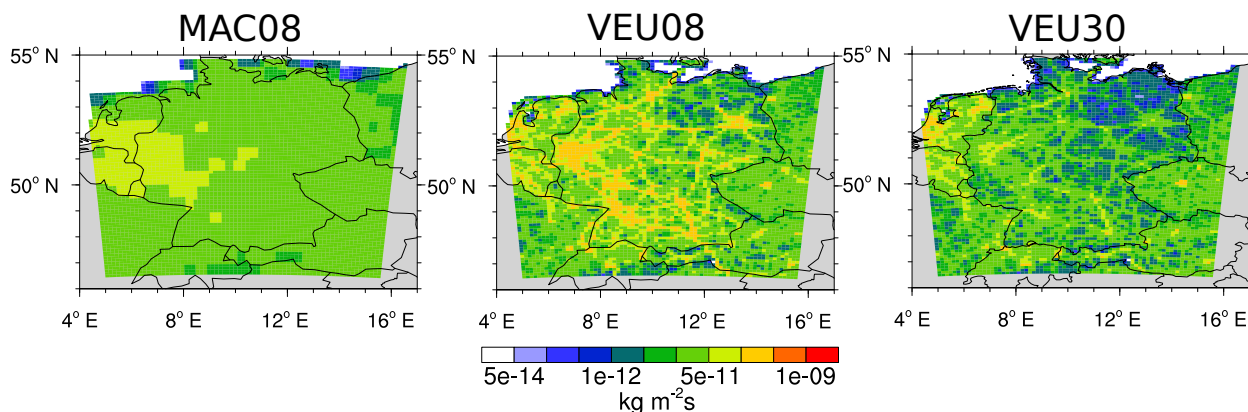


Figure 3.8: Comparison of emission fluxes from the road sector (in $\text{kg m}^{-2} \text{s}^{-1}$) between the MAC08 (left), VEU08 (middle) and VEU30 (right) inventories for NO_x (in kg NO). Values are averaged for May–August.

With respect to the CO emissions of the road traffic sector MAC08 features total emissions of 30.9 Tg, while VEU08 has a total of 23.6 Tg. Again the hotspots in VEU08 are more pronounced compared to MAC08, but the average emissions in France, Spain and parts of Eastern Europe are lower in VEU08 compared to MAC08. The projection for the year 2030, VEU30, assumes a general reduction of the CO emission to 10.1 Tg. Again, this reduction is mainly estimated for the hotspot regions in Germany and Italy, but also in Eastern Europe (e.g. Hungary) strong reductions are assumed.

Regarding the VOC road traffic emissions both inventories of the year 2008 are similar 3.3 Tg (MAC08) and 3.4 Tg (VEU08). The geographical distributions between both emission inventories are similar too, but VEU08 shows lower VOC emissions in France and Turkey, but larger emission near the hotspots and in the Southeastern Mediterranean. Compared to this VEU30 assumes a general reduction of the VOC emissions to 2.1 Tg. The largest reduction takes place in Germany and Eastern Europe, while the emissions in Portugal and Spain are assumed to increase.

The geographical distribution of the road traffic NO_x emissions for the three inventories and the CM12 domain are shown in Fig. 3.8. Compared to the resolution of 12 km of CM12 the resolution of MAC08 is too coarse. The VEU inventories are sufficiently resolved and show a much higher contrast between the hotspot regions and the rural areas. Especially the highways are visible in these emission inventories. Compared to VEU08 the VEU30 inventory features a decrease of the road traffic emissions over the whole domain. Only some regions in the Netherlands and cities like Prague show no notable reduction of the road traffic emissions.

The total emissions of the anthropogenic non-traffic and shipping sector for the three different inventories are shown in Fig. 3.9a and Fig. 3.9b, respectively. Figures showing the geographical distribution are given in Sect. A.6 (page 171).

The emission of the anthropogenic non-traffic sector in VEU08 are lower compared to MAC08. Especially the NO_x emissions are almost 50 % larger in the MAC08 (7.6 Tg) as in the VEU08 (5.1 Tg) inventory, while the CO total emissions are similar. The VOC emissions are ≈ 15 % lower in the VEU inventory compared to MAC08. The VEU30

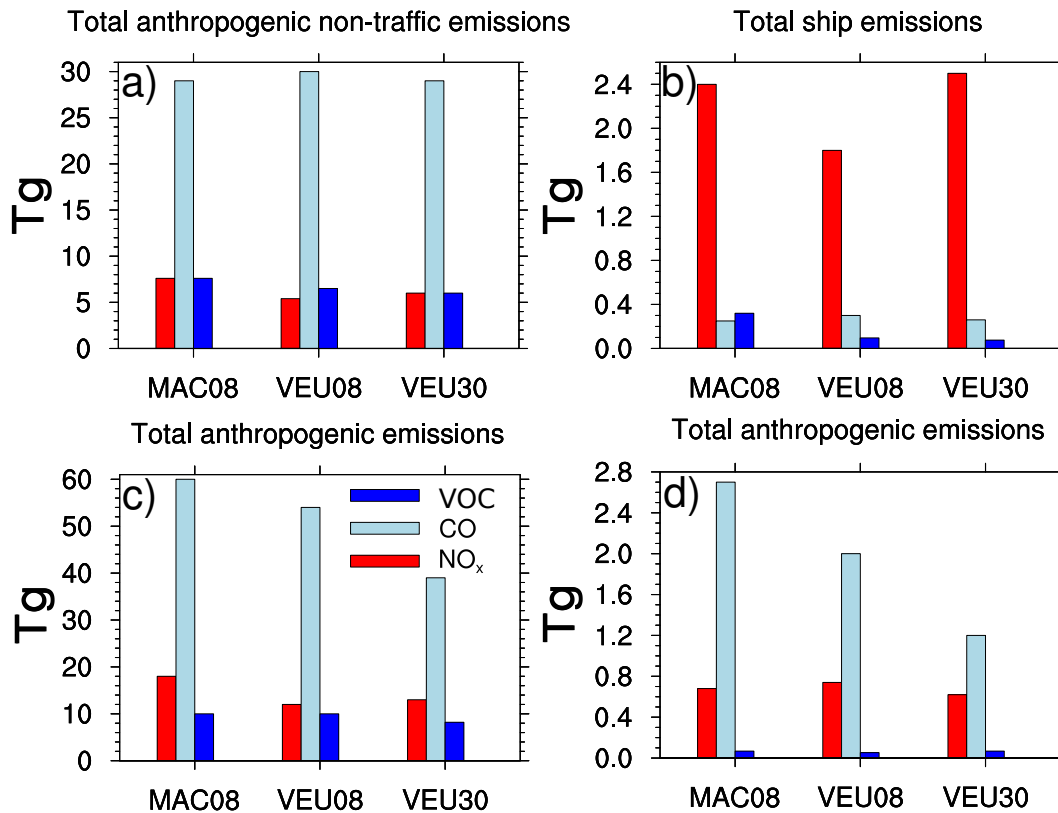


Figure 3.9: Comparison of CO, NO_x and VOC emissions of the MAC08, VEU08 and VEU30 inventories. All values are given in Tg; for NO_x in totals of NO, for VOCs in totals of C and for CO in totals of CO. (a)–(c) show annual sums for the CM50 domain of the following emission sectors: (a) total anthropogenic non-traffic sector, (b) shipping sector, and (c) sum of sectors road traffic, anthropogenic non-traffic and shipping. (d) is as (c) but for the CM12 domain and restricted to the period May–August.

emission inventory assumes an increase of the NO_x emission from 5.1 Tg to 6.0 Tg. At the same time the emission of CO and VOC are predicted to decrease slightly.

Similar as for the anthropogenic non-traffic sector, the NO_x emissions of the shipping sector are lower in VEU08 compared to MAC08. These reductions are mainly found in the harbour area around Marseilles and in the English channel. The CO emissions of both inventories are similar, while the VOC emissions of the MACCity emissions are roughly 300 % larger. The VEU inventory for the year 2030 project an increase of the NO_x emission from the shipping sector from 1.8 Tg to 2.5 Tg. This increase takes mainly place over the Atlantic ocean and over the English Channel; the CO and VOC emission rates are predicted to decrease slightly.

The total emission of the three sectors (road, shipping and anthropogenic non-traffic) for NO_x, CO and VOC for the CM50 domain are depicted in Fig. 3.9c. The total emission for the year 2008 are in general lower in VEU08 compared to MAC08. As the road traffic emissions between both inventories are similar, the share of road traffic emissions compared to all anthropogenic emissions in VEU08 is larger compared to MAC08. Total emission for the year 2030 of the VEU inventory are predicted to increase, meaning that a trade-off between the reduction through the reduced road traffic emissions and an increase

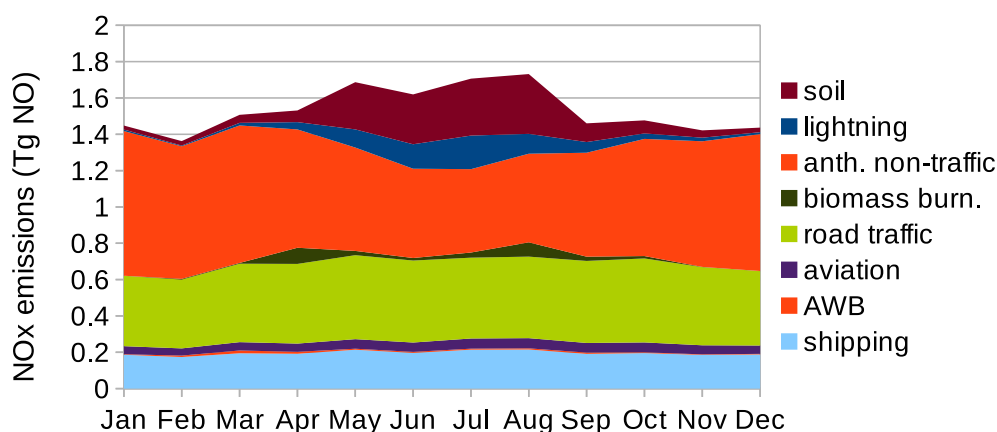


Figure 3.10: Seasonal cycles of total NO_x-emissions (in Tg NO per month) integrated over the CM50 domain for the most important emission sectors. The emissions for the anthropogenic sectors stem from MAC08.

of the emissions in the shipping and anthropogenic non-traffic sectors exists. The total CO and VOC emissions are predicted to decrease.

The total anthropogenic emissions for the CM12 domain (only period May–August) are depicted in Fig. 3.9d. Here the VEU08 inventory has the largest NO_x emissions which mostly stem from the road traffic sector (0.44 Tg). The other part (0.28 Tg) is emitted by the anthropogenic non-traffic sector; shipping emissions contribute only minor. The VEU30 emissions show a reduction of the NO_x road traffic emissions of 42 % to 0.25 Tg. The anthropogenic non-traffic emissions increase by 20 % to 0.34 Tg. The CO emissions of the VEU08 and VEU30 inventories show similar totals for the road traffic sector (1.2 Tg). However, the emissions of the anthropogenic non-traffic sector are larger in the MAC08 inventory, leading to overall higher CO emissions in MAC08.

The road traffic CO emissions of the VEU30 inventory are reduced to 0.43 Tg. The CO emissions of the anthropogenic non-traffic sector are reduced in comparison to the VEU08 inventory from 0.84 Tg to 0.76 Tg. The lower total VOC emissions of the VEU08 inventory in comparison to the MAC08 inventory are due to lower emissions in the anthropogenic non-traffic sector (0.38 Tg compared to 0.54 Tg), while the emissions of the road traffic sector are similar (0.14 Tg).

The VEU30 inventory predicts a reduction of almost 50 % for the VOC emissions of the road traffic sector to 0.08 Tg, while at the same time the emissions of the anthropogenic non-traffic sector almost double to 0.60 Tg, leading to an overall increase of the total anthropogenic VOC emissions compared to the VEU08 inventory. Tables showing the total emissions of all sectors for every simulation are given in Sect. A.6 (page 171).

3.2.5 Seasonal cycles of emissions

The seasonal cycles of the emissions play an important role for some of the analyses performed in the scope of this thesis. Therefore, Fig. 3.10 depicts the seasonal cycles of the most important NO_x sources. Overall, the total monthly emissions are largest during the summer months, when O₃ production is most active. During this time the monthly

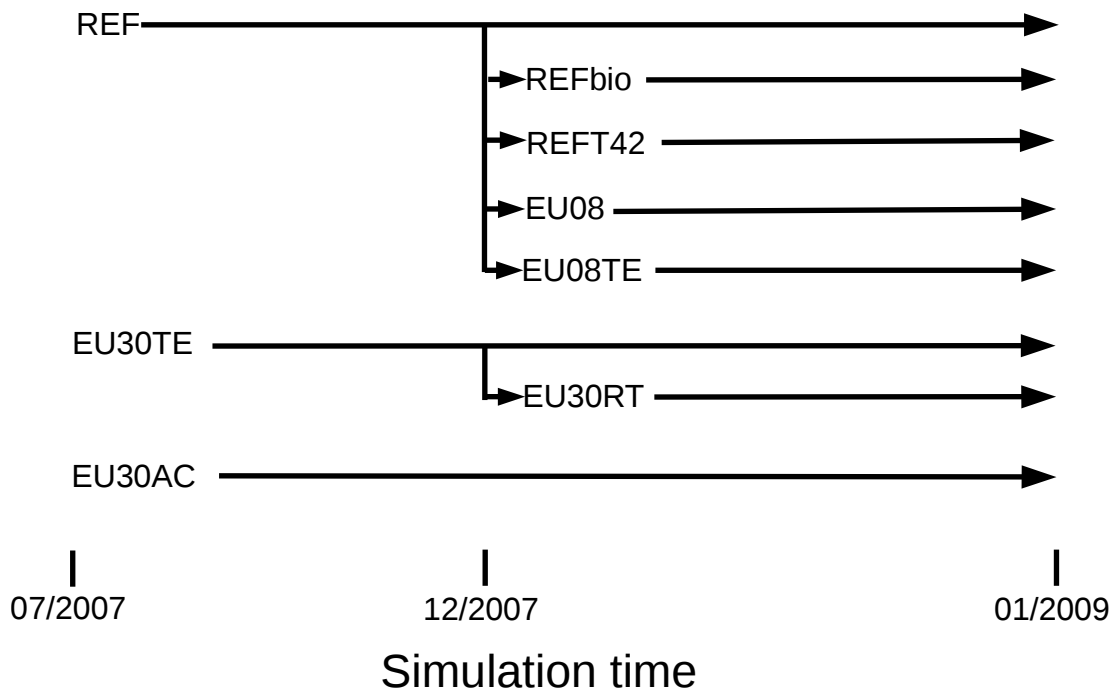


Figure 3.11: Overview of the different simulations and their specific initialisation time. Details are given in the text.

NO_x emissions are in the order of 1.7 Tg NO. During winter the total monthly emissions are lower. The emission sectors shipping, agricultural waste burning (AWB), aviation, and road traffic show only small seasonal variations. The biomass burning sector shows two peaks during April and August. The anthropogenic non-traffic sector depicts the largest emissions during winter, when most energy is consumed by the households for firing or for the generation of electricity. Compared to this, both, the lightning- NO_x and NO_x emissions from soils peak during summer. Especially the NO_x emissions from soils show a strong seasonal cycle with low emissions during winter and up to 0.3 Tg during summer.

3.3 Experimental Design

In the scope of this thesis I conducted a series of different simulations. Especially due to the use of different instances with global or regional coverage and different resolutions the set-up is rather complex and technically sophisticated. The general set-up of the simulations has been discussed in Sect. 3.2. The following overview focuses on the differences between the simulations and the specific scientific question which are tackled with the corresponding numerical experiment. Further details about the used emission inventories for the different simulations as well as the total amount of emissions are given in Sect. A.6 (page 175) and Sect. A.6 (page 171).

To answer the scientific questions raised in Sect 1.2 I performed eight different simulations using the MECO(n) set-up described in Sect. 3.2, which are listed in Fig. 3.11. First of all, these different simulations and the reasons for these different simulations are

discussed. Later on, detailed information about the initialisation procedure follow. Most of these information are technically, but they are important for later reference and the reproducibility of the results.

1. *REF*: This simulation serves as reference simulation of the MECO(n) set-up. In this simulation MECO(n) was applied for the first time with complex tropospheric and stratospheric chemistry over a longer simulation period. Therefore, the emissions in all instances were identical (MAC08 inventory) to compare the simulated results from EMAC and COSMO with observations.
2. *REFbio*: Correct tagging of biogenic emissions in EMAC (details follow below). The simulation results were used to compare the contributions simulated by EMAC and COSMO, respectively.
3. *REFT42*, investigation of the influence of the resolution of the emissions: the anthropogenic, AWB and biomass burning emissions from MAC08 were transformed to the EMAC grid before they were used in the finer resolved COSMO/MESSy instances. This means that the resolution of the emissions was decreased artificially from $0.5^\circ \times 0.5^\circ$ to $\approx 2.8^\circ \times 2.8^\circ$.
4. *EU08*, investigation of the influence of a different anthropogenic emission inventory: VEU08 was used instead of MAC08 for the COSMO/MESSy instances. VEU08 was used with monthly varying emissions and without the constructed timecurve for the VEU08 emissions (meaning that a constant emission flux serves as boundary condition for the whole month). The time curve was set aside in this simulation to disentangle the effects caused by different emission inventories and by the different temporal resolution of emissions.
5. *EU08TE*, investigation of the influence of a different temporal resolution of the emissions: In contrast to the *EU08* simulation the VEU08 inventory was here applied with hourly changing emissions.
6. *EU30TE*, investigation of the projected scenario for the year 2030: VEU30 was used instead of VEU08. To allow a direct comparison with the *EU08TE* simulation results, the 'time curves' for the emissions were used too. To disentangle the effects of changing local emissions and changing long range transport, this simulation uses the same global emission inventory as *EU08TE*.
7. *EU30AC*, investigation of the influence of changed global boundary conditions: The same regional emissions as in the *EU30TE* simulation were used, but the emissions of the EMAC instance were changed to the ACCMIP/RCP6.0 emission inventory. This includes also changed trace gas concentrations for CH_4 and N_2O as suggested by the ACCMIP/RCP6.0 inventory.
8. *EU30RT*, further investigation of the influence of changed global boundary conditions: This simulation is identical to *EU30TE*, but the NO_x emissions from road traffic in the EMAC instance were increased by 10 %.

The reason for the additional *REFbio* simulation was a problem discovered while analysing the different simulation results. This problem affected the tagging of emissions from the biogenic category in EMAC. Most of the emissions from the biogenic category are on-line calculated from the MESSy submodel ONEMIS (NO_x emissions from the soil and biogenic emissions of C_5H_8). To account for these emissions the tendencies of NO and C_5H_8 are compared by the TAGGING submodel before and after the on-line emissions are calculated by the submodel ONEMIS. In COSMO/MESSy this approach works flawless. In EMAC, however, the tendencies of the NO and C_5H_8 tracers were not directly modified. Instead, the emissions calculated by ONEMIS were distributed using the vertical diffusion (called VDIFF) routines of ECHAM5. Therefore, the TAGGING submodel accounted not correctly for the biogenic emissions. The budget, however, was still closed as due to this error the biogenic emissions were treated as bulk process (analogue to e.g. dry deposition). Accordingly, the biogenic emissions were distributed over all tagged categories, leading to an erroneous tagging of the biogenic emissions in EMAC. As the budget are still closed the detection of the problem was very delicate.

In COSMO the tagging of the biogenic emissions was working correctly, but due to the boundary conditions from EMAC also the COSMO results were affected by this problem. The problem was solved by emitting the biogenic emissions as tracer tendencies instead of using the vertical diffusion routines. Given the time required to perform all simulations, it was not possible to redo all of them. Therefore, I performed the simulation *REFbio*, which accounts correctly for the biogenic emissions in EMAC. The consequences of the incorrect tagging are further discussed at the beginning of Chapter 5. It is important to note that only the tagging diagnostic was affected by this problem. The calculation of the chemistry (and all other relevant processes) were not influenced by this problem.

All simulations are analysed for the year 2008, but additionally spin-up periods are necessary. To minimise the needed amount of computational time, different simulations were branched off at different simulation times (see Fig. 3.11). The initialisation procedure was the following:

The *REF* simulation was initialised in 07/2007 with trace gas mixing ratios from the *RC1SD-base-10a* simulation (a global simulation performed by Jöckel et al., 2016). The spin-up time of a half year was chosen in order to allow a spin-up of the tagged tracers, which were initialised with a uniform distribution over all categories. The simulations *REFbio*, *EU08*, *EU08TE*, and *REFT42* were branched off from the *REF* simulation in 12/2007.

The simulation *EU30TE* used not only different regional emissions of the short-lived species, but also the prescribed mixing ratios of the greenhouse gases CH_4 and N_2O were changed. Therefore, the simulation could not be initialised from *RC1SD-base-10a*, but it was initialised from the *RC2-base-04* simulation (a global simulation performed by Jöckel et al., 2016) with trace gas mixing ratios for July 2029 using the ACCMIP/RCP6.0 emission inventory. This initialisation was only necessary for the COSMO instance, as the EMAC instance still uses the same emissions as for the *REF* simulation. Again the longer spin-up time was chosen to allow for a spin-up of the tagged tracers. The simulation *EU30RT* was branched off in December 2007 from the *EU30TE* simulation.

For the *EU30AC* simulation both, the regional COSMO instance as well as the global EMAC instance were initialised with the trace gas mixing ratios from the *RC2-base-04* simulation. Again the simulation was initialised with data for July 2029. This initialisation procedure involves only EMAC and the first COSMO instance (CM50). The finer

resolved COSMO instance (CM12) was always initialised on the 1. May 2008 with the trace-gas mixing ratios from the CM50 instance.

In addition to that, I performed also a simulation called *GLOB* without any COSMO instances. It served as global reference in comparison to the *REF* series with a simulation period of 7 years (2004–2010). The distributions of the trace gases in the atmosphere were initialised (in 01/2004) from the *RC1SD-base-10a* simulation described by Jöckel et al. (2016).

Chapter 4

Evaluation of the MECO(n) system

I applied the MECO(n) model system for the first time with a set-up involving complex tropospheric chemistry. A prerequisite before any application is the evaluation of the model system with a focus on the tropospheric chemistry, which is presented in this Chapter. First, a short meteorological evaluation is drawn (Sect. 4.1) and the results of the applied TAGGING method are compared to results from other tagging methods (Sect. 4.2). Finally, the evaluation of the tropospheric chemistry follows in Sect. 4.3, including also a description of the observational data I used. All evaluations presented in the present chapter are based on the results of the

- *REF* simulation, using the same emissions (MAC08) in EMAC, CM50 and CM12.

4.1 Meteorological evaluation

Before focusing on the chemical evaluation, the results of the *REF* simulation have been evaluated with respect to the meteorology. This evaluation is presented here in a condensed form, highlighting the most important differences. Monthly average values for selected meteorological parameters were compared with the ERA-Interim reanalysis data Dee et al. (2011, resolution¹ of $0.5^\circ \times 0.5^\circ$). The comparison between EMAC and ERA-Interim were performed on the coarse EMAC grid, while the COSMO² data were transformed on the rectilinear grid of the ERA-Interim data.

Figure 4.1 shows the area averaged difference between the results of EMAC/CM50³ and the ERA-Interim data for the temperature at 925 hPa (left) and for the sea level pressure (SLP) (right). The temperature bias of EMAC is around -0.5 K, while the bias of CM50 is around -2.5 K. The colder temperatures of both models cause a positive bias of the SLP compared to ERA-Interim. Again, CM50 shows a larger bias compared to EMAC. The 10 meter wind speed (not shown) is underestimated by EMAC, while CM50 overestimates the 10 meter wind speed especially in coastal regions. Accordingly, CM50 simulates a quicker horizontal transport of chemical species compared to EMAC

¹Please note, that the resolution of ERA-Interim is ≈ 80 km, but the data are also available transformed to finer resolutions.

²To improve the readability the term COSMO is used instead of COSMO-CLM/MESSy.

³The terms CM50 and CM12 always refer to COSMO(50km)/COSMO(12km). The term COSMO is used to summarise general findings about the model.

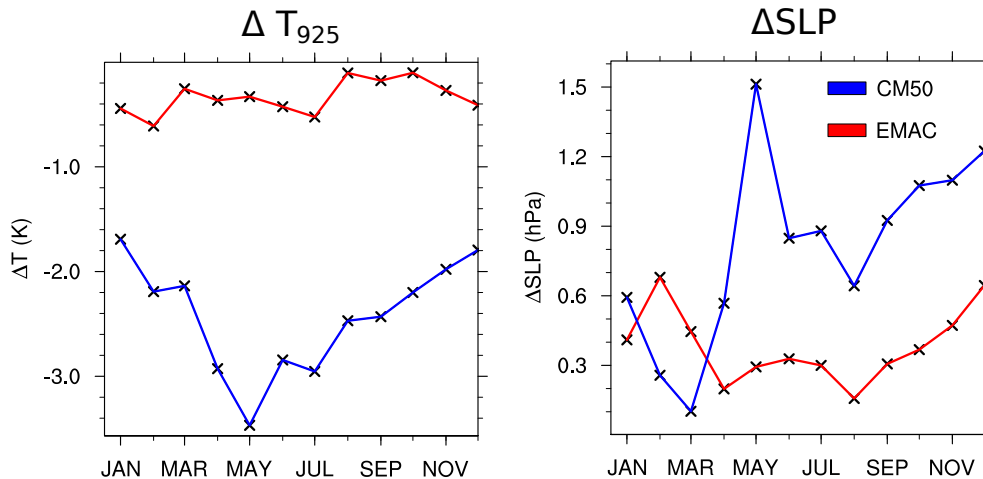


Figure 4.1: Area and monthly averaged differences for the temperature at 925 hPa (left) and the sea level pressure (right) between EMAC and CM50 to ERA-Interim data. The bias for EMAC is only calculated for the area covered by the CM50 domain. The tickmarks mark the middle of every month.

especially in coastal areas. Additional figures, showing the geographical distribution of the differences are part of the Appendix (Sect. A.7, page 178).

While discussing the differences for the temperature it must be noted that both models use the same sea surface temperatures which stem from ERA-Interim. Correspondingly, the temperature bias is largest over the continents. The large temperature bias during April–June in CM50, for example, is mainly caused by a large temperature difference over Northeastern Europe. This temperature bias of EMAC and CM50 is not restricted to the year 2008. A longer term simulation (20 years) which I performed additionally shows a similar bias over the whole simulation period. Accordingly, both EMAC and CM50 simulate a cooler climate compared to ERA-Interim.

The reason for the bias is unclear at the moment. Most likely it can be attributed to deficits in the representation of physical processes by the models (especially COSMO). To reduce the bias I performed different sensitivity studies to investigate the influence of different COSMO options. None of this simulations showed a considerable improvement of the results. Therefore investigations of the reasons are still ongoing. However, it is important to keep in mind that EMAC was nudged against ERA-Interim on synoptic scales. The dynamics of COSMO was free running and only forced in the relaxation areas (four lateral and top) against the state of the atmosphere simulated by EMAC. Therefore, COSMO had more degrees of freedom with respect to the dynamics compared to EMAC.

Higher up in the troposphere both models simulate colder temperatures in comparison with ERA-Interim (Sect. A.7, page 178). Especially in the upper troposphere colder temperatures are simulated compared to ERA-Interim (cf. Jöckel et al., 2016, for EMAC). The temperatures simulated by CM50 are warmer in the upper troposphere compared to EMAC, but these temperatures are still colder compared to ERA-Interim.

The influence of these biases is at the moment further investigated in the scope of a master thesis in which the long term simulations which I performed are analysed. The analyses of these simulations show that more convection in COSMO takes place if COSMO

is driven by EMAC data instead of ERA-Interim data. In the future, further sensitivity simulations should be conducted with a nudging of the mean temperature⁴ in EMAC. Jöckel et al. (2016) showed that this nudging of the mean temperature in EMAC removes the vertical changing bias, which could further reduce the bias in COSMO.

4.2 Evaluation of the TAGGING method⁵

Before the contribution of the road traffic emissions can be investigated using the TAGGING method (Sect. 3.1.7), the results from these method are first compared to results from the literature. Measurements of contributions of different emissions to O₃ (or other chemical species) can not be measured. These contributions can only be estimated using models. This comparison is, however, delicate because different models and methods were used in different studies. Therefore only a rather qualitatively comparison is possible to investigate if the method which I applied in the present thesis shows results within the expected range.

Figure 4.2 shows the contributions⁶ of the ten tagging categories⁷ (in percent) to O₃ based on the results of the *GLOB* simulation (the simulation without COSMO and a longer simulation period).

The zonally averaged mean contributions (2005–2010) vary strongly in height and latitude. In the Northern Hemisphere from the surface to ≈ 500 hPa anthropogenic categories contribute most to O₃. The largest contributors are the anthropogenic non-traffic (more than 20 %) and the road traffic categories (more than 10 %). The largest contribution of the shipping category (more than 10 %) is confined to a small vertical layer up to ≈ 850 hPa between 10°–60° N, because convection over oceans does not effectively transport precursors and in situ produced O₃ from the marine boundary layer upwards (e.g. Hoor et al., 2009). In contrast to this, emissions over the continents are mixed much more efficiently by convection (mainly in the summer months). The aviation category peaks with more than 5 % contribution to O₃ at ≈ 500 hPa between 30°–60° N.

In the Southern Hemisphere the contributions of the anthropogenic categories are smaller compared to the Northern Hemisphere, because less anthropogenic emissions are emitted on the Southern compared to the Northern Hemisphere. In addition, the lifetime of O₃ is too short to allow interhemispheric transport. Only the anthropogenic non-traffic category shows contributions of more than 10 %. Besides the stratospheric category the largest contributors are the lightning category, which peaks with more than 30 % contribution at the equator and the CH₄ category with a contribution larger than 15 %.

These results are similar compared to results of other tagging approaches (Lelieveld and Dentener, 2000, Grewe, 2004, 2007, Emmons et al., 2012). For example, the large contribution of the lightning category around the equator and the dominant contribution of anthropogenic categories in the Northern Hemisphere compared to the Southern Hemisphere are similar.

⁴The nudging in EMAC is performed in spectral space, usually the 'wave 0' is not nudged in EMAC.

⁵Parts of this section are used in similar form in: "Contribution of emissions to concentrations: The TAGGING 1.0 submodel for EMAC 2.51 and MECO(n)" submitted to GMD(D) (Grewe et al., 2016).

⁶The term 'contribution' always describes the relative contribution. Absolute values are indicated explicitly.

⁷A detailed description of these categories is given in Sect. 3.1.7.

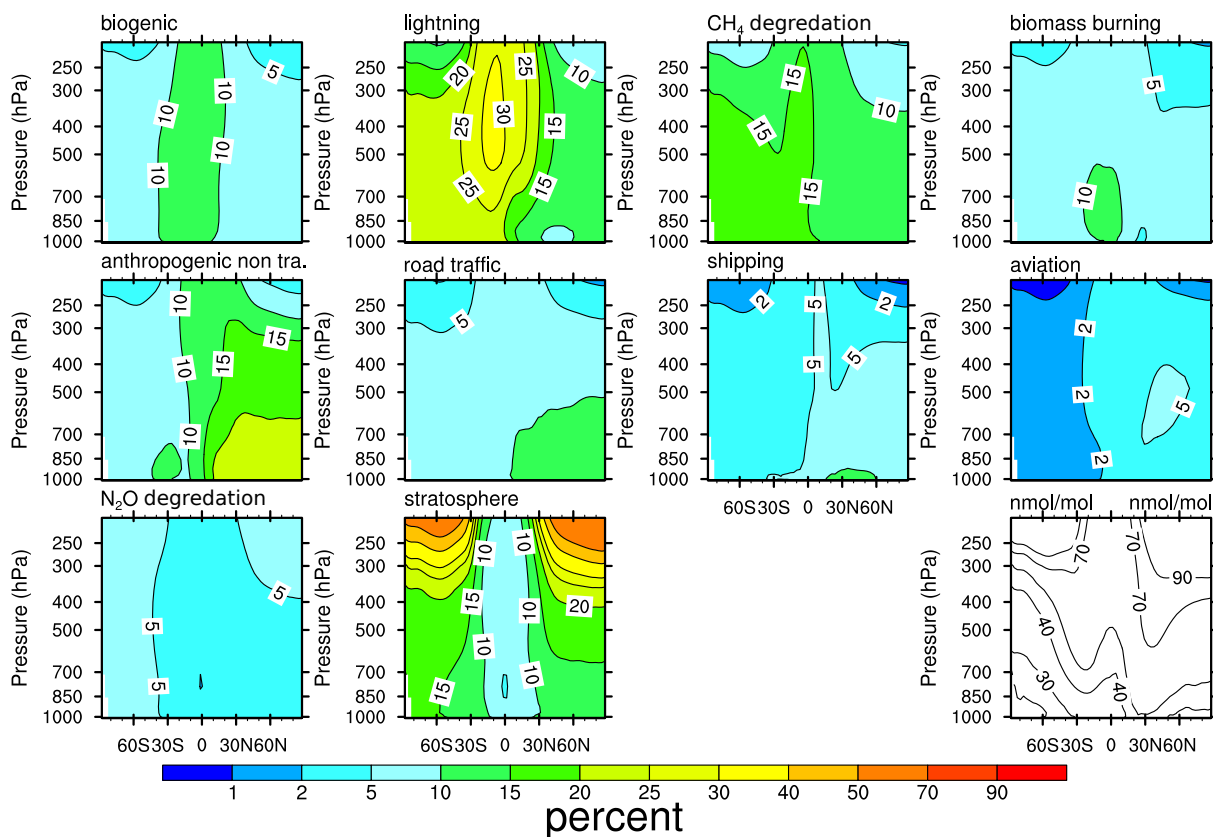


Figure 4.2: Zonal average of the O_3 contribution (in percent) of the ten tagged categories of the *GLOB* simulation. The data are averaged for the years 2005–2010. The lowermost figure on the right side shows the background O_3 mixing ratios in nmol mol^{-1} . The displayed categories are (from left to right) biogenic, lightning, CH_4 , biomass burning (first row), anthropogenic non-traffic, road traffic, shipping, aviation (second row) and N_2O , stratosphere (last row).

In detail, however, differences are apparent, but the different studies used different tagging methods, different models, different emission inventories, different simulation years and different numbers and definitions of the categories. Therefore, a quantitative comparison is not feasible. Compared to the present study Lelieveld and Dentener (2000), for example, estimated a larger contribution of the lightning category of more than 50 % in the tropics. Further, Emmons et al. (2012) reported larger mixing ratios in January and July (not shown) of the aviation category near the tropopause. Also for the other categories Emmons et al. (2012) reported larger mixing ratios, which might be attributed to the different used emission inventories or models.

Summing up, it can be concluded that variations between the different tagging methods exist. In general, the results of the method after Grewe (2013), used in the present study, are in the expected range. In addition, all previous methods only tag NO_x emissions, while with the Grewe (2013) method, also other O_3 precursors are tagged. Overall, it can be concluded that the method is well suited to investigate the contribution of the road traffic emissions in detail.

4.3 Chemical evaluation⁸

4.3.1 Observation data

Several observation data, which are described shortly, have been used for the chemical evaluation.

A comparison of the simulated tropospheric O₃ and NO₂ columns with satellite observations was performed for a qualitative evaluation. The simulated tropospheric O₃ columns (TOCs) were compared with the satellite data described by Ziemke et al. (2006), for which the stratospheric O₃ column measured by the Microwave Limb Sounder (MLS) were subtracted from the measured total O₃ column of the Aura Ozone Monitoring Instrument (OMI). This data product is hereafter called OMI TOC. The data are available as monthly mean values at a resolution of 1.00° x 1.25° (latitude x longitude).

Ziemke et al. (2006) used the definition of the tropopause according to the World Meteorological Organisation (WMO) for the calculation of the OMI TOC. Therefore, the TOCs of the simulation data were also calculated using the on-line diagnosed tropopause height according to the WMO definition⁹. Differences of the employed temperature fields for the calculations of the tropopause height used for the OMI and simulation data, can lead to differences of the diagnosed tropopause height. These differences can lead to variations of the TOC of up to 4 DU, even for multi-annual averages (as discussed by Jöckel et al., 2016). This uncertainty is in a similar range as the difference of up to 5 DU given by Ziemke et al. (2011) for the comparison of the OMI TOC climatology with other climatologies derived from ozonesondes and satellite products.

The simulated NO₂ data were compared with satellite derived NO₂ measurements from the SCanning Imaging Absorption spectroMeter for Atmospheric CHartographY (SCIAMACHY) instrument (Boersma et al., 2004) with a resolution of 0.25° x 0.25°. Similar as for the O₃ columns the on-line diagnosed tropopause following the WMO definition is used as upper limit for the vertical integration of the simulation data. The comparison performed by Blond et al. (2007) between SCIAMACHY NO₂, ground level observations and model simulations showed in general a good agreement between the observations and SCIAMACHY results. However, local hotspots, which are not well resolved by the resolution of the measurements, are underestimated.

Averaging kernels of the measurements were not taken into account for the calculations of the tropospheric columns of O₃ and NO₂. Therefore only a qualitative comparison of the data is possible. A quantification of biases is rather based on the comparison with the ground level observations.

A more quantitative inter-comparison of the simulation data were performed with observations of O₃, NO₂ and CO data from the EBAS database¹⁰. The choice was restricted to the data of the stations located within the CM50 domain from the European Monitoring and Evaluation Programme (EMEP, Tørseth et al., 2012). Only those O₃ observations which are hourly resolved were chosen, while for CO and NO₂ also observations with daily

⁸This chapter is in large parts based on: The 1-way on-line coupled model system MECO(n) – Part 4: Chemical evaluation (based on MESSy v2.52), published in GMD (Mertens et al., 2016).

⁹The tropopause height was calculated using the MESSy submodel TROPOP (Jöckel et al., 2006) using the method discussed by Reichler et al. (2003).

¹⁰<http://ebas.nilu.no>

resolution were used additionally. The simulated vertical O₃ profiles were compared with data from the world ozone database¹¹.

All observations were checked for a plausible range of the reported values. Finally, only data from stations with at least 75 % time coverage for the analysed period were employed. A detailed list of all station data, which were used for the evaluation, is part of the supplement provided by Mertens et al. (2016).

The comparison with the ground level observations and O₃ sonde data were performed with model data, sampled on-line at the geographical position of the respective station with an hourly resolution¹². To allow for a fair comparison between EMAC, COSMO, and the observations, a 'height correction' of the model results from EMAC and COSMO were applied. For the EMAC data the geometric height of each station were compared with the geopotential height of the individual model levels at the corresponding grid box in which the station is located. For the COSMO data the procedure were analogue to EMAC, but the height of the model level instead of the geopotential height were chosen.

The model results at the vertical level, where the geopotential height (EMAC)/model level height (COSMO) is nearest to the geometric height of the station were picked. No interpolation of the model results between different levels were performed. However, this option works only, if the station is located higher than the ground of the lowest model layer. In the opposite case, the values of the lowest model layer were chosen and no extrapolation of the simulated data were performed. This height correction is very important, especially over mountainous terrain, as the topography is much finer resolved by COSMO. In other words, if the observations would always be compared to the model values at the lowest model level, COSMO would outperform EMAC solely because of the finer resolved topography. The usage of these height corrected values is indicated in the corresponding sections.

The focus of the evaluation is on the results for June 2008 and December 2008, as examples for summer (with strong photochemical activity) and winter conditions, respectively. First a comparison with satellite measurements of the tropospheric O₃ and NO₂ columns is shown (Sect. 4.3.2). Subsequently, the differences between the simulation data and the ground level observations (Sect. 4.3.3) and the vertical O₃ profiles (Sect. 4.3.4) are investigated. At the end the simulated pseudo CH₄ lifetimes are analysed in view of the tropospheric oxidation capacity (Sect. 4.3.5). These sections are mainly descriptive, discussions about potential reasons for differences between observations and model results follow in Sect. 4.4.

4.3.2 Comparison with satellite observations

Figure 4.3 shows the TOCs of OMI, EMAC and CM50 for June 2008. The most striking differences at first glance are the lower values of OMI compared to EMAC and CM50. As has been discussed in Sect. 4.3.1, it is not possible to derive the magnitude of the bias for O₃ from this difference. The bias for O₃ is quantified in the following sections. However, it is known that EMAC simulates a positive O₃ bias (e.g. Righi et al., 2015).

The patterns of all TOCs look very similar with a strong north-south gradient. Investigating in more detail, some differences are apparent. CM50 simulates the maximum O₃

¹¹WOUDC, <http://woudc.org>

¹²This sampling is performed with the MESSy submodel SCOUT (Jöckel et al., 2010).

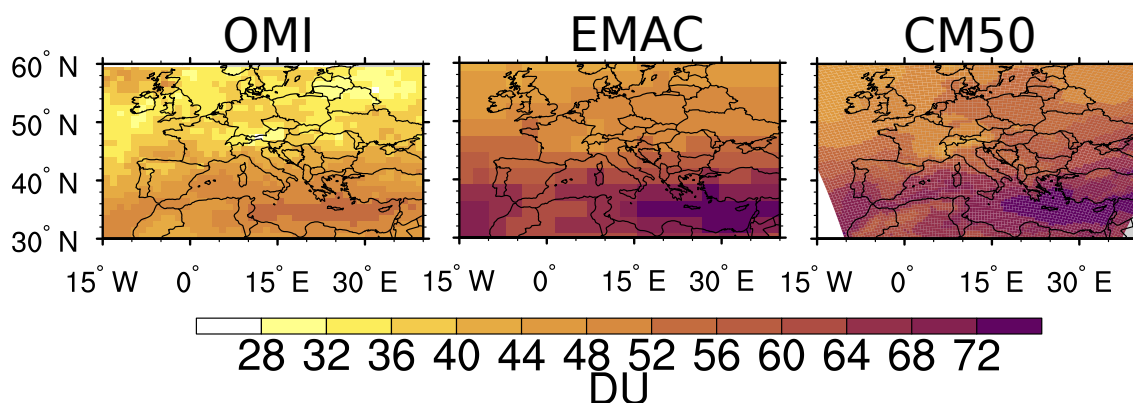


Figure 4.3: Tropospheric O₃ columns in Dobson Units (DU) of OMI (left), EMAC (centre) and CM50 (right) for June 2008.

column mainly along the coastline of Turkey. Compared to this the maximum in EMAC extends further to the West and South. This corresponds better to the satellite measurements, which show the largest values in the whole south-eastern part of the Mediterranean Sea. The low values over the Alps or the Atlas mountains in Morocco found in the OMI data are well reproduced by CM50. The resolution of EMAC is too coarse to represent these lower values well.

Also the larger O₃ values in Southwestern France, which are present in the OMI data, are better reproduced by CM50 in comparison to EMAC. Over Poland, the Baltic Sea and Eastern Germany CM50 shows larger values compared to EMAC. The OMI data for December 2008 are noisy over Europe, therefore no comparison for this month is presented.

The NO₂ columns are inhomogeneous in space with large values near the source and low values away from the source. Such inhomogeneities can not be captured by coarse resolved models. To allow a better comparison between the relative fine resolved satellite data (0.25° x 0.25°) I transformed these data additionally on the grid of EMAC and CM50, respectively.

Figure 4.4 shows the tropospheric NO₂ columns averaged for June 2008 and December 2008. Due to the finer resolution CM50 captures the hotspot regions much better than EMAC. Some examples are the Po basin, Paris, Madrid, Moscow, the Eastern Ukraine and the coastal regions of the Eastern Mediterranean. Compared to the SCIAMACHY data transformed on the grid of the respective model, both models underestimate the hotspot regions. Instead, the model results show large areas with increased NO₂ values. An example are the values over Germany (especially in December) where the SCIAMACHY data shows large values in Western- and Southern Germany. Both models, however, show relative similar values over large parts of Germany. These differences might be caused by an underestimation of these hotspot regions in the MACCItY emission inventory, which especially for the road traffic emissions shows only small variations over Germany (see Fig. 3.7, on page 3.7).

Other hotspot regions like the region around Helsinki or the Gulf of Lion are overestimated in the model results compared to the SCIAMACHY data. These region might be overestimated by the emission inventory, especially as the VEU emissions inventory shows less emission in these region (cf. Sect. 3.2.4, page 42 and Sect. A.6, page 171). As has been

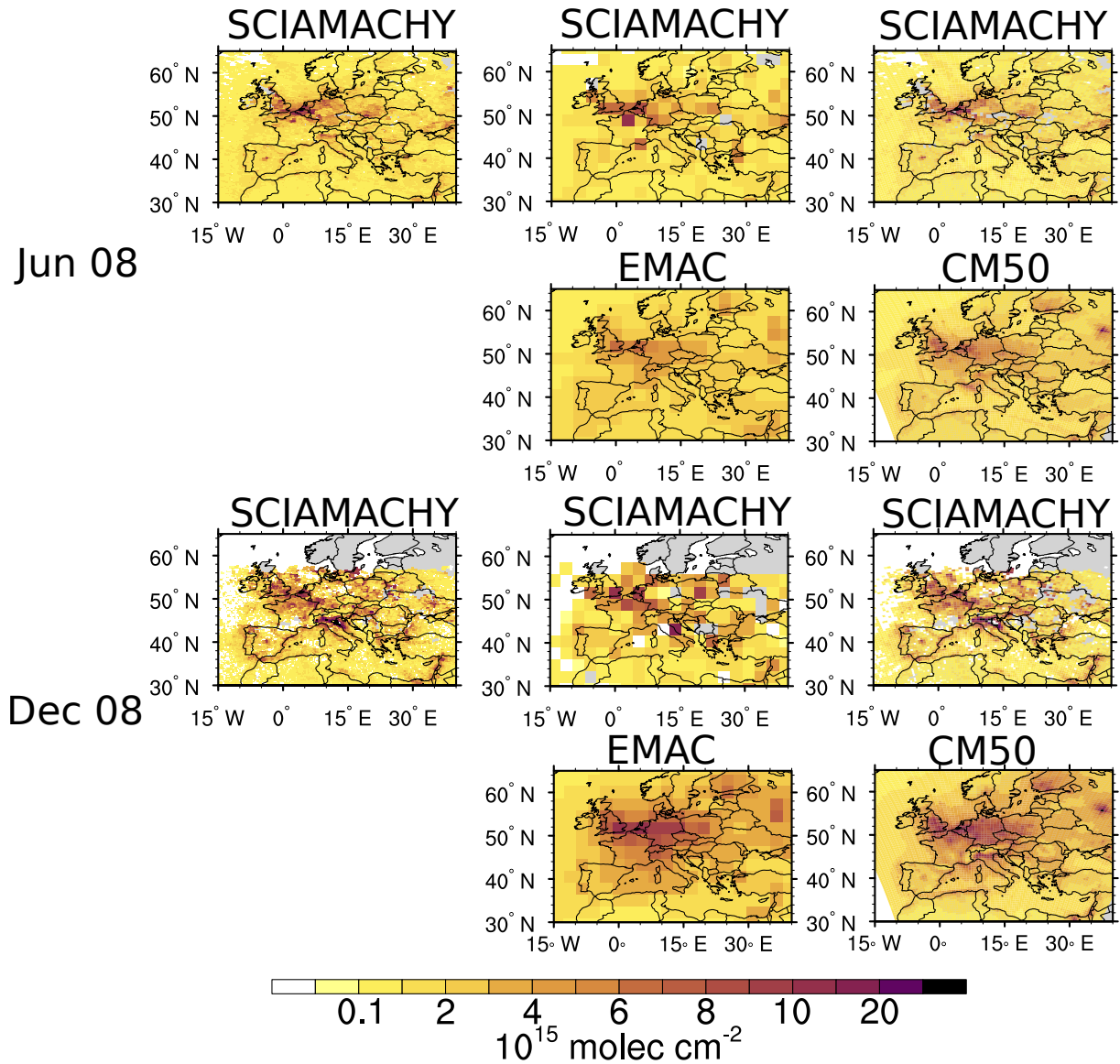


Figure 4.4: Tropospheric NO₂ columns (in 10^{15} molec cm⁻²) for June 2008 (Jun 08) and December 2008 (Dec 08). The first row for every month shows the SCIAMACHY data first on the original grid and then transformed on grids used by the EMAC and the CM50, respectively. The second row shows the model data of EMAC and CM50.

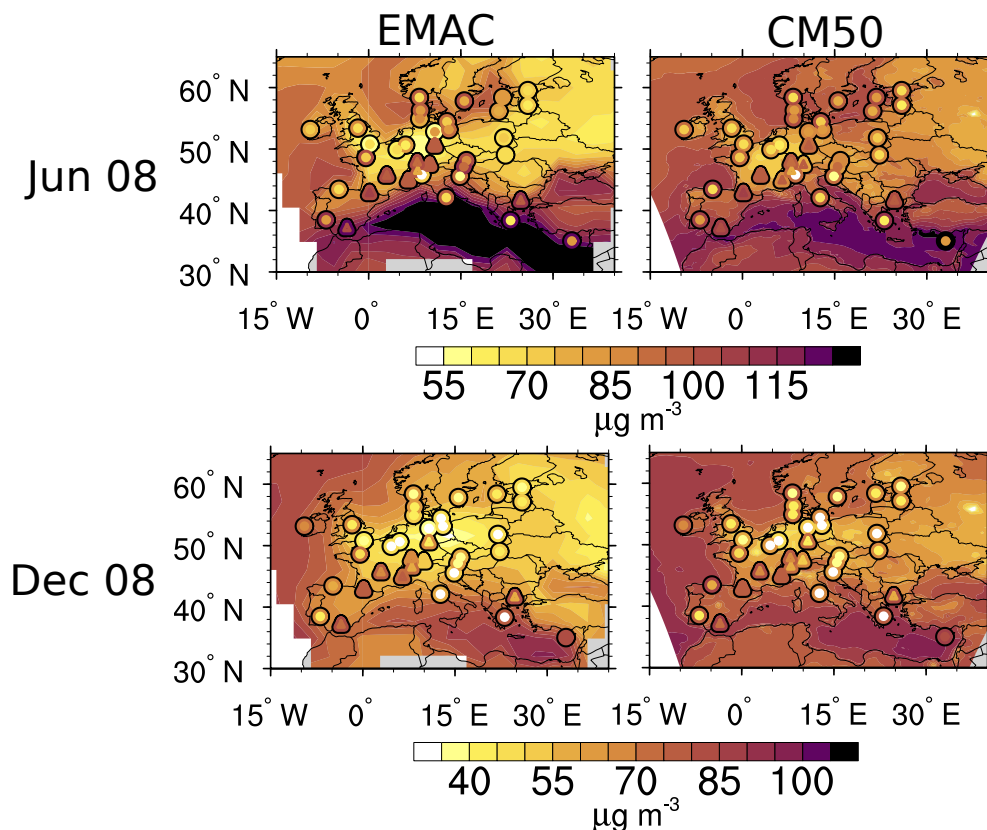


Figure 4.5: Comparison between measured and simulated monthly mean ground level O_3 concentrations for June (Jun 08) and December 2008 (Dec 08). Shown are the simulated values of EMAC (left) and CM50 (right). The contours show the simulated concentrations at the lowest model layer. The inner part of the coloured symbols indicate the values measured at the corresponding stations, while the outer part depicts the simulated value corrected for the station elevation. Triangles indicate stations with an elevation higher than 800 m, circles stations below that height.

discussed in Sect. 4.3.1 especially these localised hotspots could also be underestimated by SCIAMACHY.

4.3.3 Comparison with ground level measurements

Following the qualitative comparison with satellite data the simulated ground level values for O_3 , CO and NO_2 are compared more quantitative with observations. Two metrics are used for this comparison, the normalised mean bias error (MBE) which is defined as:

$$MBE = \left(\frac{\overline{M}}{\overline{O}} - 1 \right) \cdot 100, \quad (4.1)$$

with \overline{M} and \overline{O} being the mean values of the model results and the observations, respectively. The second metric is the root mean square error (RMSE) defined as:

$$RMSE = \left(\frac{1}{N} \sum_{i=1}^N (M_i - O_i)^2 \right)^{1/2}, \quad (4.2)$$

with N the number of stations and M_i and O_i the model results and observations at the individual stations (i). Both metrics were calculated using the height corrected model data (Sect. 4.3.1).

Figure 4.5 shows the comparison between the results of EMAC/CM50 and the observations for June and December 2008. Additionally, the simulated ground level concentrations are shown to give an impression of the ground level O₃ levels.

The results of CM50 for June show a better agreement with the observations over Germany, France and Spain compared to EMAC. Averaged over all stations, both models show an positive O₃ bias with a MBE of around 16 % for EMAC and 20 % for CM50 (see Table 4.1). Compared to EMAC this positive bias in CM50 is more pronounced over Northeastern Europe, than over Central Europe. Further discussions about this bias follow in Sect. 4.4.

The bias is in general lower than the MBE of around 30% (1.875° x 1.25° resolution) and 33 % (0.56° x 0.375° resolution) found by Stock et al. (2014) over Europe using the UKCA model. As they calculated the MBE for July 2005, additionally the MBE for July 2008 is calculated, which is 18 % for EMAC and 17 % for CM50. In comparison, Knote et al. (2011) found negative values of the MBE between -3 % and -15 % for summer conditions in June 2006 using the COSMO-ART model.

The ground level O₃ concentrations in CM50 for December 2008 (Fig. 4.5) show more details compared to EMAC. Examples are the larger values in the mountainous areas (Alps, Pyrenees) and lower values in hotspot regions like the Po basin or around Paris. Comparing the height corrected values at the mountain stations, EMAC and CM50 show similar results. The reason for these differences between the ground level concentrations and the 'height corrected' concentrations are the finer resolved topography in CM50 compared to EMAC. Apparent is also the enhanced positive bias of COSMO over Middle and Northeastern Europe.

The MBE is around 20 % in EMAC and 28 % in CM50, while for example Knote et al. (2011) found a negative bias of an approximately similar amplitude (22 %) for winter conditions in COSMO-ART.

The results of CM12 are only shortly compared to observations, because the MACCity emission inventory used in the *REF* simulation has a resolution of 0.5° x 0.5°. This resolution is too coarse compared to the resolution of 0.1° x 0.1° of CM12. For future work further evaluations of potential benefits of this finer resolution are necessary. This requires a different experimental set-up, with adequately resolved emissions and an inter comparison with a dense local measurement network like AirBase¹³.

Figure 4.6 displays the simulated O₃ concentrations for June 2008 zooming in over Germany for CM50 and CM12. Both models simulate similar ground level O₃ concentrations, though much more details are revealed by the enhanced resolution of CM12. As the same 0.5° x 0.5° emission database is used, the differences are due to the more realistic topography (e.g. the Rhine valley or the Eifel region). Compared to the measurements the RMSE slightly decreases with finer resolution, from 15 µg m⁻³ in EMAC to 12 µg m⁻³ in CM50 and to 11 µg m⁻³ in CM12. The MBE is decreasing from 10 % in EMAC to 4 % in CM50 and increases again to 7 % in CM12 (Table 4.2). While the benefit of the increased resolution (detected in a decreased RMSE and MBE) compared to EMAC is

¹³European Air quality dataBase, <http://airbase.eionet.europa.eu>

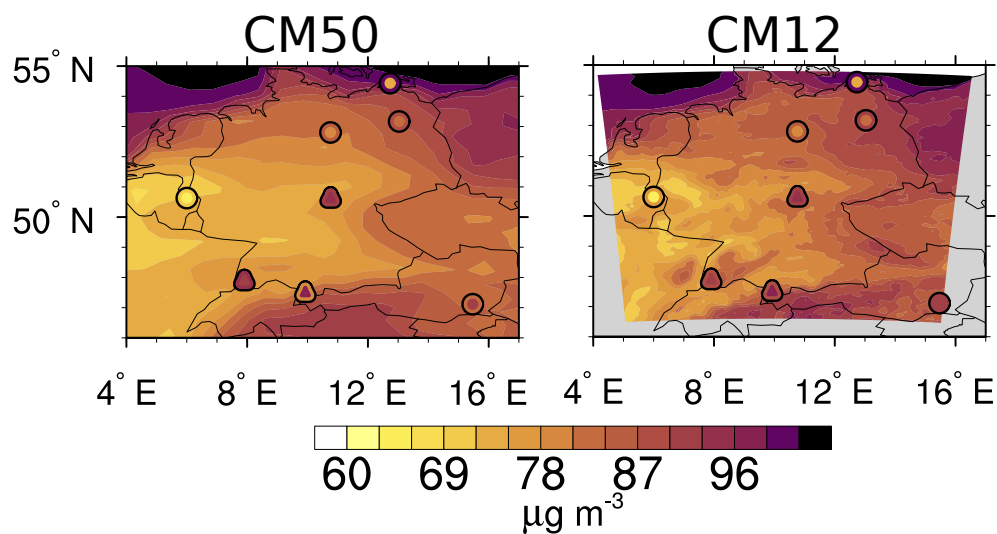


Figure 4.6: As Fig. 4.5 but comparing CM50 and CM12 for June 2008.

Table 4.1: Root-mean-square error (RMSE, in $\mu\text{g m}^{-3}$ for O_3 and NO_2 , in nmol mol^{-1} for CO) and normalised mean-bias error (MBE, in %) for EMAC and CM50 in comparison to ground level observations for June and December 2008. The values are calculated from the height corrected monthly averaged values.

	RMSE EMAC ($\mu\text{g m}^{-3}$)	RMSE CM50 ($\mu\text{g m}^{-3}$)	MBE EMAC (%)	MBE CM50 (%)
O_3 Jun.	20.0	22.1	16.1	20.3
O_3 Dec.	19.4	27.5	34.7	54.7
NO_2 Jun.	1.18	1.13	-17.6	-33.8
NO_2 Dec	2.78	2.89	-41.7	-46.2
CO Jun.	42.8	47.3	-20.2	-28.0
CO Dec	57.7	63.8	-20.1	-24.8

Table 4.2: As Table 4.1 only for June 2008 and restricted to the stations located in the CM12 domain. The values of CO are not shown as only few stations are located in the CM12 domain.

	RMSE EMAC ($\mu\text{g m}^{-3}$)	RMSE CM50 ($\mu\text{g m}^{-3}$)	RMSE CM12 ($\mu\text{g m}^{-3}$)	MBE EMAC (%)	MBE CM50 (%)	MBE CM12 (%)
O_3	14.9	12.3	11.4	10.1	3.94	6.54
NO_2	0.805	0.865	0.846	-10.6	-28.8	-29.0

obvious, a detailed comparison of CM50 and CM12 is hindered by the resolution of the used emission inventory.

The monthly mean NO_2 concentrations for June 2008 are shown in Fig. 4.7. Comparing the simulated concentrations from EMAC (left) and CM50 (right) to measurements, the

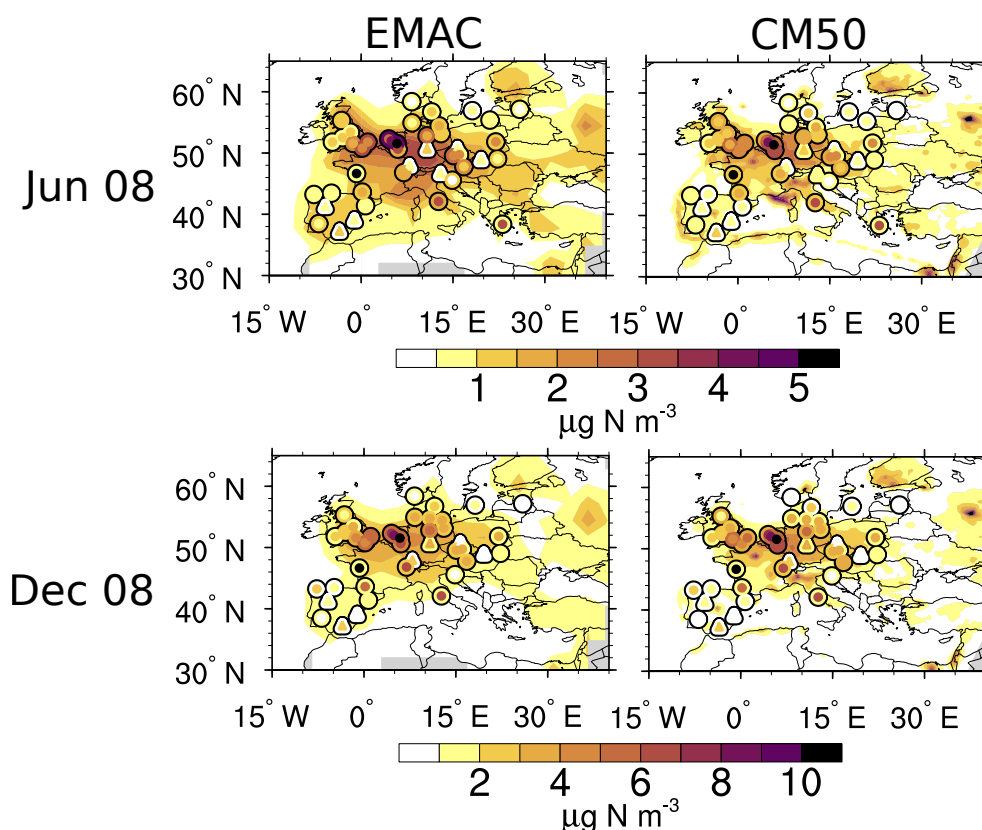


Figure 4.7: As Fig. 4.5 but for the monthly averaged NO_2 concentrations ($\mu\text{g}(\text{N}) \text{m}^{-3}$).

highly variable regional distribution, with larger concentrations near the hotspots and lower concentrations in the remote areas, is better represented by CM50. The RMSEs (Table 4.1) of EMAC and CM50 are similar ($\approx 1 \mu\text{g}(\text{N}) \text{m}^{-3}$). According to the MBE, both models show a negative bias. This bias is ≈ 16 %-points larger in CM50 than in EMAC. However, this quantity does only compare the average over all stations; positive and negative biases at different stations cancel out.

Similar results are found for the stations located in the CM12 domain. The RMSEs between EMAC and the two COSMO instances are similar, while the negative biases of the MBE are larger in both COSMO instances compared to EMAC (not shown).

A similar picture as for June 2008 is found for December 2008 (Fig. 4.7). Comparing first the ground level concentrations between EMAC and CM50 a larger contrast between remote areas and hotspot regions is present in CM50. In comparison to the measurements the strong contrast between hotspot and remote regions is simulated better by CM50 than by EMAC (e.g. south of Spain, Norway). As for June, both models show negative MBEs (-42 % for EMAC, -46 % for CM50), the RMSEs are similar ($3 \mu\text{g}(\text{N}) \text{m}^{-3}$).

Despite the better representation of hotspots in CM50 some measured concentrations are underestimated in CM50 (and EMAC). These hotspots may not be covered by the emission database, or local effects, which cannot be resolved by or are missing in the model, play an important role.

The MBE for CM50 is -34 % (June) and -46 % (December) which is of a similar order of magnitude as reported by Knote et al. (2011) for NO_2 using COSMO-ART. However,

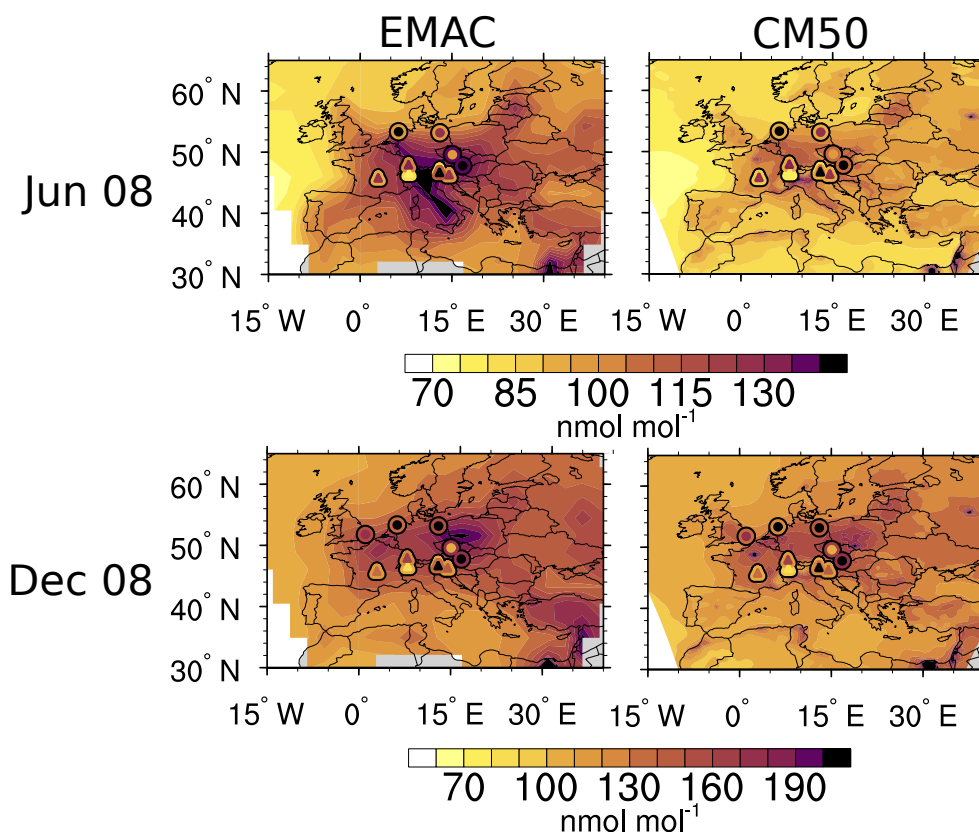


Figure 4.8: As Fig. 4.5 but for the monthly averaged CO mixing ratios (nmol mol^{-1}).

they report a positive, not a negative bias. The difference of the sign might be explained by the different emission data sets, as they used the emission data set provided by TNO (Netherlands) with an hourly time curve (Kuenen, 2011), while the MACCity data set with a constant emission flux for the whole month is used here.

The simulated ground level CO mixing ratios for June 2008 (Fig. 4.8) and December 2008 (Fig. 4.8) show a negative bias for EMAC and CM50. Again, the larger regional variation of the ground level mixing ratio with lower values over the Alps, as well as the larger values over the largely polluted Po valley, can be resolved much better by CM50, because the resolution of EMAC is too coarse to resolve these features. Comparing the height corrected values, the MBE is around -20 % for EMAC (independent of the season) and between -25 % (December) and -28 % (June) for CM50 (Table 4.1). The differences of the RMSE between EMAC and COSMO are similar for June (around 4 nmol mol^{-1}) and in December (6 nmol mol^{-1}).

4.3.3.1 Taylor diagrams

To allow a more quantitative comparison, Taylor diagrams (Taylor, 2001) were calculated. These diagrams combine the (normalised) standard deviation (as radius) and the correlation between the observed and the simulated time series (as angle). The calculations are based on hourly averaged model output and observations, respectively. The dashed

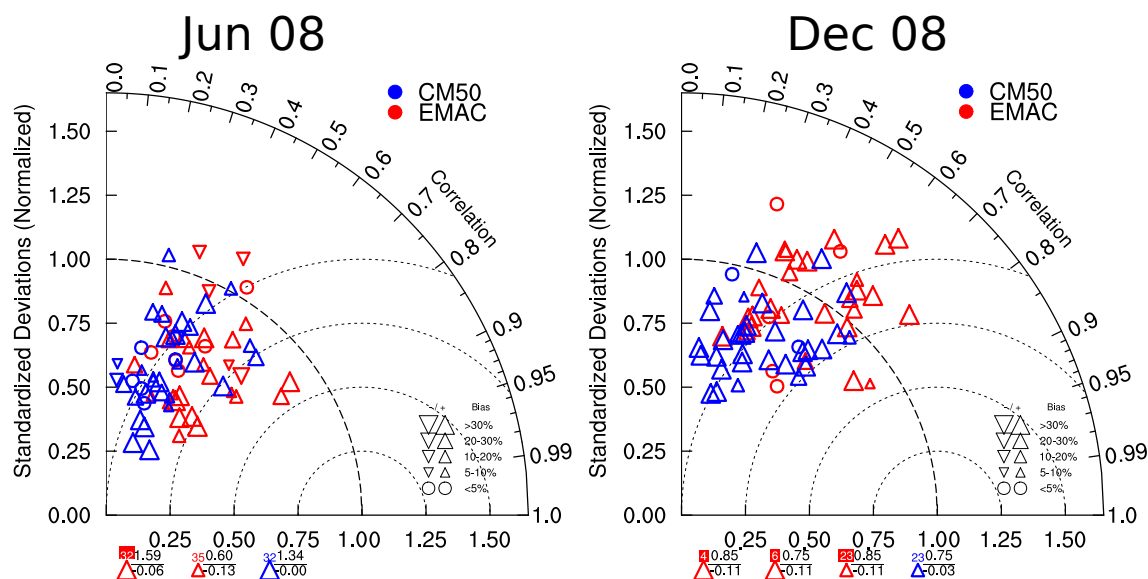


Figure 4.9: Taylor diagram of ground level O_3 concentrations for June (Jun 08) and December (Dec 08). The results for EMAC are shown in red, for CM50 in blue. The size of the symbols indicate the bias in percent; upward symbols signify a positive bias, downward symbols a negative bias. The symbols below the horizontal axis indicates the stations, which are out of range. The coloured number provides the number of the station, the upper black number depicts the normalised standard deviation and the lower number shows the correlation coefficient at the station.

circles indicate the root mean square error. Again, the height corrected values were used, which improve the results of EMAC considerably.

The resulting Taylor diagrams for June and December 2008 are shown in Fig. 4.9. Both model results underestimate the variability of the observations in June 2008. The mean values for the normalised standard deviation are larger in EMAC (0.74) compared to CM50 (0.65). The same is true for the correlation coefficient which is 0.48 for EMAC and 0.34 for CM50. In general the results at different stations in both models are similarly scattered. The biases of EMAC (17 %) and CM50 (22 %) are positive.

The model results of both models for December 2008 show a better agreement with the observed normalised standard deviations. The normalised mean standard deviation for EMAC increases to 0.97, while the normalised standard deviation for CM50 increases to 0.78. The mean correlation coefficients for both models decrease to 0.45 for EMAC and 0.38 for CM50 respectively. As for June the results at different stations in EMAC and CM50 are similarly scattered. The overall better results for EMAC compared to COSMO are likely caused by the deficits in the representation of the diurnal cycle in COSMO as discussed next. A more detailed discussion about potential reasons for this is provided in Sect. 4.4.

4.3.3.2 Diurnal Cycles

To compare the diurnal cycle at the different stations, the average diurnal cycles for all non-mountain stations (stations with an elevation lower than 800 m) and all mountain

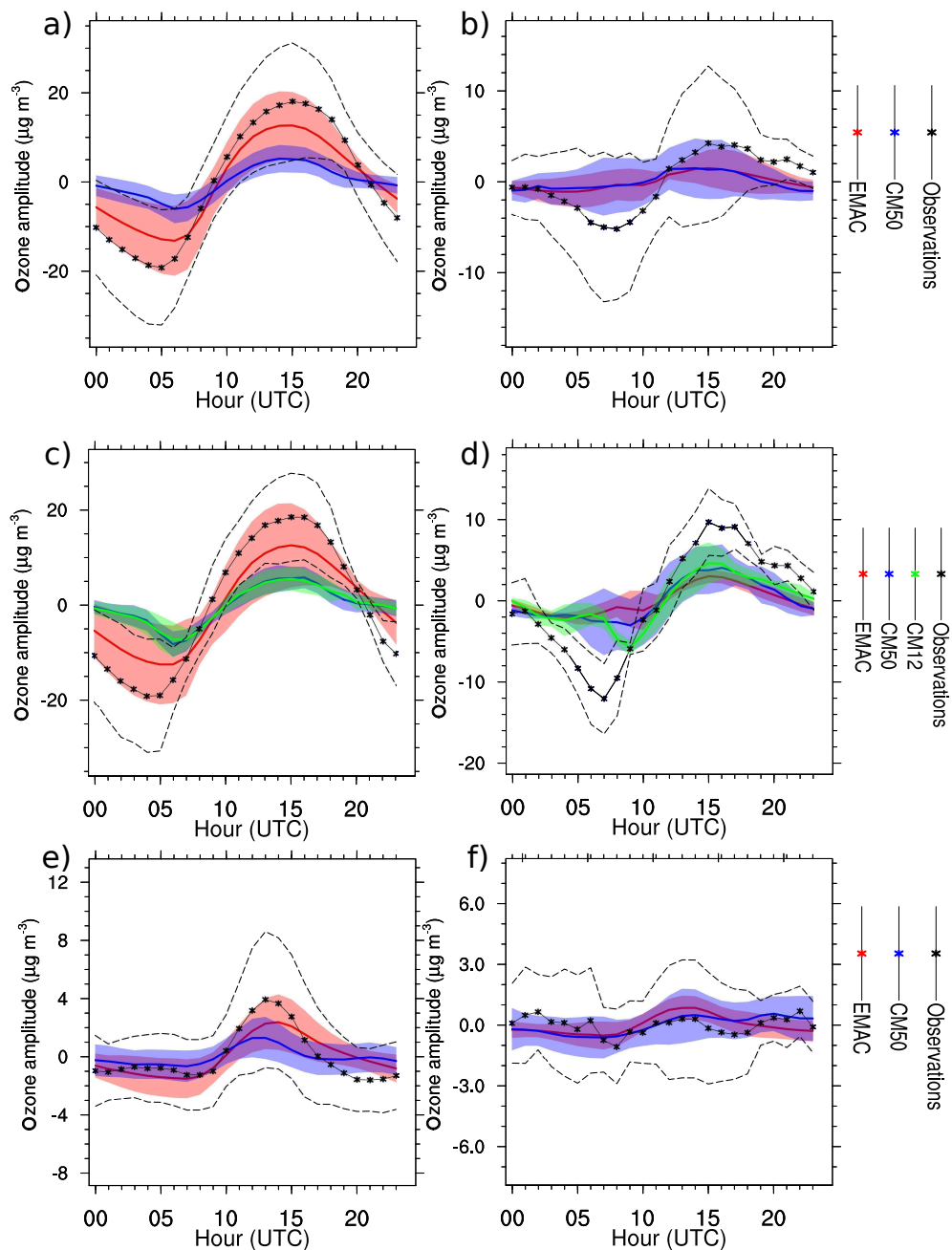


Figure 4.10: Anomalies of the O_3 diurnal cycle in $\mu\text{g m}^{-3}$. **(a)** for all non-mountain stations and **(b)** for all mountain stations for June 2008 in the CM50 domain. **(c)** for all non-mountain stations and **(d)** for all mountain stations for June 2008 in the CM12 domain. **(e)** for all non-mountain stations and **(f)** for all mountain stations for December 2008 in the CM50 domain. The observations are shown in black, while EMAC is shown in red, CM50 in blue and CM12 in green (only c and d). The dashed lines indicate lines indicate one standard of the, while the coloured areas display shows one standard deviation of the model results. These standard deviations were calculated with respect to the averaging over the stations.

stations were calculated using the height corrected model data. The analysis focuses on the anomalies of the diurnal cycles with respect to the mean values. To do so, I calculated the monthly averaged diurnal cycle of the results for every station. The mean values of the diurnal cycles were calculated and subtracted from the diurnal cycles. These mean values and the corresponding anomalies were averaged in a second step over all non-mountain and mountain stations, respectively.

Figure 4.10a shows the averaged anomalies of the diurnal cycle of the non-mountain stations for June 2008, the corresponding mean values are listed in Table A15 (page 178). The mean values of EMAC and CM50 show a positive O₃ bias, but the differences are within one standard deviation of the observations. The range of the anomaly, however, is underestimated by CM50. While the range of the observations is $\pm 18 \mu\text{g m}^{-3}$, CM50 and EMAC simulates an range of $\pm 5 \mu\text{g m}^{-3}$ and $\approx \pm 12 \mu\text{g m}^{-3}$, respectively. Comparing not the anomaly, but the complete diurnal cycle (not shown), both EMAC and CM50 simulate an identical noon peak of $\approx 100 \mu\text{g m}^{-3}$ (the observations show a peak of $\approx 93 \mu\text{g m}^{-3}$). Obviously, CM50 underestimates the decrease of O₃ during night (which is mainly due to chemical destruction and dry deposition). This issue is discussed in detail in Sect. 4.4.

The mean values for the mountain stations in June 2008 from CM50 and the observations are similar, while the EMAC results show a positive O₃ bias ($\approx 7 \mu\text{g m}^{-3}$). However, the small anomaly of the observed diurnal cycle ($\pm 4 \mu\text{g m}^{-3}$) is underestimated by both models, which show hardly any variations.

Figure 4.10c and Fig. 4.10d display the averaged anomalies of the diurnal cycles for the subset of stations, which are located in both COSMO instances. The corresponding mean values are listed in Table A16 (page 181). By and large, the results are similar as for all stations in the CM50 domain. The observed anomalies for the non-mountain stations ($\approx \pm 19 \mu\text{g m}^{-3}$) are underestimated by EMAC and both COSMO instances. Especially the two COSMO instances simulate smaller ($\approx \pm 5 \mu\text{g m}^{-3}$) values compared to EMAC ($\pm 12 \mu\text{g m}^{-3}$). The absolute values of the observed noon peak (not shown) are simulated well by both COSMO instances ($\approx 95 \mu\text{g m}^{-3}$) and overestimated by EMAC ($\approx 102 \mu\text{g m}^{-3}$). Again, the results suggest an underestimation of the O₃ loss during night. The anomaly of the diurnal cycle of the observations ($\approx \pm 10 \mu\text{g m}^{-3}$) for the mountain stations is not reproduced by EMAC and the two COSMO instances. The CM12 results show the largest anomaly ($\approx \pm 2 \mu\text{g m}^{-3}$) from all models, which is still much lower compared to the observed amplitude.

The anomalies simulated by both models for the non-mountain stations in December 2008 is similar compared to the observations (Fig. 4.10e). The (small) noon peak, however, is underestimated, yet all differences are within one standard deviation of the observations. The mean values, show a positive bias of $\approx 19 \mu\text{g m}^{-3}$ for EMAC and $\approx 29 \mu\text{g m}^{-3}$ for CM50 (Table A15 in Sect. A.7, page 181). This bias for O₃ exists also at the mountain stations, but smaller in magnitude ($8 \mu\text{g m}^{-3}$ for EMAC and $13 \mu\text{g m}^{-3}$ for CM50); the absence of a diurnal cycle is represented by both models (Fig. 4.10f).

4.3.4 Vertical O₃ profiles

In order to check, if the vertical distribution of O₃ is simulated well, the simulation results are compared with O₃ sonde data.

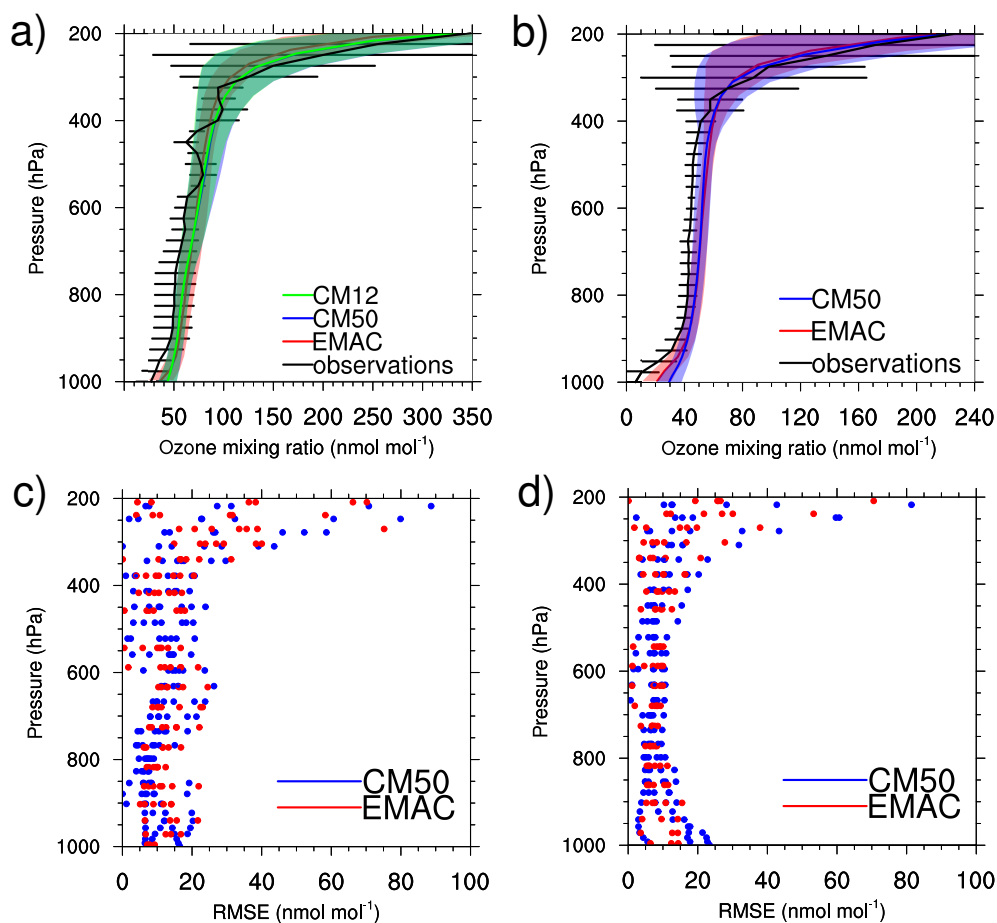


Figure 4.11: (a) and (b): Vertical O_3 profile (in nmol mol^{-1}) at De Bilt (Netherlands) for (a) June, (b) December 2008. In (a) results for all EMAC and the two COSMO instances are shown, while (b) shows the results for EMAC and CM50. The error bars for the observations and the shaded area for the simulation data indicate one standard deviation with respect to time (based on hourly model output/on the available observations per month). (c) and (d): Vertical profile showing the RMSE of the model data compared to the O_3 sonde data (in nmol mol^{-1}) for (c) June 2008 and (d) December 2008.

As first step of this comparison the O_3 sonde data were transformed to a fixed pressure grid. The O_3 sonde data are not continuously measurements in time, but represent distinct points in time (and space). To simplify the comparison with the model results all measurements within one month were averaged, without any weighting of the individual measurements. This processed observation data were compared with monthly mean model data at the location of every station. Therefore the simulated and observed data are co-located in space, but not necessarily in time.

Exemplarily the O_3 profiles of the observations, and the simulation results of EMAC and CM50 at De Bilt (Fig. 4.11a and Fig. 4.11b) are displayed. For June 2008 additionally also the vertical profiles simulated by CM12 are shown. The vertical O_3 distribution is captured well by EMAC and the two COSMO instances. The mean of the simulated O_3 mixing ratios lies, for most profiles, within one standard deviation of the observations. However, in the boundary layer a positive bias of COSMO is noted at most stations.

This bias is in line with the results already presented in the previous comparison with ground level observations.

The large variability of the observations in the upper troposphere/lower stratosphere (UTLS) area is captured much better by COSMO than by EMAC, as COSMO resolves intrusion of stratospheric air into the troposphere better. However, while comparing the variability, it is important to note that the number of data points of the observations is much lower than for the simulated data. The results of CM12 (Fig. 4.11a) are very similar to CM50, but the variability is slightly larger due to the finer horizontal resolution.

Despite the good representation of the measured O₃ mixing ratios in the free troposphere O₃ is overestimated within the planetary boundary layer (PBL) at most stations, which is more pronounced in COSMO than in EMAC. At some stations (e.g. Payerne, Legionowo) only a small or even no gradient of the mixing ratio within the PBL is simulated by COSMO. This problem is discussed in detail in Sect. 4.4.

In addition, the RMSEs (defined in Sect. 4.3.3) between the monthly average simulation data and the monthly mean of the observation were calculated. To obtain this, I transformed the observations on the vertical grid of the respective simulation. The RMSEs for all profiles in June 2008 is shown in Fig. 4.11c. In general the RMSEs of EMAC and CM50 look very similar. From the bottom up to roughly 800 hPa the RMSEs are between 0–20 nmol mol⁻¹. From 800 hPa to 600 hPa the RMSEs increase to 5–25 nmol mol⁻¹. At 600 hPa they drop back to 0–20 nmol mol⁻¹. In the UTLS the variability of the RMSEs are again increasing. In this area the variability and the absolute O₃ values are very large.

In December 2008 (Fig. 4.11d) too high values within the PBL in CM50 show up by larger values of the RMSE (up to 25 nmol mol⁻¹), while EMAC exhibits a maximum RMSE of 15 nmol mol⁻¹. At roughly 800 hPa both models show a decreased RMSE of ≈ 10 nmol mol⁻¹ at maximum, before the spread of the RMSE is again increasing in the UTLS.

4.3.5 Tropospheric oxidation capacity

To investigate if EMAC and the two COSMO instances simulate different tropospheric oxidation capacities, the lifetime of CH₄ against OH (τ_{CH_4+OH}) is calculated according to Jöckel et al. (2006) as

$$\tau_{CH_4+OH}(t) = \frac{\sum_{b,t} M_{CH_4}^b(t)}{\sum_{b,t} \kappa_{CH_4+OH}^b(t) \cdot c_{air}^b(t) \cdot OH^b(t) \cdot M_{CH_4}^b(t)} \quad (4.3)$$

with $M_{CH_4}^b(t)$ the mass of CH₄ in every grid box b at time t , $\kappa_{CH_4+OH}^b(t)$ the reaction coefficient of the reaction CH₄ + OH (which depends on the temperature), $c_{air}^b(t)$ the concentration of air and $OH^b(t)$ the mole fraction of OH.

Estimates of the CH₄ lifetime from global model simulation with a very similar set-up as used in the present study (Sect. 3.2.2.1) are in the range of 7.7 a for the year 2008 (*RC1SD-base-10a* simulation presented by Jöckel et al., 2016). As analysed in detail by Jöckel et al. (2016) this is at the lower end compared to results from other models, which are mainly in the range from 8–9 a.

In such global model simulations the CH₄ lifetime can be calculated at every time step. As the lifetime is calculated here only for a fraction of the globe, it is important to sum the

Table 4.3: Average values for June-August 2008 of the CH₄ mass (M_{CH_4}), the OH mass (M_{OH}) and the pseudo CH₄ lifetime against OH (τ) for EMAC, CM50 and CM12. All values are computed for the area of the CM12 instance. The mass of CH₄ and OH are the time averaged values. The range is one standard deviations with respect to time (based on the monthly mean values). The subscripts on the individual variables indicate the different vertical layers.

	EMAC	CM50	CM12
$M_{\text{CH}_4}^{850}$ (Tg)	0.973 ± 0.011	0.900 ± 0.012	0.916 ± 0.012
M_{OH}^{850} (kg)	60.4 ± 8.8	46.9 ± 5.3	55.5 ± 5.8
τ^{850} (a)	2.73 ± 0.46	3.43 ± 0.38	2.90 ± 0.29
$M_{\text{CH}_4}^{500}$ (Tg)	2.50 ± 0.04	2.45 ± 0.04	2.41 ± 0.04
M_{OH}^{500} (kg)	192 ± 15	209 ± 15	212 ± 15
τ^{500} (a)	3.96 ± 0.27	3.54 ± 0.22	3.51 ± 0.18
$M_{\text{CH}_4}^{200}$ (Tg)	2.12 ± 0.04	2.17 ± 0.03	2.11 ± 0.03
M_{OH}^{200} (kg)	228 ± 19	248 ± 24	247 ± 24
τ^{200} (a)	12.4 ± 1.0	11.3 ± 1.0	11.2 ± 1.1

Table 4.4: As Table 4.3 but for the European area.

	EMAC	CM50
$M_{\text{CH}_4}^{850}$ (Tg)	27.0 ± 0.3	26.7 ± 0.3
M_{OH}^{850} (kg)	1520 ± 110	1400 ± 90
τ^{850} (a)	2.71 ± 0.16	2.97 ± 0.17
$M_{\text{CH}_4}^{500}$ (Tg)	69.1 ± 1.0	73.6 ± 0.7
M_{OH}^{500} (kg)	4620 ± 400	4630 ± 400
τ^{500} (a)	4.27 ± 0.33	4.50 ± 0.36
$M_{\text{CH}_4}^{200}$ (Tg)	58.7 ± 1.0	58.7 ± 0.7
M_{OH}^{200} (kg)	5850 ± 550	5580 ± 510
τ^{200} (a)	12.8 ± 1.3	13.1 ± 1.4

numerator and denominator first over all time steps of a certain period (≥ 1 day) before the lifetime is calculated. The reason for this is, that during night OH is virtually absent and the denominator becomes arbitrary small. Of course, the results of the global calculations are not comparable to the results of the calculations performed in the present study. I calculated the CH₄ lifetime as purely diagnostic quantity to compare the tropospheric oxidation capacities. Therefore this values are denoted as pseudo CH₄ lifetime (denoted as τ).

To allow a more detailed comparison of the model results, τ is calculated separately for three different vertical layers of the atmosphere: From the ground to 850 hPa, from 850 hPa to 500 hPa and from 500 to 200 hPa. All grid boxes within the respective area were summed up for this.

First, τ is compared for the German region, which is covered by EMAC, CM50 and CM12 (Table 4.3). For the layer from the bottom up to 850 hPa EMAC calculates the shortest average pseudo lifetime (2.7 a), which is due to a larger OH mass (60 kg). In

the CM12 instance τ is shorter (2.9 a) than in CM50 (3.4 a), as more OH is present in CM12. In the second vertical layer (850–500 hPa), both COSMO instances show similar results (3.5 a). The CH₄ mass is smaller compared to EMAC, while the OH mass is larger, which leads to a shorter average pseudo CH₄ lifetime in both COSMO instances compared to EMAC.

The results from all models show comparable OH masses for the highest vertical layer (500–200 hPa). The pseudo lifetime of CH₄, however, is longer for EMAC (12.4 a) compared to CM50 (11.3 a) and CM12 (11.2 a), which mainly caused by the lower temperatures in EMAC in this vertical layer (cf. Sect. 4.1).

The pseudo CH₄ lifetimes in the European domain (Table 4.4) show similar results as over Germany. In the lowest vertical layer EMAC simulates lower values for τ (mainly due to more OH). In the second vertical layer both models simulate very similar pseudo CH₄ lifetimes, while the lifetime in the upper layer is again larger in CM50. The shorter pseudo lifetime in EMAC compared to COSMO is due to more OH in EMAC.

4.4 Discussion on deviations from observations

The comparison of the COSMO results with the observations in the previous sections has shown several differences which are:

- The ground level mixing ratios of CO are too low, while the O₃ mixing ratios are too large. Especially Northeastern Europe is affected by too large ground level O₃ concentrations during April (not shown) to June.
- The amplitude of the diurnal cycle is underestimated, showing too large values during night.

Following, I analyse and discuss potential reasons for these differences.

First of all the influence of the cold-bias of COSMO (which is a known problem of COSMO-CLM during winter, e.g. Kotlarski et al., 2014) is investigated. To do so, I performed a sensitivity study in which the chemical kinetics in CM50 were calculated with the same temperatures as in EMAC¹⁴. All other dynamical and chemical processes (like the on-line calculation of emissions) used the original temperature field of CM50.

Resulting area averaged ground level concentrations for chosen chemical species over Europe (defined as a box from 5°W–20°E, 20°N–55°N) are summarised in Table 4.5. Comparing first the area averaged concentrations between EMAC and CM50 a positive difference for all species, except O₃, is apparent. This includes short lived species like OH or NO₃ and longer lived species like bromoform (CHBr₃) and CO. The comparison between the results of CM50 and CM50_{T*} (with the changed temperature field) shows that the concentrations of most short lived species (like OH, NO₃ or HCHO) increase. These differences are due to the temperature dependence of most reaction rates. The magnitude of these increases can, however, not fully explain the observed differences between CM50 and EMAC, but are an important contributor to the difference of the short lived species between EMAC and CM50. The differences of longer lived species like O₃, CO or CHBr₃ can not be explained by the temperature differences.

¹⁴This is archived by transforming the temperature field of EMAC on the COSMO grid with INT2COSMO. The transformed temperature field was then used in MECCA.

Table 4.5: Area averaged ground level concentrations (for a box from 5°W - 20°E, 20°N - 55°N) in $\mu\text{g m}^{-3}$ of various chemical species. The columns two to four display the values for CM50, EMAC and CM50 with changed temperature for the submodel MECCA (CM50_{T*}), respectively. The fifth column indicates, if the differences between EMAC and CM50 are positive (+), negative (-), or if there is only a minor difference (\approx). The last column indicates the corresponding differences between CM50 and CM50 with changed temperature field for MECCA.

	CM50	EMAC	CM50 _{T*}	diff 2 and 1	diff 3 and 1
HO ₂	0.00453	0.00563	0.00492	+	+
OH	$4.53 \cdot 10^{-5}$	$5.67 \cdot 10^{-5}$	$4.75 \cdot 10^{-5}$	+	+
CHBr ₃	0.00388	0.00402	0.00387	+	\approx
CH ₃ Br	0.0308	0.0320	0.0308	+	\approx
CH ₃ I	0.00261	0.00412	0.00261	+	\approx
NO ₃	0.00866	0.00914	0.0126	+	+
NH ₃	2.04	4.00	2.03	+	\approx
NO	0.178	0.401	0.164	+	-
NO ₂	3.51	5.25	3.55	+	\approx
C ₅ H ₈	0.0855	0.144	0.0818	+	-
HCHO	0.85	1.14	0.938	+	+
CO	149	169	149	+	\approx
O ₃	111	99.0	114	-	+

To investigate further potential reasons for the differences between EMAC and CM50, I compared vertical profiles of ²²²Radon¹⁵ of CM50 and EMAC. The vertical profiles of ²²²Radon (not shown) show smaller concentrations in the PBL in CM50 than in EMAC, even though the sources are identical. This difference can only be explained by a stronger vertical mixing (vertical diffusion and/or convection) within the PBL in COSMO compared to EMAC. This stronger mixing explains also the differences for the longer lived trace gases like O₃, CO or CHBr₃.

The concentrations of CO and CHBr₃ are usually largest near the surface, where the source are located. The more effective vertical mixing of COSMO compared to EMAC lead to a more effective upward transport and a reduction of the ground level concentrations. The concentration of O₃ increases with height, meaning that the lower values at the surface are faster mixed with air containing more O₃. This is in agreement with the vertical O₃ profiles of CM50 (Sect. 4.3.4) showing too large O₃ mixing ratios in the PBL.

In addition to this stronger mixing there is yet another cause for the too large O₃ concentration in COSMO over Northeastern Europe: COSMO uses different soil types in some areas over Northeastern Europe. This affects for example the stomata resistance determined by the different base models, which subsequently affects the dry deposition velocities. This leads to a reduced dry deposition velocity over parts of Northeastern Europe in COSMO compared to EMAC (Fig. A11 and A12 in Sect. A.7, page 178). Moreover,

¹⁵²²²Radon is simulated using the MESSy submodel DRADON [joeckel10]. This submodel emits ²²²Radon as purely diagnostic species on all land surfaces not covered by ice or snow. The emission rate is $10000 \text{ atoms m}^{-2} \text{ s}^{-1}$ and the only sink in the atmosphere is radioactive decay with a half-life of 3.8 days.

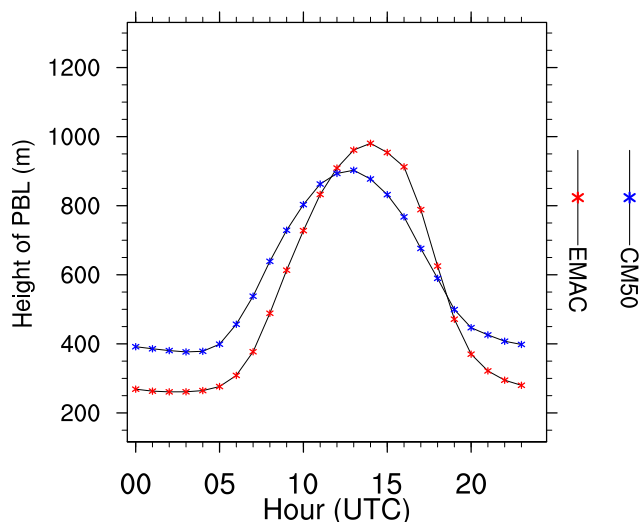


Figure 4.12: Height of the planetary boundary layer for June 2008 in m averaged over all non-mountain stations.

Stock et al. (2014) found larger ground level concentrations of O_3 over Northeastern Europe, when increasing the resolution of their simulations. As they are using the same MACCity emissions as in the present study, it can be speculated that the too large ground level mixing ratios of O_3 might also be influenced by too large emissions of O_3 precursors in this area. As the O_3 chemistry is strongly non-linear even a small amount of larger NO_x emissions would lead to an increased O_3 production in the 'NO $_x$ -limited' regime.

So far, this discussion focused on the differences of the monthly mean ground level concentrations, but not on the underestimation of the amplitude of the diurnal cycle. The underestimation of the amplitude of the diurnal cycle in COSMO has several reasons. The most important difference is the dynamics of the PBL. The diurnal cycle of the PBL is more pronounced in EMAC compared to CM50, showing larger values around noon and smaller values during night (Fig. 4.12).

The lower height of the PBL in EMAC during night leads to a much smaller 'reservoir' from which O_3 can be deposited or chemically destroyed (e.g. via reaction with NO). Nevertheless the amount of O_3 which is removed by dry deposition depends on the concentration of O_3 , which is smaller in EMAC compared to CM50, the concentration in EMAC can be faster reduced as in CM50. This leads to a more efficient destruction of ground level O_3 during night, when no photochemically production of O_3 takes place. In addition, the more efficient vertical mixing in COSMO (as has been discussed above) leads to more efficient downward transport of air with larger O_3 concentration.

This discussed effect is intensified by two additional differences between EMAC and COSMO which lead to a more pronounced diurnal cycle in EMAC. First, EMAC simulates larger dry deposition velocities during night compared to COSMO, while the values during noon are comparable. Second, the net O_3 production in the lowermost model layer is more negative during night in EMAC compared to COSMO.

To investigate if the vertical O_3 profiles and the amplitude of the diurnal cycle of O_3 in COSMO can be improved by changes to the COSMO set-up, further sensitivity studies were conducted. The main aim of these studies was to investigate the effect of changing

parameters affecting vertical mixing (diffusion). Focusing on the vertical O_3 profiles in comparison to O_3 sonde observations and the amplitude of the diurnal cycle of O_3 , none of these simulations showed a substantial improvement compared to the observations. With some parameters, however, a slight improvement of the amplitude of the diurnal cycle and a decreased cold-bias were observed (details are given by Mertens et al., 2016). For future use, however, I envisage a more detailed parameter study with a simplified set-up (e.g. using only passive tracers). This is beyond the scope of this thesis.

To improve the results with respect to the too small amplitude of the diurnal cycle of the PBL and the too strong mixing within the PBL, further model developments are necessary. An example is the turbulence scheme and thus the vertical diffusion parametrisation, which were recently further developed for the ICON model (pers. communication, M. Raschendorfer, DWD). These developments will become available in the COSMO model from version 5.3 on.

Chapter 5

Contribution of road traffic emissions in Europe for 2008

In this chapter I investigate the contribution¹ of road traffic emissions to tropospheric O₃ under present day (year 2008) conditions. To quantify this contribution as well as the sensitivity of the results to uncertainties of the emission estimates, models, and resolution of emission inventories I analyse the results of the different performed simulations. Before these analyses are performed in detail starting in Sect. 5.1, first some introductory analyses are presented. These analyses set the basis for the detailed analyses following in the next sections.

The analyses of the present day situation in this chapter concentrates on the year 2008, which is the focus year of the VEU08 inventory. Before analysing this period, it is important to investigate how representative this year is for present day conditions. Figure 5.1a shows the partial O₃ column from the surface up the 850 hPa (hereafter denoted as 850PC) for the area covered by the CM50 domain²). The results of the global EMAC simulation ranging from 2005–2010 (named *GLOB*) being compared with the results of the EMAC instance from the *REF* simulation for the year 2008. The 850PC has a minimum of ≈ 4.2 DU during winter and a maximum of ≈ 7.0 DU in May/June. This seasonal cycle of O₃ is well known (e.g. Monks et al., 2015) and mainly caused by larger photochemical activity during spring/summer and increased downward transport of O₃ from the stratosphere during May.

Figure 5.1b shows the contribution of O₃ produced from road traffic emissions (denoted as O₃^{tra3}), which depicts a minimum of ≈ 10 % in winter and a maximum of up to 16.5 % in summer. This annual cycle is caused by the complex interplay between O₃ productivity and emissions from other categories and is discussed in more detail in Sect. 5.6.1. Over the whole period small negative trends of the maximum and minimum values are present. These trends correspond to the decline of road traffic emissions in Europe and America in MAC08. Overall, the absolute values and the contributions of O₃^{tra} which are simulated for 2008 are similar to the values simulated for the period 2000–2010. Accordingly, the values for the year 2008 are representative for present day conditions.

¹The term 'contribution' describes always the relative contribution. Absolute values are indicated explicitly.

²In all analyses in this work the relaxation areas of the COSMO domains are neglected.

³Details about the naming convention are given on page 213.

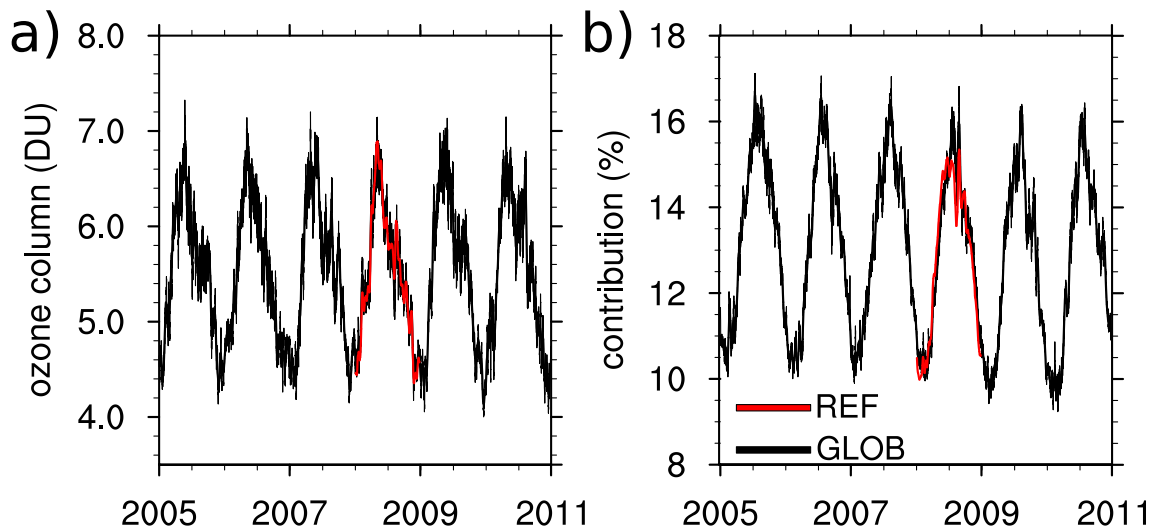


Figure 5.1: Comparison of a 10-day running average of the *GLOB* and the *REF* simulation results. **(a)** the 850PC averaged over the CM50 domain (in DU); **(b)** the contribution (in %) of O_3^{tra} to the 850PC. The labelled tickmarks mark the 1. Jan of the of corresponding year.

The results of the *REF* simulation show a lower maximum during summer compared to the results of the *GLOB* simulation (Fig. 5.1b). This is caused by different lightning- NO_x parametrisations applied in both simulations, leading to larger lightning- NO_x emissions in the *REF* compared to the *GLOB* simulation (Sect. 3.2.2.1). This results in a smaller contribution and absolute values of O_3^{tra} simulated by *REF* compared to *GLOB*. However, the two simulations agree with respect to the seasonal cycle and minimum and maximum values of the other months.

Focusing on the year 2008, Fig. 5.2a shows the contribution of O_3^{tra} to the 850PC of all conducted present day simulations. Besides the seasonal cycle, discussed already for the *GLOB* simulation, the contribution is also variable on shorter time-scales, showing fluctuations of up to 1 percentage point (hereafter denoted as ppts) over the whole year and larger drops of up to 3 ppts during August 2008. These variations on short time scales are investigated in Sect. 5.6.2.

The results shown in Fig. 5.2a are based on the simulations including the incorrect tagging of biogenic emissions in EMAC (Sect. 3.3). To investigate the influence of this incorrect tagging on the simulated contributions, the results of two simulations are compared:

- *REF* - incorrect tagging of biogenic emissions in EMAC,
- *REFbio* - correct tagging of biogenic emissions in EMAC.

Figure 5.2b shows the contribution of O_3^{tra} to the 850PC as simulated by EMAC and CM50, respectively. The difference of the results from CM50 between the *REF* and *REFbio* simulations is small during winter (≈ 0.5 ppts) and largest during summer (≈ 1.5 ppts). The annually averaged difference of the results simulated by CM50 for *REF* and *REFbio* is ≈ 1.0 ppts. This difference is solely caused by the different boundary conditions (provided by EMAC) between both simulations.

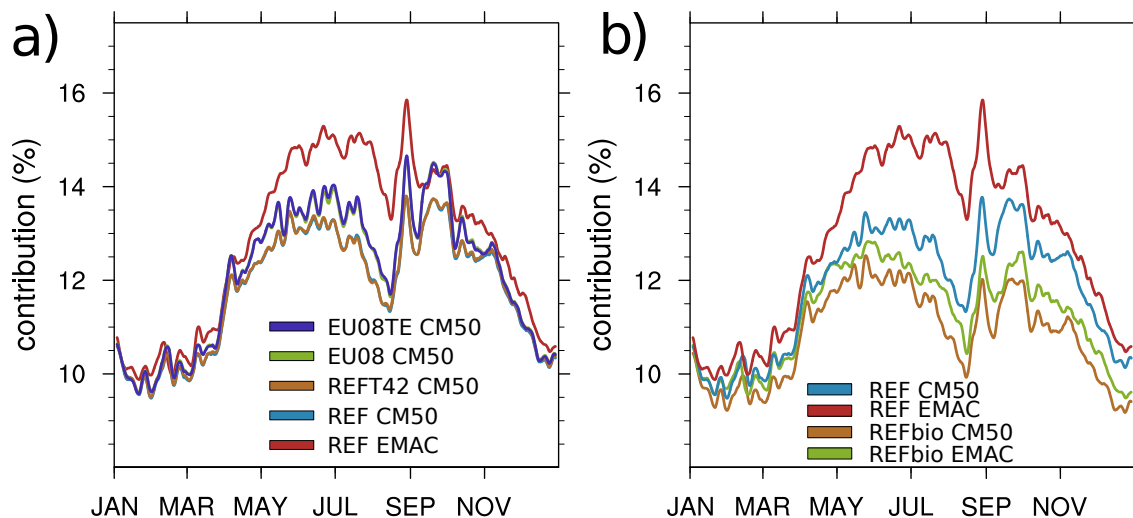


Figure 5.2: (a) 5-day running-average for the contribution (in %) of O_3^{tra} to the 850PC. The name of the simulations and the name of the model (EMAC/CM50) is given for every shown result. The results of EMAC are always shown for the area of the CM50 domain. The tickmarks on the x-axis correspond to the first day of the month. (b) as (a) but showing the results of the *REF* and the *REFbio* simulation.

During winter, EMAC simulates a difference between *REF* and *REFbio* of ≈ 0.5 ppts. The difference increase to ≈ 3.5 ppts during summer, when the soil- NO_x emissions in Europe are largest. Annually averaged EMAC simulates a difference of ≈ 1.6 ppts between *REF* and *REFbio*. The larger difference between the results of both simulations in EMAC compared to CM50 are a consequence of the incorrect contribution of the production of O_3^{biog} in EMAC. In CM50 the production of O_3^{biog} by local emissions from the biogenic category is correctly simulated (Sect. 3.2.4). In CM50 only the boundary conditions of all tagged species of the biogenic category are underestimated. This affects only the tagging diagnostic, the calculation of the chemistry and all other relevant processes is not affected in both models, EMAC and COSMO, respectively.

Because of the incorrect tagging of biogenic emissions only the results of the *REFbio* simulation are used to quantify the contribution of the road traffic emissions in Europe/Germany and for the comparison of the results from EMAC and CM50 in detail. As all other sensitivity simulations analysed in this thesis, including the reference simulation (*REF*), were performed with the incorrect tagging of biogenic emissions in EMAC, these simulations are not used to quantify the contribution. Instead, I use these simulations to investigate the sensitivity of the contribution analysis to defined changes of the emissions/model/resolution. My focus for these analyses are on the results of COSMO, which are influenced only by the incorrect boundary conditions. Therefore, it is likely that this incorrect tagging has a minor influence on the analysed sensitivities.

This following analyses in this chapter are ordered as following. First, the differences with respect to the simulated contribution of the road traffic emissions between EMAC and CM50 are compared (Sect. 5.1), followed by a comparison of the results of CM50 and CM12 (Sect. 5.2). In a next step, the four different present day sensitivity studies are compared (Sect. 5.3). Further, the sensitivity with respect to changes of the biogenic

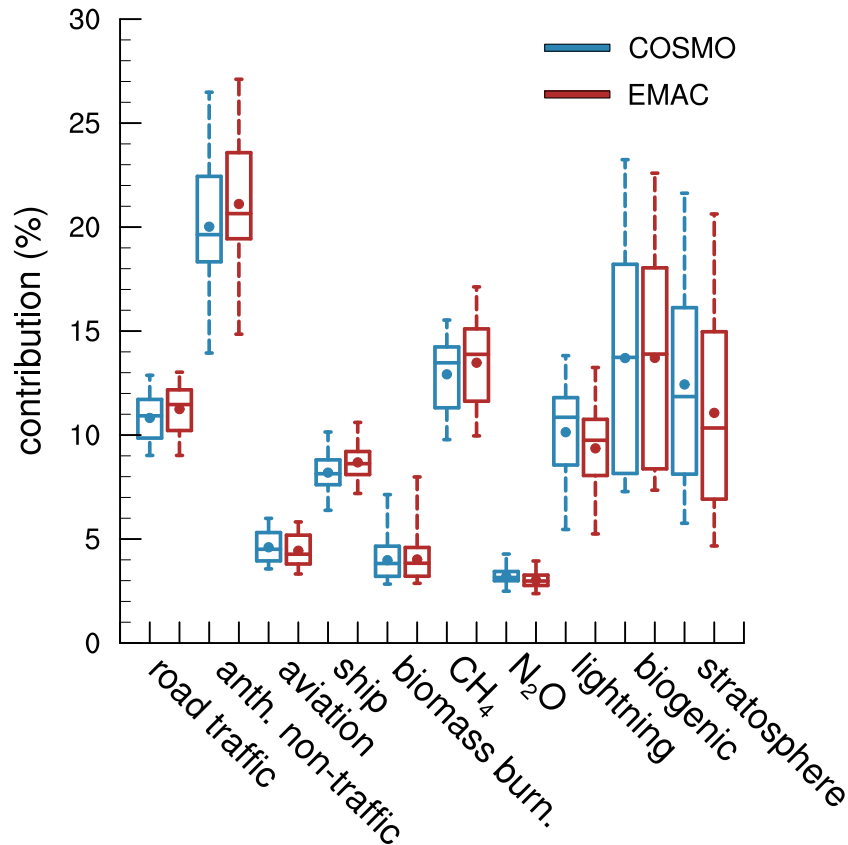


Figure 5.3: Box and whisker plot for the contribution (in %) of the different tagged categories to the 850PC. The values are area-averaged over the CM50 domain. The lower and upper end of the box indicates the 25th and 75th percentile, the bar the median, the dot the average and the whiskers the minimum and maximum of the timeseries for the year 2008. Compared are the results of the EMAC instance (EMAC) and the CM50 instance (COSMO) for the *REFbio* simulation (each 3 hour temporal resolution).

emissions are discussed (Sect. 5.4). Finally, the seasonal cycle and short term fluctuations are analysed (Sect. 5.6).

5.1 Differences between EMAC and COSMO

To investigate the differences of the contribution of O_3^{tra} simulated by CM50 and EMAC I analyse in this section

- the results from both models of the *REFbio*⁴ simulation.

5.1.1 Comparison of the simulated contributions to O₃

First of all, the differences between the contributions of O₃^{tra} simulated by EMAC and CM50 are investigated. Figure 5.3 shows the contribution of the ten tagged categories⁵ to O₃ for the results of the *REFbio* simulation (using the same emission inventory in EMAC and COSMO). Displayed are the averages, medians, 25th and 75th percentiles, and the maxima and minima of the contributions to the 850PC for the year 2008. This presentation is chosen, as the contributions of the different sectors have distinct seasonal cycles. Please note, that only the contributions are discussed here. The results of the absolute values are rather similar. The corresponding figure showing the absolute value is given in the Appendix (Fig. A13, page 183).

The contributions, simulated by both models, are rather similar. Examples for this are the categories N₂O, aviation and biomass burning with average contributions of around 3–4 %. The seasonal cycles of the contribution of these categories (corresponding to the difference between minima and maxima) are small for the N₂O and aviation categories, because the seasonal cycles of the emissions (Sect. 3.2.5) are small too. Only the biomass burning category shows a asymmetry, with a large peak of the maximum values. This is caused by the seasonal variation of the emissions (Sect. 3.2.5 and further discussion in Sect. 5.6). Also the contributions of the other categories are similarly simulated by EMAC and CM50, respectively, but small differences exist which can be attributed to different properties of both models and are therefore discussed shortly.

The contribution of the stratospheric category shows (for both models) a large seasonal cycle. The largest absolute values are found in April–May, when the O₃ values are largest too. Larger mean values of the stratospheric category are simulated by CM50 (13 %) compared to EMAC (≈ 11 %). The difference is explained by two processes: first of all the finer resolution of CM50 allows a better representation of stratosphere-troposphere-exchange (STE) as shown by Hofmann (2014) leading to more STE in CM50 compared to EMAC. Second, the stronger vertical mixing in COSMO compared to EMAC (Sect. 4.4) leads to an additional increase of the contribution of the stratospheric category, as O₃^{str} is more efficiently mixed downwards. The increased vertical mixing in COSMO compared to EMAC also explains the larger average contribution of the lightning NO_x category in COSMO (10.5 %) compared to EMAC (9.5 %), although the same emissions are applied.

EMAC simulates a slightly larger average contribution of the CH₄ category (13.5 %) compared to CM50 (13.0 %). During October–April the contributions simulated by EMAC and CM50 are similar. The contributions differ, however, during May–October as the photochemistry is most active during this time and CM50 simulates a lower contribution as EMAC. This leads to larger values of the maximum and 75th percentile for EMAC compared to CM50. This larger contribution of EMAC is in agreement with the shorter CH₄ lifetime in EMAC compared to CM50 as analysed in Sect. 4.3.5, because a shorter lifetime means that CH₄ is more efficient oxidised in EMAC compared to CM50.

Both models exhibit comparable average values of around 14 % for the biogenic category. Similar as for the stratospheric category a strong seasonal cycle of the contribution is strik-

⁴As has been discussed on page 77 the simulation is identical to the *REF* simulation, but with correct tagging of biogenic emissions in EMAC. Only the results of this simulations are used to quantify the contribution of road traffic emissions to tropospheric O₃ in detail.

⁵A detailed description of these categories is given in Sect. 3.1.7.

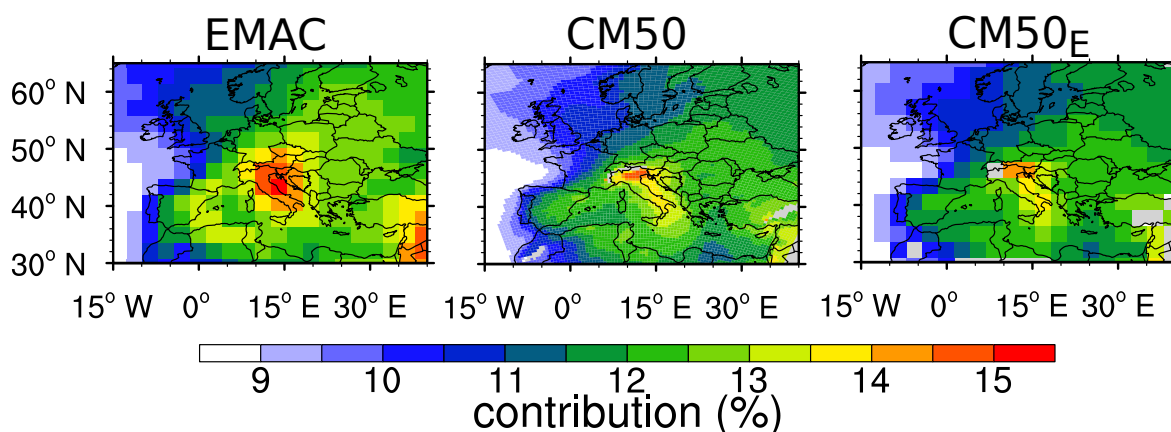


Figure 5.4: Contribution of O_3^{tra} (in %) to the 850PC averaged over JJA for EMAC, CM50 and CM50 transformed onto the EMAC grid (CM50_E).

ing. This seasonal cycle originates from the strong seasonal cycle of the soil- NO_x emissions in Europe, which are low in September–April and large in May–August (Sect. 3.2.5).

CM50 simulates mean values of 20.0 % for the anthropogenic non-traffic category, 10.8 % for the road traffic category and 9.0 % for the shipping category. Especially the contribution of the anthropogenic non-traffic category shows a large seasonal cycle, which is caused by the strong seasonal cycle of the anthropogenic non-traffic emissions. A detailed discussion of this cycle follows in Sect. 5.6. Compared to this the seasonal cycle of the road traffic category is smaller with values of ≈ 9.5 % during winter and ≈ 11.5 % during summer. Compared to CM50, EMAC simulates contributions which are 0.5–1 ppts larger. These differences, however, are small compared to the sensitivity of the results to uncertainties of the emission estimates (details follow in Sect. 5.5). Therefore it can be concluded that, for the area averaged values, the mean contribution of the road traffic category are simulated very similar between EMAC and COSMO.

In addition to the values averaged over the area of the CM50 domain, a comparison of the geographical patterns is important. Figure 5.4 shows the contribution of O_3^{tra} as simulated by EMAC and CM50. The values are averaged for the period June–August (from now on denoted as JJA) in which the photochemistry is most active. The CM50 results are shown on the original grid and transformed onto the EMAC grid. The transformed results are shown to allow an easier comparison of the results from both models. Only in case of remarkable differences between the results on the original grid and on the transformed grid these results are discussed.

Both models simulate similar geographical patterns, but the values simulated by EMAC are larger by around 1 ppts over most areas. The lowest contributions are found over the Atlantic sea (≈ 9 %), over the continents the contribution increases. Both, EMAC and CM50, simulate the largest contributions over Italy with a maximum of $\approx 15\%$. EMAC, however, simulates the largest values over a wide area in Northern Italy, while CM50 simulates the largest values in the Po basin. This large peak in this region is caused by efficient O_3 production in conjunction with a large source of road traffic emissions. The confinement of the largest values to the Po basin as simulated by CM50 is more realistic compared to the results of EMAC, because of the coarsely resolved land-sea

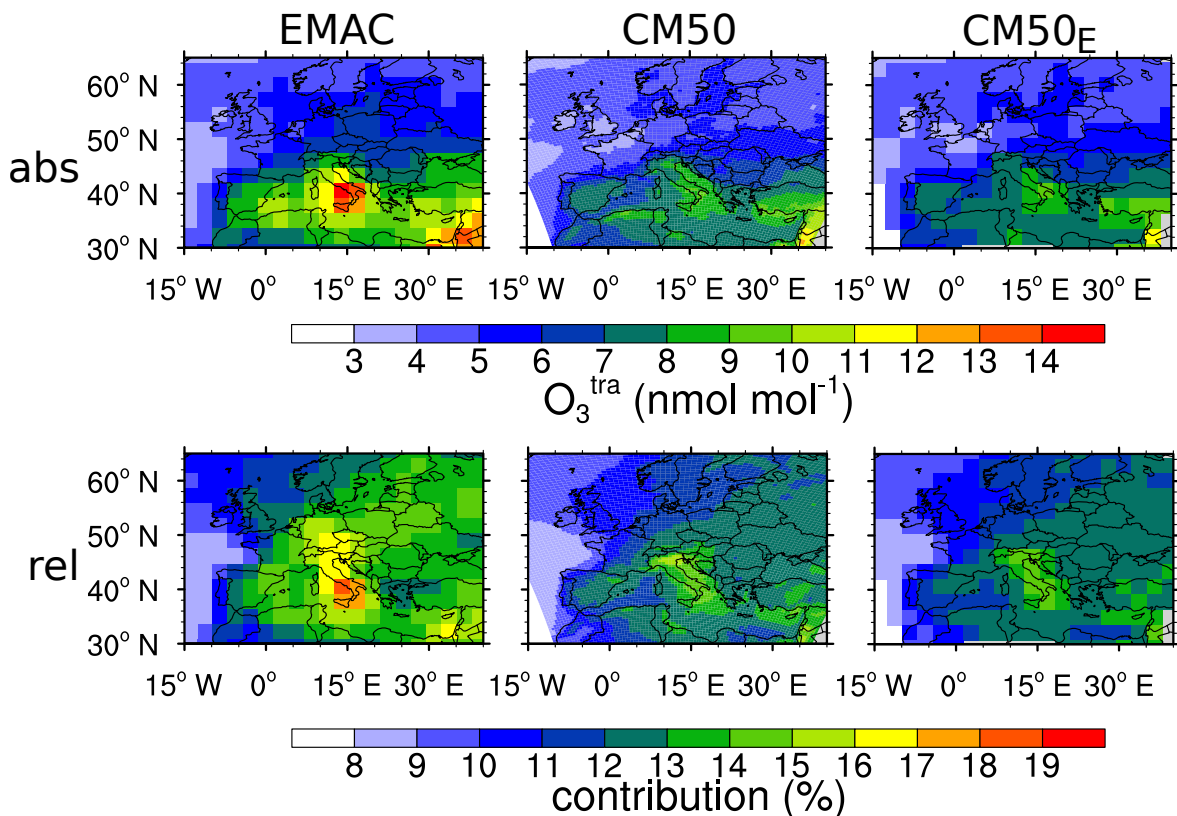


Figure 5.5: Comparison of the ground level mixing ratios of O_3^{tra} (abs, in nmol mol^{-1}) and the contribution of O_3^{tra} to ground level O_3 (rel, in %) between EMAC, CM50 and CM50 transformed onto the EMAC grid (CM50_E). The values are averaged between 9–18 UTC and over the period JJA.

mask in EMAC. Due to this land sea mask EMAC considers most grid boxes covering Italy as ocean and not as land, which lead to strong reductions of the simulated dry deposition flux in these grid boxes. Accordingly, EMAC simulates lower dry deposition rates compared to CM50 over huge parts of Italy (Sect. A.7, page 182).

The largest differences between the EMAC and CM50 results are found over Germany, France and the Eastern Mediterranean, where locally differences of up to 2 ppts exist. The largest differences of the absolute values of O_3^{tra} are found in these regions, too (see Fig. A14, page 184).

So far, this comparison focused on average values of the 850PC. Especially with respect to air quality, the ground level⁶ values are of importance. Figure 5.5 shows both, the JJA averaged absolute values and the contribution of O_3^{tra} to ground level O_3 for EMAC, CM50 and the CM50 transformed onto the EMAC grid. In comparison to the results discussed so far, only the values between 9–18 UTC are averaged. The reason for this is that the contribution of O_3^{tra} in the hotspot areas show the largest values during night. During this time O_3 is destroyed via the reaction of O_3 with NO forming NO_2 (and O_2). The tagging method, however, uses the concept of effective O_3 production (Sect. 3.1.7) and therefore does not account for the quick cycling between NO_2 and O_3 . Therefore,

⁶‘Ground level’ is a synonym for ‘in the lowest grid box’.

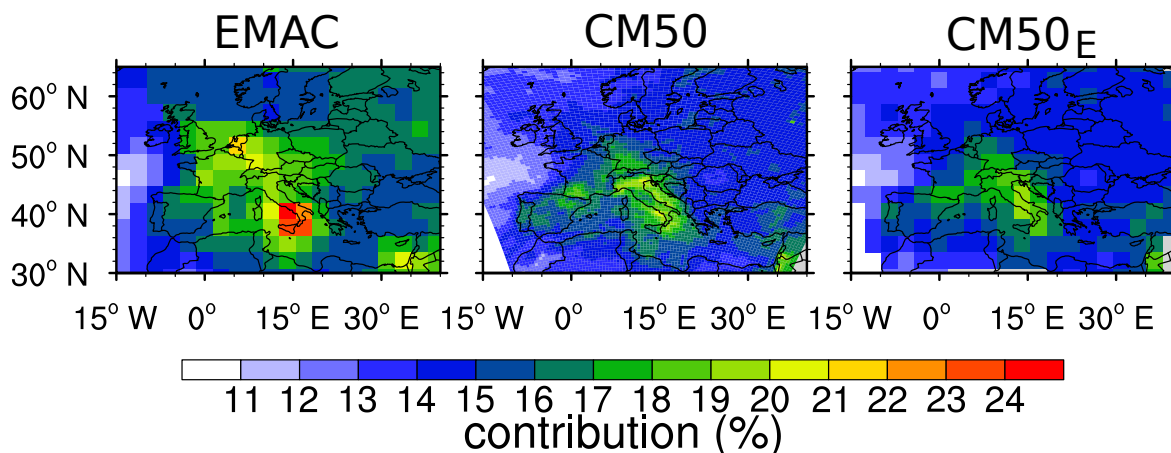


Figure 5.6: 95th percentile of the contribution of O_3^{tra} to ground level O_3 (for JJA between 9–18 UTC) for EMAC, CM50 and CM50 transformed onto the EMAC grid (CM50_E).

this large contribution during night is likely an artefact caused by this method. Further investigations are needed to analyse, if this quick cycling should be considered by the tagging method.

Although CM50 simulates larger ground level values of O_3 compared to EMAC (Sect. 4.3), the simulated absolute values for O_3^{tra} are lower in CM50 compared to EMAC. In general, both models simulate the largest values in the Mediterranean with peaks around Italy and the Eastern Mediterranean. In these regions EMAC simulates maximum values of 10–14 nmol mol^{-1} , while CM50 simulates maximum values of 8–12 nmol mol^{-1} . Compared to the absolute values the contribution of O_3^{tra} depicts a less pronounced North-South gradient. Again, both models simulate the largest contributions of O_3^{tra} in the Mediterranean. The largest values in the CM50 results are more confined to the Po basin, while the maximum values in the EMAC results are found over a wide area in Southern Italy (16–18 %).

Up to now mainly seasonal average values are analysed. Especially for periods of severe air pollution the extreme values are of interest. Therefore, Fig. 5.6 shows the 95th percentile of the contribution of O_3^{tra} for JJA. This analysis shows that EMAC simulates larger average values, as well as larger maximum values. In general, the EMAC results depict the largest values in Southern Italy, in parts of France, in the Benelux States and in Germany. Compared to this, the results for CM50 show the largest values in Italy (especially in the Po basin), in Southwestern Germany, in Southwestern France and in Northeastern Spain. The 95th percentiles of the contribution simulated by EMAC are 2–4 ppts larger than simulated by CM50. These larger values in EMAC compared to CM50 are a general behaviour of the model, indicated by a shift of the probability density function (Fig A15, page 185) towards larger values in EMAC compared to CM50. As already discussed the large values over Southern Italy as simulated by EMAC are likely an artefact of the coarse resolution of the model and the artificial reduced dry deposition rates in these areas (Sect. A.7, page 178).

To sum up: despite that COSMO simulates larger ground level O_3 mixing ratios in most areas of Europe compared to EMAC, the ground level mixing ratios of the tagged anthropogenic ground level (i.e. road traffic, shipping and anthropogenic non-traffic) categories are lower in CM50 compared to EMAC. Also for the 850PC CM50 simulates

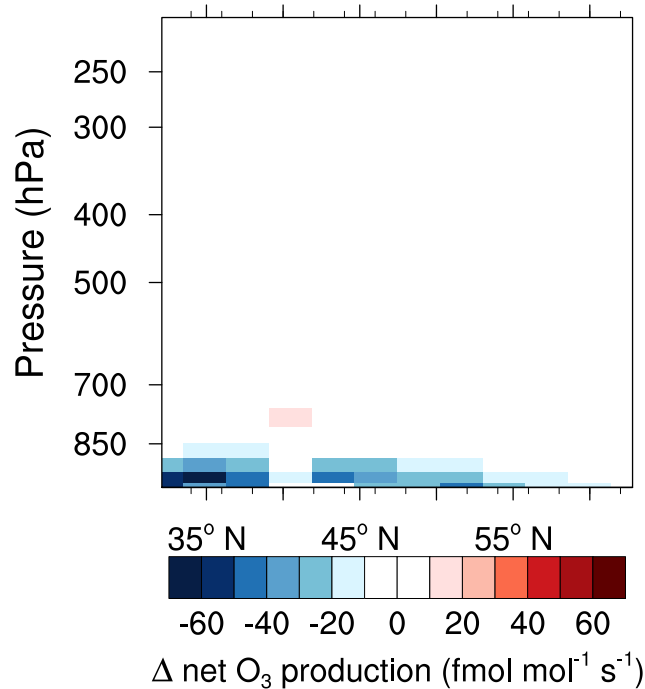


Figure 5.7: Difference ('COSMO minus EMAC') of the zonally averaged O_3 production (in $\text{fmol mol}^{-1} \text{s}^{-1}$). The values are averaged over the year 2008. The results of CM50 were transformed on the horizontal and vertical grid of EMAC.

lower values (both the absolute values and the contribution, respectively) compared to EMAC for the anthropogenic ground level categories, but these differences are smaller compared to the differences of the ground level values. Indeed the differences between EMAC and CM50 with respect to the simulated contributions are small, but they can be explained by differences of the O_3 production which is analysed next.

5.1.2 Comparison of the O_3 production

To investigate differences of the O_3 production between EMAC and CM50 the net O_3 production (PO_3) is compared. This quantity is defined as:

$$PO_3 = \text{Prod}_{O_3} - \text{Loss}_{O_3} \quad (5.1)$$

with Prod_{O_3} and Loss_{O_3} being the sums of two production and five loss terms, as defined in Sect. 3.1.7, respectively. As have been discussed in Sect. 3.1.7 only effective production and loss terms are considered. This effective net O_3 production is called net O_3 production for simplicity. Figure 5.7 shows the annually and zonally averaged difference for the net O_3 production between CM50 and EMAC. The O_3 production is lower in CM50 compared to EMAC mainly in the PBL. The depicted absolute differences in the PBL correspond to relative differences of 10–40 %. These differences are investigated in detail in the following.

Figure 5.8 shows the NO_x mixing ratio and the corresponding net O_3 production for every ground level grid box for EMAC and CM50. Shown are monthly mean values for the period

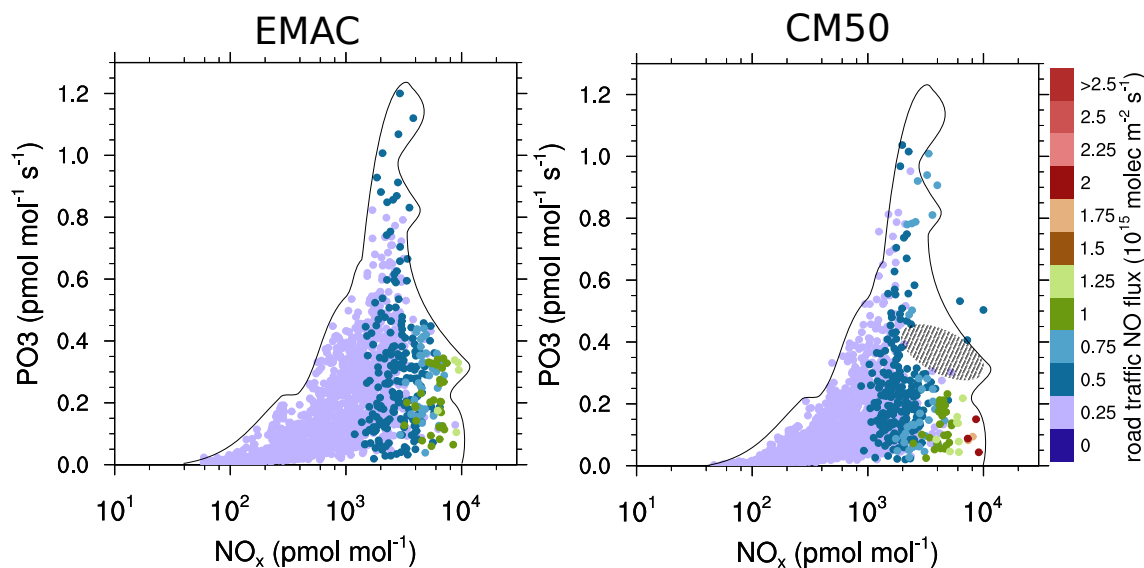


Figure 5.8: Scatter plot of the net O_3 production (in $\text{pmol mol}^{-1} \text{s}^{-1}$) versus the NO_x mixing ratio (in pmol mol^{-1}). The colour of the dots depicts the road traffic NO_x emissions (in $10^{15} \text{ molec m}^{-2} \text{s}^{-1}$). Shown are monthly averaged values of every ground level grid box for May–September. Shown are the values for EMAC and CM50, restricted to the values of the grid boxes covering the CM50 domain. The CM50 values were transformed to the EMAC grid. The hatched region is discussed in the text.

from May–September, when the photochemistry is most active. In addition, also the NO emission flux⁷ of the road traffic category is highlighted by the colours to indicate, in which grid boxes most of the road traffic NO is emitted. The simulated data show the typical dependency of the O_3 production from the NO_x and VOC mixing ratios (Fig. 2.4, page 13). At low NO_x mixing ratios the net O_3 production is low, but increases with increasing NO_x mixing ratios. With further increasing NO_x mixing ratios the net O_3 production decreases again ('VOC-limited'). This decrease is the case for NO_x mixing ratios⁸ around 0.2–0.3 nmol mol^{-1} . In comparison to Fig. 2.4 the meteorological conditions and background chemistry (e.g. mixing ratios of CO or CH_4) are different for every grid box. Therefore some grid boxes show, for example with NO_x mixing ratios around 0.1 nmol mol^{-1} , a lower O_3 production than other grid boxes with similar NO_x mixing ratios. Most of the grid boxes with larger NO_x emissions from road traffic ($> 0.25 \cdot 10^{15} \text{ molec m}^{-2} \text{s}^{-1}$) are located in the 'VOC limited' regime of the O_3 chemistry. In this regime the O_3 production is limited by VOC rather than by NO_x . Road traffic, however, also emits VOC, but the amount is small compared to the NO_x emissions.

To compare the results of CM50 with the results of EMAC the CM50 results were transformed on the EMAC grid. In CM50 up to 36 grid boxes are located within one EMAC grid box, therefore it is expected that some of the CM50 boxes located within the EMAC grid boxes indicate a different behaviour than the EMAC grid box. Important, however, is to investigate, if the average value over the area of the EMAC grid box changes. This may be caused by the non-linearity of the O_3 chemistry. To simplify the comparison

⁷ NO_x is only emitted as NO

⁸It is important to keep in mind, that the values shown here are monthly mean values.

of the EMAC and the CM50 results, the envelope of the data points of EMAC are also shown for CM50. Generally, the results of CM50 indicate a similar dependency between the net O_3 production and the NO_x mixing ratio as in EMAC. In the 'VOC-limited' regime the net O_3 production is smaller in CM50 compared to EMAC (black hatched area for CM50 in Fig. 5.8). Most of the road traffic emissions, however, take place in this 'VOC-limited' region. Hence, especially in these grid boxes with large road traffic emissions CM50 simulates less production of O_3 compared to EMAC. This explains a part of the reduced road traffic contribution in CM50 compared to EMAC.

The CM50 results of the simulation *REFT42* (with coarsely resolved emissions, Sect. 5.3.1), as well as the sensitivity studies with respect to the biogenic emissions (Sect. 5.4) show a similar behaviour as has been discussed for the CM50 results of the *REFbio* simulation. Accordingly, the smaller net O_3 production in the 'VOC-limited' regime in CM50 compared to EMAC is neither caused by the finer resolution of the emissions in CM50 compared to EMAC nor by differences in the geographical distribution of the biogenic emissions.

Further investigations show that in most grid boxes with large NO_x values CM50 simulates lower VOC values than EMAC. Accordingly, the decreased production rate of CM50 in the 'VOC-limited' regime is mainly caused by a larger ratio of NO_x to VOCs compared to EMAC (Fig. A16, page 186). Averaged over all grid boxes covered by the CM50 domain and the period May–September EMAC simulates a net O_3 production of $0.20 \text{ pmol mol}^{-1} \text{ s}^{-1}$, while CM50 simulates values of $0.15 \text{ pmol mol}^{-1} \text{ s}^{-1}$. Thus, CM50 simulates a by $1/4$ lower production of O_3 at ground level compared to EMAC in this period. The less optimal VOC to NO_x ratio in terms of O_3 production as simulated by CM50 compared to EMAC is supported by the analysis of the O_3 production channels (details follow in Sect. 5.3.3). This analysis shows that EMAC simulates more production of O_3 through reactions of VOCs compared to CM50.

As mentioned, these differences can not be explained by the finer resolution of the emissions in CM50 compared to EMAC or differences between the biogenic emissions alone. Instead, three reasons are most likely responsible for these differences:

1. The vertical mixing in COSMO is more effective compared to EMAC (details are given in Sect. 4.4). Ozone precursors are more effectively transported upwards, reducing the O_3 production rates especially in the PBL.
2. Even if the resolution of the emissions is identical between EMAC and CM50 the chemistry and especially the sink processes (e.g. dry deposition) are calculated on a finer grid in CM50 compared to EMAC. This leads to the calculation of different strengths and geographical distribution of the dry deposition rates by both models.
3. The lower temperatures within the PBL in CM50 compared to EMAC (see Sect. 4.1) reduce the O_3 production.

As these differences of the net O_3 production can not solely be attributed to one process alone it could be called a 'model factor'. Further comparisons between both models are necessary after the vertical mixing in COSMO is improved in future versions of COSMO (Sect. 4.4).

It is important to note that within the PBL regionally larger production rates of O_3^{tra} are simulated by CM50 than by EMAC. To analyse these differences the results from both

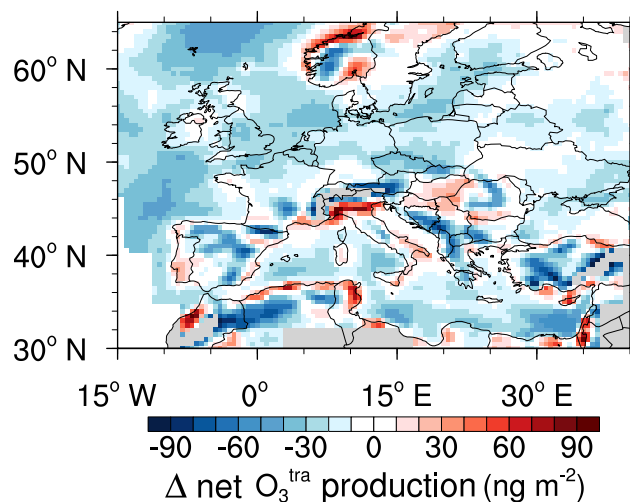


Figure 5.9: Difference ('COSMO minus EMAC') of the annual average net production of O_3^{tra} (summed up to 850 hPa, in ng m^{-2}). The results of both models were transformed to the same regular grid with $0.5^\circ \times 0.5^\circ$ resolution.

models were transformed to a common grid with $0.5^\circ \times 0.5^\circ$ resolution and the annually averaged difference was calculated (Fig. 5.9). The largest positive differences between both model results are found in the Po basin, the coastal region of North Africa and in the Eastern Mediterranean. In these areas CM50 simulated the production of up to 40 ng m^{-2} more O_3^{tra} in the PBL compared to EMAC. This corresponds to relative differences of 30–90 %. In particular in the Eastern Mediterranean positive differences over land and negative differences over sea are striking. The comparison of the CM50 results between the *REF* and the *REFT42* simulation (Sect. 5.3) reveals that the negative differences are caused mainly by the coarse resolution of the emissions. This coarse resolution dilutes the emissions over large areas, emitting road traffic emissions also over sea. Similar results are found around the Po basin, where the emissions on the coarse EMAC grid are less confined to the narrow Po basin, but are spread over the entire Alps. The differences found over North Africa might partially be explained by the larger biogenic emissions simulated by CM50 in this area. The larger emissions changes the background chemistry, leading to larger O_3 production, which can further lead to a larger production of O_3^{tra} .

To sum up, CM50 simulates overall less production of O_3 in the PBL (i.e. up to 850 hPa). This is mainly caused by a less 'optimal'⁹ VOC/ NO_x ratio. Nevertheless, CM50 simulates mostly larger ground level O_3 values than EMAC, which is caused by more intense downward transport of O_3 in CM50 compared to EMAC. This leads to the simulation of a larger contribution of the stratospheric category by EMAC compared to CM50. In addition, CM50 simulates a smaller O_3 production in the troposphere than EMAC. The combination of both processes lead to the simulation of lower absolute values and contribution of O_3^{tra} by CM50 than EMAC.

⁹Less 'optimal' in terms of large O_3 production rates.

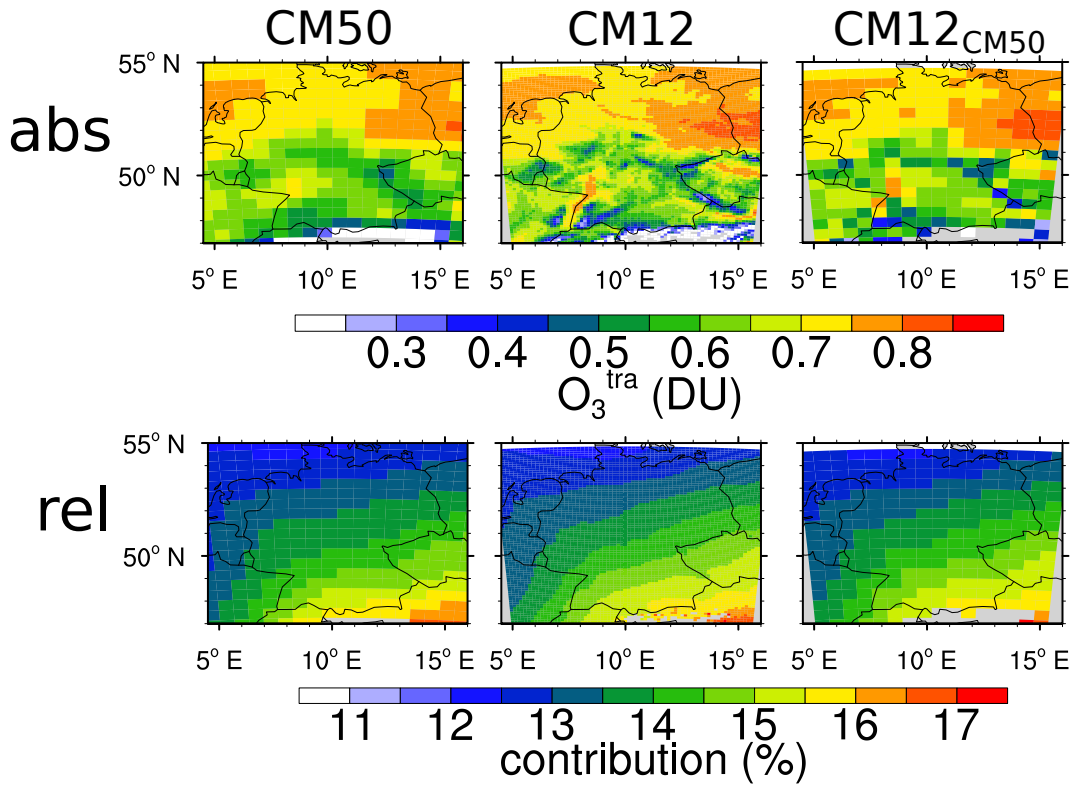


Figure 5.10: Average (JJA) values of the 850PC of O_3^{tra} (abs, in DU) and contribution (rel, in %) of O_3^{tra} to the 850PC for CM50, CM12 and CM12 transformed onto the grid of CM50 (CM12_{CM50}).

5.2 Differences between both COSMO instances

To investigate how a further refinement of the model resolution influences the results of the contribution analysis, this section

- compares the results of CM50 and CM12 of the *EU08* simulation. The used emissions dataset of this simulation is *VEU08*, which is sufficiently resolved to account for the finer resolution of CM12.

Figure 5.10 shows the geographical distribution of the 850PC for O_3^{tra} as well as the contribution of O_3^{tra} to the 850PC. The general pattern and magnitude of the 850PC for O_3^{tra} is simulated similar by both models. The topography influences the absolute values of the 850PC strongly. Therefore the largest values are found over the Northern lowlands. The finer resolved topography of CM12 in comparison to CM50 leads to much finer structures in the simulation results of CM12 (e.g. the upper Rhine valley). The contribution of O_3^{tra} to the 850PC as simulated by both models is also rather similar. The values over Germany are largest in the South-East and lowest in the North-West. This North-West to South-East gradient is mainly caused by the presence of more O_3^{ship} in the North, leading to a decrease of the contribution of O_3^{tra} . Average values over Germany, as simulated by CM50 and CM12, are listed in Table 5.1.

Table 5.1: Area averaged contributions of O_3^{tra} over Germany for the JJA period given for the *REF* and the *EU08* simulation. For a comparison also the average values for the PRUDENCE regions Mid Europe and Mediterranean are given (details see Sect. A.5, page A.5). The range indicates one standard deviation with respect to time (based on three hour model output).

	<i>REF</i> , JJA (%)	<i>EU08</i> , JJA (%)
Germany (CM12)	12.91 ± 1.62	13.66 ± 2.17
Germany (CM50)	12.82 ± 1.59	13.51 ± 2.13
Mid Europe (CM50)	12.63 ± 1.56	13.20 ± 2.01
Mediterranean (CM50)	13.52 ± 0.98	14.70 ± 1.31

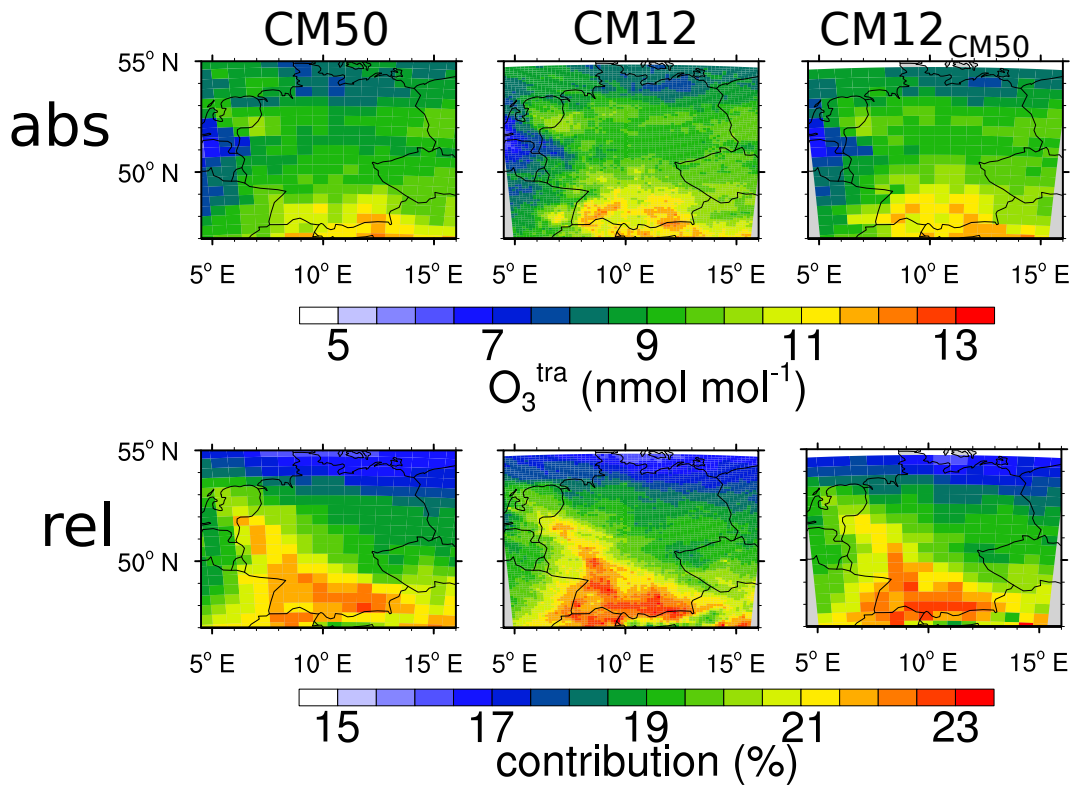


Figure 5.11: 95th percentile for the absolute values (abs, in nmol mol^{-1}) and contribution of O_3^{tra} to ground level O_3 (rel, in %) for CM50, CM12 and CM12 transformed onto the grid of CM50 (CM12_{CM50}). The percentiles were calculated for the period JJA (9–18 UTC).

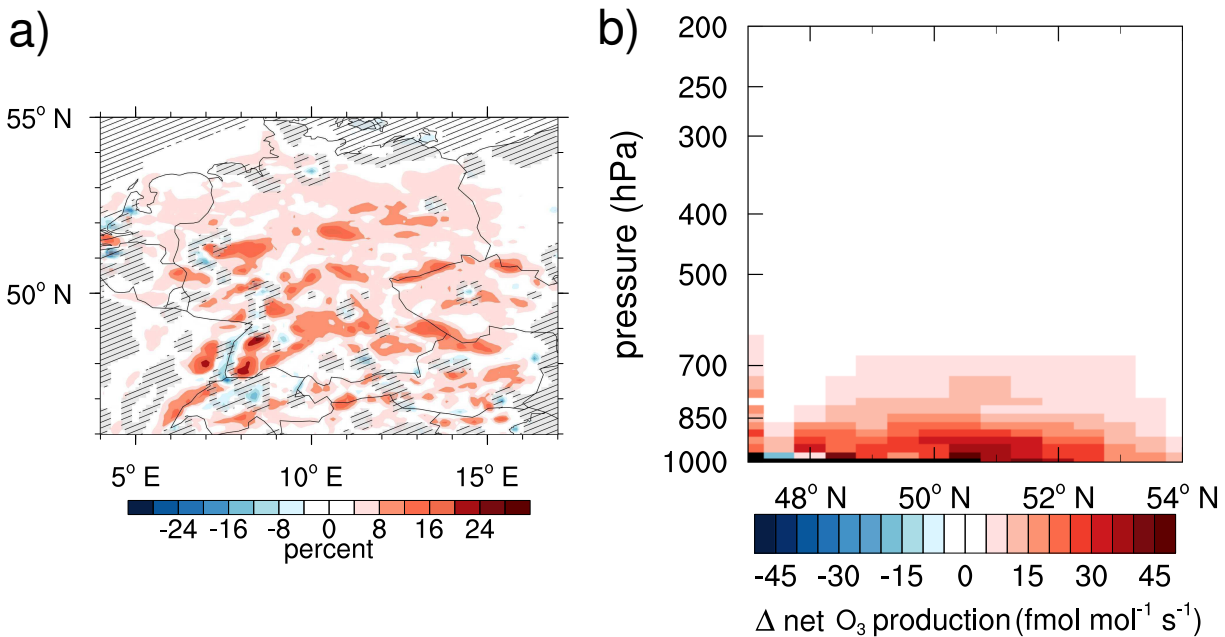


Figure 5.12: (a) Relative difference ($(\text{CM12}-\text{CM50})/\text{CM50}$) in % for ground level O₃ of the *EU08* simulation in the JJA period on a grid with $0.1^\circ \times 0.1^\circ$ resolution. The hatched areas show the areas, where both instances differ by less than one percent on the coarse grid (details see text). (b) Difference ($(\text{CM12}-\text{CM50})$) of the net O₃ production (in fmol mol s^{-1} averaged over JJA). The values are transformed to a common grid with $0.5^\circ \times 0.5^\circ$ resolution.

As the mean values for JJA simulated by CM50 and CM12 are very similar, it seems that they are largely controlled by the boundary conditions (both the emissions and also boundary conditions provided by CM50). Therefore a comparison of the extreme values is more interesting. Figure 5.11 shows the 95th percentile of the absolute ground level values of O₃^{tra} (upper row) and the contribution of O₃^{tra} (lower row) for CM50 and CM12 (both on the original grid and transformed to the grid of CM50). As in Sect. 5.1 the results are restricted to 9–18 UTC (period JJA).

The 95th percentiles of the mixing ratios of O₃^{tra} are larger in CM12 compared to CM50 in particular in South Germany. Here values which are larger than $11.5 \text{ nmol mol}^{-1}$ are simulated. CM12 simulates a larger contribution of O₃^{tra} compared to CM50. The largest maxima of the contribution are simulated in South Germany and along the densely populated regions in West Germany (Frankfurt and Ruhrgebiet). The values transformed onto the coarse grid¹⁰ are also increased in most areas. In some areas the minima and maxima are even displaced, caused by the rather coarse resolution of CM50 compared to CM12 (e.g. the Ruhrgebiet area).

In most parts of these regions contributions of 21–23 % are found for the 95th percentile. In Northern and Northeastern Germany lower maximum values of around 17–19 % are simulated by both models. As have been discussed in Sect. 5.1 the differences discussed here are small too, but they can be explained by differences of the net O₃ production.

¹⁰The shown 95th percentile of CM12_{CM50} are first calculated on the fine grid and then transformed onto the coarse grid.

To understand these differences in detail, first the simulated ground level O_3 values of CM50 and CM12 are compared. In a first step the average ground level O_3 mixing ratios for JJA of the simulation *EU08* of CM50 and CM12 were transformed to a regular grid with $0.1^\circ \times 0.1^\circ$ resolution and to a regular grid with $0.5^\circ \times 0.5^\circ$ resolution. From the results transformed to both grids, the relative differences ($(CM12 - CM50)/CM50$) were calculated. Figure 5.12a shows the relative differences between CM12 and CM50 on a grid with 0.1° resolution. The hatched areas correspond to regions where the relative differences between the results on the 0.5° grid resolution are lower than one percent. In these regions the individual grid boxes in the fine resolution of CM12 show differences, but the average values over the size of the CM50 grid box are similar. In regions with localised hotspots (like Basel, the Upper Rhine Valley or Hamburg) differences of up to $\approx 15\%$ exist. In these hotspots large amounts of NO_x are emitted, leading to a reduction of the O_3 production. This is also indicated by a decrease of O_3 production efficiency (OPE, Sect. 2.3.4) in the CM12 results compared to CM50 (Fig. A17, page 186).

Most areas in Germany, however, show larger ground level mixing ratios of O_3 in CM12 compared to CM50. Some of these larger mixing ratios are caused by the better resolved topography of CM12 compared to CM50 (e.g. the mountain bounds of the Upper Rhine Valley), but also in the North German lowlands larger O_3 mixing ratios are simulated by CM12. These larger mixing ratios are caused by a larger net O_3 production in CM12 compared to CM50. A zonal average of the difference of the net O_3 production as simulated by both models is shown in Fig. 5.12b. In CM12 the net O_3 production is larger mainly in the PBL, corresponding to a 20–30 % increase. This increased net O_3 production can mainly be attributed to a ≈ 0.5 K higher temperature simulated by CM12 compared to CM50. The higher temperature leads larger biogenic emissions¹¹, increasing the O_3 production further.

To compare the production and loss channels of O_3^{tra} simulated by both models, Table 5.2 gives an overview about these channels for the JJA period. As discussed CM12 simulate a O_3 production which is larger by 12 % compared to CM50. The production of O_3^{tra} is larger by around 16 % in CM12 compared to CM50 for both inventories. This is consistent with the larger contribution of O_3^{tra} simulated by CM12 than by CM50. The larger production of O_3 in the PBL as simulated by CM12 than by CM50 (Fig. 5.12) leads mainly to an increase of the contribution of the categories with sources within the PBL (e.g. road traffic). The contributions of the categories lightning or aviation¹² are slightly reduced in CM12 compared to CM50, because both models simulated similar values of the O_3 production in the free troposphere.

The ratio $P_{O_3}(HO_2)/P_{O_3}(RO_2)$ of O_3^{tra} decreases from 1.65 to 1.61 for the *REF* and from 1.55 to 1.51 for the *EU08* simulation with finer resolution. This is caused by the increased levels of isoprene (due to by enhanced biogenic emissions due to the increased temperature) in the results of CM12, leading to formation of more O_3^{tra} through reactions with RO_2 .

The emissions from the road traffic category contribute for between 19–24 % (depending on the used emission inventory) to the production of O_3 in Germany. The missing long range transport of biogenic emissions (see Sect. 3.3) is expected to change this results

¹¹The parametrisations used for the calculation depend on the temperature (C_5H_8 emissions) and on the surface temperature (emissions of NO_x from soils).

¹²These emissions are mainly located in the free troposphere.

Table 5.2: Production and loss channels of O_3^{tra} (in Tg) integrated over the period JJA. Shown are the results for CM50 and CM12 integrated over the domain covered by CM12 (up to 200 hPa). Listed are the values for the *REF* and the *EU08* simulation.

	<i>REF</i> , CM50	<i>EU08</i> , CM50	<i>REF</i> , CM12	<i>EU08</i> , CM12
$P_{O_3}(\text{RO}_2)$	0.368	0.438	0.420	0.500
$P_{O_3}(\text{HO}_2)$	0.607	0.679	0.677	0.756
$D_{O_3}(\text{HO}_2)$	0.0892	0.0887	0.0894	0.0881
$D_{O_3}(\text{OH})$	0.0961	0.104	0.101	0.110
$D_{O_3}(\text{RO})$	0.000521	0.000545	0.000547	0.000578
$P_{O_3}(\text{XO})$	0.0941	0.0978	0.0967	0.101
$P_{O_3}(\text{NO})$	0.00228	0.00296	0.00264	0.00341
net O_3^{tra} production	0.693	0.822	0.807	0.954
total net O_3 production	3.68	3.58	4.13	4.01
percent road traffic	18.8	23.0	19.5	23.8

only slightly, making the road traffic sector a very important contributor to O_3 produced over Germany.

To sum up: the finer resolution of CM12 compared to CM50 leads to a slightly larger O_3 production in rural areas, mainly caused by more biogenic emissions and a higher temperature. This enhancement is confined to the PBL, leading to a larger contribution of the sources located in the PBL in CM12 compared to CM50. Due to this larger production rates the absolute values of O_3^{tra} are increased in CM12 compared to CM50. In the hotspot regions the shift of the O_3 chemistry towards a larger 'VOC-limit' leads to lower O_3 values in the results of the finer resolved instance. Besides this, slightly larger 95th percentiles of the contribution are simulated by CM12 compared to CM50.

5.3 Influence of anthropogenic emission inventories

At the beginning of this chapter (Fig. 5.2a) the contribution of O_3^{tra} for the different simulations has been discussed shortly. The area averaged contributions change only slightly between most simulations. Regionally, however, larger differences between the simulation results exist. Therefore, this section is dedicated to a more detailed comparison. The focus of this comparison is on JJA, as during this period the road traffic contribution and the local production of O_3 is largest. The comparison focuses on selected trace gases (O_3 , NO_2 and OH). In general only the values at ground and for the 850PC are compared, as the results in the higher levels are mainly influenced by the boundary conditions.

5.3.1 Resolution of anthropogenic emission inventory

To investigate the influence of the resolution of the emissions on chosen trace gas mixing ratios,

- the CM50 results of the *REF* and *REFT42* simulation are compared. The *REFT42* simulation used the same anthropogenic emissions, but with artificially decreased resolution.

Figure 5.13 highlights the differences (*'REFT42 minus REF'*) for ground level mixing ratios (left side) and the 850PC (right side). The coarser resolved emissions lead to a decrease of the ground level NO_2 mixing ratios around the hotspot regions, as the emissions of the hotspots are diluted over larger grid box areas. Especially in the Gulf of Lion, in the Eastern Mediterranean and in Moscow reductions in the order of 4–6 nmol mol^{-1} are found. The 850PC in these areas is lowered by 60–100 %.

These changed NO_2 values lead to changes of the O_3 values, especially in the Gulf of Lion, the Eastern Mediterranean and in Moscow the differences are between 4–8 nmol mol^{-1} . This corresponds to a relative difference of 10–20 % in the Gulf of Lion and the Eastern Mediterranean, and up to 50 % in Moscow. The 850PC of O_3 is larger by 2–6 % in the Mediterranean region, up to 8 % in the Eastern Mediterranean and more than 12 % in Moscow. The large differences over the Mediterranean are mainly caused by the coarse resolution of the ship emissions. With finer resolution of the emissions most NO_x is emitted along the ship tracks, leading locally to a decreased OPE (Sect. 2.3.4). If these emissions are more diluted, the OPE is enhanced, leading to the production of more O_3 .

The differences of OH are confined to the Mediterranean Sea, where more OH is abundant offside the main ship routes. The absolute differences for the ground level values of around 0.06 pmol mol^{-1} correspond to relative differences of 20–40 %. The differences of the 850PC are most pronounced over Moscow and the Middle East, where relative differences of 40–60 % are simulated. The larger OH mixing ratios are caused by larger mixing ratios of O_3 and subsequent photolysis of O_3 and reactions with water vapour forming OH (Sect. 2.3).

The influence of the coarser resolutions of the emissions on the contribution of O_3^{tra} is shown in Fig. 5.14 for the ground level values and the 850PC. The contribution of O_3^{tra} to ground level O_3 is increased mainly in the Mediterranean Sea and the Eastern Mediterranean up to 2 ppts. Small decreases are simulated over Spain and Portugal. These decreases are larger for the 850PC compared to the ground level values with reductions of around 1 ppts. The same magnitude of difference, but positive, is found over the Eastern Mediterranean.

The differences for CM12 (Fig. A18, page 183) are not discussed. The results show, that the resolution of the emissions is too coarse compared to the model resolution to allow a reasonable analysis. Accordingly, no simulations should be performed where the resolution of the emissions are much coarser than the resolution of the model.

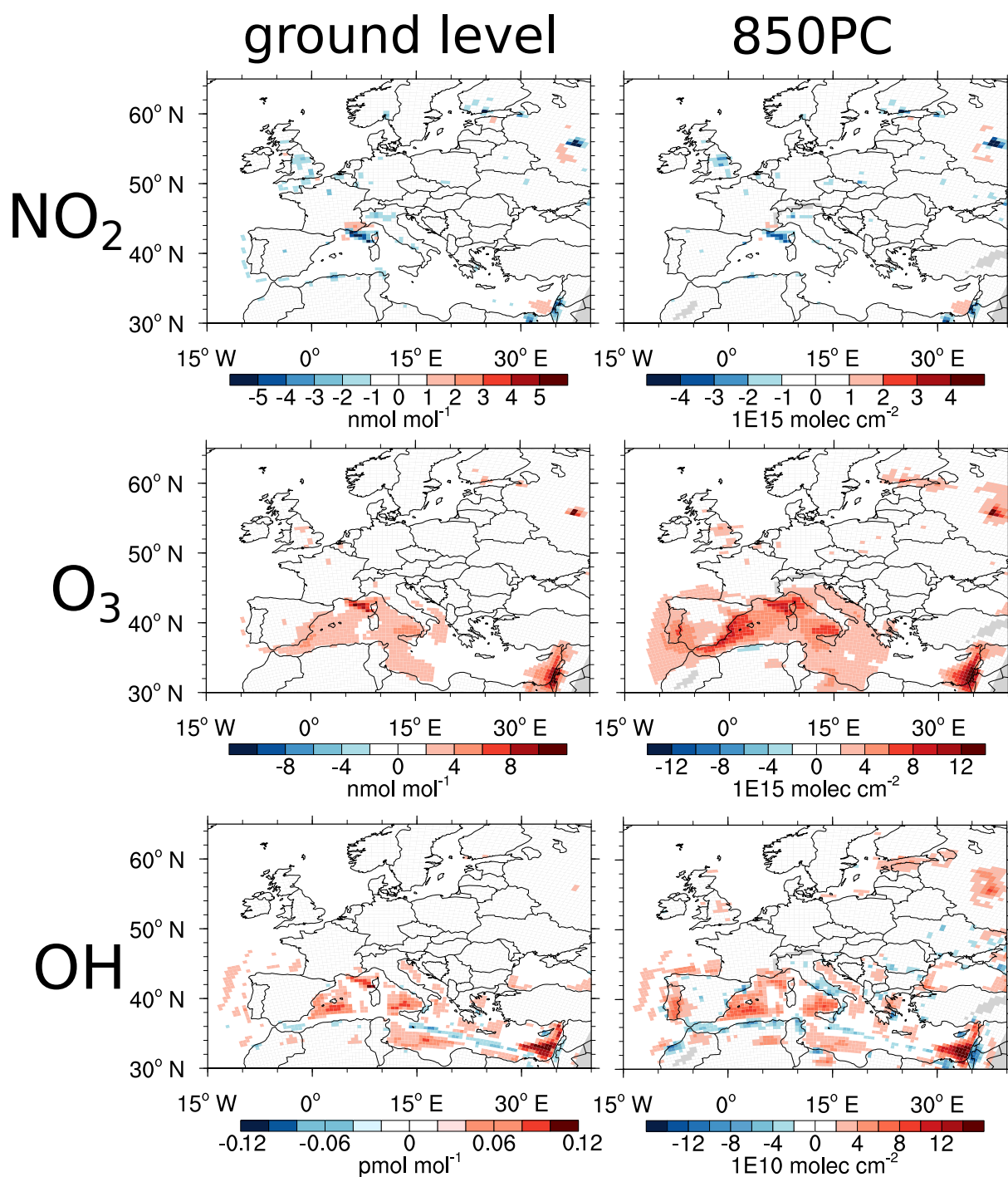


Figure 5.13: Differences (REF_{T42} minus REF) averaged over JJA: Shown are the ground level mixing ratios (left side) and the 850PC (right side) for NO_2 , O_3 and OH . Please note the different colour scales.

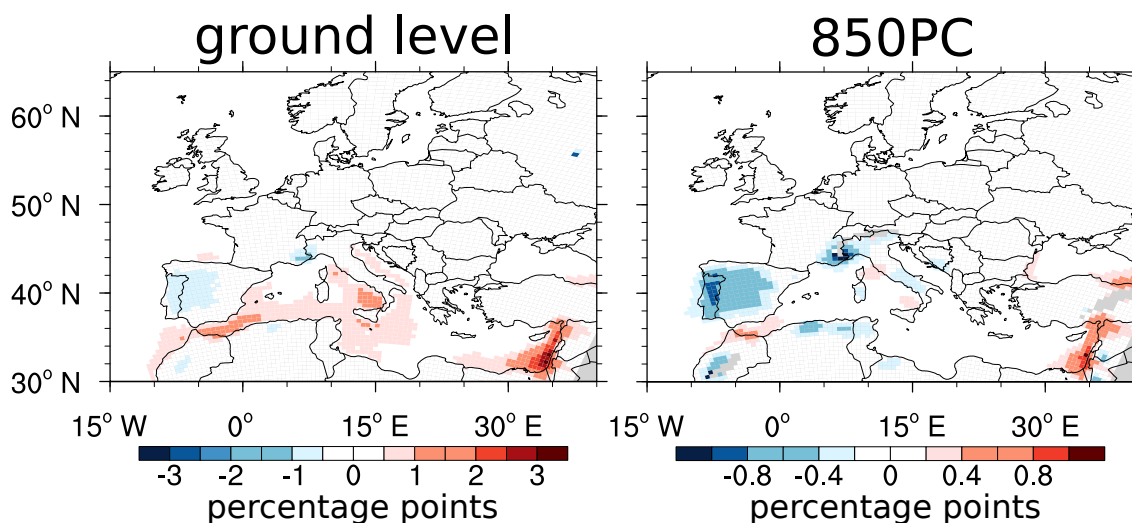


Figure 5.14: Differences (REF_{T42} minus REF) of the contribution (in ppt) of the road traffic category to O_3 at ground level and for the 850PC. Values are averaged over JJA. Please note the different colour scales.

5.3.2 Differences between the MACCity and the VEU inventory

To investigate the difference between the results using MAC08 and VEU08 the simulation results

- of CM50 from the REF and $EU08$ simulation are compared.

Figure 5.15 shows the absolute differences ($EU08$ minus REF). In the hotspot regions the ground level NO_2 mixing ratios are larger for $EU08$ compared to REF . The absolute differences are around 6–12 $nmol\ mol^{-1}$ at maximum, while the NO_2 mixing ratios in the Gulf of Lion are lower by 4–6 $nmol\ mol^{-1}$. The differences for the 850PC of NO_2 between both simulation results is largest near the hotspot regions. Locally the values are up to 100 % enhanced in the results of $EU08$ compared REF . Only in the Gulf of Lion and in Southern Finland the NO_2 values are reduced in the $EU08$ simulation results by 40–80 %. The larger NO_2 mixing ratios in the hotspot regions simulated by $EU08$ compared REF are a direct consequence of the different emission inventories, as the contrast between the emissions of the urban areas compared to the rural areas is larger in the VEU08 inventory compared to the MAC08 inventory. These larger NO_x emissions in the mentioned regions lead to the simulation of lower values of the OPE (Sect. 2.3.4) in $EU08$ compared to REF . Accordingly, the O_3 chemistry is more 'VOC limited' and the net O_3 production decreased.

This is also indicated by the differences of the O_3 mixing ratios at ground level. Especially in the hotspot areas (e.g. Ruhrgebiet, Po basin or London) the ground level O_3 values are lower, mostly by 4–8 $nmol\ mol^{-1}$, which corresponds to a relative reduction of around 10–20 %. Locally these differences can even be larger. The decrease of the 850PC of O_3 is most pronounced over Northern Africa, with maximum relative differences of 6 %. Similar magnitudes of the relative differences are found over Southeastern Europe and over the hotspot regions in Central Europe (e.g. Po basin, Benelux States and some German cities).

Further the OH values at ground level differ between the results of both simulations. The values are increased by 0.06–0.08 $pmol\ mol^{-1}$ in $EU08$ compared to REF in the Gulf

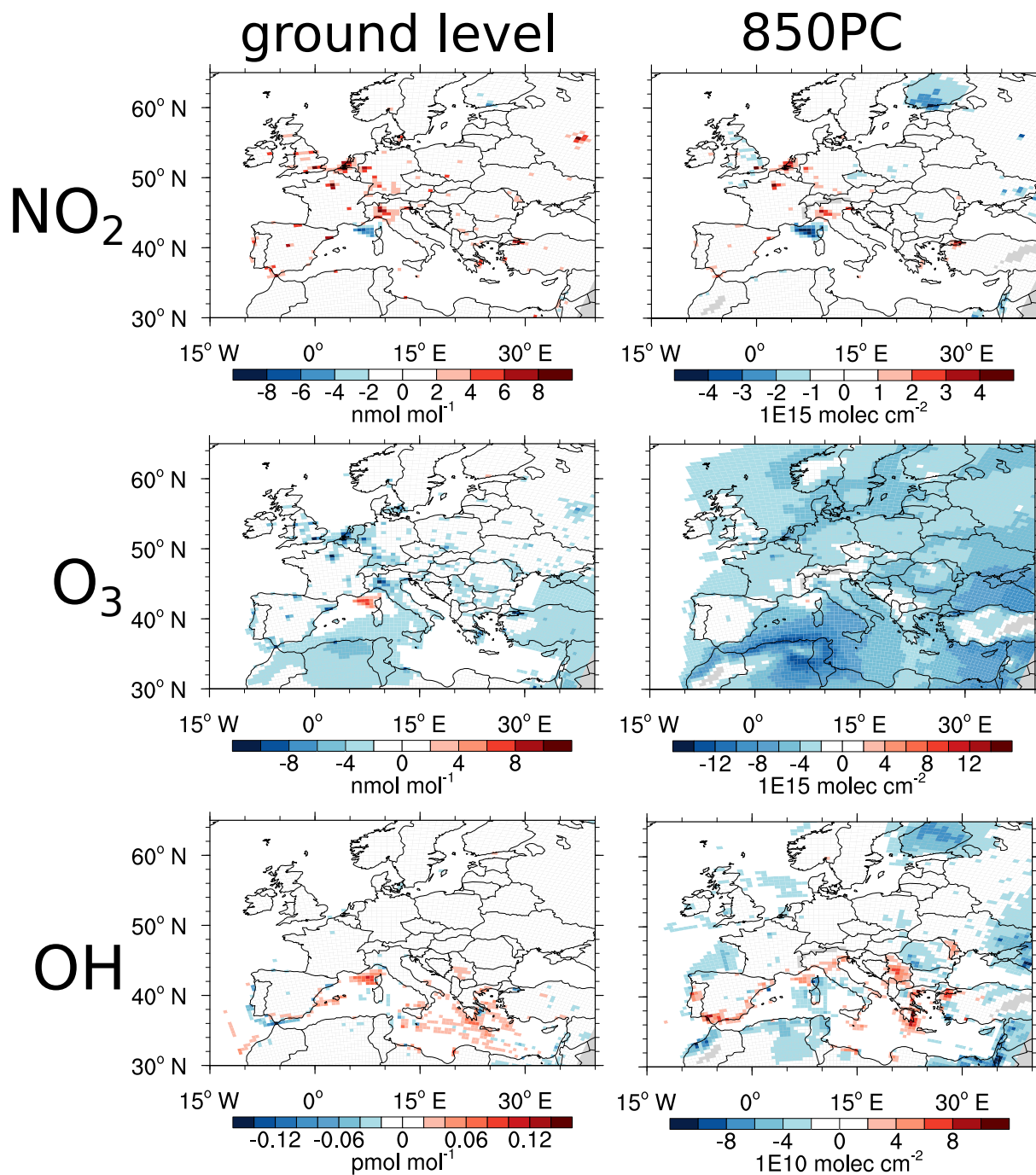


Figure 5.15: Differences (*EU08* minus *REF*) averaged over JJA: Shown are the ground level mixing ratios (left side) and the 850PC (right side) for NO_2 , O_3 and OH . Please note the different colour scales.

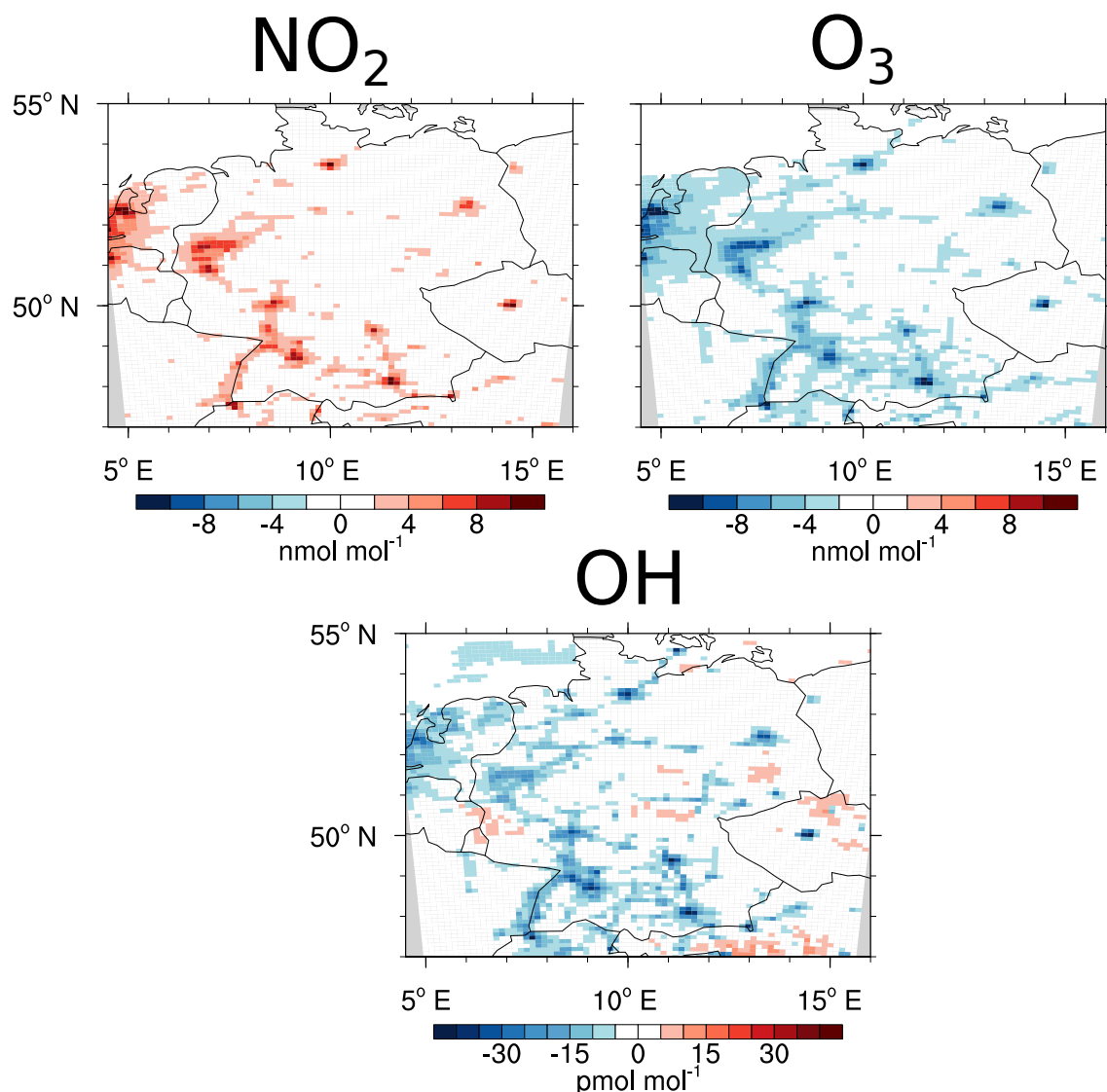


Figure 5.16: Differences (*'EU08 minus REF'*) averaged over JJA: Shown are the differences at ground level (of CM12) for NO_2 , O_3 and OH . Please note the different colour scales.

of Lion, corresponding to relative differences of 150–250 %. The 850PC of OH of the *EU08* simulation compared to the *REF* simulation is reduced largely over South Finland, North Africa and in the Middle East, where relative reductions of 15–25 % are present. Especially the changes in the Gulf of Lion can be explained by the increased OPE. This changed OPE indicates that less HNO_3 is formed in this region. This increase the OH values in the Gulf of Lion, because less OH reacts with NO_2 . In addition, more O_3 can be photolysed to $\text{O}(^1\text{D})$, which can then react with water vapour to form OH .

The differences between the results of CM12 of the *REF* and *EU08* simulation are similar to the differences discussed above for CM50. As the *VEU08* inventory features a finer resolution than the *MAC08* inventory, the regional differences are even more pronounced. Figure 5.16 shows these JJA averaged differences for the ground level values.

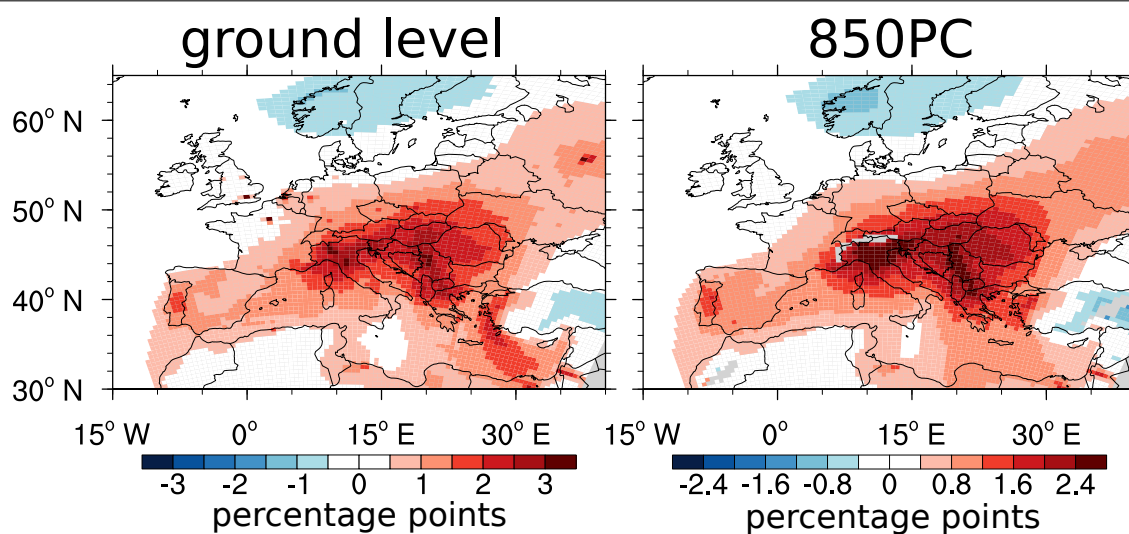


Figure 5.17: Differences ($EU08$ minus REF) of the contribution (in ppt) of the road traffic category to O_3 at ground level and for the 850PC. Values are averaged over JJA. Please note the different colour scales.

As noted for CM50, O_3 in the larger cities is lower because more NO_x is emitted there applying the VEU08 compared to the MAC08 emission inventory. This larger emissions lead to an enhancement of NO_2 by 6–8 $nmol\ mol^{-1}$, corresponding to relative differences of 100 % and more. Correspondingly, CM12 simulates 6–12 $nmol\ mol^{-1}$ lower O_3 ground level mixing ratios in most large cities for the $EU08$ compared to the REF . The relative reductions in the larger cities are in the range of 20–40 %, which is larger than the reductions found for CM50. As has been discussed in Sect. 5.2, this is caused by more confined emissions in the hotspot areas.

As noted in Sect. 3.2.4 the VEU08 inventory estimates a larger contribution of NO_x emissions of the road traffic sector compared to the anthropogenic non-traffic category. This leads to a larger contribution (and also absolute values) of O_3^{tra} in the results of the $EU08$ simulation compared to the REF simulation. Figure 5.17 shows the differences of the contribution of O_3^{tra} to ground level O_3 . Over Scandinavia a decrease of the contribution of O_3^{tra} is simulated. The largest increase are found in Northern Italy and Southeastern Europe, with differences of the contribution peak at 3 ppt. The differences of the 850PC show similar patterns as for the ground level values, but the maximum is reduced to 1.5–2.0 ppt.

To investigate the influence of a finer temporal resolution of the emissions the differences between the $EU08TE$ (hourly resolution on the emissions) and the $EU08$ (monthly resolution of the emissions) simulations were analysed. The differences between the results of both simulations are rather small and are not discussed in detail (corresponding figures are part given in Sect. A.7 on page 188). The ground level NO_2 levels are lower in the cities by 1–2 $nmol\ mol^{-1}$, which corresponds to 10–20 %. Also in most rural areas, small relative differences of 5–10 % are present, while the absolute differences are small in these regions. For the 850PC of NO_2 larger differences of 10–15 % are only found over the Po basin, the Iberian Peninsula and in some parts of Southeastern Europe as well as in the Eastern Mediterranean. These differences are caused by the night-time chemistry. The

usage of the hourly time curves of the emissions lead to smaller emission rates of NO during night, especially for the road traffic sector, which exhibits a strong diurnal cycle of the emissions (Sect. A.6, page 168). Due to the reduction of NO during night, less O₃ is titrated by the reaction of NO with O₃ forming NO₂ (and O₂). This leads to an relative increase of O₃ and a decrease of NO₂ during night (Sect. 2.3). These changes of ground level O₃ are mainly found in the large cities (1–2 nmol mol⁻¹). The 850PC for O₃ shows almost no differences (the relative differences are below 1 %). The changes of O₃^{tra} as simulated by CM50 are below 0.5 ppts.

5.3.3 Local O₃ production rates

To estimate the importance of the local production of O₃ in Europe compared to the inflow of O₃, the local production rates of O₃ and the O₃ mass are compared¹³. Comparing both quantities serves mainly as a qualitative indicator of the importance of long range transport and local production, because the local production is also influence by the long range transport of precursors.

Before comparing the O₃ mass and the net O₃ production in detail, the importance of the different production and loss channels is investigated. Table 5.3 gives an overview of the production and loss channels (Sect. 3.1.7) in the troposphere (up to 200 hPa) of O₃^{tra}¹⁴. The most important channel for the production of O₃^{tra} is the reaction of NO with HO₂. The ratio P_{O₃}(HO₂)/P_{O₃}(RO₂) changes for the different simulations and is 1.53 for the *REF* simulation and 1.56 for the *REFT42* simulation. This change of the ratio indicate that more O₃ is formed by reactions with HO₂ than by reactions with RO₂. This corresponds to a lower 'VOC limit' of the O₃ chemistry, which is an effect of the increased resolution of the emissions in *REF* compared to *REFT42*. The ratio is around 1.51 for both simulations using the VEU08 inventory, which is caused by a different NO_x/VOC ratio in the emissions.

The ratio is smaller (1.44) for EMAC using the MAC08 inventory, caused by a decreased NO_x/VOC ratio as simulated by EMAC than by CM50 (Sect. 5.1). This leads to an increase of the O₃ production by reactions of NO and RO₂. In general around 60 % of O₃^{tra} is formed by the P_{O₃}(HO₂) channel over Europe. This is in agreement with the global results from Tsati (2014), where around 65 % of O₃^{tra} are globally formed through the P_{O₃}(HO₂) channel.

The analysis of the loss channels shows rather similar results for all simulations. The most important loss reaction for O₃^{tra} over Europe is the reaction with HO₂ (D_{O₃}(HO₂), relative contribution ≈ 40%), followed by loss with untagged species (D_{O₃}(XO), ≈ 30%) and reactions with OH (P_{O₃}(OH), ≈ 30%). Loss of O₃ caused by reactions with NO_y or RO plays almost no role. In contrast to this, Tsati (2014) reported global values for the aviation and shipping category, for which the most important loss channel, with a relative contribution of around 50 %, was the D_{O₃}(XO) channel. Separate values for the road traffic category were, however, not provided by Tsati (2014).

¹³This analysis could be improved by having a diagnosis in the COSMO model which quantifies the inflow. The implementation of such an diagnosis is not straightforward, as the COSMO model is influenced over a broad relaxation area at the boundaries (Sect. 3.1.2).

¹⁴The results of the *REFbio* values are not shown, because they are similar to the results of the *REF* simulation. Accordingly, the local production of O₃ is only slightly influenced from the incorrect boundary conditions.

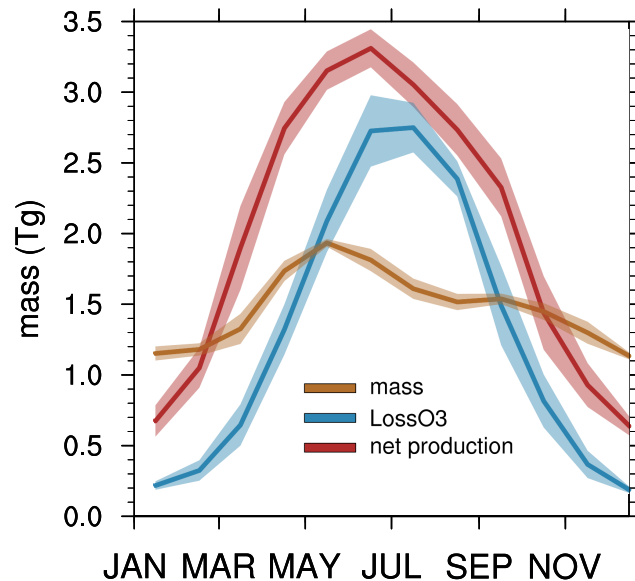


Figure 5.18: Mass, Loss_{O₃} (LossO3) and net production of O₃^{tra} (all in Tg) for the *REFbio* simulation. The values are integrated over the domain of CM50 and up to 200 hPa. Shown are monthly averaged values. The shaded areas indicate one standard deviation with respect to time of daily mean values compared to the shown monthly mean values.

All four simulations results show similar production of O₃ by the road traffic category ($\approx 24 \text{ Tg a}^{-1}$), caused by comparable total emissions of the road traffic sector in the MAC08 and VEU08 inventory. The NO_x emissions from the other anthropogenic sectors, however, are lower in VEU08 compared to MAC08. This leads to an reduced total O₃ production in the results of the simulations using the VEU08 inventory. Therefore the ratio of O₃ produced by the road traffic category is 17.9 % in the *REF* simulation and 20.4 % in the *EU08* simulation.

The net O₃ production shows a strong seasonal cycle. As an example Fig. 5.18 shows the net production of O₃^{tra}. Additionally, the total mass of O₃^{tra} and Loss_{O₃} of O₃^{tra} are shown too. The net production of O₃ from an individual category depends on the net O₃ production (which is largest in May–June) within Europe¹⁵, the amount of emissions from the individual category and the total amount of emissions. The mass is determined by the in- and outflow of the domain, chemical production and loss, as well as deposition of O₃.

The mass of O₃^{tra} fluctuates between 1.1–1.9 Tg during the year (Fig. 5.18). The annual cycles for both, the net production and the loss of O₃ are larger. The maxima of the mass, the production, and the loss are shifted. As only a subset of the glob is analysed the budgets can not be closed. Especially the mass and the production is influenced by long range transport of O₃ and precursors to Europe.

The mass and the net production of O₃^{tra} during winter (not shown) is rather similar simulated by the *REF* and *EU08*. This is caused by the long lifetime of O₃ during this time, as the loss rates of O₃ are low. In addition, less photochemical production over Europe takes place during winter. Accordingly the contribution is mainly governed by

¹⁵The tagging method weights the diagnosed production and loss rates with the amount of precursors from the individual categories (Sect. 3.1.7).

Table 5.3: Production and loss channels (in Tg a⁻¹) for O₃^{tra}. Values are integrated over the CM50 domain (up to 200 hPa) and for the year 2008.

	<i>REF</i>	<i>REFT42</i>	<i>EU08</i>	<i>EU08TE</i>
P _{O₃} (HO ₂) (Tg a ⁻¹)	25.24	25.85	24.98	25.12
P _{O₃} (RO ₂) (Tg a ⁻¹)	16.47	16.58	16.58	16.67
D _{O₃} (HO ₂) (Tg a ⁻¹)	7.25	7.26	7.30	7.31
P _{O₃} (OH) (Tg a ⁻¹)	4.51	4.58	4.59	4.61
D _{O₃} (RO) (Tg a ⁻¹)	0.06	0.03	0.03	0.06
D _{O₃} (XO) (Tg a ⁻¹)	5.47	5.50	5.51	5.52
D _{O₃} (NO) (Tg a ⁻¹)	0.32	0.32	0.32	0.33
production O ₃ ^{tra} (Tg a ⁻¹)	24.11	24.72	23.79	23.94
total O ₃ production (Tg a ⁻¹)	135.03	140.07	116.78	116.87
contribution road traffic (%)	17.85	17.65	20.37	20.49

the inflow and influenced only slightly by local emissions. During summer the lifetime of O₃ is shorter. The contribution of the different categories to O₃ are altered more effectively by local production due to local emissions. Yet, the inflow is still important, as for example besides O₃ itself, also precursors like PAN are transported to Europe and alter locally the O₃ production (Sect. 2.3.3).

5.3.4 Emission categories contributing most to the O₃ production

To understand which categories contribute most to the O₃ production in Europe a further analysis was conducted. I calculated the net production of O₃ integrated up to 850 hPa for every category, restricted to the period May–September, during which the O₃ production is largest (Sect. 5.3.3). The calculated production rates were sorted for every gridbox, starting with the category with the largest production. From top to bottom I picked up to three categories which account for at least 60 % of the O₃ production. The threshold of 60 % was chosen arbitrarily, but the general outcome of this analysis is only minor influenced if the threshold is varied slightly. However, the analysis gives no information about the absolute O₃ production rates of the different categories (and for different regions).

Figure 5.19 shows the geographical distribution of the most important categories for the MAC08 and VEU08 inventory. Applying the MAC08 inventory, the production of O₃ is simulated to be produced by a mixture of emissions from the anthropogenic non-traffic, biogenic and road traffic categories most parts of Northern, Central- and Western Europe. In most parts of Eastern Europe and Russia O₃ is mainly produced by anthropogenic and biogenic emissions. Over the Iberian Peninsula O₃ production is governed by emissions from the biogenic and road traffic category. Over most parts of the Atlantic, O₃ is mainly produced by shipping emissions, while in the Mediterranean a mixture of shipping, anthropogenic non-traffic and biogenic emissions prevail.

The geographical distribution for the VEU08 inventory in Western- and Central Europe is rather similar compared to the results obtained with the MAC08 inventory. The main

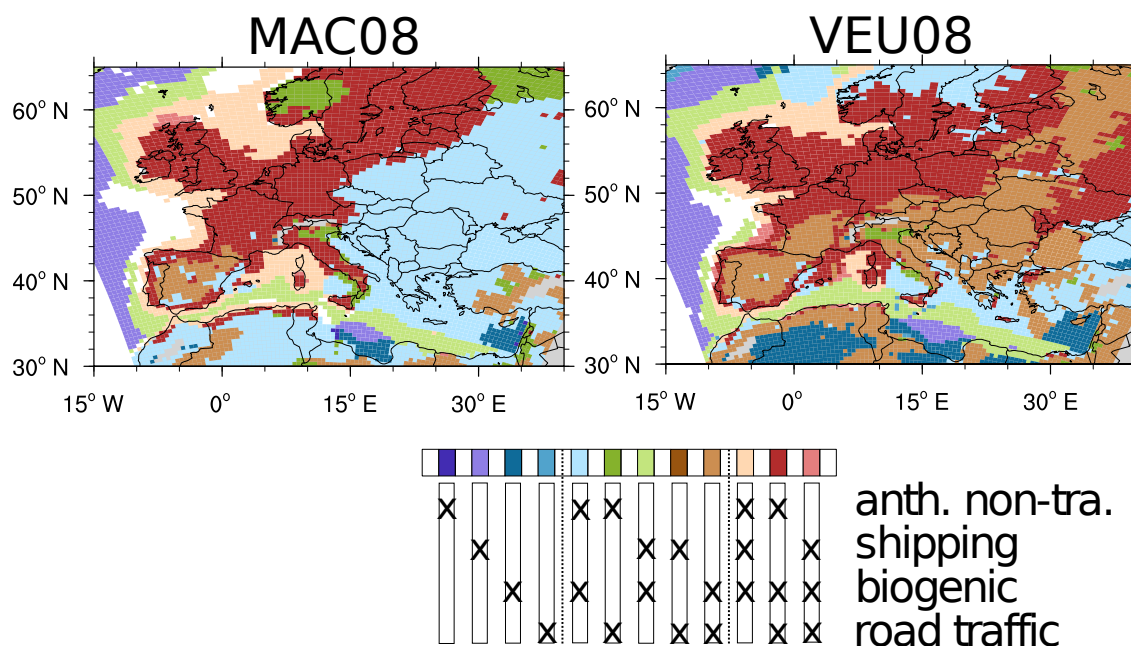


Figure 5.19: Analysis of the categories which contribute most to the O_3 production up to 850 hPa during the period May–September 2008. From left to right the colour bar indicates the different categories and combinations of categories. The first four colours indicate regions where one of the categories anthropogenic non-traffic, shipping, biogenic and road traffic contributes to more than 60 % to the production of O_3 (up to 850 hPa). The following five colours indicate regions where at least 60 % of the O_3 production is caused by a combination of two categories. The last three colours show areas where three categories contribute to more than 60 % to the O_3 production. White areas display regions where the production is dominated by other categories as shown here. For the displayed combinations of categories no differentiation of the amount of O_3 produced by the different categories is performed, meaning one grid box displayed as 'shipping + road traffic' either 'shipping' or 'road traffic' could be the largest contributor. Shows are the values for the *REF* simulation (MAC08) and the *EU08* simulation (VEU08).

differences are found in Southeastern Europe. Using MAC08, O_3 production in these regions is mainly controlled by a mixture of the anthropogenic non-traffic and biogenic emissions, while for VEU08 this mixture is replaced by a mixture of road traffic and biogenic emission over this area.

This analysis shows that O_3 in the PBL in most parts of Europe are mainly produced from precursor emissions of the anthropogenic non-traffic category, the biogenic category and the road traffic category. Accordingly, uncertainties of the estimates of these emissions can influence the analysis of the O_3 production for Europe at most.

5.4 Sensitivity to changes of biogenic emissions

So far mainly the sensitivity of the contribution on different models and resolutions, as well as anthropogenic emission inventories is investigated. Besides the estimates for anthropogenic emissions also the estimates for biogenic and natural emissions are rather uncertain. This is crucial as the emissions from soils and plants are important sources

Table 5.4: Net production of O_3 , O_3^{tra} and O_3^{biog} integrated over the CM50 domain up to 850 hPa for JJA. In addition also the ratio of net production of O_3^{tra} to O_3 (in %) is shown.

Simulation	PO_3 (in Tg)	PO_3^{tra} (in Tg)	PO_3^{biog} (in Tg)	PO_3^{tra}/PO_3 (in %)
REF_bio_EMAC	27.5	5.4	9.4	19.7
REF_no_C5H8	25.2	5.0	7.7	19.9
REF_no_NO	24.6	6.0	5.5	24.3
REF_C5H8_scaled	28.9	5.6	9.9	19.3
REF_no_biotag	27.8	7.1	5.3	25.5
REFT42a	28.8	5.6	9.6	19.6

of NO_x and VOCs and contribute to O_3 production in Europe (Sect. 5.3.4). In particular, when investigating anthropogenic ground level sources, the biogenic emissions might play an important role, as both, the anthropogenic and biogenic emissions, are located at ground level.

To further quantify the influence of changes in the biogenic emissions on the contribution of O_3^{tra} I performed additional sensitivity studies, for which the biogenic emissions are not calculated by CM50. Instead the emissions, as calculated by EMAC, were transformed onto the CM50 grid, leading to identical isoprene (C_5H_8) and soil- NO_x emissions between EMAC and CM50. The following gives a short summary of the changes made for the sensitivity studies and the questions addressed by these studies. More detailed information about these sensitivity studies are given Sect. A.1 (page 141).

- *REF_bio_EMAC*: Same biogenic C_5H_8 and soil- NO_x emissions as in EMAC are used in order to investigate the influence of the changed geographical distribution as well as the coarse resolution of the emissions.
- *REF_no_C5H8*: As *REF_bio_EMAC*, but without C_5H_8 emissions to investigate the influence of these emissions.
- *REF_no_NO*: As *REF_bio_EMAC*, but without the soil- NO_x emissions to investigate the influence of the soil- NO_x emissions.
- *REF_C5H8_scaled*: As *REF_bio_EMAC*, but the C_5H_8 emissions are scaled with 0.60 instead of 0.45 in CM50, to investigate the influence of the different scaling factors for the biogenic C_5H_8 emissions between EMAC and COSMO.
- *REF_no_biotag*: As *REF_bio_EMAC*, but neglecting the soil- NO_x and biogenic C_5H_8 emissions for the TAGGING submodel to investigate, if the results are comparable to the values of EMAC for the *REF* simulation.
- *REFT42a*: As *REFT42* simulation but using the same biogenic C_5H_8 and soil- NO_x emissions as in EMAC, to investigate how the results change, if both the anthropogenic and natural emissions are resolved with a coarse spatial resolution.

Table 5.4 lists the net production of O_3 , O_3^{tra} , O_3^{biog} and the relative contribution of PO_3^{tra} to the total production of O_3 (PO_3^{tra}/PO_3) integrated for JJA. The net production

is largest in the simulations with coarse emissions (*REF_T42a*) and with enhanced C₅H₈ emissions (*REF_C5H8_scaled*) and lowest in the two simulations with reduced biogenic emissions (*REF_no_NO*, *REF_no_C5H8*). The decrease of the production is larger for the simulation without NO_x emissions from soils (*REF_no_NO*) compared to the simulation without biogenic C₅H₈ emissions (*REF_no_C5H8*).

The production of PO₃^{tra} is largest in the simulation, in which the biogenic emissions are not tagged correctly (*REF_no_biotag*). In this case the biogenic emissions are treated by the TAGGING diagnostic as a bulk process, similar as dry deposition. The emissions are spread over all categories (details about this approach are provided by Grewe et al., 2016). This leads to an increase of NO_y^{tra} and NMHC^{tra} in comparison to the correct treatment of the biogenic emissions, which causes a strong increase of PO₃^{tra}.

The contribution of PO₃^{tra} to PO₃ is around 19–20 % for most of the simulations, only in the simulation *REF_no_NO* and *REF_no_biotag* this contribution is larger by ≈ 5 ppts. To understand this behaviour the basic idea of the tagging method (Sect. 3.1.7) is recapped. The temporal evolution of O₃ of the category *j* is¹⁶:

$$\frac{\partial O_3^j}{\partial t} = \frac{1}{2} P_{O_3}(\text{HO}_2) \left(\frac{NO_y^j}{NO_y} + \frac{HO_2^j}{HO_2} \right), \quad (5.2)$$

meaning the production of O₃ of a category *j* is governed by P_{O₃}(HO₂), the ratio of NO_y from category *j* and the total NO_y as well as the ratio of HO₂ from category *j* and the total HO₂. Increasing values of P_{O₃}(HO₂) with unchanged fractions of the precursors from category *j* lead to an increase of the absolute values of category *j*, but no changes of the relative contributions. The fraction of NO_y, however, does change remarkably only for the simulations *REF_no_NO* and *REF_no_biotag*, as here the NO emissions (the fraction of the precursors) are changed.

Table 5.5 shows the contribution of the road traffic category and 850PC absolute values of O₃ and O₃^{tra}. Corresponding to the analysis of the net O₃ production as have been discussed above, the simulations with larger values of the O₃ production show also larger values of O₃ and O₃^{tra}. The usage of the soil-NO_x and biogenic C₅H₈ emissions from EMAC (*REF_bio_EMAC*) leads to an increase of O₃. Over most parts of Europe the differences are small, only in the Mediterranean and in Eastern Europe the 850PC of O₃ and O₃^{tra} increase by 4–5 %. Accordingly, the contribution of O₃^{tra} does not change. Figures showing these differences are given in the Appendix (Fig. A21, page 190).

Compared to the results of *REF_bio_EMAC* the 100 % reduction of the soil-NO_x emissions (*REF_no_NO*) lead to a reduction of O₃ in Eastern and Southern Europe. In both regions ground level O₃ and the 850PC of O₃ is decreased by around 5 %. In Mid Europe, however, ground level O₃ increases by 2–3%. In contrast to the reduction of O₃ in Southern- and Eastern Europe the 850PC of O₃^{tra} increases over most parts of Europe by approx 5 %. Accordingly O₃^{tra} is formed more efficiently and the contribution increases by ≈ 0.8 ppts.

The 100 % reduction of the biogenic C₅H₈ emissions (*REF_no_C5H8*) decreases the 850PC of O₃ mainly south of 45° N by around 5 %. A similar decrease is found for the 850PC of O₃^{tra}, resulting in small changes of the contribution of O₃^{tra}. Accordingly, the increase of the C₅H₈ emissions (*REF_no_C5H8*) lead to an increase of the 850PC of O₃ by

¹⁶This example considers for simplicity only the production of O₃ through reactions of NO and HO₂.

Table 5.5: Contribution of O_3^{tra} to the 850PC of O_3 (in %). Shown are JJA averaged values for the CM50 domain. The ranges indicate one standard deviation with respect to time (based on 3 hour model output).

	O_3^{tra} (%)	850PC O_3^{tra} (DU)	850PC O_3 (DU)
REF	12.67 ± 0.69	0.74 ± 0.07	5.83 ± 0.27
REF_no_NO	13.56 ± 0.70	0.78 ± 0.06	5.77 ± 0.27
REF_bio_EMAC	12.72 ± 0.69	0.75 ± 0.06	5.90 ± 0.26
REF_no_C5H8	12.61 ± 0.71	0.72 ± 0.07	5.72 ± 0.28
REF_C5H8_scaled	12.74 ± 0.68	0.76 ± 0.06	5.95 ± 0.26
REF_no_biotag	14.26 ± 0.70	0.84 ± 0.07	5.90 ± 0.26
REFT42	12.68 ± 0.69	0.75 ± 0.06	5.88 ± 0.27
REFT42a	12.73 ± 0.69	0.76 ± 0.07	5.95 ± 0.26

2 % in the Mediterranean, with a similar increase for O_3^{tra} , resulting in a small difference of the contribution of O_3^{tra} .

The largest differences of the contribution of O_3^{tra} are simulated by *REF_no_biotag*. As has been discussed, O_3^{tra} is artificially increased by the incorrect tagging of soil- NO_x and biogenic C_5H_8 . The values of O_3 are not altered, increasing also the contribution of O_3^{tra} .

The difference of the contribution of O_3^{tra} between the *REF_bio_EMAC* and *REF_no_biotag* simulation is comparable with the difference found for EMAC between the *REF* and *REFbio* simulation (see discussion on page 77). The results of the *REFT42a* generally confirms the discussed results. The usage of the biogenic and soil- NO_x emissions from EMAC in CM50 increase the absolute values of O_3 and O_3^{tra} , but that the contribution in only slightly changed.

The different importance of biogenic C_5H_8 compared to soil- NO_x with respect to the contribution can be understood in terms of the OPE concept (Sect. 2.3.4). Depending on the chemical background, one NO_x molecule can undergo multiple cycles, thus forming multiple O_3 molecules. The C_5H_8 emissions control these background conditions in such a way that the oxidation products (a very simplified version is discussed in Sect. 2.3.2) react with NO_x to form O_3 . Especially in the 'VOC-limited' regime C_5H_8 is important to allow an efficient O_3 production. In comparison to NO_x the reactions of C_5H_8 are not catalytic, because the oxidation products of C_5H_8 are consumed by this reaction. The NO_x molecules are not consumed during the production cycle of O_3 (Sect. 2.3). Nevertheless, one C_5H_8 molecule can form several O_3 molecules, as oxidation products of C_5H_8 can undergo further reactions forming O_3 (Sect. 2.3.2).

To sum up, the investigated sensitivity studies show that the contribution of the road traffic category is most sensitive to uncertainties in the NO_x emissions from soils. Differences in the C_5H_8 emissions or the resolution of the biogenic emissions mainly change the net O_3 production (and thus the absolute values) but only slightly the contribution. More details follow in the next section.

Table 5.6: Area averaged O_3^{tra} contributions for the JJA period of the road traffic sector for the different PRUDENCE regions (see Sect. A.5, page 166). The range denotes one standard deviation with respect to time (based on three hour model output).

region	<i>REFbio</i> , 2008 (%)	<i>REFbio</i> , JJA (%)
CM50 domain	10.82 ± 1.00	11.42 ± 0.71
Eastern Europe	10.67 ± 1.60	11.50 ± 1.60
Mediterranean	11.37 ± 1.53	12.53 ± 1.03
Alps	11.63 ± 2.01	13.35 ± 1.53
Scandinavia	10.47 ± 1.26	11.28 ± 1.20
Mid Europe	10.56 ± 1.53	11.29 ± 1.60
France	10.18 ± 1.60	10.18 ± 1.72
Iberian Peninsula	10.44 ± 1.44	11.27 ± 1.50
British Isles	9.92 ± 1.28	10.10 ± 1.36

5.5 Intercomparison of the results from the different simulations

As analysed in this chapter so far, the differences between the results of the simulations depend on the region. Therefore, these differences of the simulations are analysed focusing on the so called PRUDENCE subdomains, which were defined in the scope of the EU project PRUDENCE¹⁷. Before focusing on the differences between the results of the different simulations, the differences between the regions are investigated. Table 5.6 lists the contribution of O_3^{tra} to the 850PC, for the different PRUDENCE subdomains¹⁸. Shown are the results of the *REFbio* simulation, as only here the long range transport from biogenic sources is tagged correctly (details are given on page 77). Averaged over the area of the CM50 domain the contribution of O_3^{tra} is 10.8 % for the annual average and 11.4 % during JJA. Most regions in Europe show average values which are similar to the domain averaged values. Only the Mediterranean and Alps show larger contributions compared to the values for the whole domain. The region of the Alps is small compared to other regions, due to the topography of this region no 850PC values are available at some grid boxes. Therefore, the values for this region are dominated by the large contributions found in the Po basin.

To compare the results of the different simulations, Fig. 5.20 summarises the differences, averaged for JJA, of the 850PC of O_3^{tra} and the contribution of O_3^{tra} for all simulations and regions. The difference of the *REF_no_biotag* simulation is shown for the sake of completeness only and will not be discussed in detail, due to the artificial increase of O_3^{tra} caused by the incorrect tagging of biogenic emissions. As have been discussed in Sect. 5.4, the absolute values of the 850PC of O_3^{tra} (Fig. 5.20a) change slightly when decreasing the emission resolution or changing the amount of biogenic C_5H_8 emissions. The contribution of O_3^{tra} (Fig. 5.20b), however, shows almost no sensitivity due to these changes.

¹⁷More details are given in Sect. A.5, page 166.

¹⁸Please note, that prior to all analyses on the PRUDENCE subdomains the simulations results were transformed onto a regular grid with $0.5^\circ \times 0.5^\circ$ resolution

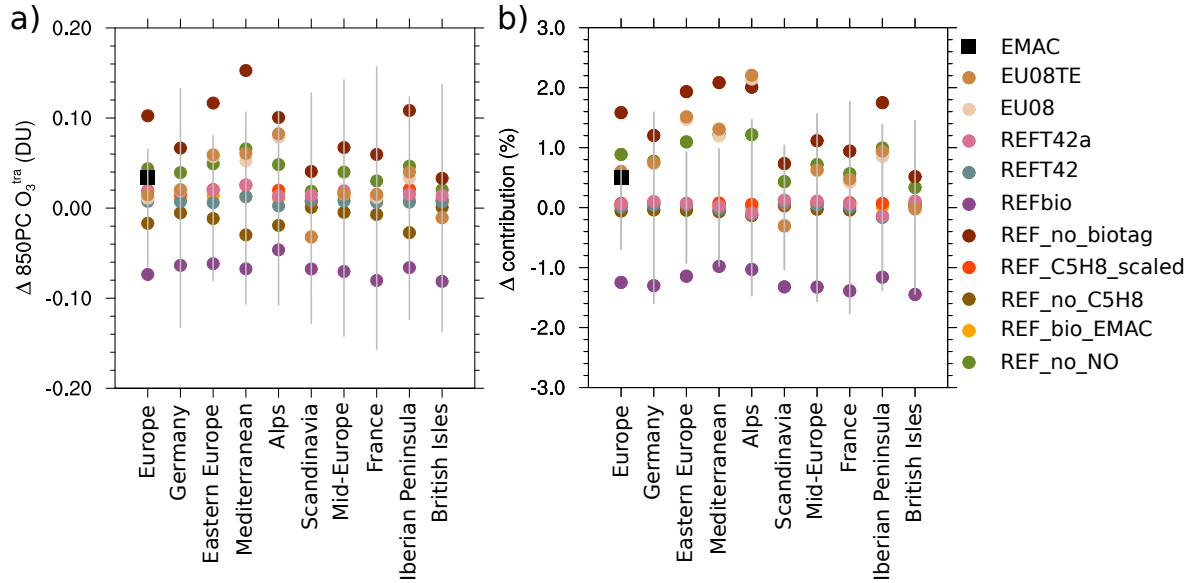


Figure 5.20: Differences ('SIMULATION minus *REF*') for the individual simulation results compared to the *REF* simulation, averaged for JJA and over the whole domain (Europe), Germany as well as the different PRUDENCE regions. EMAC indicates in addition the difference ('EMAC minus COSMO') between COSMO and EMAC for the *REFbio* simulation. The grey bars indicate one standard deviation with respect to time for the *REF* simulation (based on three hour model output). (a) the difference of the 850PC of O_3^{tra} (in DU); (b) the difference for the contribution of O_3^{tra} to the 850PC of O_3 (in ppts).

The simulations with larger changes of the NO_x emissions (*REF_no_NO*, *EU08* and *EU08TE*) show the largest changes of the 850PC of O_3^{tra} and the contribution of O_3^{tra} . Especially in Eastern Europe, the Mediterranean and the Alps a large sensitivity to the changes of the soil- NO_x and anthropogenic emissions, which correspond to $\approx 10\%$ relative difference compared to the *REF* simulation, is observed (Fig. A22 on page 191 shows the relative differences). These regions do also show the lowest sensitivity to the too low inflow of O_3 and precursors from the biogenic category (*REFbio*). However, even in these regions correct boundary conditions are of importance. Compared to this only the results of the simulation with changed boundary conditions (*REFbio*) shows a larger difference (around 10 %) compared to the other results. This indicates that the contribution of road traffic emissions over the British Islands is mainly controlled by the large scale inflow.

Summarising the findings from these results it can be concluded that the contribution is most sensitive to changes of the NO_x emissions, as already shown in Sect. 5.4. The absolute values are also sensitive to the NO_x emissions, but also to changes of the net O_3 production (caused e.g. by lower resolution of the emissions or changes in the biogenic VOC emissions). Also the differences between EMAC and CM50 are larger for the absolute values than for the contribution (caused by the differences of the O_3 production, Sect. 5.1.2). Accordingly, the absolute values are much more sensitive to differences of the used models, emission resolutions and uncertainties of the emission estimates of (biogenic) VOC emissions compared to the contribution. The differences of the results between EMAC and CM50, however, are in the range of differences caused by uncertainties in the emission estimates.

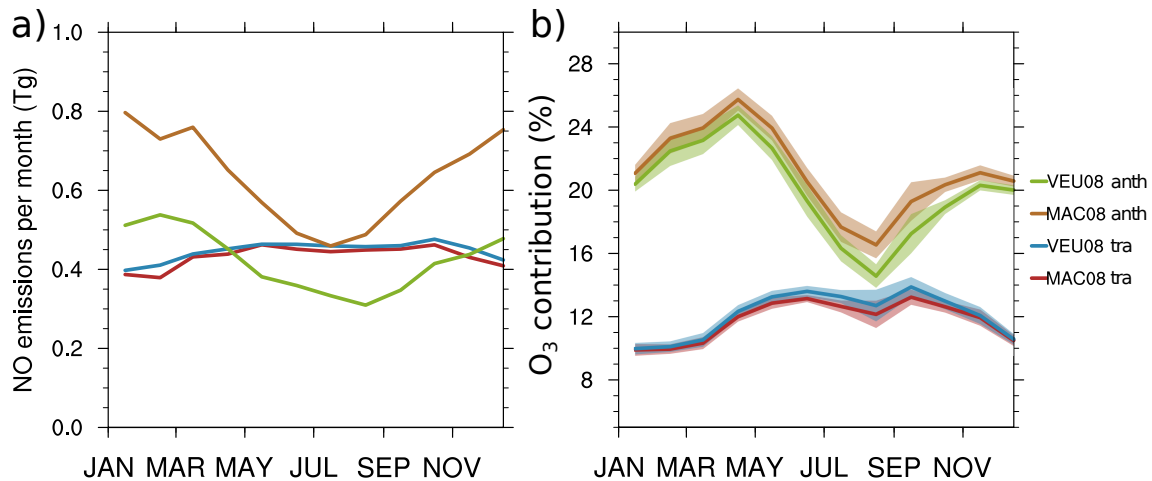


Figure 5.21: (a) Annual cycle for 2008 of the monthly total NO_x emissions (in Tg) integrated over the CM50 domain. (b) Annual cycle for 2008 of the area weighted averaged contribution to the 850PC of O_3 of the corresponding sectors. Both figures show the values for the anthropogenic non traffic and the road traffic category for the MAC08 and the VEU08 inventory. The shaded areas in (b) indicate one standard deviation with respect to time (based on daily data).

In addition it is important to note that for most regions the temporal variation of the 850PC of O_3^{tra} and the contribution of O_3^{tra} is larger than the individual changes of the emissions. Reasons for this strong temporal variations are discussed in the next section.

5.6 Temporal and spatial variations of the contributions

5.6.1 Seasonal cycle of the contributions

In all simulations the contribution of O_3^{tra} shows a strong seasonal cycle, with a minimum during winter and a maximum during summer. The road traffic emissions themselves, however, show only a small seasonal cycle, but the emissions of the anthropogenic non-traffic sector shows a distinct seasonal cycle. The emissions are large during winter and low during summer. This seasonal cycle is caused by increased emissions in households (e.g. firing, heating) and larger needs for electricity during winter (Sect. 3.2.5). The corresponding seasonal cycles of the NO_x emissions of the anthropogenic non-traffic sector and the road-traffic sector for MAC08 and the VEU08 are shown in Fig. 5.21a. The MAC08 total emissions of the anthropogenic non-traffic category peak at 0.80 Tg in January and have a minimum of 0.46 Tg in July. The emissions of VEU08 peak in February at 0.85 Tg and have a minimum during August of 0.31 Tg. This seasonal cycle of the emissions in MAC08 is not unique in Europe, but also present globally (e.g. in the USA, not shown). Accordingly, not only the emissions over Europe are altered by the seasonal cycle but also the emissions in other regions. These seasonal cycle in other regions further affects the contributions in Europe through the long range transport.

The contribution of O_3^{tra} and O_3^{anth} to the 850PC is displayed in Fig. 5.21b. The strong seasonal cycle of the anthropogenic non-traffic emissions leads to a strong seasonal cycle of the contribution of the corresponding sector. The lowest values of the contribution of O_3^{anth} are reached in August (16.5 % for the MAC08 inventory and 14.6 % for the VEU08 inventory). In April the contributions reach a maximum of 25.7 % and 24.7 %, respectively. The seasonal cycles of the absolute values of the 850PC for O_3^{tra} and O_3^{anth} are rather similar (not shown).

This seasonal cycle is, however, not directly related to the seasonal cycle of the emissions, because the processes leading to the seasonal cycles of the contributions are much more complex. Two processes are most important.

1. The O_3 production: As an example the difference of the seasonal cycle between the emissions of the anthropogenic non-traffic category and the corresponding emissions are considered. The emissions are largest during winter. In this time the O_3 production over Europe is rather small. Only if sufficiently large emissions and large O_3 production coincide the contribution is large (as during April–May for the anthropogenic non traffic category).
2. The amount of emissions from the other sectors influence the contribution of one specific sector. As an example the biogenic category is considered (not shown) with strong seasonal cycle of the emissions. Especially during August the contribution of the biogenic category is large, leading to decreased contributions of all other categories.

Both processes influence the contribution of the road traffic category. The emissions of the category shows almost no seasonal cycle. The contribution increases during spring, when the O_3 production increases. During August, however, when the emissions of the anthropogenic non-traffic category are lowest, the contribution of the road traffic category decreases. This decrease is caused by increased emissions of the biomass burning sector during this period (analysis follows in Sect. 5.6.2).

5.6.2 Small scale fluctuations of the contribution

Superimposed on the seasonal cycle of the contribution of O_3^{tra} are short scale fluctuations. Exemplary, the decrease of the contribution in mid May and in August is analysed in detail (see Fig. 5.2a on page 77.).

To analyse the reason for the decrease in May, Fig. 5.22a shows the contribution of O_3^{tra} for 14–17 May 2008 and the corresponding wind vectors. In this period contributions of up to 16 % are simulated, especially in Southern Germany, Northern Italy and Austria. The regions with these large contributions are dominated by an airflow from the Mediterranean region. During the period from 18–21 May 2008 (Fig. 5.22b) the weather in Central Europe is dominated by a low pressure system over Scandinavia. The resulting circulation brings air from Scandinavia, the Northern Atlantic and the British Islands to Central Europe. In these air masses the contribution of O_3^{tra} is lower compared to air masses coming from the Mediterranean region. This lower contribution is mainly caused by lower net O_3 production in Northern Europe in connection with lower road traffic emissions in this region. In the downwind regions from Germany the contribution of O_3^{tra} increases again.

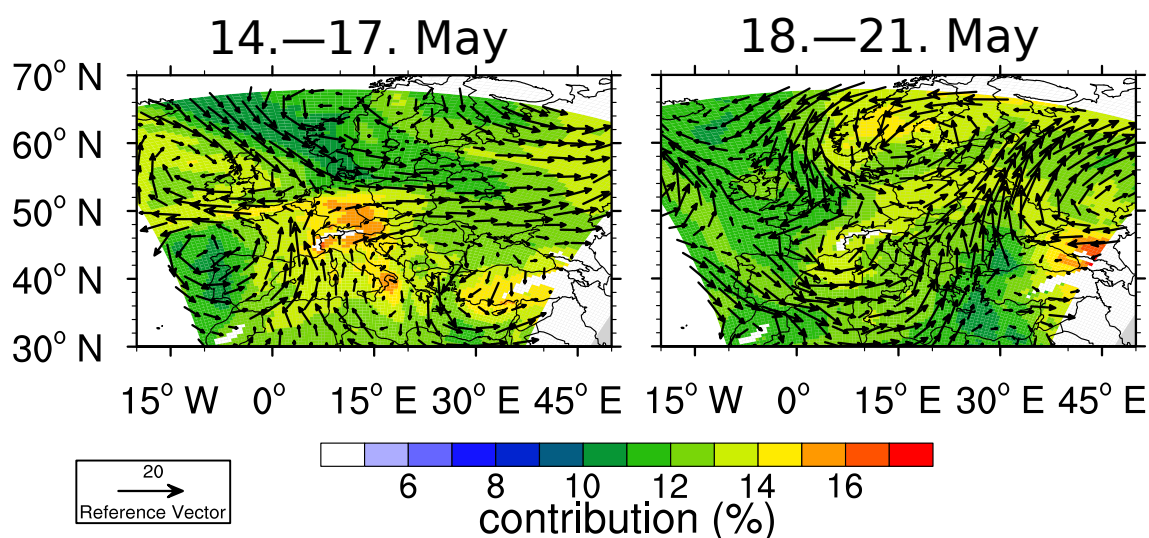


Figure 5.22: Contribution of the road traffic sector at 850 hPa. The wind vectors indicate the horizontal wind at 850 hPa. The reference vector indicates the wind speed in m s^{-1} . Shown are the average values for 14–17 May and for 18.–21. May 2008 of the *REF* simulation.

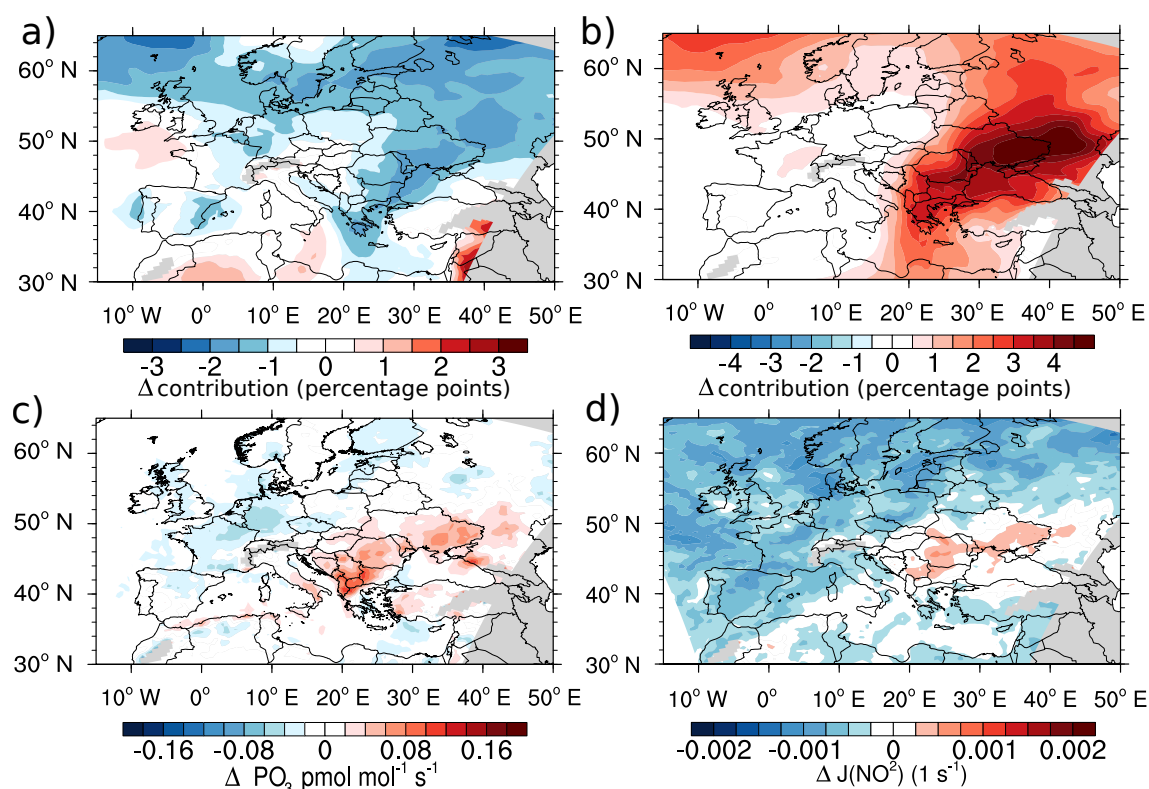


Figure 5.23: Difference ('August minus July') of monthly averaged values from the *REF* simulation. (a) difference of O_3^{tra} contribution to the 850PC (in ppt); (b) difference in O_3^{bio} contribution to the 850PC (in ppt); (c) difference of the net O_3 production averaged from the surface to 850 hPa (in $\text{pmol mol}^{-1} \text{s}^{-1}$); (d) difference of the NO_2 photolysis rate averaged from the surface to 850 hPa (in 1 s^{-1}). The shown values are from the *REF* simulation.

As a second example on how the contribution of the road traffic category can be altered, even on the timescale of around one month, the reason for the decreased contribution of O_3^{tra} in August compared to July is investigated. Figure 5.23a shows the difference ('August minus July') of the contribution of O_3^{tra} to the 850PC. The contribution of O_3^{tra} decreases in most parts of Europe, while the contribution of the biomass burning category increases mainly in Eastern Europe and Northwestern Europe (Fig. 5.23b). The increase over Eastern Europe is caused by a large biomass burning source in August in Russia, while the increase in Northwestern Europe is caused by an increase of the contribution due to long range transport.

These two effects of a large local biomass burning source and inflow of air with large contribution of the biomass category is further intensified by a decrease of the O_3 production. The O_3 production decreases in August compared to July especially in Central Europe (Fig. 5.23c). In this region the the largest sources of road traffic emissions are located and a decrease of the O_3 production in this region leads to a decrease of the contribution of O_3^{tra} . In Eastern Europe, and especially in Russia, where the local biomass burning source is located, the net O_3 production increases in August compared to July. This change in the O_3 production is mainly caused by changes in the photolysis rates (Fig. 5.23d), which are enhanced in August compared to July over parts of Eastern Europe. The large local biomass burning source there leads too an enhanced production of O_3 from biomass burning. In addition, reduced photolysis rates over parts of Middle Europe, where most of the road traffic emissions are present, leads to a decrease of O_3 produced from emissions of the road traffic sector.

5.7 Discussion

My analysis indicates that the contribution of road traffic emissions to the European 850PC of O_3 is around 11 %, using CM50 together with the MAC08 emission inventory. During winter the contribution is around 10 % and increases to around 12 % during JJA. The contribution to ground level O_3 is around 13–14 %, which corresponds to absolute mixing ratios of 5–10 nmol mol⁻¹ during JJA. Regionally the values are larger, especially in the Mediterranean area and the Po basin. Especially in Central Europe the contribution of O_3^{tra} is strongly controlled by the meteorological conditions, determined mainly from inflow over the Atlantic, but also by transport from the Mediterranean or Scandinavia. In years with longer heatwaves (e.g. 2003) and stagnant meteorological conditions the influence of the inflow might be smaller.

My findings with respect to the contribution are in the range of results from previous studies using a 100 % perturbation approach. Granier and Brasseur (2003) reported an impact of road traffic emissions on ground level O_3 for Europe of 10–15 % in July, considering only NO_x emission from the road traffic sector. Niemeier et al. (2006) also included CO and NMHC emissions from the road traffic sector and found an impact of 10–25 % during summer in Europe, which corresponds to 5–10 nmol mol⁻¹. Using similar emissions Matthes et al. (2007) reported an impact of the traffic sector of 16 % during summer, corresponding to 10 nmol mol⁻¹. A detailed comparison with the findings of Reis et al. (2000), Tagaris et al. (2015) using regional models for Europa and a 100 %

perturbation are not feasible, because these studies investigated the impact of road traffic emissions on certain O₃ metrics. These impacts were in the range of 10–20 %.

Compared to the results from the global studies, Hoor et al. (2009, Fig. 5, scaled to 100 %) found an impact of the road traffic emission in the range of 4–6 nmol mol⁻¹ on O₃ in the lower troposphere (surface–800 hPa). Averaged annually and zonally from 30° N to 60° N an impact of 3.7 % was reported. Smaller values are reported by Hodnebrog et al. (2012), who found a maximum impact in the lower troposphere of 3 nmol mol⁻¹ during July for the zonal average at 30°N. The results from Hoor et al. (2009) and Hodnebrog et al. (2012) were based on a 5 % perturbation and are lower compared to my results and the results using a 100 % perturbation. These differences of the results can be attributed to the different magnitudes of the perturbations. Additionally, different emission inventories were used.

When comparing my results to results of previous studies using the perturbation approach the underestimation of the contribution by the perturbation approach compared to the tagging approach must be considered. As an example, Grewe et al. (2012) reported an underestimation of the contribution of the road traffic sector by a factor of 5 using a 100 % perturbation compared to a tagging method. The global average contribution of 13 % to the tropospheric O₃ column reported by Grewe et al. (2012) is larger compared to my findings¹⁹, but Grewe et al. (2012) used an emission inventory for the year 1990 and a simplified tagging method, considering only NO_x.

Compared to all these studies I used a tagging method which considers all O₃ precursors and therefore takes the competing effects of NO_x and VOC for the production of O₃ into account. Further, I used a finer resolution for the model simulation which can affect the results due to the non-linearity of the O₃ chemistry. Nevertheless, my results are in a similar range compared to the values reported using a 100 % perturbation approach. This similarity between my results and the results using the 100 % perturbation might be attributed to older emission inventories used in previous studies. Accordingly, previous studies using a 100 % perturbation underestimated the contribution because of the used method. The larger emissions in these studies increase the contribution of road traffic emissions compared to present day conditions, leading to findings in these studies, which are comparable to my results.

My analyses of the O₃ production rates further showed, that the emissions from road traffic contribute more than 20 % to the production of O₃ in the troposphere over Germany. The average values for Europe are smaller, but still around 18 %. This makes the road traffic sector an important contributor the production of tropospheric O₃ in Europe and Germany. Accordingly, the road traffic sector has a large potential to decrease its contribution to the O₃ production by decreasing the road traffic emissions.

I analysed that the results with respect to the contribution are most sensitive to the distribution and amount of NO_x emitted from different sources. In particular the different anthropogenic emission inventories (VEU08, increase of the contribution by 0.5 ppts during JJA), missing soil-NO_x emissions in Europe (+0.9 ppts during JJA), or missing global boundary conditions for biogenic emissions (-1.3 ppts) lead to the largest changes of the contribution of the road traffic category. To reduce the uncertainties of contribution analyses in the future, it is very important to reduce the uncertainties of the emission

¹⁹Grewe et al. (2012) reported only global average values for the whole troposphere while I give only values for Europe and up to 850 hPa.

estimates of all NO_x sources (both anthropogenic and natural), especially for the sources located near the ground. Especially the soil- NO_x emission estimates are rather uncertain. Vinken et al. (2014) for example gives a global range of soil- NO_x emissions of 4–15 Tg a⁻¹. The global total emissions of my simulations is at the lower end of this estimates. Larger emissions from soil- NO_x would likely decrease the contribution of road traffic emissions.

Compared to the differences caused by uncertainties of the emission estimates my results indicate a rather small dependency of the model resolution on the results, which is between 0.3–0.5 ppts for the contribution of EMAC, CM50 and CM12. These differences are mainly caused by different net O_3 productions of the different models or model resolutions, caused by differences in the temperature, biogenic emissions and the vertical transport of precursors. These results refer to the average values of the contribution for Europe. The analysis showed that regionally much larger differences are found between the results of the different models. Comparing EMAC and CM50, the larger production rates of O_3^{tra} simulated by CM50 in the Po basin are striking. A further increase of the resolution leads to larger maximum values (expressed as 95th percentiles) in CM12 compared to CM50 especially in Southern Germany. To my knowledge, no similar comparisons of O_3 contributions between results from a coarse resolved model and a fine resolved model has been conducted so far, but Stock et al. (2013) investigated a similar problem. The authors investigated the influence of megacities on the global tropospheric O_3 budget and removed the emissions of these cities and distributed these emissions globally. The effect of this removal was mainly local near the cities and not globally. Similar as my findings this result underlines that for regional analyses a fine resolution is indispensable. Further, a fine resolution is important if extreme values are analysed. Average values over larger areas (such as Europe) are only slightly influenced.

Further, my results show that the differences between the different simulations and models are larger for the absolute values of O_3^{tra} than for the contribution of O_3^{tra} . Especially, EMAC simulates larger absolute ground level mixing ratios of O_3^{tra} compared to COSMO. This increase can partially be attributed to the differences in temperature, vertical mixing and biogenic emissions as discussed above. In addition, also the coarser resolution of the emissions in EMAC compared to CM50 increases the production of O_3 . The dependency of the O_3 production on the resolution of the emission is well known. Wild and Prather (2006) found that especially the production in the boundary layer is overestimated by a coarse resolution of the model (and the emissions), while the production in the free troposphere is only slightly affected. Similar results were also found by Jang et al. (1995a,b), showing that especially the NO_x chemistry is very sensitive to different resolutions, while the VOC chemistry is only slightly influenced. These changes of the net O_3 production are a direct consequence of the non-linearity of the O_3 chemistry, as with finer resolution the O_3 chemistry, especially near the hotspots, is more 'VOC-limited' (e.g. Cohan et al., 2006, Stock et al., 2014). A direct comparison of these previous findings with my results should be performed with care, because most of these studies used CTMs. In CTMs the meteorology is prescribed, while I applied a CCM, calculating both, meteorology and chemistry consistently. CM12, for example, simulated a higher temperature compared to CM50 leading to increased O_3 production despite a increased resolution. A similar influence of the meteorological conditions, however, was also shown by Tie et al. (2010) using a regional CCM for simulations in the area of Mexico City.

Similarly, isoprene emissions influence the production of O_3 (e.g. Andersson and Engardt, 2010). An increase of this emissions increase the absolute O_3 values, but the contributions of NO_x from different categories are only slightly influenced. The small differences of the contributions in the results of the simulations with changed O_3 production (e.g. C_5H_8 emissions or emission resolution) might be explained by the resolution. Even with 12 km resolution emissions are mixed over large areas, meaning that always a mixture of precursors from different categories is present. In addition, the required input-parameters for the calculation of the biogenic emissions and the dry deposition rates were only available with a horizontal resolution of $0.5^\circ \times 0.5^\circ$. This is especially important for the biogenic emissions and leads to relative homogeneous emissions over large areas. For future work, it is therefore important to test, if a further increase of the resolution up to 1–3 km decreases this mixing and leads to larger changes of the contributions.

Based on my analyses I suggest to distinguish two different types of sensitivities:

- Absolute values: The absolute values are rather sensitive to all processes which influence the O_3 production. Accordingly analyses of the absolute values of O_3 produced from road traffic emissions can be influenced by processes like differences in the meteorology (meaning temperature and radiation influencing the (photo)-chemistry), (vertical) transport processes, the amount of biogenic emissions and the efficiency of loss processes.
- Contribution: The contribution analyses seems to be rather robust. The results are mainly influenced by the amount (and geographical distribution) of the different NO_x sources. Accordingly the uncertainties of the contribution analyses are mainly governed by uncertainties of emission estimates. The reduction of these uncertainties is rather challenging.

However, it is important to keep in mind that I analysed mainly the sensitivity of the results to different models, resolutions and emissions. Others factors, which were not analysed (Sect. 2.8), might also influence the results.

My results also show that the used nesting technique together with the used tagging method is a well suited approach allowing for contribution analyses in a consistent manner from the global down to the regional scale. The question, whether the increased resolution due to the nesting steps is necessary, depends on the scientific questions of the study. A global model is sufficient for studies investigating for instance the average global contribution of a emission sector to O_3 , knowing that regionally larger errors are made and the absolute values are rather overestimated. A finer resolved (regional) model is necessary for investigating regional contributions, analyses of extreme pollution events, or potential regional mitigation options.

5.8 Conclusions

The most important findings of my analyses of the contribution of road traffic emissions for year 2008 conditions are:

- Emissions of the road traffic category contribute 11 % to the ozone column up to 850 hPa in Europe.

- The contribution is lowest during winter (10 %) and increases during summer up to 12 %.
- Emissions from road traffic contribute more than 20 % to the production of O₃ in the troposphere over Germany and around 18 % in Europe.
- No large difference for the coarse resolution of the EMAC model or coarse resolved emissions compared to results with finer resolution could be found for average values over Europe. Regionally, however, large differences are visible (e.g. the Po basin). In these regions fine resolved simulations are necessary for a correct assessment of the contribution of road traffic emissions to O₃.
- The analysis of the contribution of the road traffic emissions to O₃ is most sensitive to uncertainties of the estimates of NO_x emissions from anthropogenic and natural sources.

Chapter 6

Contribution of road traffic emissions in Europe projected for 2030

The analyses in Chap. 5 have focused on the investigation of the influence of different models, resolution of models, and emissions, as well as different emission inventories on the contribution of the road traffic emissions on tropospheric O₃ for present day conditions. The present chapter is dedicated to a scenario of a possible future. Analysed are the results of the simulations which were conducted using the VEU30 inventory. This emission inventory assumes an increase of the travelled kilometres in Germany, but a decrease of the total emissions in Germany caused by a reduction of the emissions per travelled kilometre compared to 2008. Overall, the NO_x emissions from road traffic are assumed to decrease by roughly 25 % in Europe compared to the year 2008, while the emissions of the anthropogenic non-traffic sector are assumed to increase by roughly 18 % (Sect. 3.2.3 and Sect. 3.2.4). Compared are the results of three different simulations which are recapped shortly (Sect. 3.3):

- *EU30TE*: Applying the VEU30 instead of the VEU08 inventory for CM50 and CM12. The global boundary conditions from EMAC are identical to the *EU08TE* simulation.
- *EU30RT*: The emissions of CM50 are identical to *EU30TE*, but the road traffic NO_x emissions are increased by 10 % in EMAC. CM12 was not active in this simulation.
- *EU30AC*: The emissions of CM50 and CM12 are identical to *EU30RT*, but for EMAC the ACCMIP/RCP6.0 emission inventory instead of MAC08 is used.

The simulated contributions of O₃^{tra} for the different simulations are shown in Figure 6.1. Additionally, the CM50 results of the *EU08TE* simulation (Sect. 5.3) are displayed. *EU30TE* simulates a lower contribution of the road traffic sector during summer compared to present day conditions. During winter the differences are rather small. In this period the lifetime of O₃ is relatively long and the contributions are mainly determined by the inflow. The results of the *EU30TE* and the *EU30AC* simulations support this hypothesis: In these two simulations the emissions of the CM50 instance are identical and the differences are only governed by the different inflow (Sect. 6.2).

The differences between the contribution simulated by *EU08TE* and *EU30TE* starts to increase in April/May. During this time the photochemical activity increases and

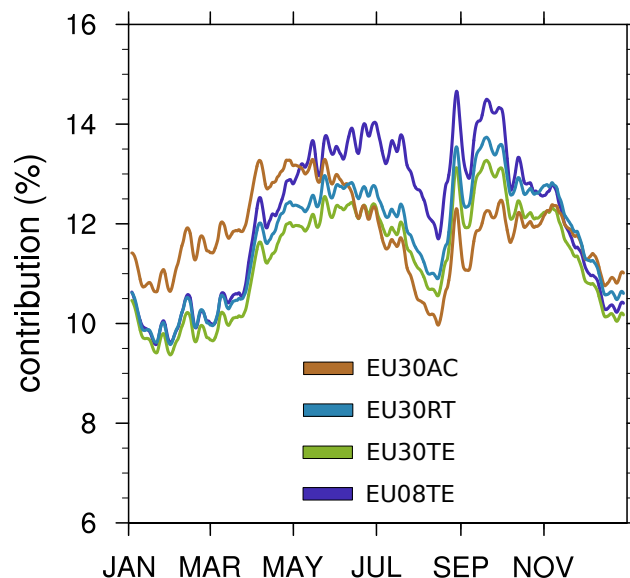


Figure 6.1: 5-day running-average of O_3^{tra} to the 850PC of O_3 . Indicated are the average values for the CM50 instance for the different simulations.

EU08TE simulates larger contributions of O_3^{tra} compared to *EU30TE* because of the larger emissions in VEU emission inventory for the year 2008 (VEU08). All three *EU30* simulations show a similar temporal evolution and similar contributions during summer. However, the contribution simulated by *EU30RT* is larger compared to *EU30TE*, while *EU30AC* simulate lower values in this period. Table 6.1 lists the annually area averaged contributions, calculated for the CM50 domain, the PRUDENCE regions and Germany (Sect. A.5, page 166).

The analyses of the results from these simulations are organised as follows. First the simulated differences when applying VEU emission inventory for the year 2030 (VEU30) instead of VEU08 with identical global boundary conditions are investigated (Sect. 6.1), followed by a discussion of the influence of changed boundary conditions (Sect. 6.2). Finally changes in the O_3 production efficiency (Sect. 6.3) and in the radiative forcing as well as the pseudo CH_4 lifetime are analysed (Sect. 6.4). It is important to keep in mind that all simulations are affected by the problem of a too low contribution from the biogenic category. During summer the contribution in the results of CM50 is therefore artificially increased by around 1.5 %, and by 1 % for the annual average (see discussion on page 77).

Table 6.1: Annual average contribution of O_3^{tra} to the 850PC (in %). The values are area averaged for the CM50 domain, the different PRUDENCE regions and Germany. No results of the *EU30RT* simulation are given for Germany (CM12), because the CM12 instance was not active in this simulation. The range indicates one standard deviation with respect to time based on 3 hourly model output.

	EU08TE (%)	EU30TE (%)	EU30RT (%)	EU30AC (%)
CM50 domain	12.14 ± 1.46	11.33 ± 1.08	11.45 ± 1.11	11.82 ± 0.84
Eastern Europe	12.98 ± 2.23	11.69 ± 1.51	11.81 ± 1.53	12.14 ± 1.23
Mediterranean	12.95 ± 2.20	11.80 ± 1.51	11.90 ± 1.50	12.40 ± 1.15
Alps	13.58 ± 3.10	12.24 ± 2.15	12.41 ± 2.22	12.80 ± 1.77
Scandinavia	11.47 ± 1.40	10.91 ± 1.09	11.14 ± 1.26	11.20 ± 1.10
Mid Europe	11.96 ± 2.13	11.12 ± 1.53	11.27 ± 1.73	11.55 ± 1.36
France	11.54 ± 2.10	10.93 ± 1.57	11.02 ± 1.67	11.41 ± 1.45
Iberian Peninsula	11.90 ± 1.98	11.24 ± 1.48	11.38 ± 1.50	11.82 ± 1.23
British Isles	11.03 ± 1.59	10.61 ± 1.25	10.77 ± 1.44	10.97 ± 1.22
Germany (CM12)	13.67 ± 2.17	11.95 ± 1.68	-	11.69 ± 1.86
Germany (CM50)	13.51 ± 2.13	11.92 ± 1.66	12.31 ± 1.70	11.65 ± 1.86

6.1 Projected differences for the 2030 emission inventory

Figure 6.2 shows the difference (*EU30TE* minus *EU08TE*) for NO_2 , O_3 and, OH averaged for JJA at ground level and for the 850PC. The ground level mixing ratios are mainly reduced over Germany, Northern Italy and Austria. Especially in the Po basin and Germany the mixing ratios are reduced by up to 3 nmol mol⁻¹, corresponding to changes of 20–40 % in most German areas. In contrast to these areas, an increase of ground level NO_2 by 2–4 nmol mol⁻¹ is simulated in Belgium, the English Channel and Gibraltar. The differences of the 850PC for NO_2 are geographically similar distributed as the ground level differences. The relative difference is around ±20–40 % in the regions with the largest absolute differences.

The changes of the NO_2 values has consequences on the simulated O_3 values. Especially in Southern and Western Germany, where the NO_x emissions are reduced, the ground level O_3 values increase by 2–4 nmol mol⁻¹. This corresponds to an increase of ≈ 10 %. In these regions, *EU08TE* simulates a O_3 chemistry which is mainly 'VOC limited'. A decrease of the NO_x emissions enhances the O_3 productivity, leading to an increase of the OPE. Accordingly, the O_3 chemistry in the polluted areas is less VOC limited in the projected scenario (cf. Fig. A23, page 192). Not only the ground level values, but also the 850PC of O_3 is larger by by around 1.5 % over South Germany.

Larger reductions of the ground level O_3 mixing ratios are simulated only in the Gulf of Lion, the Benelux States and in some areas in Southeastern Europe. The largest reductions are in the order of 2–3 nmol mol⁻¹, which corresponds to relative differences of 4–6 % in the Gulf of Lion. These reductions are caused by an increase of the NO_x

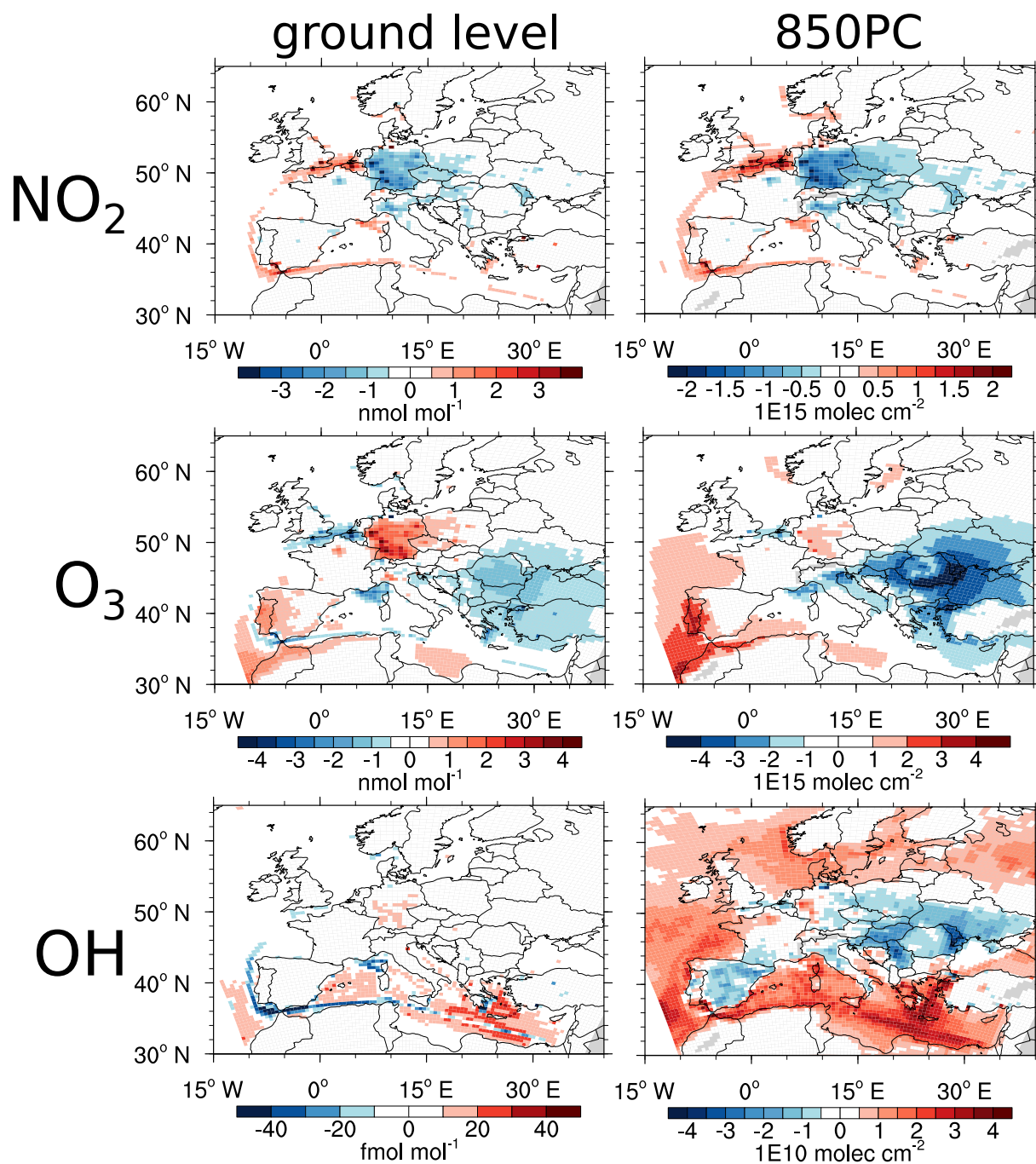


Figure 6.2: Differences ($\text{EU}_{30\text{TE}}$ minus $\text{EU}_{08\text{TE}}$) averaged over JJA: Shown are the ground level mixing ratios (left side) and the 850PC (right side) for NO_2 , O_3 and OH . Please note the different colour scales.

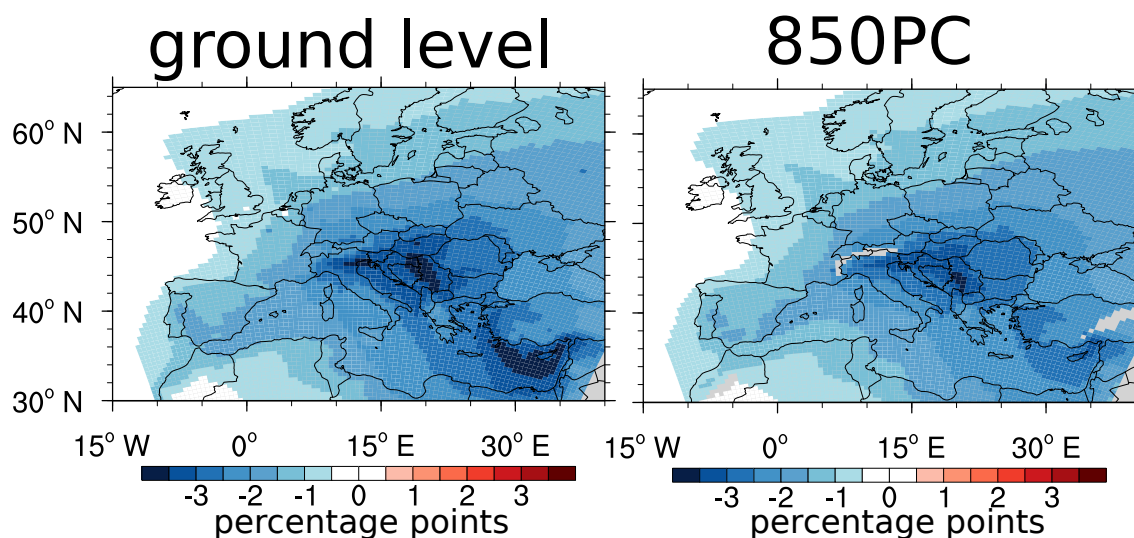


Figure 6.3: Differences ($'EU30TE$ minus $EU08TE'$) averaged over JJA of the contribution of O_3^{tra} to O_3 (in ppt) at ground level and for the 850PC.

emissions, leading to an decrease of the OPE which corresponds to lower O_3 production and O_3 values.

The emissions changes in VEU30 compared to VEU08 has further consequences on the simulated OH values. The largest differences of the ground level OH values are simulated in the Mediterranean region. Alongside the main ship tracks OH increases by up to 30 fmol mol^{-1} , while OH is reduced along the main ship tracks and in the Gulf on Lion by the same magnitude. The relative enhancement is 40 % at maximum. Compared to this, the relative reductions along the ship tracks are around 30–50 %. This decrease of OH is caused by an increase of the NO_x ship emissions in VEU30, leading to an increase of reactions of OH with NO_2 . Accordingly, ground level HNO_3 values increase by 20–30 % in the Mediterranean. Offside the main shipping routes the increased O_3 levels lead to an increase of OH mainly in the Mediterranean Sea.

The comparison of the 850PC for OH between both simulation results show large differences over the whole domain which seems not to correlate with the differences of NO_2 and O_3 , but care must be taken because of the different colour scales. In general, the shown absolute differences correspond to relative differences of 5–10 % in Eastern Europe and the Iberian Peninsula. The increased values over the ocean correspond mostly to an increase of 5–10 %. The regions with decreased values of OH correspond to areas with decreased values of NO_2 and decreased values of HNO_3 . Accordingly, the increase of OH can mainly be attributed to a decrease of the reaction of NO_2 and OH. The increased values over the oceans mainly correspond to regions with increased O_3 values, leading to increased OH values by photolysis. In addition, other factors (e.g. changed VOC or CO emissions), which are not analysed in detail here, can influence the OH levels.

Figure 6.3 shows the difference of the simulated contribution of O_3^{tra} to ground level O_3 and the 850PC for JJA. In both cases the reductions of the contribution of O_3^{tra} are largest in Southern and Eastern Europe. In these regions the contribution for both, the ground level values and the 850PC, is reduced by 2–3 ppt. Over Northern Europe the

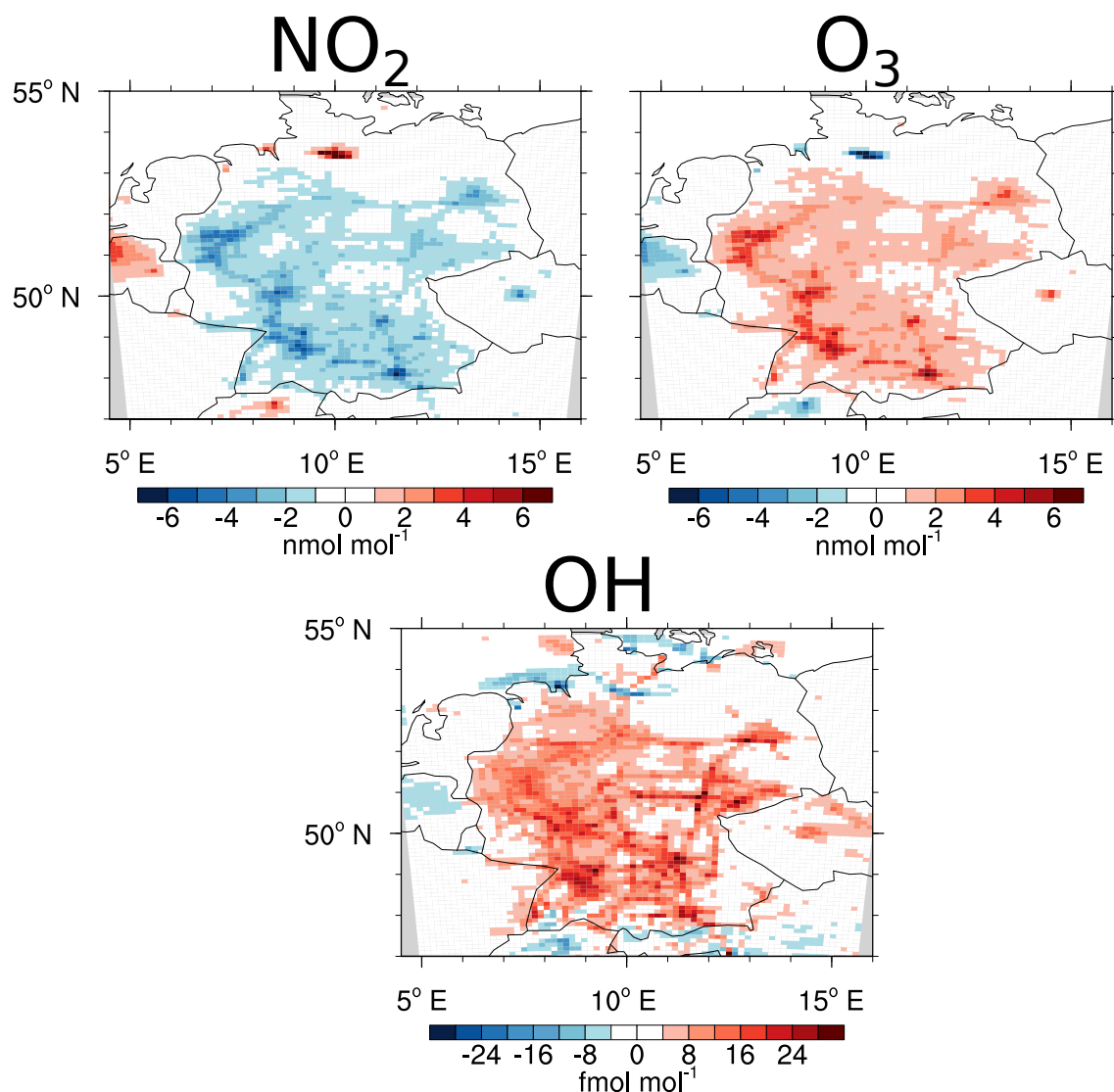


Figure 6.4: Differences ($'EU30TE$ minus $EU08TE'$) averaged over JJA: Shown are the ground level mixing ratios of CM12 for NO_2 , O_3 and OH . Please note the different colour scales.

differences are smaller (0.5–1.0 ppt). These differences are caused by a general decrease of the road traffic emissions in VEU30 compared to VEU08. The increase of the NO_x emissions of the anthropogenic non-traffic and of the shipping sector additionally reduced the contribution of the road traffic category.

As the differences between the VEU08 and VEU30 emission inventory are largest over Germany, Fig. 6.4 shows the difference ($'EU30TE$ minus $EU08TE'$) of the results of CM12. Shown are only the differences of the ground level values, because the magnitude of the differences for the 850PC are very similar as derived with CM50.

In the larger German cities ground level NO_2 is reduced by 4–6 nmol mol⁻¹, despite Hamburg where the values are larger by 4–7 nmol mol⁻¹. A similar enhancement is found around Zurich. In general, the differences of 850PC for NO_2 are even more pronounced compared to the ground level values. Here, the relative differences are around 20–40 % over Germany. In Southeastern Germany reductions of up to 60 % are found.

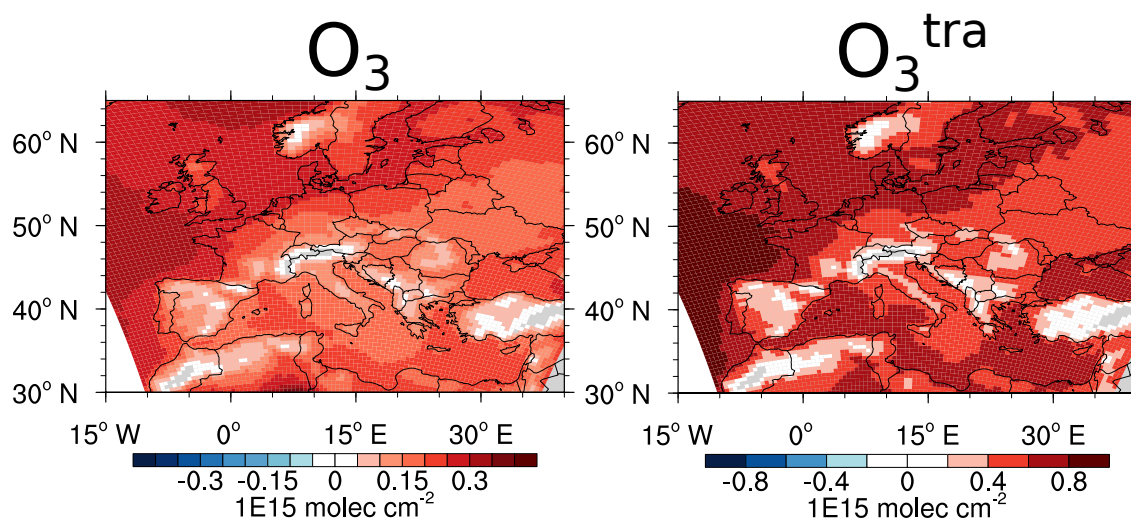


Figure 6.5: Differences (*'EU30RT minus EU30TE'*), daily mean values averaged for JJA. Shown are the differences of the 850PC for O_3 and for O_3^{tra} . Please note the different colour scale in both figures.

As already discussed these reductions lead to an increase of the ground level O_3 values by 4–6 nmol mol⁻¹ in the hotspots. Only around Hamburg and Zurich a decrease of O_3 of up to 6 nmol mol⁻¹ is simulated. The changes in Hamburg are mainly attributed to an increase of the NO_x emissions of the shipping emissions, while the increase in the Switzerland are associated with an increase of the NO_x emissions of the anthropogenic non-traffic sector in the VEU30 scenario.

The largest increase of OH at ground level is found around the larger cities and along the main highways in Germany. The relative differences are 20–40 % in these regions. In these areas not only OH but also HO_2 is increased by 60–100 %. Also the 850PC of OH increases by 5–15 % around the largest cities, despite Hamburg, where OH is reduced by around 20 %. In Southern- and Western Germany the decrease of NO_x emission lead to an decrease of the production of HNO_3 and increased OH values. The reductions of OH around Hamburg are mostly attributed to the decrease of O_3 values, but as noted above also differences of the VOC and CO emissions as well as the different applied CH_4 boundary conditions at the surface can attribute to changes of OH.

The discussed results, however, are based on the same meteorological conditions, one simulated year and a specific emission scenario. Therefore, the shown results can not be generalised for future conditions in Europe/Germany. Such an investigation would require more complex simulations.

6.2 Influence of changed global boundary conditions

To investigate the influence of changed boundary conditions the results simulated by *EU30RT* and *EU30AC* are compared with the results of the *EU30TE* simulation.

The differences (*'EU30RT minus EU30TE'*) of the mixing ratios of most trace gases (e.g. NO_x , OH, HNO_3) are rather small. Consequently, also the differences of O_3 itself

are rather small. Figure 6.5 shows the simulated difference¹ of the 850PC for O_3 and O_3^{tra} between both simulations. As noted the differences of O_3 are rather small (0.15–0.25 %). The largest differences occur near the Western boundaries, where the air flows into the regional domain. Compared to the rather small differences of O_3 the differences of O_3^{tra} are larger, corresponding to an increase of the average contribution of O_3^{tra} for the period JJA from 11.8 % (*EU30TE*) to 12.2 % (*EU30RT*).

To investigate the reason for the larger increase of O_3^{tra} compared to O_3 the differences of the 850PC of O_3 and all tagged O_3 categories were calculated. Figure 6.6 shows the absolute differences ('*EU30RT* minus *EU30TE*') for O_3 (named 'total') and the tagged categories. Shown are only the values of the road traffic and anthropogenic non-traffic category explicitly, while the other categories are summarised. The differences were calculated from the EMAC results for the zonal average (30° N : 70° N) and for the average over North America (NA)². Additionally, the differences were calculated for the CM50 results.

The differences of the zonal average (30° N:70° N) of O_3 is 0.011 DU (0.22 %), while O_3^{tra} is larger by 0.028 DU (0.52 %). The 850PCs for O_3 of the other categories are reduced by the 10 % increase of the road traffic NO_x emissions. This is caused by the nonlinearity of the O_3 chemistry and decreasing O_3 production from the emissions of these sectors.

The average values over NA are more interesting as the zonal average values, as the air from NA is transported directly over the Atlantic Ocean to Europe. The 850PC of O_3 increases by 0.014 DU (0.26 %), while the 850PC of O_3^{tra} increases by 0.031 DU (0.58 %). Compared to this, the CM50 results are changed by 0.013 DU (0.23 %), which is an increase similar as over NA in EMAC. The change of the O_3^{tra} values of the 850PC in CM50 is 0.022 DU (0.40 %), which is lower as the changes simulated by EMAC for NA.

The contribution of the road traffic sector would be calculated with the perturbation approach by comparing the difference of the O_3 values between the simulation *EU30RT* and *EU30TE* (shown as 'total' in Fig. 6.6). The differences of O_3^{tra} calculated for the values averaged for 30° N:70° N are larger by a factor of 2.5 compared to the difference of O_3 . Accordingly, the perturbation approach underestimates the contribution of the road traffic sector for this case by this factor. This difference between the results achieved with the perturbation and the tagging method is caused by non-linearity of the O_3 chemistry. The increase of the road traffic emissions lead overall to an decrease of the amount of O_3 produced per NO_x molecule. As only the emissions of the road traffic sector are changed, the amount of O_3 produced by emissions from most other sectors³ are decreased.

The values averaged over NA show that the perturbation approach underestimates the contribution by a factor of 2.2. These results and the factor of 2.5 discussed above are similar to the factor of 2 found by Grewe et al. (2016) for the underestimation of the perturbation approach on the impact of road traffic emissions. This factor of 2, however, was derived for global values and for a reduction of road traffic emissions by 5 %. Other studies found larger differences, but also with different perturbations (factor 5 for a 100 %

¹Please note, that the differences are smallest in mountainous terrain as here also the absolute values of the 850PC are reduced.

²North America is defined as a rectangular box from 230° W : 320° W and 20° N : 70° N.

³Due to competing effects (e.g. reactions of e.g. NO_x with VOC) and further simplifications some other sectors show increased O_3 values too. These effects are not discussed here in detail.

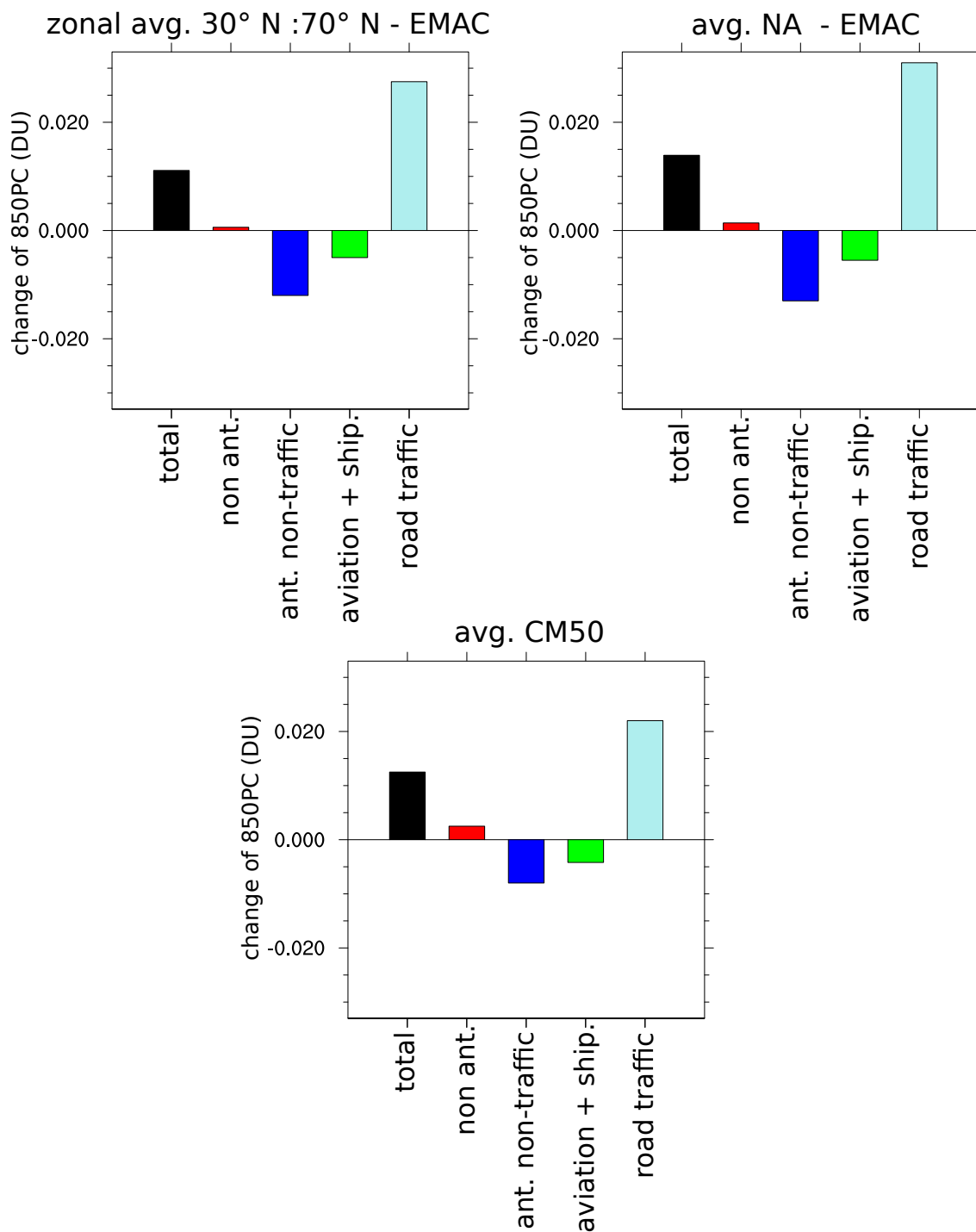


Figure 6.6: Absolute difference of the 850PC for O_3 and several tagged categories (details see text) between the *EU30RT* and the *EU30TE* simulation results. The values are averaged for the year 2008. Shown are the results for EMAC, averaged between 30°N:70°N, the results for EMAC averaged over North America and the results for CM50.

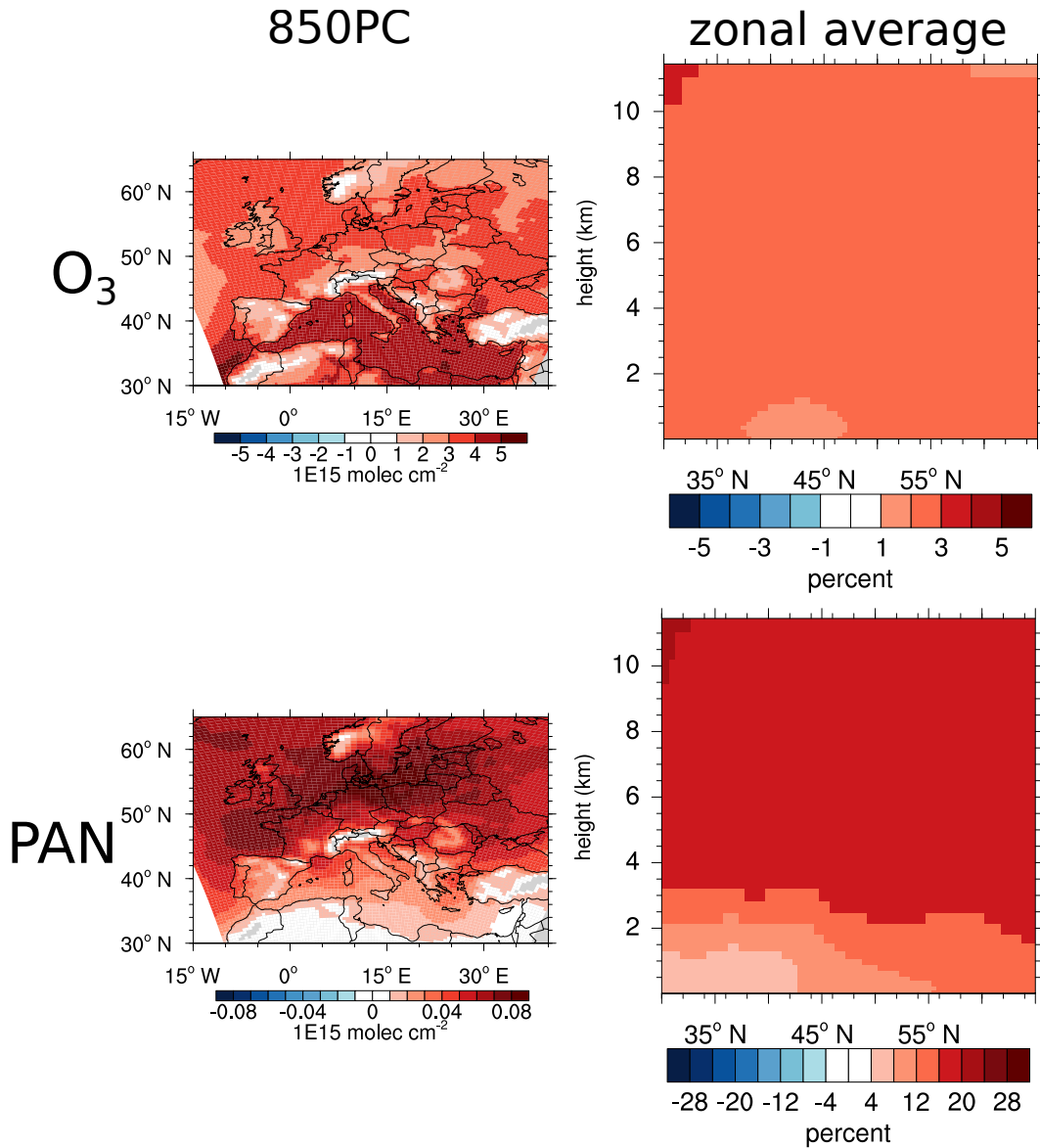


Figure 6.7: Difference (*EU30AC* minus *EU30TE*), daily mean values averaged over the period JJA. Shown are the 850PC (left side) and the zonal average for the CM50 domain (right side) for O_3 and PAN.

reduction of road traffic emissions by Grewe et al. (2012), and factor 3 for the biomass burning sector by Emmons et al.,2012).

Most interesting is the comparison of the differences between the EMAC results over NA and the results of CM50. Here, the change of the O_3 values is rather similar, while CM50 simulates a smaller difference of O_3^{tra} compared to the differences simulated by EMAC over NA. Accordingly, global increasing values of O_3^{tra} can locally be reduced by keeping the emissions constant. Nevertheless, almost 70 % of the increase of O_3^{tra} simulated over NA, from where most air is transported towards Europe, is also simulated over Europe. Due to the constant emission values in CM50 the factor of the underestimation of the contribution by the perturbation approach reduces to 1.7.

This larger increase of O_3^{tra} compared to O_3 in CM50 shows that the contribution of the different categories is even more sensitive to emission changes than O_3 itself. Thus realistic global boundary conditions (meaning also realistic global emissions) for the contributions to O_3 are even more important as for O_3 itself. This is only possible with a very consistent global-regional model chain and a high update frequency of the boundary conditions.

The difference between the results of the *EU30AC* and *EU30TE* is larger, compared to the difference between *EU30RT* and *EU30TE*. Figure 6.7 shows the difference ('*EU30AC* minus *EU30TE*') of O_3 and PAN for the 850PC (left side, absolute values) and for the zonal average (right side, relative differences). The values of O_3 are increased by around 3 % almost homogeneously over the whole domain. The absolute difference (not shown) increases with height. Only within the PBL in the Mediterranean region the differences are slightly smaller and between 1–2 %. The differences of PAN are rather homogeneous, too. The absolute differences for the 850PC are largest around 50°N and are lowest in Southern Europe, where the relative differences are 5 % at maximum. The differences in the rest of Europe are around 10–15 %, except for the western boundaries of the domain, where differences of 20 % are simulated. The differences of the zonal average of PAN are around 12–16 % in most areas, but they decrease with height to values below 10 %. Both, PAN and O_3 can be transported over long distances because of their long lifetime. Almost no differences are found for NO_x , because direct long range transport is not important for these species. The detailed investigation of changes of other species due to the changed long range transport is beyond the scope of the present study.

The seasonal cycle of the differences ('*EU30AC* minus *EU30TE*') for the 850PC of O_3 and O_3^{tra} is shown in Fig. 6.8 for NA (EMAC) and Europe (CM50). In general the difference is negative for O_3 during the first half of the year and positive for the second half of the year. The sign of the differences of O_3^{tra} is opposite, showing positive differences in the first half and negative differences in the second half of the year. This leads to a larger contribution of O_3^{tra} during the first half, and a smaller contribution during the second half of the year simulated by *EU30AC* compared to *EU30TE*. The seasonal cycle of the differences is a direct consequence of the missing seasonal cycle of ACCMIP/RCP60 emission inventory. This missing cycle shifts the contributions considerably, as especially the anthropogenic non-traffic category for the MAC08 and the VEU emission inventories feature a strong seasonal cycle (Sect. 5.6.1). This change of the O_3 precursors change both, the contributions to O_3 , and the O_3 mixing ratios.

As has been discussed in the comparison of the results of the *EU30TE* and the *EU30RT* simulation, the differences for O_3 and O_3^{tra} between the EMAC results over NA and the CM50 results are rather similar. Only during April–August larger differences are found. As the differences for O_3^{tra} are larger than for O_3 the contributions are modified too (not shown). This is in agreement with the findings from the *EU30RT* simulation. During April–August the local production of O_3 (driven by local emissions) is largest and can influence the contributions most. A more detailed comparison between the differences of both simulations is not feasible. The missing seasonal cycle of the emissions leads to monthly changing differences between the MAC08 and ACCMIP/RCP60 emission inventories. Compared to the *EU30RT* simulation, with a well defined 10 % perturbation of the emissions, the difference can even change in sign, rendering any detailed quantification difficult.

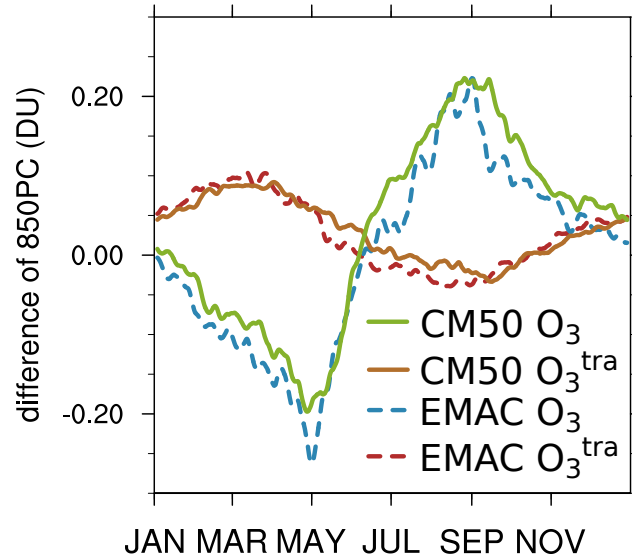


Figure 6.8: 5-day running means for the absolute difference ($'EU30AC - EU30TE'$) of the 850PC for O_3 and O_3^{tra} . The values for EMAC (E.) are area averaged over NA, the COSMO results are area averaged over the CM50 domain.

6.3 Changes in the O_3 production efficiency

To investigate how the emission changes of the future projection alters the net production of O_3 , Table 6.2 lists the net O_3 production (PO_3 , integrated up to 200 hPa). Only the values of the three most important anthropogenic ground level sources are shown. In addition, the total NO_x emissions (E_{NO_x}) and the ratio $R_{prod} = PO_3 / E_{NO_x}$ are listed. This ratio indicates the efficiency of O_3 production for the specific source.

The efficiency of the road traffic emissions (R_{prod}) increases slightly from 4.5 to 4.6 using VEU30 instead of VEU08, indicating that per NO_x molecule slightly more O_3 molecules are formed. Due to the decrease of the emissions, however, the total amount of O_3^{tra} is reduced by more than 20 % between both simulations.

The R_{prod} values for the anthropogenic non-traffic category decrease from 5.6 to 5.3. The production of O_3^{anth} , in contrast, is increased by 11 % due to larger NO_x emissions. Similar results are found for the shipping category, where VEU30 features larger NO_x emissions than VEU08. The larger amount of emissions leads to a reduction of R_{prod} from 5.3 to 4.5. The production of O_3^{ship} increases, however, by more than 35 %. Remarkable is that R_{prod} for the shipping category decreases to levels below the road traffic category. Normally emissions from the shipping sector are more effective in forming O_3 than the emissions from the road traffic category (as also found for the present day conditions, e.g. Hoor et al., 2009, Koffi et al., 2010, Dahlmann et al., 2011). These studies, however, focused on global effects and the efficiency from the ship sector is large especially in clean environments (e.g. Lawrence and Crutzen, 1999, Eyring et al., 2007). These clean environments are not found over the oceans directly surrounding Europe.

Comparing the results of the *EU30TE* and the *EU30RT* simulation, where the boundary conditions are changed but the local emissions are unchanged, R_{prod} increases for all categories. Here, the additional precursors increase the O_3 production inside the domain.

Table 6.2: Net O₃ production (P_{O₃}, in Tg a⁻¹), NO_x emissions (E_{NO_x}, in Tg a⁻¹ in amount of NO) and R_{prod} (P_{O₃}/E_{NO_x}) for the three most important anthropogenic ground level sources (road traffic, anthropogenic non-traffic, shipping). The values are integrated over the CM50 domain up to 200 hPa and over the whole year.

	road traffic			anthropogenic non-traffic			shipping		
	P _{O₃} ^{tra} O ₃ ^{tra} (Tg a ⁻¹)	E _{NO_x} (Tg a ⁻¹)	R _{prod}	P _{O₃} ^{anth.} O ₃ ^{anth.} (Tg a ⁻¹)	E _{NO_x} (Tg a ⁻¹)	R _{prod}	P _{O₃} ^{ship} O ₃ ^{ship} (Tg a ⁻¹)	E _{NO_x} (Tg a ⁻¹)	R _{prod}
<i>EU08TE</i>	23.94	5.36	4.47	28.28	5.08	5.57	9.62	1.81	5.32
<i>EU30TE</i>	18.61	4.06	4.59	31.59	6.02	5.25	11.19	2.49	4.49
<i>EU30RT</i>	20.51	4.06	5.05	32.01	6.02	5.32	11.57	2.49	4.65

The results in the CM12 domain are overall similar and are not discussed here. The corresponding numbers are given in Sect. A.7 (page 192).

6.4 Implications for the radiative forcing and the methane lifetime

The radiation routine of COSMO uses internal climatologies for the calculation of the radiation. This hinders a investigation of the radiative forcing of different trace gases for different scenarios in COSMO. To overcome this limitation the possibilities of the MESSy submodel MMD2WAY were used. Besides the handling and exchange of the necessary initial and boundary conditions from EMAC to COSMO, this submodel allows the exchange of data-fields from COSMO to EMAC⁴. Here the O₃ field calculated by COSMO is on-line exchanged to EMAC and transformed from the finer COSMO grid to the coarser EMAC grid (both vertically and horizontally). Only the parts of the field which are outside the horizontal and lateral relaxation area are considered. This interpolated field is further passed to the radiation routine of EMAC, which performs a second diagnostic radiation call (details are given by Dietmüller et al., 2016) using this interpolated O₃ field from COSMO, calculating the radiative fluxes. More details are given in Sect. A.2.

The differences of the radiative fluxes for O₃ are shown in Fig. 6.9. Displayed are the annually and area averaged differences between the results of the simulation using the VEU30 inventory and the *EU08TE* simulation. The differences of the net radiative flux is positive for all three simulations. This, however, does not hold for all wavelengths, because the short-wave component of the radiative flux is negative up to 300–400 hPa.

The difference of the radiative fluxes at 200 hPa simulated by *EU30TE* and *EU08TE* is ≈ 0.9 mW m⁻². The change of the boundary conditions lead to an increased radiative forcing at 200 hPa. This increase is 4.5 mW m⁻² for the *EU30RT* and 23 mW m⁻² for the *EU30AC* simulation.

⁴This option has been developed to open the possibility of two-way nesting.

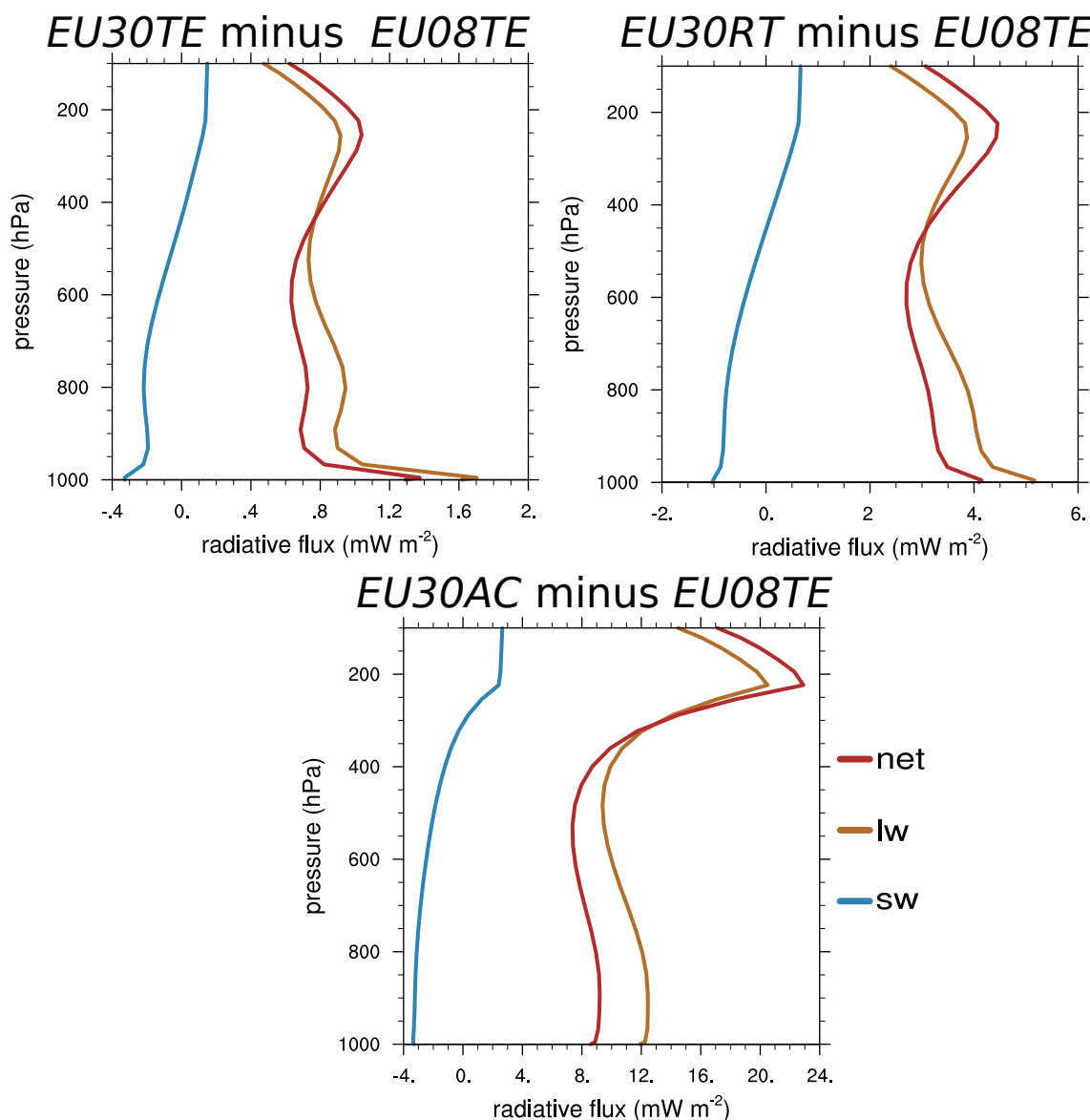


Figure 6.9: Vertical profiles of the change of the short-wave (sw), long-wave (lw) and net instantaneous radiative fluxes (in mW m^{-2}). The values are averaged annually over a region defined as $250^\circ \text{ W}:30^\circ \text{ E}$ and $35^\circ \text{ N}:60^\circ \text{ N}$. Shown are the differences of 'EU30TE minus EU08TE', 'EU30RT minus EU08TE' and 'EU30AC minus EU08TE'. Please note the different scales of the x-axis.

Further, it is remarkable that for the simulations *EU30TE* and *EU30RT* the net flux changes at the surface are larger or at least comparable to the change near the tropopause. This is consistent with the findings from the last two subsections namely that the largest differences for O_3 for both inventories are confined to the PBL, where the emissions occur.

The analysed radiative forcing accounts only for the direct effect on the radiation due to changed O_3 concentrations. In addition, the changes of O_3 and its precursors alter the OH abundance in the atmosphere which alters the CH_4 lifetime. As has been discussed in Sect. 4.3.5 the global lifetime of CH_4 can not be calculated from the results of a regional

Table 6.3: Averaged values for JJA of the CH₄ mass (M_{CH_4}), the OH mass (M_{OH}) and the pseudo CH₄ lifetime against OH (τ) for CM50. The mass of CH₄ and OH are the time averaged values. The subscripts on the individual variables indicate the different vertical layers (in hPa). The ranges indicates one standard deviation with respect to time based on monthly mean values.

	<i>EU08TE</i>	<i>EU30TE</i>	<i>EU30RT</i>	<i>EU30AC</i>
$M_{\text{CH}_4}^{850}$ (Tg)	26.09 ± 0.36	26.12 ± 0.36	26.12 ± 0.35	26.21 ± 0.36
M_{OH}^{850} (kg)	1306 ± 79	1337 ± 86	1338 ± 89	1307 ± 86
τ^{850} (a)	3.10 ± 0.18	3.03 ± 0.18	3.03 ± 0.19	3.10 ± 0.18
$M_{\text{CH}_4}^{500}$	71.99 ± 0.79	72.01 ± 0.80	72.00 ± 0.85	72.62 ± 0.80
M_{OH}^{500}	4501 ± 345	4551 ± 351	4557 ± 361	4439 ± 351
τ^{500} (a)	4.53 ± 0.36	4.48 ± 0.36	4.48 ± 0.39	4.60 ± 0.36
$M_{\text{CH}_4}^{200}$ (Tg)	57.38 ± 0.57	57.38 ± 0.57	57.38 ± 0.67	57.98 ± 0.57
M_{OH}^{200} (kg)	5466 ± 445	5507 ± 444	5513 ± 448	5311 ± 444
τ^{200} (a)	13.08 ± 1.35	12.97 ± 1.33	12.95 ± 1.43	13.56 ± 1.33

model. Instead, a pseudo lifetime of CH₄ against OH were calculated to investigate if the tropospheric oxidation budget is changed. This calculation of the pseudo CH₄ lifetime were performed as described in Sect. 4.3.5, meaning that the lifetime were calculated from the ground to 850 hPa, 850–500 hPa and 500–200 hPa.

Table 6.3 lists the pseudo CH₄ lifetime as calculated from the results of the three simulations using VEU30. Additionally, the values of the *EU08TE* simulation are shown for comparison. The differences between the results of all simulations are small, especially compared to the monthly variability (indicated by the given standard deviations). In general, the VEU30 inventory leads to a slightly larger OH mass, caused by an increase of O₃. This leads to a decrease of the CH₄ lifetime for all vertical sections. The results of the *EU30AC* simulation are different. The different global boundary conditions lead to a slightly lower OH mass. At the same time also the CH₄ mass is larger, caused by the changed boundary conditions (Sect. 3.3). Correspondingly the lifetime of CH₄ increases.

6.5 Discussion

The results of the three simulations using VEU30 were analysed and compared to results of the simulations using VEU08. As has been discussed in Chap. 5, the contribution of O₃^{tra} during winter is driven mainly by the global boundary conditions. Accordingly, a strong reduction of road traffic emissions in Europe leads only to a small decrease of the contribution during winter. Compared to spring and summer, the absolute values of O₃^{tra} during winter are low. During summer, however, the contribution of O₃^{tra} is lowered by 2–3 ppts when applying VEU30 instead of VEU08. Additionally, the absolute values of O₃^{tra} are reduced too.

The mixing ratios of most trace gases over large parts of Europe are only slightly altered when applying VEU30 compared to VEU08. Especially in Germany my results show an increase of O₃, even though the NO_x emissions are reduced. This is caused by an increase of the OPE with decreasing NO_x road traffic emissions. A similar increase of

O₃ with decreasing NO_x levels was claimed by Roustan et al. (2011) over the Paris area for a future (2020) road traffic scenario. Compared to the simulations I performed, only the road traffic emissions were adapted and the boundary conditions were kept constant for the simulations of the present day and future scenario. This increase of O₃ with decreasing NO_x levels highlights the importance of VOC reductions in conjunction with NO_x reductions, to decrease urban O₃ levels in the future (see also Markakis et al., 2014). Accordingly, it is important to decrease not only NO_x but also VOC for future mitigation scenarios. However, for future work it is important to evaluate the model system in more detail to investigate how well the threshold from 'VOC-limited' to the 'NO_x-limited' regime is simulated (e.g. with methods discussed by Sillman, 1995, Xie et al., 2011)

In addition to the projected decrease of the road traffic emissions in VEU30, the other anthropogenic emissions are projected to increase. The increase of the emissions from the shipping sector seems to be a realistic scenario (e.g. Eyring et al., 2007, Koffi et al., 2010, Matthias et al., 2016), an increase of the for the anthropogenic non-traffic NO_x emissions (compared to the year 2008), however, seems to be unrealistic. Compared to this, the RCP6.0 scenario projects a decrease of the anthropogenic non-traffic NO_x emissions⁵ for Europe from 6.7 Tg (2005) to 5.1 Tg (2030), and the RCP8.5 scenario projects a decrease from 7.0 Tg to 5.3 Tg.

The increase of NO_x emissions for the anthropogenic non-traffic sector in VEU30 compared to VEU08 might be caused by the assumed 'business as usual' scenario in this inventory (details see Sect. 3.2.3). After the outcome of the COP21⁶, an even larger reduction of the emissions as projected for RCP6.0 might be more realistic.

This unrealistic increase of the anthropogenic non-traffic emissions has important implications for the contribution of O₃^{tra}, as overestimated anthropogenic non-traffic emissions lead to a further decrease of the contribution of O₃^{tra} for given emissions from the road traffic category. In addition, the O₃ chemistry itself is influenced by the increasing emissions, influencing not only the net O₃ production for the emitted source, but changing also the background for other sources (e.g. Dahlmann et al., 2011).

This leads to the conclusion that the results derived with the VEU30 inventory should be taken with care. The decrease of the contribution of road traffic emissions to tropospheric O₃ might be overestimated. Therefore, future studies should investigate different regional emission inventories to assess the effect of the uncertainties of future projections.

Hodnebrog et al. (2012), for example, showed an even stronger decrease of the impact of O₃^{tra} (using a 5 % perturbation approach), and claimed that the road traffic sector becomes the traffic sector with the smallest impact on O₃. Different from the present study, a scenario for the year 2050 was chosen, in which emissions from the road traffic sector are strongly reduced. Similar results are shown by Koffi et al. (2010), who compared present day and two scenarios for 2050, showing that globally the aviation sector becomes the transport mode with the highest impact on O₃. The assumed reduction of road traffic emissions was larger compared to the present study. In addition, Hodnebrog et al. (2012) and Koffi et al. (2010) focused on the global scale only.

The investigations of the VEU30 inventory performed in the present study has an important limitation of the chosen methodology. Due to the application of the QCTM mode,

⁵Numbers estimated on the 20.04.2016 using <http://eccad.sedoo.fr> for the continent of Europe (including Russia).

⁶Convention on Climate Change, 21st conference of the parties which took place in Paris 2015.

the meteorology is identical in all simulation. Changes in the meteorology (due to climate change) might influence the results. As an example, studies suggest an increase of stagnant conditions in mid-latitudes (caused by a northward shift of the storm tracks), which likely increases ground level O₃ values (Jacob and Winner, 2009, and references therein). Increasing temperature further influences the reaction kinetics, leading for instance to a decrease of the PAN lifetime towards thermal decomposition (e.g. Doherty et al., 2013). In addition, climate and land-use change modifies the biogenic emissions, which change the contribution of the biogenic categories and influence the background chemistry. A problem with these biogenic emissions is that projections about possible developments of the biogenic emissions for the future are very uncertain. With the parametrisations used in the present study, Jöckel et al. (2016) showed that using the RCP6.0 scenario both, C₅H₈ and NO_x emissions from soils are projected to increase. But especially the estimates of C₅H₈ emissions from plants are rather uncertain. While rising temperatures probably lead to an increase of C₅H₈ emissions, increasing CO₂ levels and land-use or vegetation changes can inhibit this increase or even lead to decreasing emissions (e.g. Pacifico et al., 2012, Tai et al., 2013, Squire et al., 2014). Compared to this, the NO_x emissions from soils mainly depend on fertilizer use, soil temperature and soil water content (e.g. Oikawa et al., 2015). Therefore NO_x emissions from soils are likely to increase in future, but projections about future fertilizer usage are highly uncertain.

To include the effects of changing meteorology, ensemble free-running simulations (meaning without QCTM mode and not nudged towards reanalysis data) are necessary. Without decoupling chemistry and dynamics every simulation with changed boundary and initial conditions simulates a different meteorology. The changed meteorology feeds back on the chemistry. Therefore it is hard to detect, if changes of the chemistry are caused by changed emissions or by changed meteorology. Accordingly these simulations have a small signal to noise ratios and long simulation times are necessary, which are beyond the scope of this work.

Concerning the biogenic emissions, it is also important to note that the simulations I analysed in this chapter are missing the correct contribution of the biogenic emissions in the boundary conditions (meaning in the EMAC simulation). With correct boundary conditions, the values of the contribution of the road traffic emissions would presumably be lower by 1.0–1.5 % during summer (see Chap. 5, page 77).

My analyses further show that from the assumed increase of road traffic NO_x emissions by 10 %, around 70 % of the changes over North America are transported to Europe by long range transport. Similar experiments were performed in the scope of HTAP (2010a, mainly Sect. 4.2.5 therein). HTAP (2010a) decreased the anthropogenic emissions in different regions of the world by 20 %. Compared to my results, HTAP (2010a) reported that around 40 % of the changes caused by the decreasing emissions are transported to Europe. The different results might be explained by three differences: First, HTAP (2010a), focused on ground level values and not on the impact on the 850PC. Second, the magnitude of the emission change between the study of HTAP (2010a) and the present study are not comparable. Third, I applied for the first time a tagging method in a combination of a regional and global model. Compared to the methods used by HTAP (2010a) the tagging method accounts for the non-linearity of the O₃ chemistry.

Therefore, my results confirms the importance of global to regional consistency of mitigation scenarios. Lower emissions of O₃ precursors in Europe decreases the O₃ levels

in Europe, but also changes of emissions e.g. in America alters the O_3 levels in Europe substantially. Mitigating the emissions only regionally might not be enough to meet air quality standards. More quantitative analyses of this problem are necessary for the future (cf. Sect. 7.2).

Moreover, my results with respect to the importance of the global boundary conditions have important consequences for the application of regional chemistry-climate models. Especially the results of the *EU30AC* simulation, which used the ACCMIP emission inventory instead of the MAC08 inventory for EMAC, show, how unrealistic boundary conditions of the regional model deteriorate the contribution analysis within the regional model. Yet, not only the contributions in CM50 are strongly influenced by the changed boundary conditions, but also the trace gas mixing ratios are considerably influenced. The O_3 mixing ratios increase by 3–5 %, the relative differences for PAN and NO_2 are even larger.

This impact of the boundary conditions on the results is well known and was already analysed in various studies. Studies using regional models over America tested the influence of boundary conditions from models (Tang et al., 2007) and from satellite data (Pour-Biazar et al., 2011). These studies in general claimed the largest impact of the boundary conditions on O_3 in the free troposphere and less impact on the values in the PBL.

None these studies, however, tested a well defined perturbation of the boundary conditions (e.g. an 10 % change of the boundary conditions) as I performed in the present study (*EU30RT* simulation). Therefore, a direct comparison between my results and previous studies is not possible. But in general it seems that previous studies simulate a smaller impact of the boundary conditions on O_3 . Keeping in mind the too strong vertical mixing of tracers in COSMO (Sect. 4.4), this seems plausible. Accordingly, the results of the present study with respect to the influence of the boundary conditions on O_3 in the PBL provide an estimate at the upper end of the range.

Furthermore, when evaluating the radiative forcing and the pseudo CH_4 lifetime of the future inventory the importance of global mitigation is corroborated, as the forcing over Europe is largest for the changed boundary conditions. The reason is that the largest sensitivity of the radiative forcing in the troposphere due to tropospheric O_3 changes is found in the upper troposphere more specifically in the tropical troposphere (e.g. Worden et al., 2011, Riese et al., 2012, Rap et al., 2015).

The changed emissions over Europe might lead to a larger radiative forcing downwind of Europe, after O_3 is transported higher upwards in the troposphere. To assess this effect additional global simulations, in which the emissions are only changed in Europe/Germany, are necessary. These would be used to investigate, where the radiative forcing caused by this perturbation is largest. In addition, a 2-way feedback approach could be used, meaning that the regionally changed trace gas fields from COSMO are feed back to the trace gas fields of the global model. Overall the changes of the radiative forcing and pseudo CH_4 lifetime found for the VEU30 inventory compared to the VEU08 inventory are rather small. The differences caused by the global boundary conditions are larger than the differences of the results between VEU08 and VEU30.

6.6 Conclusion

My analyses of the contribution of road traffic emissions for a year o 2030 projection reveal the following most important results:

- A decrease of the contribution of the road traffic category to O_3 by 2–3 ppts is simulated for Europe applying the VEU30 instead of the VEU08 inventory.
- Especially in Germany, the reduction of NO_x emissions lead to an increase of ground level O_3 , showing the need to mitigate also VOCs.
- The boundary conditions have a large impact, in particular on O_3 . This has important implications for the application of regional models and for the assessment of regional mitigation options.
- The impact of the changed boundary conditions on the pseudo CH_4 lifetime and the change of the radiative forcing of O_3 was larger then for the regional emission reductions. This implies that global mitigation of road traffic emissions is very important to reduce the climate impact of these emissions.

Chapter 7

Concluding remarks

7.1 Summary

Ozone (O_3) in the troposphere has several negative aspects. On the one hand, O_3 acts as a greenhouse gas, contributing to global warming. On the other hand, O_3 is a strong oxidant, being harmful to humans and animals and causing damage to plants. Besides this, O_3 is an important source for the hydroxyl radical (OH), which is important for cleansing the atmosphere from many pollutants (e.g. carbon monoxide (CO) and methane (CH_4)). Sources of O_3 in the troposphere are downward transport from the stratosphere and photochemical production of O_3 from precursors including nitrogen oxides (NO_x) and volatile organic compounds (VOCs). One important source of these precursors is the exhaust from road traffic, especially as these emissions are located mainly in densely populated regions.

The contribution of road traffic emissions to tropospheric O_3 were investigated in different studies. Most of these studies calculated the contribution by comparing the results from two simulations: one simulation with all emissions and a second simulation with reduced road traffic emissions. Due to the non-linearity of the O_3 chemistry, this method is inappropriate and can lead to inaccurate results. Further, these studies mostly used coarsely resolved global models, which do not resolve regional information.

To overcome these limitations, I applied for the first time a model system, which allows for regional refinements together with a detailed tagging method for source attribution. The used MECO(n) model system consists of the global chemistry-climate-model EMAC and regional refinements with finer resolution using the regional chemistry climate model COSMO-CLM/MESSy. The applied tagging method is an accounting system following the reaction pathways from the individual emission sources, allowing a quantification of the contribution from individual emission sources to O_3 (source attribution).

As preparatory work for this thesis, I modified the MESSy submodel for the application of the tagging method in order to allow its application in COSMO-CLM/MESSy. Besides technical changes, several further improvements were necessary, in order to account for the finer resolution. Further, a DLR specific regional emission inventory for Europe required extensive preprocessing to allow its application for the aims of this thesis.

As the MECO(n) model system were not used for studies focussing on tropospheric gas phase chemistry before, an important task of my work has been the evaluation of MECO(n) with respect to the gas phase chemistry in the troposphere. Accordingly, the

results from EMAC and two COSMO-CLM/MESSy (from now on denoted as COSMO) refinements with 50 km (covering Europe) and 12 km (covering Germany) resolutions were compared with satellite measurements of O₃ and nitrogen dioxide (NO₂), and with ground-based measurements of O₃ and its precursors. In addition, the results were compared with O₃ sonde data.

The comparison with observations showed that COSMO is in general able to represent the geographical distribution and annual cycle of O₃ and its precursors in Europe and Germany. In detail, however, a positive bias for O₃ and negative biases for CO and NO₂ were found. Comparisons with O₃ sonde data showed further that most of these biases are likely attributable to a too strong vertical mixing. This too strong vertical mixing is also the likely reason for a better representation of the diurnal cycle of O₃ in EMAC in comparison to COSMO. Further sensitivity studies showed that with the current physical parametrisations only a minimal improvement of the vertical mixing is possible. More extensive parameter studies were beyond the scope of this thesis, but these studies are necessary in the near future. In addition, ongoing developments of the physical parametrisations for the vertical diffusion at the Deutscher Wetterdienst (DWD) might reduce this issue.

After this evaluation I investigated the results of MECO(n) focussing on the contribution of the road traffic emission on tropospheric O₃ for present day conditions. First, the results for Europe as simulated by EMAC and COSMO were compared. This comparison revealed that both models simulate a comparable contribution of road traffic emissions to the tropospheric O₃ column up to 850 hPa of $\approx 11\%$ averaged for 2008 over Europe. Regionally, however, larger differences exist, especially in the Po basin. There, average contributions during summer of $\approx 15\%$ were simulated. In these regions, a fine resolution is required to investigate the regional contribution correctly. The analysis further showed, that around 20 % of O₃ chemically produced over Germany are caused by road traffic emissions. This makes the road traffic emissions to an important contributor to local production of O₃ in Germany. The simulated values for Europe are slightly lower, but still around 18 % of the tropospheric O₃ in Europe are produced by road traffic emissions.

My analysis further showed that the average contribution over Germany is mainly governed by the inflow. With 12 km resolution, however, larger extreme values are simulated than with 50 km resolution. This shows that for the investigation of extreme events, a fine resolution is indispensable.

To assess the sensitivity of the contribution of road traffic emissions to uncertainties of the emission estimates, I performed several sensitivity studies, for which the resolution of the emissions, the anthropogenic emissions, and the biogenic emissions were changed systematically. The analyses showed that the contribution is most sensitive to uncertainties of the different NO_x emission estimates. The sources, which are most important for the production of tropospheric O₃ over Europe are anthropogenic non-traffic emissions (which include industry, energy production and household), road traffic emissions and NO_x emissions from soils. Correspondingly, the uncertainties of emission from these sources should be reduced in future. However, this reduction is only possible to a limited extent. The simulation results show a maximum difference of the contribution of road traffic emissions to the partial O₃ column up to 850 hPa of around $\pm 10\%$ for most regions in Europe. This corresponds to differences of the contribution in Europe of around one percentage point for present day conditions. It is, however, important to keep in mind,

that the main focus of the present study was on the sensitivity to changed emissions in Europe. Uncertainties of emission estimates on other parts of the globe, especially for the road traffic emissions, were not investigated in detail. In addition, simplifications in the representation (or limited understanding) of other dynamical and chemical processes in the model have likely an impact of the results, which have not been investigated.

My analysis of the future projection for the year 2030 shows a reduction of the contribution of the road traffic category by 2–3 percentage points over Europe during summer, with the largest reductions over Northern Italy and Eastern Europe. In Germany, the reductions of NO_x emissions for the projection lead to an increase of surface O_3 in most areas by $\approx 10\%$. Accordingly, the decrease of NO_x emissions alone is not sufficient for mitigating O_3 in Germany. Follow up studies are necessary to investigate in which order of magnitude VOC emissions should be reduced to overcome the increase of O_3 . The results of the projection for the year 2030 should, however, be taken with some caution, because the projection assumes an increase of NO_x emissions of the anthropogenic non-traffic sector in Europe, compared to the year 2008. This increase might be unrealistic.

In addition, I performed an idealised simulation in which the global NO_x emissions from road traffic are increased by 10 % everywhere but in Europe. The emissions over Europe were kept at the levels of the projection for the year 2030. My analysis of the results from this simulation revealed that the increase found over Europe (where the emissions are unchanged) corresponds to $2/3$ of the increase over North America. The increase is caused only by the transport of polluted air masses over the Atlantic Ocean. This highlights the importance of global mitigation efforts with respect to tropospheric O_3 as well as the importance of realistic boundary conditions for regional source attribution.

7.2 Conclusions and Outlook

The most important findings and the answers to the scientific questions raised by this study (see page 2) are briefly summarised as follows:

Q₁: What is the contribution of the road traffic emissions to tropospheric O_3 in Europe for present day conditions? How do long range transport and local production influence the contribution?

A₁: The contribution of road traffic emissions to the tropospheric O_3 column up to 850 hPa is $\approx 11\%$ over Europe averaged for the year 2008. During winter the contribution is lower ($\approx 10\%$) and mainly determined by long range transport. During summer the contribution increases to $\approx 12\%$ and local production is more important. The contribution to ground level O_3 is $\approx 13\%$, corresponding to 5–10 nmol mol⁻¹.

Q₂: How sensitive are the results with respect to uncertainties of anthropogenic and natural emission estimates?

A₂: The largest differences found between the different simulation results are in the order of 10 % for the contribution of road traffic emissions to the 850 hPa, corresponding to differences of the contribution of around one percentage point. This range, however, heavily depends on the region. Generally, the sensitivity was largest to differences

of the inflow to Europe (caused e.g. by emission changes in North America or Asia), changed NO_x emissions from the anthropogenic non-traffic sector, and to local NO_x emissions from soils.

Q₃: How does the contribution of road traffic emissions to tropospheric O₃ change for a future projection and how are these results affected by global changes of the emissions?

A₃: The contribution of road traffic emissions to tropospheric O₃ in Europe for the future projection in the year 2030 is reduced by 2–3 percentage points during summer compared to conditions of the year 2008. Since the emissions for the rest of the world were kept constant, only a small change was simulated during winter, when local production plays only a minor role (see A₁). An increase of the NO_x emissions in the rest of the world (except for Europe) leads to an increase of the contribution in Europe corresponding to ²/₃ of the increase found over North America.

Q₄: Do the results of the contribution depend on the resolution of the model and/or the emissions?

A₄: The domain averaged values over Europe (continental scale) showed only small differences between the results of the simulations applying different emissions- or model resolutions. Regionally the differences are larger, especially for regions like the Po Basin or the Mediterranean area. In addition, a fine resolution is important, if O₃ extreme events are to be analysed.

From these findings and the discussion about the state of the art (page 21) further questions arise. I conclude this thesis with a (not complete) list of some most important next steps.

- As shown, long range transport influences the contribution of road traffic emissions in Europe strongly. The detailed quantification of O₃ caused by long range transport and by local production is still a challenging task. To allow such a quantification further model developments are necessary. This can be achieved by adding additional categories to the tagging method to distinguish O₃ produced in Europe and O₃ transported over long range better.
- My work investigated mainly the sensitivity of the results to uncertainties of the emission estimates in Europe. Emission estimates for other regions are uncertain too. After the tagging method is improved as discussed above the sensitivity of these uncertainties of the emission estimates should be performed. In this context also the sensitivity of the results to the resolution of the driving model (EMAC) and the convection parametrisation are important which are known to influence the long range transport.
- The tagging method does not account for the quick cycling between O₃ and NO₂, which might lead to artificially large tagged O₃ values near hotspot regions. Therefore, further investigations are necessary to assess if the tagging method should be equipped with a possibility to allow for the quick cycle between O₃ and NO₂.

- As shown, the contribution of road traffic emissions to tropospheric O₃ in Europe is most sensitive to changes of other NO_x emissions. In Europe, especially anthropogenic non-traffic emissions and emissions of NO_x from soils are important near ground sources of NO_x. It is known that the parametrisation of NO_x from soils used in this study is rather simple. Improved parametrisations exist, which should be implemented to simulate NO_x emissions from soil which are in a better agreement with current estimates.
- Many parametrisations used by the applied model rely on external parameters (such as soil type). Even with the applied 12 km resolution these external parameters are averaged over relatively large areas. In addition, the emissions are mixed over relatively large areas, too. Therefore, a further increase of the resolution should be envisaged. Challenging is, however, the generation/availability of external data sets which are adequately resolved.
- As the O₃ chemistry is highly non-linear, the contribution simulated by a global and a regional model should be performed for a region with larger emissions than in Europe (e.g. Southeast Asia). If emissions are much larger compared to Europe, the differences between results simulated by a coarsely resolved and a fine resolved model might differ more strongly. In addition, other meteorological conditions (e.g. decreased inflow or higher temperatures) might influence these results further.
- Simulations of longer simulation periods should be performed to investigate the representativeness of the reported results on longer time scales. Especially the possible changes of the meteorological conditions for the simulations of a future scenario should be considered. These changes of the meteorology can alter biogenic emissions and transport patterns. Such investigations, however, are computationally very demanding, because long integration times are necessary.
- The fine resolution of the newly developed model system allows the investigation of extreme events and mitigation studies in more detail. If such analyses are planned in the future, it is important to evaluate the model in more detail with regional measurements of NO_x, NO_y and different VOCs. This is important to investigate, if the model predicts the threshold from NO_x to VOC limited O₃ production, well. With finer resolution, a more detailed chemical mechanism might be important to account in more detail for the organic chemistry.
- Finally, it is in general important to reduce the uncertainties of the models by detailed intercomparison with in situ observations. Compared to coarse resolved global models, where the model results can hardly be directly compared to measurements, the fine resolution allows a much better intercomparison with observations. This will possibly strengthen our understanding of processes.

Appendix A

Appendix

A.1 Description of additional sensitivity studies

This section provides a short summary of the most important information regarding the additional sensitivity studies analysed in Sect. 5.4. The simulations *REF_bio_EMAC*, *REF_no_C5H8*, *REF_no_NO*, *REF_C5H8_scaled* and *REF_no_biotag* were branched off from the *REF* simulation on 1. May 2008. The simulation *REFT42a* was branched off on 1. May 2008 from the *REFT42* simulation. All simulation were carried out for the period May–August 2008. Only EMAC and CM50 were active for this simulations.

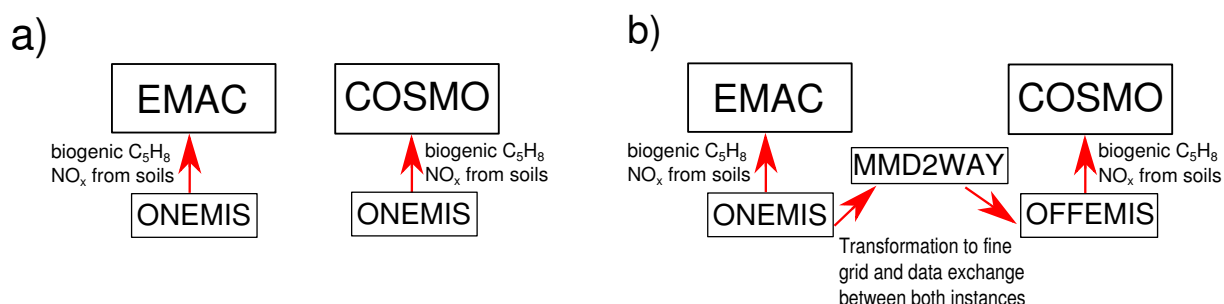


Figure A1: Treatment of biogenic C₅H₈ emissions and emissions of NO_x from soils for. (a) the standard treatment (b) the treatment for the sensitivity studies discussed in this section. More details are given in the text.

All simulations feature a special treatment of the biogenic C₅H₈ emissions and NO_x emissions from soils. Normally, these emissions are calculated by the submodel ONEMIS in EMAC and COSMO (compare Fig. A1a). Despite that the submodel uses the same external files in EMAC and COSMO, the calculations of these emissions depends on meteorological parameters (e.g. temperature). Even if the total amount of emissions over the European area are similar, the geographical distribution differs. To investigate the dependency of the results on the geographical distribution of the emissions, all sensitivity studies use the same biogenic C₅H₈ emissions and emissions of NO_x from soils in EMAC and CM50, respectively. Therefore, the submodel OENMIS was switched off in CM50 (compare Fig. A1a). Accordingly, no biogenic C₅H₈ and soil-NO_x emissions were calculated by CM50. Instead the emissions of C₅H₈ and soil-NO_x as calculated by EMAC are

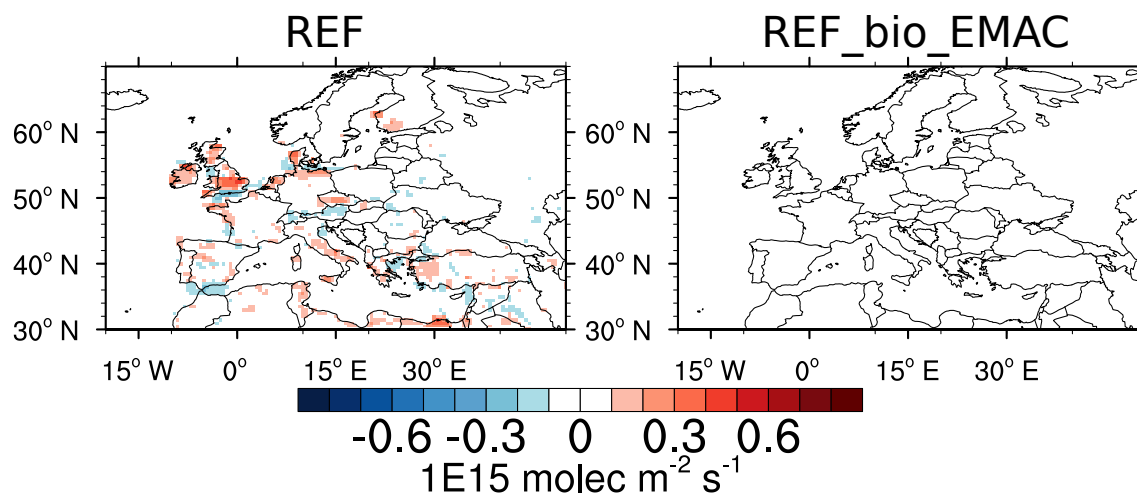


Figure A2: Difference ('CM50 minus EMAC') of the soil-NO_x flux (in 1E15 molec m⁻² s⁻¹) averaged over the period June–August 2008 for the simulation *REF* and *REF_bio_EMAC*.

Table A1: Differences between simulations to investigate the sensitivity to biogenic emissions. Displayed are the scaling factors for soil-NO_x and C₅H₈. Further the resolution of the emissions is given.

simulation	scaling factor soil-NO _x	scaling factor C ₅ H ₈	resolution on-line emissions	identical geographical distribution of emissions in EMAC and CM50
REF	1.0	0.45	0.44° x 0.44°	no
REFc	0.0	0.45	T42	yes
REFg	1.0	0.45	T42	yes
REFh	1.0	0.00	T42	yes
REFk	1.0	0.60	T42	yes
REFl	1.0	0.45	T42	yes
REFT42a	1.0	0.45	T42	yes

transformed during runtime from the coarse EMAC grid onto the CM50 grid using the submodel MMD2WAY. These emissions are treated as 'offline' emissions and are emitted in COSMO by the submodel OFFEMIS.

The total amount of soil-NO_x as simulated by EMAC and CM50 is similar, but the geographical distribution differs. As an example, Fig. A2 shows the difference between the flux of NO_x emissions from soils between CM50 and EMAC for the *REF* simulation and the *REF_bio_EMAC* simulation. While for the *REF* simulation regionally larger differences exist, the differences for the *REF_bio_EMAC* simulation are only small and due to the interpolation.

Further, Table A1 summarises the differences between the simulations with respect to the scaling factors for the emissions, the resolution and the geographical distribution of the emissions.

A.2 Pasing COSMO fields to EMAC for radiation calculations

As has been discussed in Sect. 6.4 COSMO itself does not allow to calculate a radiative forcing of the O_3 field calculated by COSMO. Therefore, the O_3 field calculated by COSMO were passed to EMAC. EMAC then calculated the radiative forcing. The necessary steps are sketched in Fig. A3 and are discussed in more detail next.

First, the O_3 field calculated by COSMO was transformed to the EMAC grid by the submodel MMD2WAY. Hereby only these parts of the field were transformed which are outside the lateral relaxation area or the upper damping zone. This field is only defined on a horizontal and vertical subset of the computational domain of EMAC. Therefore I added an addition to the submodel SCALC (which does simple calculations, Jöckel et al., 2010). The additional operator (called 'SUMGE0') performs the following operation with two (two or three dimensional fields) A and B:

$$\begin{aligned} C &= A + B \text{ for all } A \leq 1 \cdot 10^{-20} \\ C &= A \end{aligned} \tag{A.1}$$

In this case the field transformed from COSMO corresponds to A, while B represents the O_3 climatology used by EMAC for the QCTM mode. Finally, a second diagnostic radiation call is performed (see also Dietmüller et al., 2016) with the field C provided by SCALC. Accordingly, the following sequence of calls of the MESSy submodels is necessary in EMAC: First MMD2WAY must be called, after this SCALC and RAD follow.

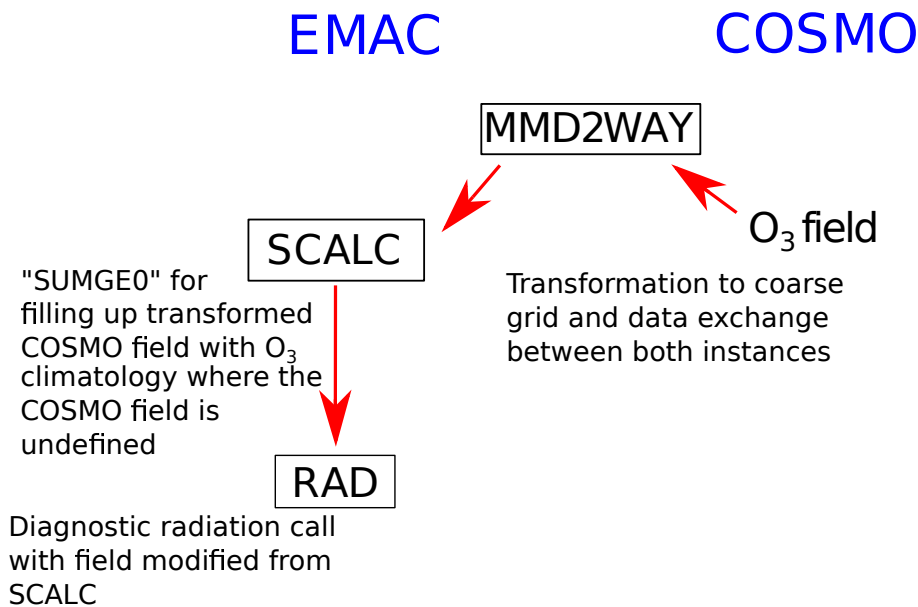


Figure A3: Schematic illustration of the steps and MESSy submodels involved in the calculation of the radiative forcing from the O_3 field calculated by COSMO in EMAC. More details are given in the text.

A.3 Detailed list of used MESSy submodels

The following Table provides a detailed overview of the MESSy submodels applied in the simulation performed for the present thesis.

Table A2: Overview of the submodels running in EMAC and COSMO/MESSy respectively. Both COSMO/MESSy instances use the same submodels. MMD* comprise all MMD submodels.

Submodel	EMAC	COSMO	short description	references
AEROPT	x		calculation of aerosol optical properties	Dietmüller et al. (2016)
AIRSEA	x	x	exchange of tracers between air and sea	Pozzer et al. (2006)
CH4	x		methane oxidation and feedback to hydrological cycle	
CLOUD	x		cloud parametrisation	Roeckner et al. (2006), Jöckel et al. (2006)
CLOUDOPT	x		cloud optical properties	
CONVECT	x		convection parametrisation	Tost et al. (2006b)
CVTRANS	x	x	convective tracer transport	Tost et al. (2010)
DRADON	x	x	emission and decay of ²²² Radon	Jöckel et al. (2010)
DDEP	x	x	dry deposition of aerosols and tracer	Kerkweg et al. (2006a)
E2COSMO	x		additional ECHAM5 fields for COSMO coupling	Kerkweg and Jöckel (2012b)
GWAVE	x		parametrisation of non-orographic gravity waves	Roeckner et al. (2003)
H2O	x		stratospheric water vapour and its feedback	Jöckel et al. (2006)
JVAL	x	x	calculation of photolysis rates	Landgraf and Crutzen (1998), Jöckel et al. (2006)
LNOX	x		NO _x -production by lightning	Tost et al. (2007a), Jöckel et al. (2010)
MECCA	x	x	tropospheric and stratospheric gas-phase chemistry	Sander et al. (2011), Jöckel et al. (2010)
MMD*	x	x	coupling of EMAC and COSMO/MESSy (including libraries and all submodels)	Kerkweg and Jöckel (2012b)
MSBM	x	x	multiphase chemistry of the stratosphere	Jöckel et al. (2010)
O3ORIG	x		ozone origin diagnostics	Grewe (2006)
OFFEMIS	x	x	prescribed emissions of trace gases and aerosols	Kerkweg et al. (2006b)
ONEMIS	x	x	on-line calculated emissions of trace gases and aerosols	Kerkweg et al. (2006b)
ORBIT	x	x	Earth orbit calculations	Dietmüller et al. (2016)

Continued on next page

Table A2 – *Continued from previous page*

Submodel	EMAC	COSMO	short description	references
PTRAC	x	x	definition of prognostic tracers	Jöckel et al. (2008)
QBO	x		Newtonian relaxation of the quasi-biennial oscillation (QBO)	Giorgetta and Bengtsson (1999), Jöckel et al. (2006)
RAD	x		radiative transfer calculations calculation	Dietmüller et al. (2016)
S4D	x	x	diagnostic sampling along predefined tracks	Jöckel et al. (2010)
SATSIMS	x		satellite simulator	
SCALC	x	x	simple calculations	Jöckel et al. (2010)
SCAV	x	x	wet deposition and scavenging of trace gases and aerosols	Tost et al. (2006a)
SCOUT	x	x	diagnostic sampling at predefined locations	Jöckel et al. (2010)
SEDI	x	x	sedimentation of aerosols	Kerkweg et al. (2006a)
SORBIT	x	x	sampling along sun synchronous satellite orbits	Jöckel et al. (2010)
SURFACE	x		surface properties	Jöckel et al. (2016)
TAGGING	x	x	TAGGING of source attributions	Grewe et al. (2016)
TBUDGET	x		contribution of processes to a tracer	Jöckel et al. (2016)
TNUDGE	x	x	Newtonian relaxation of tracers	Kerkweg et al. (2006b)
TREXP	x		emission of tracers at point sources	Jöckel et al. (2010)
TROPOP	x	x	diagnostic calculation of tropopause height and additional diagnostics	Jöckel et al. (2006)
VISO	x	x	sampling on isosurfaces	Jöckel et al. (2010)

A.4 Mechanism of the gas phase chemistry

The following is a document automatically generated when creating the gas phase mechanism using MECCA (Sander et al., 2011). Only the most important parts of the document are shown. The complete document is part of the Supplement provided by (Mertens et al., 2016).

The Chemical Mechanism of MECCA

KPP version: 2.2.1_rs5

MECCA version: 3.7f

Date: April 7, 2015.

Selected reactions:

“(((Tr && (G || Het) && !I) || St) && !Hg)”

Number of aerosol phases: 0

Number of species in selected mechanism:

Gas phase: 164

Aqueous phase: 0

All species: 164

Number of reactions in selected mechanism:

Gas phase (Gnnn): 218

Aqueous phase (Annn): 0

Henry (Hnnn): 0

Photolysis (Jnnn): 68

Aqueous phase photolysis (PHnnn): 0

Heterogeneous (HETnnn): 12

Equilibria (EQnn): 0

Isotope exchange (DGnnn): 0

Dummy (Dnn): 0

All equations: 298

This document is part of the electronic supplement to our article

“The atmospheric chemistry box model CAABA/MECCA-3.0”

in Geosci. Model Dev. (2011), available at:

<http://www.geosci-model-dev.net>

Table 1: Gas phase reactions

#	labels	reaction	rate coefficient	reference
G1000	UpStTrG	$O_2 + O(^1D) \rightarrow O(^3P) + O_2$	$3.3E-11 * EXP(55./temp)$	Sander et al. (2011)
G1001	UpStTrG	$O_2 + O(^3P) \rightarrow O_3$	$6.E-34 * ((temp/300.) ** (-2.4)) * cair$	Sander et al. (2011)
G1002a	UpStG	$O_3 + O(^1D) \rightarrow 2.0 \text{ o3lossxo} + 2.0 \text{ LossO3O} + 2. \text{ LossO3} + 2 \text{ O}_2$	$1.2E-10$	Sander et al. (2011)*
G1003	UpStG	$O_3 + O(^3P) \rightarrow 2.0 \text{ LossO3O} + 2. \text{ LossO3} + 2 \text{ O}_2$	$8.E-12 * EXP(-2060./temp)$	Sander et al. (2011)
G2100	UpStTrG	$H + O_2 \rightarrow HO_2$	$k_3rd(temp, cair, 4.4E-32, 1.3, 7.5E-11, -0.2, 0.6)$	Sander et al. (2011)
G2101	UpStG	$H + O_3 \rightarrow 1.0 \text{ o3lossxo} + \text{LossO3H} + 1. \text{ LossO3} + OH + O_2$	$1.4E-10 * EXP(-470./temp)$	Sander et al. (2011)
G2102	UpStG	$H_2 + O(^1D) \rightarrow 1.0 \text{ o3lossxo} + \text{LossO3H} + 1. \text{ LossO3} + H + OH$	$1.2E-10$	Sander et al. (2011)
G2103	UpStG	$OH + O(^3P) \rightarrow \text{LossO3H} + 1. \text{ LossO3} + H + O_2$	$1.8E-11 * EXP(180./temp)$	Sander et al. (2011)
G2104	UpStTrG	$OH + O_3 \rightarrow 1.0 \text{ o3lossoh} + 1.0 \text{ LossG2104} + \text{LossO3H} + \text{LossOH} + 1. \text{ LossO3} + HO_2 + O_2$	$1.7E-12 * EXP(-940./temp)$	Sander et al. (2011)
G2105	UpStTrG	$OH + H_2 \rightarrow H_2O + H$	$2.8E-12 * EXP(-1800./temp)$	Sander et al. (2011)
G2106	UpStG	$HO_2 + O(^3P) \rightarrow 1.0 \text{ LossG2106} + \text{LossO3H} + 1. \text{ LossO3} + OH + O_2$	$3.E-11 * EXP(200./temp)$	Sander et al. (2011)
G2107	UpStTrG	$HO_2 + O_3 \rightarrow 1.0 \text{ o3lossho2} + 1.0 \text{ LossG2107} + \text{LossO3H} + \text{LossHO2} + 1. \text{ LossO3} + OH + 2 \text{ O}_2$	$1.E-14 * EXP(-490./temp)$	Sander et al. (2011)
G2108a	UpStG	$HO_2 + H \rightarrow 2 \text{ OH}$	$7.2E-11$	Sander et al. (2011)
G2108b	UpStG	$HO_2 + H \rightarrow H_2 + O_2$	$6.9E-12$	Sander et al. (2011)
G2108c	UpStG	$HO_2 + H \rightarrow \text{LossO3Hn} + 1. \text{ ProdO3} + O(^3P) + H_2O$	$1.6E-12$	Sander et al. (2011)
G2109	UpStTrG	$HO_2 + OH \rightarrow \text{lossho2oh} + H_2O + O_2$	$4.8E-11 * EXP(250./temp)$	Sander et al. (2011)
G2110	UpStTrG	$HO_2 + HO_2 \rightarrow \text{ho2lossHO2} + 1.0 \text{ LossG2110} + H_2O_2 + O_2$	k_H02_H02	Christensen et al. (2002), Kircher and Sander (1984)*
G2111	UpStTrG	$H_2O + O(^1D) \rightarrow 1.0 \text{ o3lossxo} + \text{LossO3O} + \text{LossO1D} + 1. \text{ LossO3} + 2 \text{ OH}$	$1.63E-10 * EXP(60./temp)$	Sander et al. (2011)
G2112	UpStTrG	$H_2O_2 + OH \rightarrow H_2O + HO_2$	$1.8E-12$	Sander et al. (2011)
G3100	UpStGN	$N + O_2 \rightarrow \text{LossO3Nn} + 1. \text{ ProdO3} + NO + O(^3P)$	$1.5E-11 * EXP(-3600./temp)$	Sander et al. (2011)
G3101	UpStTrGN	$N_2 + O(^1D) \rightarrow O(^3P) + N_2$	$2.15E-11 * EXP(110./temp)$	Sander et al. (2011)
G3102a	UpStGN	$N_2O + O(^1D) \rightarrow 1.0 \text{ o3lossxo} + \text{noprodN2O} + \text{LossO3O} + 1. \text{ LossO3} + 2 \text{ NO}$	$7.25E-11 * EXP(20./temp)$	Sander et al. (2011)
G3102b	StGN	$N_2O + O(^1D) \rightarrow 1.0 \text{ o3lossxo} + \text{LossO3O} + 1. \text{ LossO3} + N_2 + O_2$	$4.63E-11 * EXP(20./temp)$	Sander et al. (2011)

Table 1: Gas phase reactions (... continued)

#	labels	reaction	rate coefficient	reference
G3103	U _p St _t GN	NO + O ₃ → 1.0 LossG3103 + NO ₂ + O ₂	3.E-12*EXP(-1500./temp)	Sander et al. (2011)
G3104	U _p St _t GN	NO + N → LossO3Nn + 1. ProdO3 + O(³ P) + N ₂	2.1E-11*EXP(100./temp)	Sander et al. (2011)
G3105	U _p St _t GN	NO ₂ + O(³ P) → 1.0 LossG3105 + 2.0 LossO3N2 + 2.0 LossO3N + 2. LossO3 + NO + O ₂	5.1E-12*EXP(210./temp)	Sander et al. (2011)
G3106	St _t GN	NO ₂ + O ₃ → 1.0 LossG3106 + NO ₃ + O ₂	1.2E-13*EXP(-2450./temp)	Sander et al. (2011)
G3107	U _p St _t GN	NO ₂ + N → N ₂ O + O(³ P)	5.8E-12*EXP(220./temp)	Sander et al. (2011)
G3108	St _t GN	NO ₃ + NO → 2 NO ₂	1.5E-11*EXP(170./temp)	Sander et al. (2011)
G3109	U _p St _t GN	NO ₃ + NO ₂ → N ₂ O ₅	k_NO3_NO2	Sander et al. (2011)*
G3110	St _t GN	N ₂ O ₅ → NO ₂ + NO ₃	k_NO3_NO2/(2.7E-27*EXP(11000./temp))	Sander et al. (2011)*
G3200	TrGN	NO + OH → HONO	k_3rd(temp, cair, 7.0E-31, 2.6, 3.6E-11, 0.1, 0.6)	Sander et al. (2011)
G3201	U _p St _t GN	NO + HO ₂ → 1.0 o3prodhO2 + 1.0 LossG3201 + ProdHO2 + 1. ProdO3 + NO ₂ + OH	3.3E-12*EXP(270./temp)	Sander et al. (2011)
G3202	U _p St _t GN	NO ₂ + OH → ohlossNO2 + 1.0 LossG3202 + HNO ₃	k_3rd(temp, cair, 1.8E-30, 3.0, 2.8E-11, 0., 0.6)	Sander et al. (2011)
G3203	St _t GN	NO ₂ + HO ₂ → HNO ₄	k_NO2_HO2	Sander et al. (2011)*
G3204	TrGN	NO ₃ + HO ₂ → 1.0 o3lossno + LossO3N + 1. LossO3 + NO ₂ + OH + O ₂	3.5E-12	Sander et al. (2011)
G3205	TrGN	HONO + OH → 1.0 o3prodhO2 + ohlossNO2 + LossO3Nn + 1. ProdO3 + NO ₂ + H ₂ O	1.8E-11*EXP(-390./temp)	Sander et al. (2011)
G3206	St _t GN	HNO ₃ + OH → 1.0 o3prodhO2 + ohlossNO2 + LossO3Nn + 1. ProdO3 + H ₂ O + NO ₃	k_HNO3_OH	Sander et al. (2011)*
G3207	St _t GN	HNO ₄ → NO ₂ + HO ₂	k_NO2_HO2/(2.1E-27*EXP(10900./temp))	Sander et al. (2011)*
G3208	St _t GN	HNO ₄ + OH → NO ₂ + H ₂ O	1.3E-12*EXP(380./temp)	Sander et al. (2011)
G3209	TrGN	NH ₃ + OH → NH ₂ + H ₂ O	1.7E-12*EXP(-710./temp)	Kohlmann and Poppe (1999)
G3210	TrGN	NH ₂ + O ₃ → 1. LossO3 + NH ₂ O + O ₂	4.3E-12*EXP(-930./temp)	Kohlmann and Poppe (1999)
G3211	TrGN	NH ₂ + HO ₂ → NH ₂ O + OH	4.8E-07*EXP(-628./temp)*temp**(-1.32)	Kohlmann and Poppe (1999)
G3212	TrGN	NH ₂ + HO ₂ → HNO + H ₂ O	9.4E-09*EXP(-356./temp)*temp**(-1.12)	Kohlmann and Poppe (1999)
G3213	TrGN	NH ₂ + NO → HO ₂ + OH + N ₂	1.92E-12*(temp/298.)**(-1.5))	Kohlmann and Poppe (1999)
G3214	TrGN	NH ₂ + NO → N ₂ + H ₂ O	1.41E-11*(temp/298.)**(-1.5))	Kohlmann and Poppe (1999)
G3215	TrGN	NH ₂ + NO ₂ → 1. LossO3 + N ₂ O + H ₂ O	1.2E-11*(temp/298.)**(-2.0))	Kohlmann and Poppe (1999)
G3216	TrGN	NH ₂ + NO ₂ → 1. LossO3 + NH ₂ O + NO	0.8E-11*(temp/298.)**(-2.0))	Kohlmann and Poppe (1999)
G3217	TrGN	NH ₂ O + O ₃ → 1. LossO3 + NH ₂ + O ₂	1.2E-14	Kohlmann and Poppe (1999)
G3218	TrGN	NH ₂ O → NHOH	1.3E3	Kohlmann and Poppe (1999)
G3219	TrGN	HNO + OH → NO + H ₂ O	8.0E-11*EXP(-500./temp)	Kohlmann and Poppe (1999)

Table 1: Gas phase reactions (... continued)

#	labels	reaction	rate coefficient	reference
G3220	TrGN	HNO + NHOH → NH ₂ OH + NO	1.66E-12*EXP(-1500./temp)	Kohlmann and Poppe (1999)
G3221	TrGN	HNO + NO ₂ → 1. LossO3 + HONO + NO	1.0E-12*EXP(-1000./temp)	Kohlmann and Poppe (1999)
G3222	TrGN	NHOH + OH → HNO + H ₂ O	1.66E-12	Kohlmann and Poppe (1999)
G3223	TrGN	NH ₂ OH + OH → NHOH + H ₂ O	4.13E-11*EXP(-2138./temp)	Kohlmann and Poppe (1999)
G3224	TrGN	HNO + O ₂ → HO ₂ + NO	3.65E-14*EXP(-4600./temp)	Kohlmann and Poppe (1999)
G4100	UpStG	CH ₄ + O(¹ D) → 1.0 o3lossxo + 1. LossO3 + .75 CH ₃ O ₂ + .75 OH + .25 HCHO + .4 H + .05 H ₂	1.75E-10	Sander et al. (2011)
G4101	StTrG	CH ₄ + OH → CH ₃ O ₂ + H ₂ O	1.85E-20*EXP(2.82*LOG(temp)-987./temp)	Atkinson (2003)
G4102	TrG	CH ₃ OH + OH → HCHO + HO ₂	2.9E-12*EXP(-345./temp)	Sander et al. (2011)
G4103	StTrG	CH ₃ O ₂ + HO ₂ → ho2loss + CH ₃ OOH + O ₂	4.1E-13*EXP(750./temp)	Sander et al. (2011)*
G4104	UpStTrGN	CH ₃ O ₂ + NO → 1.0 o3prodro2 + noprodro2 + ProdMeO2 + 1. ProdO3 + HCHO + NO ₂ + HO ₂	2.8E-12*EXP(300./temp)	Sander et al. (2011)
G4105	TrGN	CH ₃ O ₂ + NO ₃ → 1.0 o3lossno + LossO3N + 1. LossO3 + HCHO + HO ₂ + NO ₂	1.3E-12	Atkinson et al. (2006)
G4106a	StTrG	CH ₃ O ₂ + CH ₃ O ₂ → 2 HCHO + 2 HO ₂	9.5E-14*EXP(390./temp)/(1.+1./26.2*EXP(1130./temp))	Sander et al. (2011)
G4106b	StTrG	CH ₃ O ₂ + CH ₃ O ₂ → HCHO + CH ₃ OH + O ₂	9.5E-14*EXP(390./temp)/(1.+26.2*EXP(-1130./temp))	Sander et al. (2011)
G4107	StTrG	CH ₃ OOH + OH → .7 CH ₃ O ₂ + .3 HCHO + .3 OH + H ₂ O	k_CH3OOH_OH	Wallington et al.
G4108	StTrG	HCHO + OH → CO + H ₂ O + HO ₂	9.52E-18*EXP(2.03*LOG(temp)+636./temp)	Sivakumaran et al. (2003)
G4109	TrGN	HCHO + NO ₃ → 1.0 o3lossno + LossO3N + 1. LossO3 + HNO ₃ + CO + HO ₂	3.4E-13*EXP(-1900./temp)	Sander et al. (2011)*
G4110	UpStTrG	CO + OH → 1.0 LossG4110 + H + CO ₂	(1.57E-13+cair*3.54E-33)	McCabe et al. (2001)
G4111	TrG	HCOOH + OH → CO ₂ + HO ₂ + H ₂ O	4.0E-13	Sander et al. (2011)
G4200	TrGC	C ₂ H ₆ + OH → C ₂ H ₅ O ₂ + H ₂ O	1.49E-17*temp*temp*EXP(-499./temp)	Atkinson (2003)
G4201	TrGC	C ₂ H ₄ + O ₃ → 1.0 o3lossro + LossO3R + 1. LossO3 + HCHO + .63 CO + .13 HO ₂ + 0.23125 HCOOH + 0.13875 HCHO + 0.13875 H ₂ O ₂ + .13 OH	1.2E-14*EXP(-2630./temp)	Sander et al. (2011)*
G4202	TrGC	C ₂ H ₄ + OH → .6666667 CH ₃ CH(O ₂)CH ₂ OH	k_3rd(temp, cair, 1.0E-28, 4.5, 7.5E-12, 0.85, 0.6)	Sander et al. (2011)
G4203	TrGC	C ₂ H ₅ O ₂ + HO ₂ → C ₂ H ₅ OOH	7.5E-13*EXP(700./temp)	Sander et al. (2011)
G4204	TrGNC	C ₂ H ₅ O ₂ + NO → 1.0 o3prodro2 + ProdRO2 + 1. ProdO3 + CH ₃ CHO + HO ₂ + NO ₂	2.6E-12*EXP(365./temp)	Sander et al. (2011)
G4205	TrGNC	C ₂ H ₅ O ₂ + NO ₃ → 1.0 o3lossno + 1. LossO3 + CH ₃ CHO + HO ₂ + NO ₂	2.3E-12	Wallington et al.

Table 1: Gas phase reactions (... continued)

#	labels	reaction	rate coefficient	reference
G4206	TrGC	$C_2H_5O_2 + CH_3O_2 \rightarrow .75 HCHO + HO_2 + .75 CH_3CHO + .25 CH_3OH$	$1.6E-13*EXP(195./temp)$	see note*
G4207	TrGC	$C_2H_5OOH + OH \rightarrow .3 C_2H_5O_2 + .7 CH_3CHO + .7 OH$	k_CH3OOH_OH	see note*
G4208	TrGC	$CH_3CHO + OH \rightarrow CH_3C(O)OO + H_2O$	$4.4E-12*EXP(365./temp)$	Atkinson et al. (2006)
G4209	TrGNC	$CH_3CHO + NO_3 \rightarrow 1.0 o3lossno + LossO3N + 1. LossO3 + CH_3C(O)OO + HNO_3$	$1.4E-12*EXP(-1900./temp)$	Sander et al. (2011)
G4210	TrGC	$CH_3COOH + OH \rightarrow CH_3O_2 + CO_2 + H_2O$	$4.2E-14*EXP(855./temp)$	Atkinson et al. (2006)
G4211a	TrGC	$CH_3C(O)OO + HO_2 \rightarrow CH_3C(O)OOH$	$4.3E-13*EXP(1040./temp)/(1.+1./37*EXP(660./temp))$	Tyndall et al. (2001)
G4211b	TrGC	$CH_3C(O)OO + HO_2 \rightarrow 1.0 o3prodro2 + 1. ProdO3 + CH_3COOH + O_3$	$4.3E-13*EXP(1040./temp)/(1.+37*EXP(-660./temp))$	Tyndall et al. (2001)
G4212	TrGNC	$CH_3C(O)OO + NO \rightarrow 1.0 o3prodro2 + ProdRO2 + 1. ProdO3 + CH_3O_2 + CO_2 + NO_2$	$8.1E-12*EXP(270./temp)$	Tyndall et al. (2001)
G4213	TrGNC	$CH_3C(O)OO + NO_2 \rightarrow panprod + PAN$	k_CH3CO3_NO2	Sander et al. (2011)*
G4214	TrGNC	$CH_3C(O)OO + NO_3 \rightarrow 1.0 o3lossno + LossO3N + 1. LossO3 + CH_3O_2 + NO_2 + CO_2$	$4.E-12$	Camosa-Mas et al. (1996)
G4215a	TrGC	$CH_3C(O)OO + CH_3O_2 \rightarrow HCHO + HO_2 + CH_3O_2 + CO_2$	$0.9*2.0E-12*EXP(500./temp)$	Sander et al. (2011)
G4215b	TrGC	$CH_3C(O)OO + CH_3O_2 \rightarrow CH_3COOH + HCHO$	$0.1*2.0E-12*EXP(500./temp)$	Sander et al. (2011)
G4216	TrGC	$CH_3C(O)OO + C_2H_5O_2 \rightarrow .82 CH_3O_2 + CH_3CHO + .82 HO_2 + .18 CH_3COOH$	$4.9E-12*EXP(211./temp)$	Wallington et al., Kirchner and Stockwell (1996)
G4217	TrGC	$CH_3C(O)OO + CH_3C(O)OO \rightarrow 2 CH_3O_2 + 2 CO_2 + O_2$	$2.5E-12*EXP(500./temp)$	Tyndall et al. (2001)
G4218	TrGC	$CH_3C(O)OOH + OH \rightarrow CH_3C(O)OO + H_2O$	$0.6*k_CH3OOH_OH$	Rickard and Pascoe (2009)
G4219	TrGNC	$NACA + OH \rightarrow NO_2 + HCHO + CO$	$5.6E-12*EXP(270./temp)$	Pöschl et al. (2000)
G4220	TrGNC	$PAN + OH \rightarrow panloss + HCHO + CO + NO_2 + H_2O$	$9.50E-13*EXP(-650./temp)$	Rickard and Pascoe (2009)
G4221	TrGNC	$PAN \rightarrow panloss + CH_3C(O)OO + NO_2$	k_PAN_M	Sander et al. (2011)*
G4300	TrGC	$C_3H_8 + OH \rightarrow .82 iC_3H_7O_2 + .18 C_2H_5O_2 + H_2O$	$1.65E-17*temp*temp*EXP(-87./temp)$	Atkinson (2003)
G4301	TrGC	$C_3H_6 + O_3 \rightarrow LossO3R + 1. LossO3 + .57 HCHO + .47 CH_3CHO + .33 OH + .26 HO_2 + .07 CH_3O_2 + .06 C_2H_5O_2 + .23 CH_3C(O)OO + .04 MGLYOX + .06 CH_4 + .31 CO + .22 HCOOH + .03 CH_3OH$	$6.5E-15*EXP(-1900./temp)$	Sander et al. (2011)
G4302	TrGC	$C_3H_6 + OH \rightarrow CH_3CH(O_2)CH_2OH$	$k_3rd(temp, cair, 8.E-27, 3.5, 3.E-11, 0., 0.5)$	Wallington et al.
G4303	TrGNC	$C_3H_6 + NO_3 \rightarrow 1.0 o3lossno + 1. LossO3 + LC4H9NO3$	$4.6E-13*EXP(-1155./temp)$	Wallington et al.
G4304	TrGC	$iC_3H_7O_2 + HO_2 \rightarrow iC_3H_7OOH$	k_PrO2_HO2	Atkinson (1997)

Table 1: Gas phase reactions (... continued)

#	labels	reaction	rate coefficient	reference
G4305	TrGNC	$iC_3H_7O_2 + NO \rightarrow 1.0 \text{ } o_3\text{prodho2} + \text{ProdRO2} + 1. \text{ ProdO3}$ $+ .96 \text{ CH}_3\text{COCH}_3 + .96 \text{ HO}_2 + .96 \text{ NO}_2 + .04 \text{ } iC_3H_7ONO_2$	k_PrO2_N0	Wallington et al.
G4306	TrGC	$iC_3H_7O_2 + CH_3O_2 \rightarrow CH_3COCH_3 + .8 \text{ HCHO} + .8 \text{ HO}_2$ $+ .2 \text{ CH}_3OH$	k_PrO2_CH3O2	Kirchner and Stockwell (1996)
G4307	TrGC	$iC_3H_7OOH + OH \rightarrow .3 \text{ } iC_3H_7O_2 + .7 \text{ CH}_3COCH_3 + .7$ OH	k_CH300H_OH	see note*
G4308	TrGC	$CH_3CH(O_2)CH_2OH + HO_2 \rightarrow CH_3CH(OOH)CH_2OH$	6.5E-13*EXP(650./temp)	Müller and Brasseur (1995)
G4309	TrGNC	$CH_3CH(O_2)CH_2OH + NO \rightarrow 1.0 \text{ } o_3\text{prodho2} + \text{ProdRO2}$ $+ 1. \text{ ProdO3} + .98 \text{ CH}_3CHO + .98 \text{ HCHO} + .98 \text{ HO}_2 +$ $.98 \text{ NO}_2 + .02 \text{ LC4H9NO3}$	4.2E-12*EXP(180./temp)	Müller and Brasseur (1995)
G4310	TrGC	$CH_3CH(OOH)CH_2OH + OH \rightarrow .5 \text{ CH}_3CH(O_2)CH_2OH +$ $.5 \text{ CH}_3COCH_2OH + .5 \text{ OH} + \text{H}_2O$	3.8E-12*EXP(200./temp)	Müller and Brasseur (1995)
G4311	TrGC	$CH_3COCH_3 + OH \rightarrow CH_3COCH_2O_2 + \text{H}_2O$	1.33E-13+3.82E-11*EXP(-2000./temp)	Sander et al. (2011)
G4312	TrGC	$CH_3COCH_2O_2 + HO_2 \rightarrow CH_3COCH_2O_2H$	8.6E-13*EXP(700./temp)	Tyndall et al. (2001)
G4313	TrGNC	$CH_3COCH_2O_2 + NO \rightarrow 1.0 \text{ } o_3\text{prodho2} + \text{ProdRO2} + 1. \text{ ProdO3}$ $+ CH_3C(O)OO + HCHO + NO_2$	2.9E-12*EXP(300./temp)	Sander et al. (2011)
G4314	TrGC	$CH_3COCH_2O_2 + CH_3O_2 \rightarrow .5 \text{ MGLYOX} + .5 \text{ CH}_3OH +$ $.3 \text{ CH}_3C(O)OO + .8 \text{ HCHO} + .3 \text{ HO}_2 + .2 \text{ CH}_3COCH_2OH$	7.5E-13*EXP(500./temp)	Tyndall et al. (2001)
G4315	TrGC	$CH_3COCH_2O_2H + OH \rightarrow .3 \text{ CH}_3COCH_2O_2 + .7$ $\text{MGLYOX} + .7 \text{ OH}$	k_CH300H_OH	see note*
G4316	TrGC	$CH_3COCH_2OH + OH \rightarrow \text{MGLYOX} + \text{HO}_2$	2.15E-12*EXP(305./temp)	Dillon et al. (2006)
G4317	TrGC	$\text{MGLYOX} + OH \rightarrow CH_3C(O)OO + CO$	8.4E-13*EXP(830./temp)	Tyndall et al. (1995)
G4320	TrGNC	$iC_3H_7ONO_2 + OH \rightarrow CH_3COCH_3 + NO_2$	6.2E-13*EXP(-230./temp)	Wallington et al.
G4400	TrGC	$nC_4H_{10} + OH \rightarrow LC_4H_9O_2 + H_2O$	1.81E-17*temp*temp*EXP(114./temp)	Atkinson (2003)
G4401	TrGC	$LC_4H_9O_2 + CH_3O_2 \rightarrow .88 \text{ MEK} + .68 \text{ HCHO} + 1.23 \text{ HO}_2$ $+ .12 \text{ CH}_3CHO + .12 \text{ C}_2\text{H}_5O_2 + .18 \text{ CH}_3OH$	k_PrO2_CH3O2	see note*
G4402	TrGC	$LC_4H_9O_2 + HO_2 \rightarrow LC_4H_9OOH$	k_PrO2_HO2	see note*
G4403	TrGNC	$LC_4H_9O_2 + NO \rightarrow 1.0 \text{ } o_3\text{prodho2} + \text{ProdRO2} + 1. \text{ ProdO3}$ $+ .84 \text{ NO}_2 + .56 \text{ MEK} + .56 \text{ HO}_2 + .28 \text{ C}_2\text{H}_5O_2 + .28$ $CH_3CHO + .16 \text{ LC4H9NO3}$	k_PrO2_N0	see note*
G4404	TrGC	$LC_4H_9OOH + OH \rightarrow .15 \text{ LC}_4H_9O_2 + .85 \text{ MEK} + .85 \text{ OH}$ $+ .85 \text{ H}_2O$	k_CH300H_OH	see note*
G4405	TrGC	$\text{MVK} + O_3 \rightarrow 1.0 \text{ } o_3\text{lossro} + \text{LossO3R} + 1. \text{ LossO3} + .45$ $\text{HCOOH} + .9 \text{ MGLYOX} + .1 \text{ CH}_3C(O)OO + .19 \text{ OH} +$ $.22 \text{ CO} + .32 \text{ HO}_2$.5*(1.36E-15*EXP(-2112./temp) +7.51E-16*EXP(-1521./temp))	Pöschl et al. (2000)

Table 1: Gas phase reactions (... continued)

#	labels	reaction	rate coefficient	reference
G4406	TrGC	MVK + OH → MVK ₂	.5*(4.1E-12*EXP(452./temp) + 1.9E-11*EXP(175./temp))	Pöschl et al. (2000)
G4407	TrGC	MVK ₂ + HO ₂ → MVKOOH	1.82E-13*EXP(1300./temp)	Pöschl et al. (2000)
G4408	TrGNC	MVK ₂ + NO → 1.0 o3prod _{ro2} + Prod _{RO2} + 1. Prod _{o3} + NO ₂ + .25 CH ₃ C(O)OO + .25 CH ₃ COCH ₂ OH + .75 HCHO + .25 CO + .75 HO ₂ + .5 MGLYOX	2.54E-12*EXP(360./temp)	Pöschl et al. (2000)
G4409	TrGNC	MVK ₂ + NO ₂ → MPAN	.25*k_3rd(temp, ca1r, 9.7E-29, 5.6, 9.3E-12, 1.5, 0.6)	Pöschl et al. (2000)
G4410	TrGC	MVK ₂ + CH ₃ O ₂ → .5 MGLYOX + .375 CH ₃ COCH ₂ OH + .125 CH ₃ C(O)OO + 1.125 HCHO + .875 HO ₂ + .125 CO + .25 CH ₃ OH	2.E-12	von Kuhlmann (2001)
G4411	TrGC	MVK ₂ + MVK ₂ → CH ₃ COCH ₂ OH + MGLYOX + .5 CO + .5 HCHO + HO ₂	2.E-12	Pöschl et al. (2000)
G4412	TrGC	MVKOOH + OH → MVK ₂	3.E-11	Pöschl et al. (2000)
G4413	TrGC	MEK + OH → LMEKO ₂	1.3E-12*EXP(-25./temp)	Wallington et al.
G4414	TrGC	LMEKO ₂ + HO ₂ → LMEKOOH	k_Pr02_H02	see note*
G4415	TrGNC	LMEKO ₂ + NO → 1.0 o3prod _{ro2} + Prod _{RO2} + 1. Prod _{o3} + .985 CH ₃ CHO + .985 CH ₃ C(O)OO + .985 NO ₂ + .015 LC4H9NO ₃	k_Pr02_NO	see note*
G4416	TrGC	LMEKOOH + OH → .8 BIACET + .8 OH + .2 LMEKO ₂	k_CH300H_OH	see note*
G4417	TrGNC	LC4H9NO ₃ + OH → MEK + NO ₂ + H ₂ O	1.7E-12	Wallington et al.
G4418	TrGNC	MPAN + OH → CH ₃ COCH ₂ OH + NO ₂	3.2E-11	Orlando et al. (2002)
G4419	TrGNC	MPAN → MVK ₂ + NO ₂	k_PAN_M	see note*
G4500	TrGC	C ₅ H ₈ + O ₃ → Loss _{o3R} + 1. Loss _{o3} + .28 HCOOH + .65 MVK + .1 MVK ₂ + .1 CH ₃ C(O)OO + .14 CO + .58 HCHO + .09 H ₂ O ₂ + .08 CH ₃ O ₂ + .25 OH + .25 HO ₂	7.86E-15*EXP(-1913./temp)	Pöschl et al. (2000)
G4501	TrGC	C ₅ H ₈ + OH → ISO ₂	2.54E-11*EXP(410./temp)	Pöschl et al. (2000)
G4502	TrGNC	C ₅ H ₈ + NO ₃ → 1.0 o3loss _{no} + 1. Loss _{o3} + ISON	3.03E-12*EXP(-446./temp)	Pöschl et al. (2000)
G4503	TrGC	ISO ₂ + HO ₂ → ISOOH	2.22E-13*EXP(1300./temp)	Boyd et al. (2003)
G4504	TrGNC	ISO ₂ + NO → 1.0 o3prod _{ro2} + Prod _{RO2} + 1. Prod _{o3} + .956 NO ₂ + .956 MVK + .956 HCHO + .956 HO ₂ + .044 ISON	2.54E-12*EXP(360./temp)	Pöschl et al. (2000)
G4505	TrGC	ISO ₂ + CH ₃ O ₂ → .5 MVK + 1.25 HCHO + HO ₂ + .25 MGLYOX + .25 CH ₃ COCH ₂ OH + .25 CH ₃ OH	2.E-12	von Kuhlmann (2001)
G4506	TrGC	ISO ₂ + ISO ₂ → 2 MVK + HCHO + HO ₂	2.E-12	Pöschl et al. (2000)

Table 1: Gas phase reactions (... continued)

#	labels	reaction	rate coefficient	reference
G4507	TrGC	ISOOH + OH → MVK + OH	1.E-10	Pöschl et al. (2000)
G4508	TrGNC	ISON + OH → CH ₃ COCH ₂ OH + NACA	1.3E-11	Pöschl et al. (2000)
G6100	UpStTrGCl	Cl + O ₃ → ClO + O ₂	2.8E-11*EXP(-250./temp)	Atkinson et al. (2007)
G6101	UpStGCl	ClO + O(³ P) → 2.0 LossO3Cl + 2. LossO3 + Cl + O ₂	2.5E-11*EXP(110./temp)	Atkinson et al. (2007)
G6102a	StTrGCl	ClO + ClO → 2. LossO3 + Cl ₂ + O ₂	1.0E-12*EXP(-1590./temp)	Atkinson et al. (2007)
G6102b	StTrGCl	ClO + ClO → 2. LossO3 + 2 Cl + O ₂	3.0E-11*EXP(-2450./temp)	Atkinson et al. (2007)
G6102c	StTrGCl	ClO + ClO → 1. LossO3 + Cl + OCIO	3.5E-13*EXP(-1370./temp)	Atkinson et al. (2007)
G6102d	StTrGCl	ClO + ClO → Cl ₂ O ₂	k_C1O_C1O	Atkinson et al. (2007)
G6103	StTrGCl	Cl ₂ O ₂ → ClO + ClO	k_C1O_C1O/(1.72E-27*EXP(8649./temp))	Atkinson et al. (2007), Sander et al. (2011)*
G6200	StGCl	Cl + H ₂ → HCl + H	3.9E-11*EXP(-2310./temp)	Atkinson et al. (2007)
G6201a	StGCl	Cl + HO ₂ → HCl + O ₂	4.4E-11-7.5E-11*EXP(-620./temp)	Atkinson et al. (2007)
G6201b	StGCl	Cl + HO ₂ → LossO3Cln + 1. ProdO3 + ClO + OH	7.5E-11*EXP(-620./temp)	Atkinson et al. (2007)
G6202	StTrGCl	Cl + H ₂ O ₂ → HCl + HO ₂	1.1E-11*EXP(-980./temp)	Atkinson et al. (2007)
G6203	StGCl	ClO + OH → LossO3Cl + 1. LossO3 + .94 Cl + .94 HO ₂ + .06 HCl + .06 O ₂	7.3E-12*EXP(300./temp)	Atkinson et al. (2007)
G6204	StTrGCl	ClO + HO ₂ → HOCl + O ₂	2.2E-12*EXP(340./temp)	Atkinson et al. (2007)*
G6205	StTrGCl	HCl + OH → Cl + H ₂ O	1.7E-12*EXP(-230./temp)	Atkinson et al. (2007)
G6206	StGCl	HOCl + OH → ClO + H ₂ O	3.0E-12*EXP(-500./temp)	Sander et al. (2011)
G6300	UpStTrGNCI	ClO + NO → 1.0 LossO3Cl + LossO3Nn + NO ₂ + Cl	6.2E-12*EXP(295./temp)	Atkinson et al. (2007)
G6301	StTrGNCI	ClO + NO ₂ → ClNO ₃	k_3rd_iupac(temp, cair, 1.6E-31, 3.4, 7.E-11, 0., 0.4)	Atkinson et al. (2007)
G6302	TrGNCI	ClNO ₃ → ClO + NO ₂	6.918E-7*EXP(-10909./temp)*cair	Anderson and Fahey (1990)
G6303	StGNCI	ClNO ₃ + O(³ P) → ClO + NO ₃	4.5E-12*EXP(-900./temp)	Atkinson et al. (2007)
G6304	StTrGNCI	ClNO ₃ + Cl → Cl ₂ + NO ₃	6.2E-12*EXP(145./temp)	Atkinson et al. (2007)
G6400	StTrGCl	Cl + CH ₄ → HCl + CH ₃ O ₂	6.6E-12*EXP(-1240./temp)	Atkinson et al. (2006)
G6401	StTrGCl	Cl + HCHO → HCl + CO + HO ₂	8.1E-11*EXP(-34./temp)	Atkinson et al. (2006)
G6402	StTrGCl	Cl + CH ₃ OOH → HCHO + HCl + OH	5.9E-11	Atkinson et al. (2006)*
G6403	StTrGCl	ClO + CH ₃ O ₂ → 1.0 o3lossro + LossO3Cl + 1. LossO3 + HO ₂ + Cl + HCHO	3.3E-12*EXP(-115./temp)	Sander et al. (2011)
G6404	StGCl	CCl ₄ + O(¹ D) → 4.0 ProdLCl + ClO + 3 Cl	3.3E-10	Sander et al. (2011)
G6405	StGCl	CH ₃ Cl + O(¹ D) → 1.0 o3lossxo + 1.0 ProdLCl + LossO3Cl + 1. LossO3 + OH + Cl	1.65E-10	see note*
G6406	StGCl	CH ₃ Cl + OH → 1.0 ProdLCl + H ₂ O + Cl	2.4E-12*EXP(-1250./temp)	Sander et al. (2011)

Table 1: Gas phase reactions (... continued)

#	labels	reaction	rate coefficient	reference
G6407	StGCCl	$\text{CH}_3\text{CCl}_3 + \text{O}(^1\text{D}) \rightarrow 1.0 \text{ o3lossxo} + 3.0 \text{ ProdLCl} + 3.\text{E}-10$		see note*
G6408	StTrGCCl	$\text{LossO3Cl} + 1. \text{ LossO3} + \text{OH} + 3 \text{ Cl}$		
G6409a	TrGCCl	$\text{CH}_3\text{CCl}_3 + \text{OH} \rightarrow 3.0 \text{ ProdLCl} + \text{H}_2\text{O} + 3 \text{ Cl}$ $\text{Cl} + \text{C}_2\text{H}_4 \rightarrow .6666667 \text{ CH}_3\text{CH}(\text{O}_2)\text{CH}_2\text{OH} + \text{HCl}$	$1.64\text{E}-12*\text{EXP}(-1520./\text{temp})$ $k_{3rd_iupac}(\text{temp}, \text{cair}, 1.85\text{E}-29, 3.3,$ $6.0\text{E}-10, 0.0, 0.4)$	Sander et al. (2011) Atkinson et al. (2006)
G6410	TrGCCl	$\text{Cl} + \text{CH}_3\text{CHO} \rightarrow \text{HCl} + \text{CH}_3\text{C}(\text{O})\text{OO}$	$8.0\text{e}-11$	Atkinson et al. (2006)
G6500	StGFCl	$\text{CF}_2\text{Cl}_2 + \text{O}(^1\text{D}) \rightarrow 2.0 \text{ ProdLCl} + \text{ClO} + \text{Cl}$	$1.4\text{E}-10$	Sander et al. (2011)
G6501	StGFCl	$\text{CFCl}_3 + \text{O}(^1\text{D}) \rightarrow 3.0 \text{ ProdLCl} + \text{ClO} + 2 \text{ Cl}$	$2.3\text{E}-10$	Sander et al. (2011)
G7100	StTrGBr	$\text{Br} + \text{O}_3 \rightarrow \text{BrO} + \text{O}_2$	$1.7\text{E}-11*\text{EXP}(-800./\text{temp})$	Atkinson et al. (2007)
G7101	StGBr	$\text{BrO} + \text{O}(^3\text{P}) \rightarrow 2.0 \text{ LossO3Br} + 2. \text{ LossO3} + \text{Br} + \text{O}_2$	$1.9\text{E}-11*\text{EXP}(230./\text{temp})$	Atkinson et al. (2007)
G7102a	StTrGBr	$\text{BrO} + \text{BrO} \rightarrow 2.0 \text{ LossO3Br} + 2. \text{ LossO3} + 2 \text{ Br} + \text{O}_2$	$2.7\text{E}-12$	Atkinson et al. (2007)
G7102b	StTrGBr	$\text{BrO} + \text{BrO} \rightarrow 2.0 \text{ LossO3Br} + 2. \text{ LossO3} + \text{Br}_2 + \text{O}_2$	$2.9\text{E}-14*\text{EXP}(840./\text{temp})$	Atkinson et al. (2007)
G7200	StTrGBr	$\text{Br} + \text{HO}_2 \rightarrow \text{HBr} + \text{O}_2$	$7.7\text{E}-12*\text{EXP}(-450./\text{temp})$	Atkinson et al. (2007)
G7201	StTrGBr	$\text{BrO} + \text{HO}_2 \rightarrow \text{HOBr} + \text{O}_2$	$4.5\text{E}-12*\text{EXP}(500./\text{temp})$	Atkinson et al. (2007)
G7202	StTrGBr	$\text{HBr} + \text{OH} \rightarrow \text{Br} + \text{H}_2\text{O}$	$6.7\text{E}-12*\text{EXP}(155./\text{temp})$	Atkinson et al. (2007)
G7203	StGBr	$\text{HOBr} + \text{O}(^3\text{P}) \rightarrow \text{LossO3Br} + 1. \text{ LossO3} + \text{OH} + \text{BrO}$	$1.2\text{E}-10*\text{EXP}(-430./\text{temp})$	Atkinson et al. (2007)
G7204	StTrGBr	$\text{Br}_2 + \text{OH} \rightarrow 1. \text{ ProdO3} + \text{HOBr} + \text{Br}$	$2.0\text{E}-11*\text{EXP}(240./\text{temp})$	Atkinson et al. (2007)
G7300	TrGNBr	$\text{Br} + \text{BrNO}_3 \rightarrow \text{Br}_2 + \text{NO}_3$	$4.9\text{E}-11$	Orlando and Tyndall (1996)
G7301	StTrGNBr	$\text{BrO} + \text{NO} \rightarrow \text{LossO3Br} + \text{LossO3Nn} + \text{Br} + \text{NO}_2$	$8.7\text{E}-12*\text{EXP}(260./\text{temp})$	Atkinson et al. (2007)
G7302	StTrGNBr	$\text{BrO} + \text{NO}_2 \rightarrow \text{BrNO}_3$	$k_{\text{BrO_NO2}}$	Atkinson et al. (2007)*
G7303	TrGNBr	$\text{BrNO}_3 \rightarrow \text{BrO} + \text{NO}_2$	$k_{\text{BrO_NO2}}/(5.44\text{E}-9*\text{EXP}(14192./\text{temp})$	Orlando and Tyndall (1996),
G7400	StTrGBr	$\text{Br} + \text{HCHO} \rightarrow \text{HBr} + \text{CO} + \text{HO}_2$	$*1.\text{E}6*\text{R_gas*temp}/(\text{atm2Pa*N_A})$	Atkinson et al. (2007)*
G7401	TrGBr	$\text{Br} + \text{CH}_3\text{OOH} \rightarrow \text{CH}_3\text{O}_2 + \text{HBr}$	$7.7\text{E}-12*\text{EXP}(-580./\text{temp})$	Atkinson et al. (2006)
G7402a	TrGBr	$\text{BrO} + \text{CH}_3\text{O}_2 \rightarrow \text{HOBr} + \text{HCHO}$	$2.6\text{E}-12*\text{EXP}(-1600./\text{temp})$	Kondo and Benson (1984)
G7402b	TrGBr	$\text{BrO} + \text{CH}_3\text{O}_2 \rightarrow 1.0 \text{ o3lossro} + \text{LossO3Br} + 1. \text{ LossO3} + \text{Br} + \text{HCHO} + \text{HO}_2$	$\text{G7402a_yield*}5.7\text{E}-12$ $(1.-\text{G7402a_yield})*5.7\text{E}-12$	Aranda et al. (1997) Aranda et al. (1997)
G7403	StTrGBr	$\text{CH}_3\text{Br} + \text{OH} \rightarrow 1.0 \text{ ProdLBr} + \text{H}_2\text{O} + \text{Br}$	$2.35\text{E}-12*\text{EXP}(-1300./\text{temp})$	Sander et al. (2011)
G7404a	TrGCBBr	$\text{Br} + \text{C}_2\text{H}_4 \rightarrow .6666667 \text{ CH}_3\text{CH}(\text{O}_2)\text{CH}_2\text{OH} + \text{HBr}$	$2.8\text{E}-13*\text{EXP}(224./\text{temp})/(1.+$ $1.13\text{E}24*\text{EXP}(-3200./\text{temp}))$	Atkinson et al. (2006)
G7405	TrGCBBr	$\text{Br} + \text{CH}_3\text{CHO} \rightarrow \text{HBr} + \text{CH}_3\text{C}(\text{O})\text{OO}$	$1.8\text{e}-11*\text{EXP}(-460./\text{temp})$	Atkinson et al. (2006)
G7407	TrGBr	$\text{CHBr}_3 + \text{OH} \rightarrow 3.0 \text{ ProdSBr} + \text{H}_2\text{O} + 3 \text{ Br}$	$1.35\text{E}-12*\text{EXP}(-600./\text{temp})$	Sander et al. (2011)*
G7408	TrGBr	$\text{CH}_2\text{Br}_2 + \text{OH} \rightarrow 2.0 \text{ ProdSBr} + \text{H}_2\text{O} + 2 \text{ Br}$	$2.0\text{E}-12*\text{EXP}(-840./\text{temp})$	Sander et al. (2011)*
G7600	TrGCIBr	$\text{Br} + \text{BrCl} \rightarrow \text{Br}_2 + \text{Cl}$	$3.32\text{E}-15$	Manton et al. (2010)
G7601	TrGCIBr	$\text{Br} + \text{Cl}_2 \rightarrow \text{BrCl} + \text{Cl}$	$1.10\text{E}-15$	Dolson and Leone (1987)

Table 1: Gas phase reactions (... continued)

#	labels	reaction	rate coefficient	reference
G7602	TrGCIBr	Br ₂ + Cl → BrCl + Br	2.3E-10*EXP(135./temp)	Bedjanian et al. (1998)
G7603a	StTrGCIBr	BrO + ClO → 1. LossO3 + Br + OCIO	1.6E-12*EXP(430./temp)	Atkinson et al. (2007)
G7603b	StTrGCIBr	BrO + ClO → LossO3Br + LossO3Cl + 2. LossO3 + Br + Cl + O ₂	2.9E-12*EXP(220./temp)	Atkinson et al. (2007)
G7603c	StTrGCIBr	BrO + ClO → LossO3Br + LossO3Cl + 2. LossO3 + BrCl + O ₂	5.8E-13*EXP(170./temp)	Atkinson et al. (2007)
G7604	TrGCIBr	BrCl + Cl → Br + Cl ₂	1.45E-11	Clyne and Cruse (1972)
G7605	TrGCIBr	CHCl ₂ Br + OH → 1.0 ProdSBr + H ₂ O + Br	2.0E-12*EXP(-840./temp)	see note*
G7606	TrGCIBr	CHClBr ₂ + OH → 2.0 ProdSBr + H ₂ O + 2 Br	2.0E-12*EXP(-840./temp)	see note*
G7607	TrGCIBr	CH ₂ ClBr + OH → 1.0 ProdSBr + H ₂ O + Br	2.4E-12*EXP(-920./temp)	Sander et al. (2011)*
G9200	StTrGS	SO ₂ + OH → 1. LossO3 + H ₂ SO ₄ + HO ₂	k_3rd(temp, cair, 3.3E-31, 4.3, 1.6E-12, 0., 0.6)	Sander et al. (2011)
G9400a	TrGS	DMS + OH → CH ₃ SO ₂ + HCHO	1.13E-11*EXP(-253./temp)	Atkinson et al. (2004)*
G9400b	TrGS	DMS + OH → DMSO + HO ₂	k_DMS_OH	Atkinson et al. (2004)*
G9401	TrGNS	DMS + NO ₃ → 1.0 o3lossro + 1. LossO3 + CH ₃ SO ₂ + HNO ₃ + HCHO	1.9E-13*EXP(520./temp)	Atkinson et al. (2004)
G9402	TrGS	DMSO + OH → 0.6 ProdO3 + .6 SO ₂ + HCHO + .6 CH ₃ O ₂ + .4 HO ₂ + .4 CH ₃ SO ₃ H	1.E-10	Hynes and Wine (1996)
G9403	TrGS	CH ₃ SO ₂ → 1. ProdO3 + SO ₂ + CH ₃ O ₂	1.8E13*EXP(-8661./temp)	Barone et al. (1995)
G9404	TrGS	CH ₃ SO ₂ + O ₃ → 1.0 o3lossxo + 1. LossO3 + CH ₃ SO ₃	3.E-13	Barone et al. (1995)
G9405	TrGS	CH ₃ SO ₃ + HO ₂ → CH ₃ SO ₃ H	5.E-11	Barone et al. (1995)
G9600	TrGSCl	DMS + Cl → CH ₃ SO ₂ + HCl + HCHO	3.3E-10	Atkinson et al. (2004)
G9700	TrGSBr	DMS + Br → CH ₃ SO ₂ + HBr + HCHO	9.E-11*EXP(-2386./temp)	Jefferson et al. (1994)
G9701	TrGSBr	DMS + BrO → 1. LossO3 + DMSO + Br	4.4E-13	Ingham et al. (1999)
G01Diag	StTrG	O ₃ (s) → LO ₃ (s)	k_03s	Roelofs and Lelieveld (1997)

General notes

RO₂ self and cross reactions

Three-body reactions

Rate coefficients for three-body reactions are defined via the function `k_3rd(T, M, k0300, n, kinf300, m, fc)`. In the code, the temperature *T* is called `temp` and the concentration of "air molecules" *M* is called `cair`. Using the auxiliary variables *k₀(T)*, *k_{inf}(T)*, and *k_{ratio}*, `k_3rd` is defined as:

$$k_0(T) = k_0^{300} \times \left(\frac{300\text{K}}{T}\right)^n \quad (1)$$

$$k_{\text{inf}}(T) = k_{\text{inf}}^{300} \times \left(\frac{300\text{K}}{T}\right)^m \quad (2)$$

$$k_{\text{ratio}} = \frac{k_0(T)M}{k_{\text{inf}}(T)} \quad (3)$$

$$k_{\text{3rd}} = \frac{k_0(T)M}{1 + k_{\text{ratio}}} \times f_c \left(\frac{1}{1 + (\log_{10}(k_{\text{ratio}}))^2} \right) \quad (4)$$

A similar function, called `k_3rd_inpac` here, is used by T. J. Wallington et al. (2014) for three-body reactions. It has the same function parameters as `k_3rd` and it is defined as:

$$k_0(T) = k_0^{300} \times \left(\frac{300\text{K}}{T}\right)^n \quad (5)$$

$$k_{\text{inf}}(T) = k_{\text{inf}}^{300} \times \left(\frac{300\text{K}}{T}\right)^m \quad (6)$$

$$k_{\text{ratio}} = \frac{k_0(T)M}{k_{\text{inf}}(T)} \quad (7)$$

$$N = 0.75 - 1.27 \times \log_{10}(f_c) \quad (8)$$

$$k_{\text{3rd_inpac}} = \frac{k_0(T)M}{1 + k_{\text{ratio}}} \times f_c \left(\frac{1}{1 + (\log_{10}(k_{\text{ratio}}/N))^2} \right) \quad (9)$$

The self and cross reactions of organic peroxy radicals are treated according to the permutation reaction formalism as implemented in the MCM (Rickard and Pascoe, 2009). Every organic peroxy radical reacts in a pseudo-first-order reaction with a rate constant that is expressed as $k^{\text{1st}} = 2 \times \sqrt{k_{\text{self}}} \times k_{\text{CH3O2}} \times [\text{RO}_2]$ where k_{self} = second-order rate coefficient of the self reaction of the organic peroxy radical, `k_CH3O2` = second-order rate coefficient of the self reaction of CH₃O₂, and [RO₂] = sum of the concentrations of all organic peroxy radicals.

Specific notes

G1002a: The path leading to 2 O(³P) + O₂ results in a null cycle regarding odd oxygen and is neglected.

G2110: The rate coefficient is: `k_HO2_HO2 = (1.5E-12*EXP(19./temp)+1.7E-33*EXP(1000./temp)*cair) * (1+1.4E-21*EXP(2200./temp)*C(ind_H2O))`. The value for the first (pressure-independent) part is from Christensen et al. (2002), the water term from Kircher and Sander (1984).

G3109: The rate coefficient is: `k_NO3_NO2 = k_3rd(temp, cair, 2.E-30, 4.4, 1.4E-12, 0.7, 0.6)`.

G3110: The rate coefficient is defined as backward reaction divided by equilibrium constant.

G3203: The rate coefficient is: `k_NO2_HO2 = k_3rd(temp, cair, 1.8E-31, 3.2, 4.7E-12, 1.4, 0.6)`.

G3206: The rate coefficient is: `k_HNO3_OH = 2.4E-14 * EXP(460./temp) + 1./ (1./ (6.5E-34 * EXP(1335./temp))*cair) + 1./ (2.7E-17 * EXP(2199./temp)))`

G3207: The rate coefficient is defined as backward reaction divided by equilibrium constant.

G4109: Sander et al. (2006) recommend a zero product yield for HCHO.

G4109: The same temperature dependence assumed as for CH₃CHO+NO₃. At 298 K, $k = 5.8 \times 10^{-16}$.

G4201: The product distribution is from Rickard and Pascoe (2009), after substitution of the Chiege intermediate by its decomposition products.

G4206: The product C₂H₅OH, which reacts only with OH, is substituted by its degradation products $\approx 0.1 \text{HOCH}_2\text{CH}_2\text{O}_2 + 0.9 \text{CH}_3\text{CHO} + 0.9 \text{HO}_2$.

G4207: Same value as for G4107

G4213: The rate coefficient is: `k_CH3CO3_NO2 = k_3rd(temp, cair, 9.7E-29, 5.6, 9.3E-12, 1.5, 0.6)`.

G4221: The rate coefficient `isk_PAN_M = k_CH3CO3_NO2/9.E-29*EXP(-14000./temp)`, i.e. the rate coefficient is defined as backward reaction divided by equilibrium constant.

G4307: Same value as for G4107

G4315: Same value as for G4107

G4401: Same value as for G4306

G4402: Same value as for G4304

G4403: Same value as for G4305

G4404: Same value as for G4107

G4414: Same value as for G4304

G4415: Same value as for G4305

G4416: Same value as for G4107

G4419: Same value as for G4221

G6103: The rate coefficient is defined as backward reaction divided by equilibrium constant.

G6204: At low temperatures, there may be a minor reaction channel leading to O₃+HCl. See Finkbenner et al. (1995) for details. It is neglected here.

- G6402: The initial products are probably HCl and CH₂OOH (Atkinson et al., 2006). It is assumed that CH₂OOH dissociates into HCHO and OH.
- G6405: Average of reactions with CH₃Br and CH₃F from Sander et al. (2006) (B. Steil, pers. comm.).
- G6407: Rough extrapolation from reactions with CH₃CF₃, CH₃CClF₂, and CH₃CCl₂F from Sander et al. (2006).
- G7302: The rate coefficient is: $k_{\text{BrO}_2} = k_{\text{3rd}}(\text{temp}, \text{cair}, 5.2\text{E}-31, 3.2, 6.9\text{E}-12, 2.9, 0.6)$.
- G7303: The rate coefficient is defined as backward reaction (Atkinson et al., 2007) divided by equilibrium constant (Orlando and Tyndall, 1996).
- G7407: It is assumed that the reaction liberates all Br atoms. The fate of the carbon atom is currently not considered.
- G7408: It is assumed that the reaction liberates all Br atoms. The fate of the carbon atom is currently not considered.
- G6402: The initial products are probably HCl and CH₂OOH (Atkinson et al., 2006). It is assumed that CH₂OOH dissociates into HCHO and OH.
- G6405: Average of reactions with CH₃Br and CH₃F from Sander et al. (2006) (B. Steil, pers. comm.).
- G6407: Rough extrapolation from reactions with CH₃CF₃, CH₃CClF₂, and CH₃CCl₂F from Sander et al. (2006).
- G7302: The rate coefficient is: $k_{\text{BrO}_2} = k_{\text{3rd}}(\text{temp}, \text{cair}, 5.2\text{E}-31, 3.2, 6.9\text{E}-12, 2.9, 0.6)$.
- G7303: The rate coefficient is defined as backward reaction (Atkinson et al., 2007) divided by equilibrium constant (Orlando and Tyndall, 1996).
- G7407: It is assumed that the reaction liberates all Br atoms. The fate of the carbon atom is currently not considered.
- G7408: It is assumed that the reaction liberates all Br atoms. The fate of the carbon atom is currently not considered.
- considered.
- G7605: Same value as for G7408: CH₂Br₂+OH assumed. It is assumed that the reaction liberates all Br atoms but not Cl. The fate of the carbon atom is currently not considered.
- G7606: Same value as for G7408: CH₂Br₂+OH assumed. It is assumed that the reaction liberates all Br atoms but not Cl. The fate of the carbon atom is currently not considered.
- G7607: It is assumed that the reaction liberates all Br atoms but not Cl. The fate of the carbon atom is currently not considered.
- G9400a: For the abstraction path, the assumed reaction sequence (omitting H₂O and O₂ as products) according to Yin et al. (1990) is:
- $$\begin{array}{l} \text{DMS} + \text{OH} \rightarrow \text{CH}_3\text{SCH}_2 \\ \text{CH}_3\text{SCH}_2 + \text{O}_2 \rightarrow \text{CH}_3\text{SCH}_2\text{OO} \end{array}$$
- G9400b: For the addition path, the rate coefficient is: $k_{\text{DMS_OH}} = 1.0\text{E}-39 \cdot \text{EXP}(5820./\text{temp}) \cdot \text{C}(\text{ind_O2}) / (1.+5.0\text{E}-30 \cdot \text{EXP}(6280./\text{temp}) \cdot \text{C}(\text{ind_O2}))$.
- $$\begin{array}{l} \text{CH}_3\text{SCH}_2\text{OO} + \text{NO} \rightarrow \text{CH}_3\text{SCH}_2\text{O} + \text{NO}_2 \\ \text{CH}_3\text{SCH}_2\text{O} \rightarrow \text{CH}_3\text{S} + \text{HCHO} \\ \text{CH}_3\text{S} + \text{O}_3 \rightarrow \text{CH}_3\text{SO} \\ \text{CH}_3\text{SO} + \text{O}_3 \rightarrow \text{CH}_3\text{SO}_2 \\ \text{DMS} + \text{OH} + \text{NO} + 2\text{O}_3 \rightarrow \text{CH}_3\text{SO}_2 + \text{HCHO} + \text{NO}_2 \end{array}$$
- Neglecting the effect on O₃ and NO_x, the remaining reaction is:
- $$\text{DMS} + \text{OH} + \text{O}_3 \rightarrow \text{CH}_3\text{SO}_2 + \text{HCHO}$$

Table 2: Photolysis reactions

#	labels	reaction	rate coefficient	reference
J1000a	UpStTrGJ	$O_2 + h\nu \rightarrow o3prodO2 + 2. ProdO3 + O(^3P) + O(^3P)$	$jx(1p_02)$	Sander et al. (2014)
J1001a	UpStTrGJ	$O_3 + h\nu \rightarrow O(^1D) + O_2$	$jx(1p_01D)$	Sander et al. (2014)
J1001b	UpStTrGJ	$O_3 + h\nu \rightarrow O(^3P) + O_2$	$jx(1p_03P)$	Sander et al. (2014)
J2100a	UpStGJ	$H_2O + h\nu \rightarrow H + OH$	$jx(1p_H2O)$	Sander et al. (2014)
J2101	UpStTrGJ	$H_2O_2 + h\nu \rightarrow 2 OH$	$jx(1p_H2O2)$	Sander et al. (2014)
J3100	UpStGNJ	$N_2O + h\nu \rightarrow 1.0 o3prodho2 + 1. ProdO3 + O(^1D) + N_2$	$jx(1p_N2O)$	Sander et al. (2014)
J3101	UpStTrGNJ	$NO_2 + h\nu \rightarrow 1.0 LossJ3101 + NO + O(^3P)$	$jx(1p_NO2)$	Sander et al. (2014)
J3102a	UpStGNJ	$NO + h\nu \rightarrow 1. ProdO3 + N + O(^3P)$	$jx(1p_NO)$	Sander et al. (2014)
J3103a	UpStTrGNJ	$NO_3 + h\nu \rightarrow 1.0 LossJ3103a + NO_2 + O(^3P)$	$jx(1p_NO2O)$	Sander et al. (2014)
J3103b	UpStTrGNJ	$NO_3 + h\nu \rightarrow 2.0 LossO3N + 2. LossO3 + NO + O_2$	$jx(1p_NO02)$	Sander et al. (2014)
J3104	StTrGNJ	$N_2O_5 + h\nu \rightarrow NO_2 + NO_3$	$jx(1p_N2O5)$	Sander et al. (2014)
J3200	TrGNJ	$HONO + h\nu \rightarrow NO + OH$	$jx(1p_HONO)$	Sander et al. (2014)
J3201	StTrGNJ	$HNO_3 + h\nu \rightarrow NO_2 + OH$	$jx(1p_HNO3)$	Sander et al. (2014)
J3202	StTrGNJ	$HNO_4 + h\nu \rightarrow 0.333 o3prodho2 + 0.333 ProdO3 + .667 NO_2 + .667 HO_2 + .333 NO_3 + .333 OH$	$jx(1p_HNO4)$	Sander et al. (2014)
J4100	StTrGJ	$CH_3OOH + h\nu \rightarrow HCHO + OH + HO_2$	$jx(1p_CH3OOH)$	Sander et al. (2014)
J4101a	StTrGJ	$HCHO + h\nu \rightarrow H_2 + CO$	$jx(1p_CHO2)$	Sander et al. (2014)
J4101b	StTrGJ	$HCHO + h\nu \rightarrow H + CO + HO_2$	$jx(1p_CHOH)$	Sander et al. (2014)
J4102	StGJ	$CO_2 + h\nu \rightarrow 1. ProdO3 + CO + O(^3P)$	$jx(1p_CO2)$	Sander et al. (2014)
J4103	StGJ	$CH_4 + h\nu \rightarrow CO + 0.31 H + 0.69 H_2 + 1.155 H_2O$	$jx(1p_CH4)$	Sander et al. (2014)
J4200	TrGCJ	$C_2H_5OOH + h\nu \rightarrow CH_3CHO + HO_2 + OH$	$jx(1p_CH3OOH)$	von Kuhlmann (2001)
J4201	TrGCJ	$CH_3CHO + h\nu \rightarrow CH_3O_2 + HO_2 + CO$	$jx(1p_CH3CHO)$	Sander et al. (2014)
J4202	TrGCJ	$CH_3C(O)OOH + h\nu \rightarrow CH_3O_2 + OH + CO_2$	$jx(1p_CH3CO3H)$	Sander et al. (2014)
J4203	TrGNCGJ	$NACA + h\nu \rightarrow NO_2 + HCHO + CO$	$0.19*jx(1p_CHOH)$	von Kuhlmann (2001)
J4204	TrGNCGJ	$PAN + h\nu \rightarrow CH_3C(O)OO + NO_2$	$jx(1p_PAN)$	Sander et al. (2014)
J4300	TrGCJ	$iC_3H_7OOH + h\nu \rightarrow CH_3COCH_3 + HO_2 + OH$	$jx(1p_CH3OOH)$	von Kuhlmann (2001)
J4301	TrGCJ	$CH_3COCH_3 + h\nu \rightarrow CH_3C(O)OO + CH_3O_2$	$jx(1p_CH3CO3H)$	Sander et al. (2014)
J4302	TrGCJ	$CH_3COCH_2OH + h\nu \rightarrow CH_3C(O)OO + HCHO + HO_2$	$0.074*jx(1p_CHOH)$	see note*
J4303	TrGCJ	$MGLYOX + h\nu \rightarrow CH_3C(O)OO + CO + HO_2$	$jx(1p_MGLYOX)$	Sander et al. (2014)
J4304	TrGCJ	$CH_3COCH_2O_2H + h\nu \rightarrow CH_3C(O)OO + HCHO + OH$	$jx(1p_CH3OOH)$	see note*
J4306	TrGNCGJ	$iC_3H_7ONONO_2 + h\nu \rightarrow CH_3COCH_3 + NO_2 + HO_2$	$3.7*jx(1p_PAN)$	von Kuhlmann et al. (2003)*
J4400	TrGCJ	$LC_4H_6OOH + h\nu \rightarrow OH + .67 MEK + .67 HO_2 + .33 C_2H_5O_2 + .33 CH_3CHO$	$jx(1p_CH3OOH)$	Rickard and Pascoe (2009)

Table 2: Photolysis reactions (... continued)

#	labels	reaction	rate coefficient	reference
J4401	TrGCJ	MVK + hν → CH ₃ C(O)OO + HCHO + CO + HO ₂	0.019*jx(ip_COH2)+.015*jx(ip_MGLYOX)	Sander et al. (2014)
J4402	TrGCJ	MVKOOH + hν → OH + .5 MGLYOX + .25 CH ₃ COCH ₂ OH + .75 HCHO + .75 HO ₂ + .25 CH ₃ C(O)OO + .25 CO	jx(ip_CH3OOH)	see note*
J4403	TrGCJ	MEK + hν → CH ₃ C(O)OO + C ₂ H ₅ O ₂	0.42*jx(ip_CHOH)	von Kuhlmann et al. (2003)
J4404	TrGCJ	LMEKOOH + hν → CH ₃ C(O)OO + CH ₃ CHO + OH	jx(ip_CH3OOH)	Rickard and Pascoe (2009)
J4405	TrGCJ	BIACET + hν → 2 CH ₃ C(O)OO	2.15*jx(ip_MGLYOX)	see note*
J4406	TrGNCLJ	LC4H9NO ₃ + hν → NO ₂ + .67 MEK + .67 HO ₂ + .33 C ₂ H ₅ O ₂ + .33 CH ₃ CHO	3.7*jx(ip_PAN)	von Kuhlmann (2001)
J4407	TrGNCLJ	MPAN + hν → CH ₃ COCCH ₂ OH + NO ₂	jx(ip_PAN)	see note*
J4500	TrGCJ	ISOOH + hν → MVK + HCHO + HO ₂ + OH	jx(ip_CH3OOH)	see note*
J4501	TrGNCLJ	ISON + hν → MVK + HCHO + NO ₂ + HO ₂	3.7*jx(ip_PAN)	von Kuhlmann (2001)
J6000	StTrGCLJ	Cl ₂ + hν → Cl + Cl	jx(ip_Cl2)	Sander et al. (2014)
J6100	StTrGCLJ	Cl ₂ O ₂ + hν → 2. LossO3 + 2 Cl	jx(ip_Cl2O2)	Sander et al. (2014)
J6101	StTrGCLJ	OCIO + hν → 1. ProdO3 + ClO + O(³ P)	jx(ip_OC10)	Sander et al. (2014)
J6200	StGCLJ	HCl + hν → Cl + H	jx(ip_HCl)	Sander et al. (2014)
J6201	StTrGCLJ	HOCl + hν → LossO3Cl + 1. LossO3 + OH + Cl	jx(ip_HOCl)	Sander et al. (2014)
J6300	TrGNCLJ	ClNO ₂ + hν → 1. ProdO3 + Cl + NO ₂	jx(ip_ClNO2)	Sander et al. (2014)
J6301a	StTrGNCLJ	ClNO ₃ + hν → Cl + NO ₃	jx(ip_ClNO3)	Sander et al. (2014)
J6301b	StTrGNCLJ	ClNO ₃ + hν → ClO + NO ₂	jx(ip_ClNO2)	Sander et al. (2014)
J6400	StGCLJ	CH ₃ Cl + hν → 1.0 ProdLCl + Cl + CH ₃ O ₂	jx(ip_CH3Cl)	Sander et al. (2014)
J6401	StGCLJ	CCl ₄ + hν → 4.0 ProdLCl + 4 Cl	jx(ip_CCl4)	Sander et al. (2014)
J6402	StGCLJ	CH ₃ CCl ₃ + hν → 3.0 ProdLCl + 3 Cl	jx(ip_CH3CCl3)	Sander et al. (2014)
J6500	StGFCLJ	CFCl ₃ + hν → 3.0 ProdLCl + 3 Cl	jx(ip_CFCl3)	Sander et al. (2014)
J6501	StGFCLJ	CF ₂ Cl ₂ + hν → 2.0 ProdLCl + 2 Cl	jx(ip_CF2Cl2)	Sander et al. (2014)
J7000	StTrGBrJ	Br ₂ + hν → Br + Br	jx(ip_Br2)	Sander et al. (2014)
J7100	StTrGBrJ	BrO + hν → Br + O(³ P)	jx(ip_BrO)	Sander et al. (2014)
J7200	StTrGBrJ	HOBr + hν → LossO3Br + 1. LossO3 + Br + OH	jx(ip_HOBr)	Sander et al. (2014)
J7300	TrGNBrJ	BrNO ₂ + hν → 1. ProdO3 + Br + NO ₂	jx(ip_BrNO2)	Sander et al. (2014)
J7301	StTrGNBrJ	BrNO ₃ + hν → 0.85 Br + 0.85 NO ₃ + 0.15 BrO + 0.15 NO ₂	jx(ip_BrNO3)	Sander et al. (2014)*
J7400	StGBrJ	CH ₃ Br + hν → 1.0 ProdLBr + Br + CH ₃ O ₂	jx(ip_CH3Br)	Sander et al. (2014)
J7401	TrGBrJ	CH ₂ Br ₂ + hν → 2.0 ProdSBr + 2 Br	jx(ip_CH2Br2)	Sander et al. (2014)
J7402	TrGBrJ	CHBr ₃ + hν → 3.0 ProdSBr + 3 Br	jx(ip_CHBr3)	Sander et al. (2014)
J7500	StGFBrJ	CF ₃ Br + hν → 1.0 ProdLBr + Br	jx(ip_CF3Br)	Sander et al. (2014)

Table 2: Photolysis reactions (... continued)

#	labels	reaction	rate coefficient	reference
J7600	StTtGCIBr-J	BrCl + h ν \rightarrow Br + Cl	jx(ip_BrCl)	Sander et al. (2014)
J7601	StGFBt-J	CF ₂ CIBr + h ν \rightarrow 1.0 ProdlBr + 1.0 ProdlCl + Br + Cl	jx(ip_CF2ClBr)	Sander et al. (2014)
J7602	TtGCIBr-J	CH ₂ CIBr + h ν \rightarrow 1.0 ProdsBr + 1.0 ProdlCl + Br + Cl	jx(ip_CH2ClBr)	Sander et al. (2014)
J7603	TtGCIBr-J	CHCl ₂ Br + h ν \rightarrow 1.0 ProdsBr + 2.0 ProdlCl + Br + 2 Cl	jx(ip_CHCl2Br)	Sander et al. (2014)
J7604	TtGCIBr-J	CHCIBr ₂ + h ν \rightarrow 2.0 ProdsBr + 1.0 ProdlCl + 2 Br + Cl	jx(ip_CHClBr2)	Sander et al. (2014)
J8401a	TtGJ	CH ₃ I + h ν \rightarrow CH ₃ O ₂	Jx(ip_CH3I)	Sander et al. (2014)

General notes

J-values are calculated with an external module (e.g., JVAL) and then supplied to the MECCA chemistry.

Values that originate from the Master Chemical Mechanism (MCM) by Rickard and Pascoe (2009) are translated according in the following way:

J(11) \rightarrow jx(ip_COH2)
 J(12) \rightarrow jx(ip_CHOH)
 J(15) \rightarrow jx(ip_HOCH2CHO)
 J(18) \rightarrow jx(ip_MACR)
 J(22) \rightarrow jx(ip_ACETOL)
 J(23)+J(24) \rightarrow jx(ip_MVK)
 J(31)+J(32)+J(33) \rightarrow jx(ip_GLYOX)
 J(34) \rightarrow jx(ip_MGLYOX)

J(41) \rightarrow jx(ip_CH3OOH)
 J(53) \rightarrow J(iC₃H₇ONO₂)
 J(54) \rightarrow J(iC₃H₇ONO₂)
 J(55) \rightarrow J(iC₃H₇ONO₂)
 J(56)+J(57) \rightarrow jx(ip_MOA)

Specific notes

J4302: It is assumed that J(CH₃COCH₂OH) is 0.074 times that of J4101b.
 J4304: It is assumed that J(CH₃COCH₂O₂H) is the same as J(CH₃OOH).
 J4306: Following von Kuhlmann et al. (2003), we use J(iC₃H₇ONO₂) = 3.7*jx(ip_PAN).

J4402: It is assumed that J(MVKOOH) is the same as J(CH₃OOH).

J4405: It is assumed that J(BIACET) is 2.15 times larger than J(MGLYOX), consistent with the photolysis rate coefficients used in the MCM (Rickard and Pascoe, 2009).

J4407: It is assumed that J(MPAN) is the same as J(PAN).

J4500: It is assumed that J(ISSOOH) is the same as J(CH₃OOH).

J7301: The quantum yields are recommended by Sander et al. (2011) for $\lambda > 300$ nm and used here for the entire spectrum.

Table 3: Henry's law coefficients

substance	$\frac{k_H^\ominus}{M/atm}$	$\frac{-\Delta_{soln}H/R}{K}$	reference
O ₂	1.3×10^{-3}	1500.	Wilhelm et al. (1977)
O ₃	1.2×10^{-2}	2560.	Chameides (1984)
OH	3.0×10^1	4300.	Hanson et al. (1992)
HO ₂	3.9×10^3	5900.	Hanson et al. (1992)
H ₂ O ₂	$1. \times 10^5$	6338.	Lind and Kok (1994)
H ₂ O	BIG	0.	see note
NH ₃	58.	4085.	Chameides (1984)
NO	1.9×10^{-3}	1480.	Schwartz and White (1981)
NO ₂	7.0×10^{-3}	2500.	Lee and Schwartz (1981)*
NO ₃	2.	2000.	Thomas et al. (1993)
N ₂ O ₅	BIG	0.	see note
HONO	4.9×10^1	4780.	Schwartz and White (1981)
HNO ₃	$2.45 \times 10^6 / 1.5 \times 10^1$	8694.	Brimblecombe and Clegg (1989)*
HNO ₄	1.2×10^4	6900.	Régimbal and Mozurkewich (1997)
CH ₃ OH	2.20×10^2	5200.	Snider and Dawson (1985)
CH ₃ O ₂	6.	5600.	Jacob (1986)*
CH ₃ OOH	3.0×10^2	5322.	Lind and Kok (1994)
CO ₂	3.1×10^{-2}	2423.	Chameides (1984)
HCHO	7.0×10^3	6425.	Chameides (1984)
HCOOH	3.7×10^3	5700.	Chameides (1984)
CH ₃ COOH	4.1×10^3	6200.	Sander et al. (2006)
PAN	2.8	5730.	Sander et al. (2006)
C ₂ H ₅ O ₂	6.	5600.	see note
CH ₃ CHO	1.29×10^1	5890.	Sander et al. (2006)
CH ₃ COCH ₃	28.1	5050.	Sander et al. (2006)
MGLYOX	3.70×10^3	7500.	Berterton and Hoffmann (1988)
Cl ₂	9.2×10^{-2}	2081.	Bartlett and Margerum (1999)
HCl	2./1.7	9001.	Brimblecombe and Clegg (1989)
HOCl	6.7×10^2	5862.	Huthwelker et al. (1995)
ClNO ₃	BIG	0.	see note
Br ₂	7.7×10^{-1}	3837.	Bartlett and Margerum (1999)
HBr	1.3	10239.	Brimblecombe and Clegg (1989)*
HOBr	9.3×10^1	5862.	Vogt et al. (1996)*

Table 3: Henry's law coefficients (... continued)

substance	$\frac{k_{\text{H}}^{\ominus}}{\text{M/atm}}$	$\frac{-\Delta_{\text{soln}}H/R}{\text{K}}$	reference
Br-NO ₃	BIG	0.	see note
Br-Cl	9.4×10^{-1}	5600.	Bartlett and Margerum (1999)
SO ₂	1.2	3120.	Chameides (1984)
H ₂ SO ₄	$1. \times 10^{11}$	0.	see note
CH ₃ SO ₃ H	BIG	0.	see note
DMS	5.4×10^{-1}	3500.	Staudinger and Roberts (2001)
DMSO	$5. \times 10^4$	6425.	De Bruyn et al. (1994)*

General notes

The value "BIG" corresponds to virtually infinite solubility which is represented in the model using a very large but arbitrary number.

The temperature dependence of the Henry constants is:

$$K_{\text{H}} = K_{\text{H}}^{\ominus} \times \exp\left(\frac{-\Delta_{\text{soln}}H}{R} \left(\frac{1}{T} - \frac{1}{T^{\ominus}}\right)\right)$$

where $\Delta_{\text{soln}}H$ = molar enthalpy of dissolution [J/mol] and $R = 8.314 \text{ J}/(\text{mol K})$.

Specific notes

NO₂: The temperature dependence is from Chameides (1984).

HNO₃: Calculated using the acidity constant from Davis and de Bruin (1964).

CH₃O₂: This value was estimated by Jacob (1986).
C₂H₅O₂: Assumed to be the same as $K_{\text{H}}(\text{CH}_3\text{O}_2)$.

HBr: Calculated using the acidity constant from Lax (1969).

HOBr: This value was estimated by Vogt et al. (1996).

H₂SO₄: To account for the very high Henry's law coefficient of H₂SO₄, a very high value was chosen arbitrarily.

DMSO: Lower limit cited from another reference.

Table 4: Accommodation coefficients

substance	α^{\ominus}	$\frac{-\Delta_{\text{obs}}H/R}{K}$	reference
O ₂	0.01	2000.	see note
O ₃	0.002	(default)	DeMore et al. (1997)*
OH	0.01	(default)	Takami et al. (1998)*
HO ₂	0.5	(default)	Thornton and Abbatt (2005)
H ₂ O ₂	0.077	3127.	Worsnop et al. (1989)
H ₂ O	0.0	(default)	see note
NH ₃	0.06	(default)	DeMore et al. (1997)*
NO	5.0×10^{-5}	(default)	Saastad et al. (1993)*
NO ₂	0.0015	(default)	Ponche et al. (1993)*
NO ₃	0.04	(default)	Rudich et al. (1996)*
N ₂ O ₅	(default)	(default)	DeMore et al. (1997)*
HONO	0.04	(default)	DeMore et al. (1997)*
HNO ₃	0.5	(default)	Abbatt and Waschewsky (1998)*
HNO ₄	(default)	(default)	DeMore et al. (1997)*
CH ₃ OH	(default)	(default)	see note
CH ₃ O ₂	0.01	2000.	see note
CH ₃ OOH	0.0046	3273.	Magi et al. (1997)
CO ₂	0.01	2000.	see note
HCHO	0.04	(default)	DeMore et al. (1997)*
HCOOH	0.014	3978.	DeMore et al. (1997)
CH ₃ COOH	2.0×10^{-2}	4079.	Davidovits et al. (1995)
PAN	(default)	(default)	see note
C ₂ H ₅ O ₂	(default)	(default)	see note
CH ₃ CHO	3.0×10^{-2}	(default)	see note
CH ₃ COCH ₃	3.72×10^{-3}	6395.	Davidovits et al. (1995)
MGLYOX	(default)	(default)	see note
Cl ₂	0.038	6546.	Hu et al. (1995)
HCl	0.074	3072.	Schweitzer et al. (2000)*
HOCl	0.5	(default)	see note
ClNO ₃	0.108	(default)	Deiber et al. (2004)*
Br ₂	0.038	6546.	Hu et al. (1995)
HBr	0.032	3940.	Schweitzer et al. (2000)*
HOBr	0.5	(default)	Abbatt and Waschewsky (1998)*
BrNO ₃	0.063	(default)	Deiber et al. (2004)*

Table 4: Accommodation coefficients (... continued)

substance	α^\ominus	$-\frac{\Delta_{\text{obs}}H/R}{K}$	reference
BrCl	0.038	6546.	see note
SO ₂	0.11	(default)	DeMore et al. (1997)
H ₂ SO ₄	0.65	(default)	Pöschl et al. (1998)*
CH ₃ SO ₃ H	0.076	1762.	De Brryn et al. (1994)
DMS	(default)	(default)	see note
DMSO	0.048	2578.	De Brryn et al. (1994)

General notes

If no data are available, the following default values are used:

$$\alpha^\ominus = 0.1$$

$$-\Delta_{\text{obs}}H/R = 0 \text{ K}$$

The temperature dependence of the accommodation coefficients is given by (Jayne et al., 1991):

$$\frac{\alpha}{1-\alpha} = \exp\left(\frac{-\Delta_{\text{obs}}G}{RT}\right)$$

$$= \exp\left(\frac{-\Delta_{\text{obs}}H}{RT} + \frac{\Delta_{\text{obs}}S}{R}\right)$$

where $\Delta_{\text{obs}}G$ is the Gibbs free energy barrier of the transition state toward solution (Jayne et al., 1991), and $\Delta_{\text{obs}}H$ and $\Delta_{\text{obs}}S$ are the corresponding enthalpy and entropy, respectively. The equation can be rearranged to:

$$\ln\left(\frac{\alpha}{1-\alpha}\right) = \frac{-\Delta_{\text{obs}}H}{R} \times \frac{1}{T} + \frac{-\Delta_{\text{obs}}S}{R}$$

and further:

$$d \ln\left(\frac{\alpha}{1-\alpha}\right) / d\left(\frac{1}{T}\right) = \frac{-\Delta_{\text{obs}}H}{R}$$

Specific notes

O₂: Estimate.

O₃: Value measured at 292 K.

OH: Value measured at 293 K.

NH₃: Value measured at 295 K.

NO: Value measured between 193 and 243 K.

NO₂: Value measured at 298 K.

NO₃: Value is a lower limit, measured at 273 K.

N₂O₅: Value for sulfuric acid, measured between 195 and 300 K.

HONO: Value measured between 247 and 297 K.

HNO₃: Value measured at room temperature. Abbatt and Waschewsky (1998) say $\gamma > 0.2$. Here $\alpha = 0.5$ is used.

HNO₄: Value measured at 200 K for water ice.

CH₃O₂: Estimate.

CO₂: Estimate.

HCHO: Value measured between 260 and 270 K.

PAN: Estimate.

C₂H₅O₂: Estimate.

CH₃CHO: Using the same estimate as in the CAPRAM 2.4 model (http://projects.tropos.de/capram/capram_24.html).

HCl: Temperature dependence derived from published data at 2 different temperatures

HOCl: Assumed to be the same as $\alpha(\text{HOBr})$.

ClNO₃: Value measured at 274.5 K.

HBr: Temperature dependence derived from published data at 2 different temperatures

HOBr: Value measured at room temperature. Abbatt and Waschewsky (1998) say $\gamma > 0.2$. Here $\alpha = 0.5$ is used.

BrNO₃: Value measured at 273 K.

BrCl: Assumed to be the same as $\alpha(\text{Cl}_2)$.

H₂SO₄: Value measured at 303 K.

Table 5: Reversible (Henry’s law) equilibria and irreversible (“heterogenous”) uptake

#	labels	reaction	rate coefficient	reference
---	--------	----------	------------------	-----------

General notes

The forward (`k_exf`) and backward (`k_extb`) rate coefficients are calculated in the file `messy_mecca_aero.f90` using the accommodation coefficients in subroutine `mecca_aero_alpha` and Henry’s law constants in subroutine `mecca_aero_henry`.

For uptake of X ($X = N_2O_5, ClNO_3, \text{ or } BrNO_3$) and

subsequent reaction with $H_2O, Cl^-, \text{ and } Br^-$ in H3201, H6300, H6301, H6302, H7300, H7301, H7302, H7601, and H7602, we define:

$$k_{\text{exf}}(X) = \frac{k_{\text{int}}(X) \times LWC}{[H_2O] + 5 \times 10^2 [Cl^-] + 3 \times 10^5 [Br^-]}$$

Here, k_{int} = mass transfer coefficient, and LWC = liquid water content of the aerosol. The total uptake rate of X is only determined by k_{int} . The factors only affect

the branching between hydrolysis and the halide reactions. The factor 5×10^2 was chosen such that the chloride reaction dominates over hydrolysis at about $[Cl^-] > 0.1 \text{ M}$ (see Fig. 3 in Behnke et al. (1997)), i.e. when the ratio $[H_2O]/[Cl^-]$ is less than 5×10^2 . The ratio $5 \times 10^2 / 3 \times 10^5$ was chosen such that the reactions with chloride and bromide are roughly equal for sea water composition (Behnke et al., 1994).

A.5 Definition of the PRUDENCE subdomains

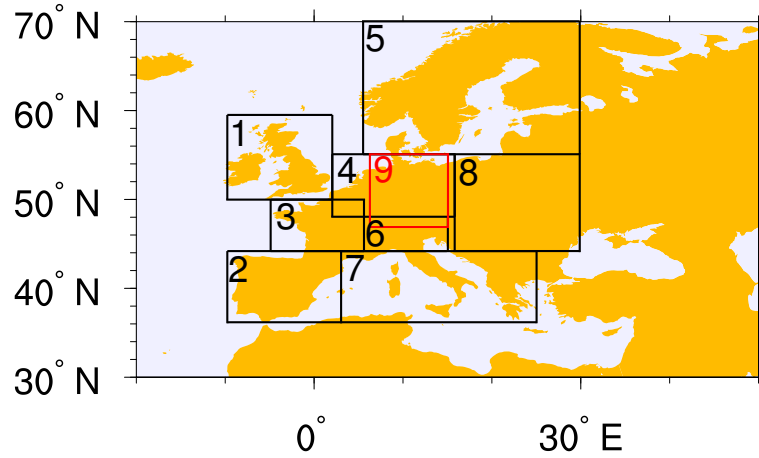


Figure A4: Geographical definition of the eight PRUDENCE subdomains (black, 1–8) and the additional subdomain covering Germany (red).

I performed some analyses on regional subdomains. Chosen were the eight domains defined in the PRUDENCE project (Christensen et al., 2007). These subdomains are commonly used in regional analysis (e.g. Kotlarski et al., 2014, and references therein). Eight defined PRUDENCE subdomains exist. Besides these domains an extra domain is added in the present work covering Germany. The geographical position of these domains is given in Fig. A4. The exact geographical definition and the names of these subdomains is given in Table A3.

Table A3: Definition of subdomains used in the present work.

number	name	west (in ° E)	east (in ° E)	south (in ° N)	north (in ° N)
1	British Isles	-10	2	50	59
2	Iberian Peninsula	-10	3	36	44
3	France	-5	5	44	50
4	Mid-Europe	2	16	48	55
5	Scandinavia	5	30	55	70
6	Alps	5	15	44	48
7	Mediterranean	3	25	36	44
8	Eastern Europe	16	30	44	55
9	Germany	6	15	47	55

A.6 Details about applied emissions

Details about the VEU emission data set

First, the DLR Institute of Transport Research submitted activity data for traffic on roads, rails and inland navigation to the Institut für Energiewirtschaft und Rationelle Energieanwendung (IER). From this activity data emissions over Germany for the three traffic sectors were calculated as described in detail by Kugler et al. (2013). The activity data distinguishes between different car types (like passenger cars or light duty vehicles), technology (petrol or diesel, European emission standard). In addition to this, IER calculated the traffic density from the activity data. With this information the emissions were calculated using the emission factors from the HBEF 3.1¹. The emission factors for the two other sectors mainly stem from the emission inventory guidebook (European Environment Agency, 2009).

Emissions of all other sectors in Germany, as well as for all emission sectors in Europe, were estimated by a top-down approach, meaning that given total emissions are distributed within the country. In the case of the VEU inventory these total emissions correspond usually to the values, which were reported by the countries in the scope of the United Nations Economic Commission for Europe (UNECE) Convention on Long-range Transboundary Air Pollution (CLRTAP). An own ansatz was used at the IER for countries for which no emissions were reported. It is important to note, that this approach leads to an inconsistency as only the traffic emissions in Germany are modelled in detail.

The emission inventory covers parts of North Africa, however, no emissions were calculated for this area. Instead, the IER backfilled the emissions over Africa with the emissions reported in the Emission Database for Global Atmospheric Research (EDGAR) 4.2 emission database².

During the generation of VEU08 it were assumed that $\frac{1}{4}$ of the travelled kilometres of passenger cars in Germany were performed with combustion engines using diesel as fuel, while $\frac{3}{4}$ were done with petrol as fuel. Compared to this, more than 90 % of the travelled of the light and heavy duty vehicles were performed with diesel engines.

Activity data of the transport sector for year 2020 and 2030 separate were calculated separately. Compared to 2008 a 10 % increase of the travelled kilometres of passenger cars was assumed in 2030. An increase of around 61 % was assumed for the heavy duty vehicles. Further, it was assumed that 10 % of the total travelled kilometres will be covered by vehicles powered by electricity. Most parts of the other 90 % will be covered by vehicles with conventional combustion engines. Altogether almost 90 percent of the travelled kilometres were assumed to be covered with vehicles, which fulfill the European emission standard 6 (EURO-6).

An EU energy model (TIMES PanEU, Blesl et al., 2010) were used at IER for the calculations of the other traffic emissions in Europe, as well as the non traffic sectors in Germany an EU. This energy model calculates possible developments of the European energy market based on assumptions (e.g. population, economy, energy price). For this calculation the 'current legislation' state was assumed.

¹Handbook of emission factors, <http://www.hbefa.net/>, last access 14.07.2016

²available at <http://edgar.jrc.ec.europa.eu/>, last access 12.02.2016

Preprocessing of regional emissions files

While the used global emissions files (MAC08 and ACCMIP/RCP6) are available in the sectoral resolution, which is used in the MECO(n) model system (details are provided in the supplement of Jöckel et al., 2016), the regional emission files require extensive preprocessing.

The original file from the IER contains information about the annual total emissions per gridbox. The sectoral resolution corresponds to the definition according to the significant new alternatives policy (SNAP) sectors. This sectoral resolution consists of ten emission sectors which are listed in Table A4 and differs largely from the standard treatment in the MECO(n) model system. Here, usually five anthropogenic categories are distinguished: road traffic, shipping, aviation, AWB and anthropogenic non-traffic (consists of all other anthropogenic sources including industry and domestic combustion). Only the road traffic sector can be directly converted from the SNAP sectors to the MECO(n) sectors.

Especially the SNAP sector 8 needed a special treatment, as this sector mixes different sources including shipping and aviation. The shipping emissions were separated from the SNAP sector 8. To allow this, I assumed that all emissions in the sector 8 taking place over international waters are shipping emissions. The VEU inventory considers only landing and take-off (LTO) emissions of the aviation sector. With the available information in the emission database it was not possible to separate the LTO emissions from the other emission in the sector 8. Further, emissions from the AWB sector are not provided by the VEU inventory.

All emissions from the regional emission databases, except for the emissions from sector 7 and the emissions on international waters in sector 8, were combined to emissions of the anthropogenic non-traffic sector. A small contribution of other sectors (e.g. LTO from aviation, inland water ways) in this anthropogenic non-traffic part could not be avoided, due to the definition of the SNAP sectors. Compared to the total anthropogenic non-traffic emissions the contribution of this sectors is small.

Additional efforts were needed for the time curves determining the hourly shares of the emissions. These time dependent curves are available for every sector, every country, every pollutant and every day. The IER 'time curves' were split into a monthly averaged diurnal cycle and daily shares of the annual total emissions. Using these daily shares, files with a daily resolution of the emissions were constructed.

For the anthropogenic non-traffic sector the monthly averaged hourly shares of combined SNAP sectors have been summed. Therefore the hourly shares of the corresponding SNAP sector were weighted by the contribution of the corresponding sector to the total anthropogenic non-traffic emissions. As ships on international waters usually are emitting continuously, no time curve for the shipping sector has been assumed.

During the model simulation the time curve and the daily emissions of the sectors are combined by a specific MESSy submodel called TEMIS, which I programmed in the scope of this thesis. It multiplies the total daily emissions with the corresponding hourly share.

Examples of the calculated 'time curves' for three countries (Germany, United Kingdom and Turkey) are shown in Fig. A5. The hourly shares for the road traffic sector (Fig. A5a) are the same for all countries, showing a double-peak structure (one peak in the morning and one in the evening). The difference between the countries is determined by the time shift compared to the UTC time in the respective countries.

Table A4: Description of the emissions sectors following the SNAP definition.

Sector number	Description
1	Combustion in energy and transformation industries
2	Non-industrial combustion plants
3	Combustion in manufacturing industry
4	Production processes
5	Extraction and distribution of fossil fuels and geothermal energy
6	Solvents and other product use
7	Road transport
8	Other mobile sources and machinery
9	Waste treatment and disposal
10	Agriculture

The 'time curve' of the anthropogenic non-traffic sector for January (Fig. A5b) shows more differences between the different countries. Overall, a similar double peak structure is present in all 'time curves'. This double peak structure is caused by contributions from the off-road traffic sector (SNAP8), which assumes the same hourly share as the traffic sector, as well as the 'non-industrial combustion plants' (SNAP2), which is determined mainly by the working hours of the people (e.g. for water heating). The differences between the different countries are determined mainly by differences in the 'combustion in energy and transformation industries' (SNAP1) sector, for which different 'time curves' for the countries exist (depending on time zone, culture and strength of the individual industries). Due to the weighting of the different 'time curves' by the total emissions of the respective SNAP-sector additional differences between the countries arise. The 'time curve' of the anthropogenic non-traffic sector for June is shown in Fig. A5c especially in Germany and Turkey the double peak structure is almost vanished, as the peak around evening gets smaller (e.g. the emission scenario assumes that in Germany the main peak for the electricity production in June is around noon, while in winter a peak around noon and a second peak in the evening is assumed).

The regional VEU emission data covers not the whole computational grid of the CM50 domain, because the data set was tailor-made for the COSMO-EU domain with a finer resolution (7 km). Due to the coarser resolution of the grid used in the present work compared to the COSMO-EU domain, the relaxation area would cover a greater parts of the domain (including parts of the European mainlands). To overcome this problem a larger domain was chosen. Parts of the computational domain which are not covered by the regional emission dataset are therefore backfilled with the MACCity (for the 2008 emissions) or ACCMIP/RCP6.0 (for the year 2030) emissions. This part of the domain is almost completely located within the relaxation area. Compared to the original MACCity and ACCMIP/RCP6.0 emissions these backfilled emissions are scaled additionally. I computed these scaling factors by comparing the totals for the area which is covered by the VEU emission datasets. A different scaling factor were calculated for every sector. These emissions are only needed for the CM50 domain as the CM12 domain is completely covered by the VEU inventory.

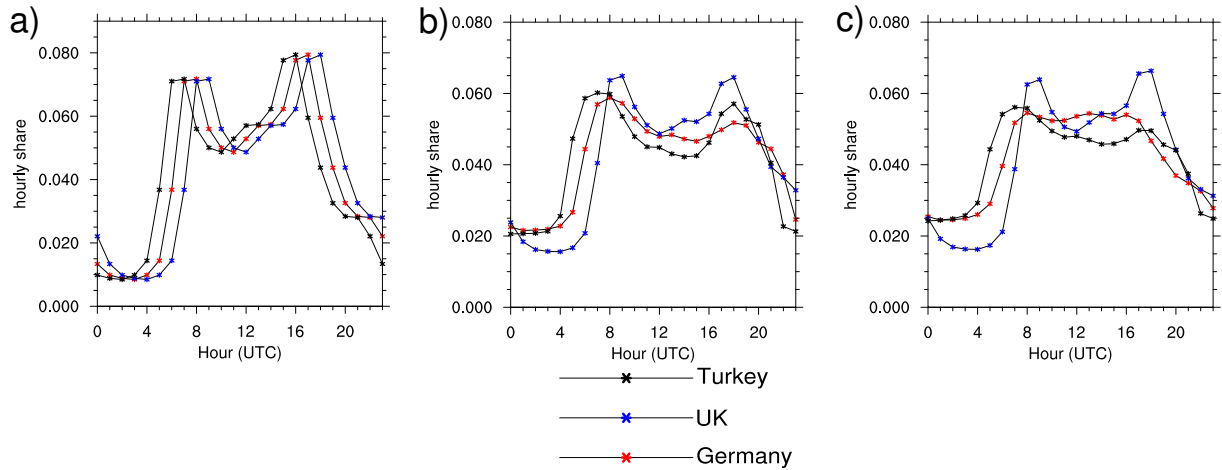


Figure A5: Simplified 'time curves' which are derived from the 'time curves' calculated by the IER. (a) the road traffic 'time curves' for January, (b) the anthropogenic non-traffic 'time curve' for January and (c) the anthropogenic non-traffic 'time curve' for June. The 'time curves' are shown for three different countries (red - Germany, blue - United Kingdom, and black - Turkey).

The VEU inventory contains no emissions of the aviation sector, therefore the MACCity (year 2008)/RCP6.0 (year 2030) emissions were used. In order to avoid a double accounting of the LTO emissions, which are already included in the VEU emissions data set in the sector anthropogenic non-traffic, the aviation emissions from MACCity/RCP6.0 are set to zero at the lowest layer.

Total emissions of the different simulations

The following Tables summaries the emissions of NO_x, CO and VOCs from all anthropogenic and natural sources applied in the different simulations. Please note, that for every specie only these emission sectors are given where emissions occur. These sector are:

- **road t.:** Road traffic emissions
- **anth. nt:** Anthropogenic non-traffic emissions
- **shipping:** Shipping emissions
- **aviation:** Aviation emissions
- **Soil-NO_x:** NO_x emissions from soils calculated by the model
- **LNOX:** Lightning NO_x emissions
- **AWB:** Agricultural waste burning emissions
- **BB :** Biomass burning emissions
- **biog.:** Further biogenic emissions, not calculated by the model but prescribed as annual climatology
- **biog.** C₅H₈: Biogenic isoprene emissions, calculated by the model

Tables A5–A7 give the total emissions of EMAC of NO_x, CO and VOC, respectively. Tables A8–A10 give the total emissions of CM50 and Table A11–A13 of CM12. Please note, that the given total emissions for C₅H₈ from biogenic origin are scaled with 0.6 for EMAC (Jöckel et al., 2006) and 0.45 for COSMO/MESSy (Mertens et al., 2016). Further, Figures A6 and A7 give an overview about the geographical distribution of the anthropogenic non-traffic and shipping emissions, respectively.

Table A5: Total emissions of NO_x (in Tg a⁻¹ in amount of NO) for EMAC. Given are the annual totals for the year 2008.

Simulation	road t.	anth. nt	shipping	aviation	Soil NO _x	LNOX	AWB	BB	Sum
REF	20.4	36.9	12.7	2.14	12.5	12.1	0.416	9.47	97.2
REFT42	20.4	36.9	12.7	2.14	12.5	12.1	0.416	9.47	97.2
EU08	20.4	36.9	12.7	2.14	12.5	12.1	0.416	9.47	97.2
EU08TE	20.4	36.9	12.7	2.14	12.5	12.1	0.416	9.47	97.2
EU30TE	20.4	36.9	12.7	2.14	12.5	12.1	0.416	9.47	97.2
EU30AC	17.2	30.4	8.55	2.50	12.5	12.1	0.265	11.9	95.4
EU30RT	22.4	36.9	12.7	2.14	12.5	12.1	0.416	9.47	99.2

Table A6: Total emissions of CO (in Tg a^{-1}) for EMAC. Given are the annual totals for the year 2008.

Simulation	road t.	anth. nt	shipping	AWB	biog.	BB	Sum
REF	153	412	1.33	20.2	113	328	1030
REF	153	412	1.33	20.2	113	328	1030
REFT42	153	412	1.33	20.2	113	328	1030
EU08	153	412	1.33	20.2	113	328	1030
EU08TE	153	412	1.33	20.2	113	328	1030
EU30TE	153	412	1.33	20.2	113	328	1030
EU30AC	189	351	0.901	21	113	467	1140
EU30RT	153	412	1.33	20.2	113	328	1030

Table A7: Total emissions of VOC (in Tg a^{-1} in amount of C) for EMAC. Given are the annual totals for the year 2008.

Simulation	road t.	anth. nt	shipping	biog. C_5H_8	AWB	biog.	BB	Sum
REF	17.5	73.4	2.19	450	0.943	108	14.5	667
REF	17.5	73.4	2.19	450	0.943	108	14.5	667
REFT42	17.5	73.4	2.19	450	0.943	108	14.5	667
EU08	17.5	73.4	2.19	450	0.943	108	14.5	667
EU08TE	17.5	73.4	2.19	450	0.943	108	14.5	667
EU30TE	17.5	73.4	2.19	450	0.943	108	14.5	667
EU30AC	26.2	73.2	2.05	450	2.18	108	21.4	683
EU30RT	17.5	73.4	2.19	450	0.943	108	14.5	667

Table A8: Total emissions of NO_x (in Tg a^{-1} in amount of NO) for CM50. Given are the annual totals for the year 2008.

Simulation	road t.	anth. nt	shipping	aviation	Soil NO_x	LNOX	AWB	BB	Sum
REF	5.19	7.60	2.35	0.595	1.57	0.715	0.0762	0.28	18.4
REFT42	5.2	7.65	2.35	0.591	1.57	0.715	0.0762	0.276	18.4
EU08	5.35	5.08	1.81	0.534	1.57	0.715	0.0762	0.28	15.4
EU08TE	5.35	5.08	1.81	0.534	1.57	0.715	0.0762	0.28	15.4
EU30TE	4.06	6.02	2.49	0.623	1.57	0.715	0.0806	0.287	15.8
EU30AC	4.06	6.02	2.49	0.623	1.57	0.715	0.0806	0.287	15.8
EU30RT	4.06	6.02	2.49	0.623	1.57	0.715	0.0806	0.287	15.8

Table A9: Total emissions of CO (in Tg a⁻¹) for CM50. Given are the annual totals for the year 2008.

Simulation	road t.	anth. nt	shipping	AWB	biog.	BB	Sum
REF	30.9	28.7	0.241	2.89	4.84	8.87	76.4
REFT42	30.9	28.9	0.246	2.88	4.84	9.03	76.8
EU08	23.6	30.1	0.299	2.89	4.84	8.87	43.6
EU08TE	23.6	30.1	0.299	2.89	4.84	8.87	70.6
EU30TE	10.1	29.4	0.262	3.11	4.84	9.48	57.2
EU30AC	10.1	29.4	0.262	3.11	4.84	9.48	57.2
EU30RT	10.1	29.4	0.262	3.11	4.84	9.48	57.2

Table A10: Total emissions of VOC (in Tg a⁻¹ in amount of C) for CM50. Given are the annual totals for the year 2008.

Simulation	road t.	anth. nt	shipping	biog. C ₅ H ₈	AWB	biog.	BB	Sum
REF	3.29	14.2	0.343	31.8	0.0994	4.59	0.377	54.7
REFT42	3.31	14.4	0.351	31.8	0.0994	4.59	0.377	54.9
EU08	3.39	6.56	0.0954	31.8	0.0994	4.59	0.377	46.9
EU08TE	3.39	6.58	0.0954	31.8	0.0994	4.59	0.377	46.9
EU30TE	2.08	6.04	0.0762	31.8	0.223	4.59	0.43	45.2
EU30AC	2.08	6.04	0.0762	31.8	0.223	4.59	0.43	45.2
EU30RT	2.08	6.04	0.0762	31.8	0.223	4.59	0.43	45.2

Table A11: Total emissions of NO_x (in Tg in amount of NO) for CM12. Given are the annual totals for the May–August 2008.

Simulation	road t.	anth. nt	shipping	aviation	Soil NO _x	LNOX	AWB	BB	Sum
REF	0.342	0.335	0.0333	0.0642	0.167	0.0456	0.000761	0.00361	0.988
REFT42	0.341	0.332	0.035	0.0638	0.167	0.0456	0.000761	0.0044	0.985
EU08	0.441	0.277	0.0263	0.0555	0.167	0.0456	0.000761	0.00361	1.01
EU08TE	0.441	0.277	0.0261	0.0555	0.167	0.0456	0.000761	0.00361	1.01
EU30TE	0.253	0.335	0.0445	0.0515	0.167	0.0456	0.000761	0.00363	0.897
EU30AC	0.253	0.335	0.0445	0.0515	0.167	0.0456	0.000761	0.00363	0.897

Table A12: Total emissions of CO (in Tg) for CM12. Given are the annual totals for the May–August 2008.

Simulation	road t.	anth. nt	shipping	AWB	biog.	BB	Sum
REF	1.27	1.41	0.00348	0.0333	4.81	0.12	7.65
REFT42	1.27	1.41	0.00366	0.0322	4.81	0.145	7.67
EU08	1.18	0.842	0.000719	0.0333	4.81	0.12	6.98
EU08TE	1.18	0.842	0.000719	0.0333	4.81	0.12	6.98
EU30TE	0.322	0.497	0.00462	0.0366	4.81	0.12	5.79
EU30AC	0.322	0.497	0.00462	0.0366	4.81	0.12	5.79

Table A13: Total emissions of VOC (in Tg in amount of C) for CM12. Given are the annual totals for the May–August 2008.

Simulation	road t.	anth. nt	shipping	biog. C ₅ H ₈	AWB	biog.	BB	Sum
REF	0.141	0.538	0.00413	0.423	0.0111	0.372	0.00516	1.49
REFT42	0.141	0.539	0.00424	0.423	0.0107	0.372	0.00623	1.49
EU08	0.143	0.383	0.00175	0.423	0.0111	0.372	0.00516	1.34
EU08TE	0.143	0.383	0.00175	0.423	0.0111	0.372	0.00516	1.34
EU30TE	0.118	0.394	0.00136	0.423	0.0034	0.372	0.00366	1.32
EU30AC	0.118	0.394	0.00136	0.423	0.0034	0.372	0.00366	1.32

Overview over anthropogenic emissions applied in the different simulations

Table A14 gives an overview about the emission inventories applied in the different simulations.

Table A14: Overview of the simulations performed in this study. A detailed description is given in the text. 'MACCity T42' means the MACCity emissions in EMAC resolution, 'MACCity - LTO' the MACCity emissions without the aviation emissions in the lowest layer.

MECO(n) instance	road, ship, anth. non-traffic	aviation	AWB, biomass burning
<i>GLOB</i> - longer term simulation			
0	MACCity	MACCity	MACCity
<i>REF</i> - Reference with same emissions for all instances			
0	MACCity	MACCity	MACCity
1	MACCity	MACCity	MACCity
2	MACCity	MACCity	MACCity
<i>REFT42</i> - Influence of the emissions resolution			
0	MACCity	MACCity	MACCity
1	MACCity T42	MACCity T42	MACCity T42
2	MACCity T42	MACCity T42	MACCity T42
<i>EU08</i> - Influence of changed anthropogenic emissions			
0	MACCity	MACCity	MACCity
1	VEU08	MACCity - LTO	MACCity
2	VEU08	MACCity - LTO	MACCity
<i>EU08TE</i> - Influence of detailed 'time curves' for emissions			
0	MACCity	MACCity	MACCity
1	VEU08	MACCity - LTO	MACCity
2	VEU08	MACCity - LTO	MACCity
<i>EU30TE</i> - Influence of projection for the year 2030			
0	MACCity	MACCity	MACCity
1	VEU30	ACCMIP - LTO	ACCMIP
2	VEU30	ACCMIP - LTO	ACCMIP
<i>EU30RT</i> - Influence of changed boundary conditions			
0	MACCity + 10 % NO _x road traffic	MACCity	MACCity
1	VEU30	ACCMIP - LTO	ACCMIP
<i>EU30AC</i> - Influence of changed boundary conditions			
0	ACCMIP	ACCMIP	ACCMIP
1	VEU30	ACCMIP - LTO	ACCMIP
2	VEU30	ACCMIP - LTO	ACCMIP

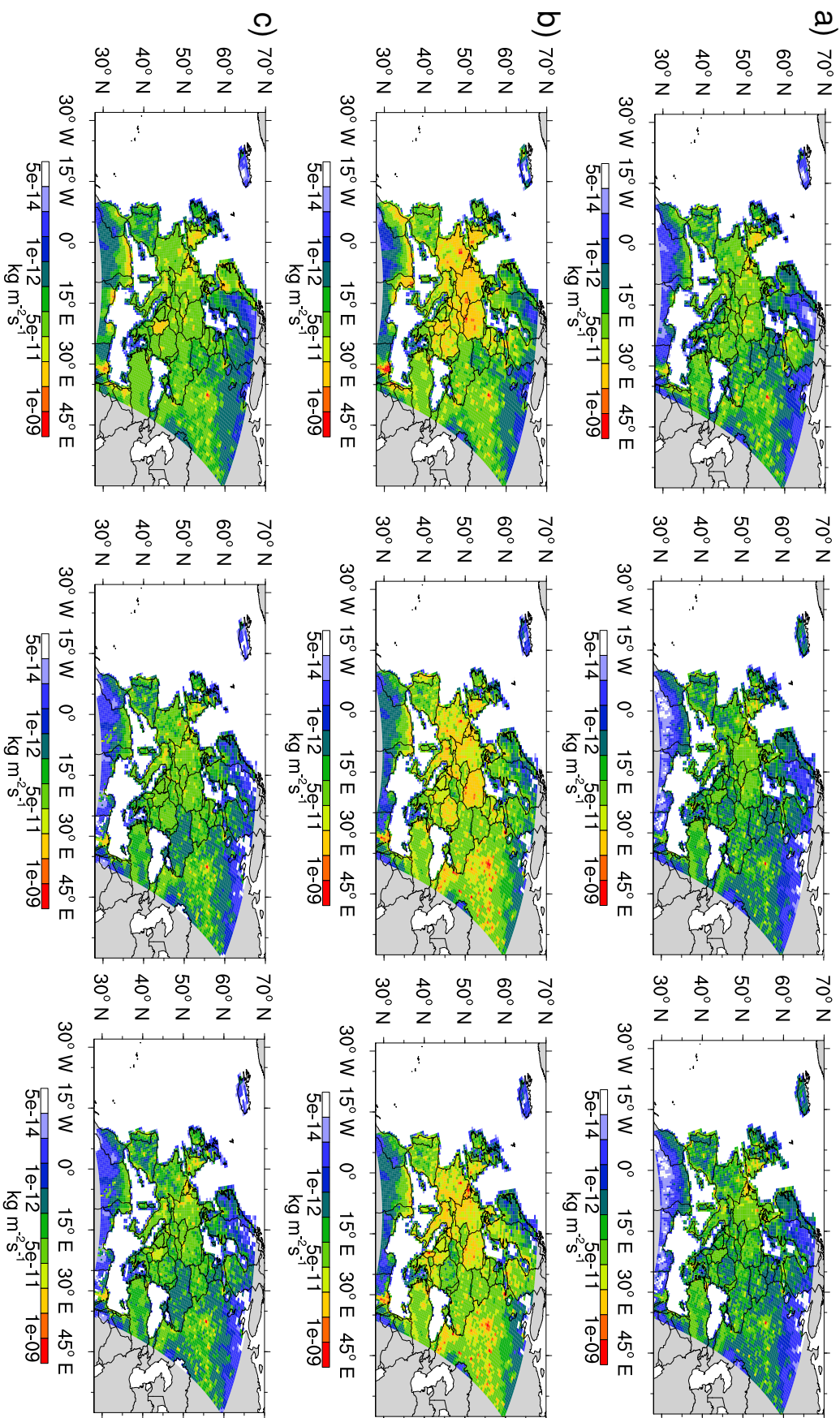


Figure A6: Comparison of the annually averaged emissions from the anthropogenic non-traffic sector (in kg m⁻²s⁻¹) between the MAC08 (left), VEU08 (middle) and VEU30 (right) inventory. (a) for NO_x (in kg NO); (b) for CO (in kg CO); (c) for VOC (in kg carbon). In general only the part of the CM50 domain without the relaxation area is shown.

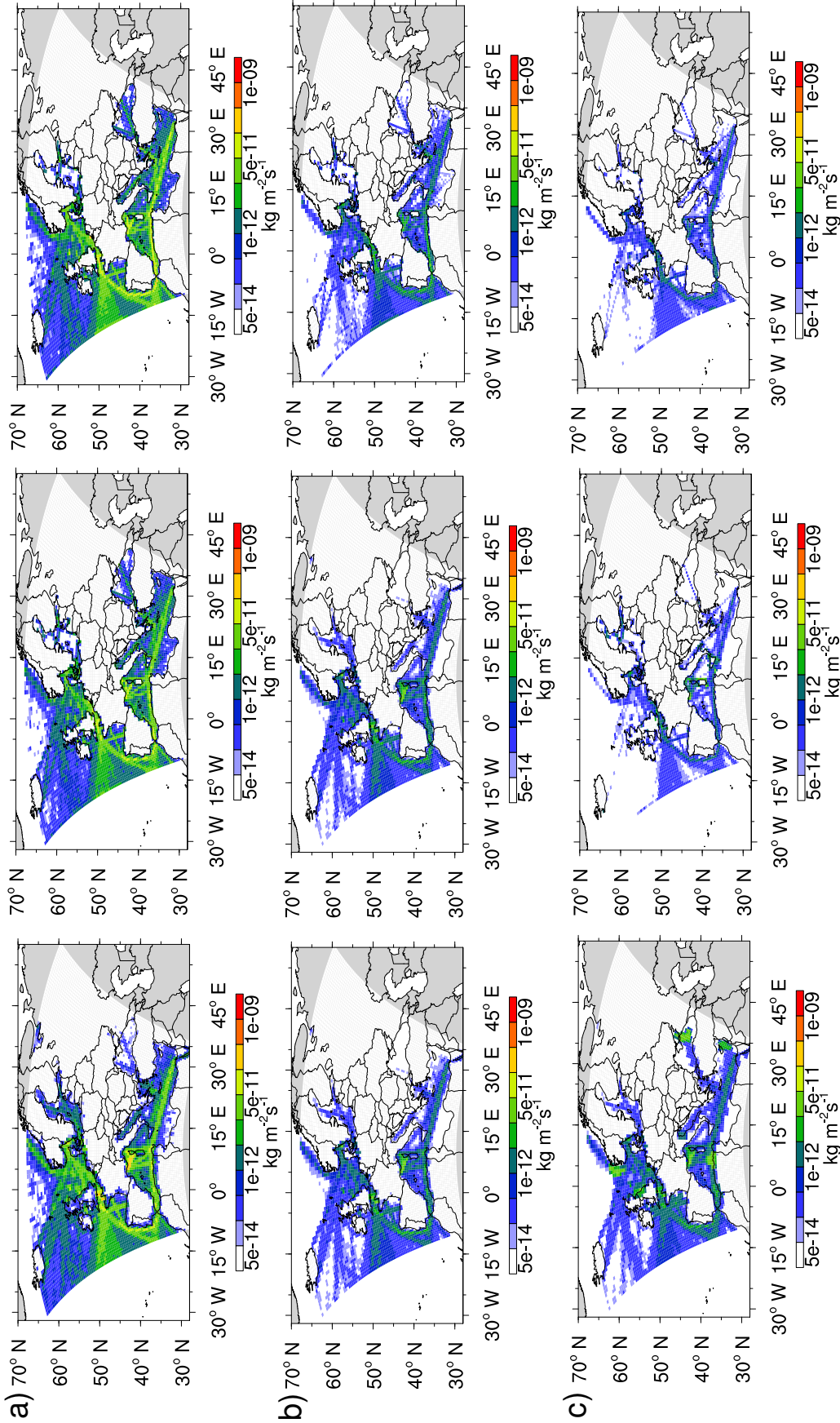


Figure A7: Comparison of the annually averaged emissions from the shipping sector (in $\text{kg m}^{-2}\text{s}^{-1}$ between the MAC08 (left), VEU08 (middle) and VEU30 (right) inventory. (a) for NO_x (in kg NO); (b) for CO (in kg CO); (c) for VOC (in kg carbon). In general only the part of the CM50 domain without the relaxation area is shown.

A.7 Additional figures

Chapter 4

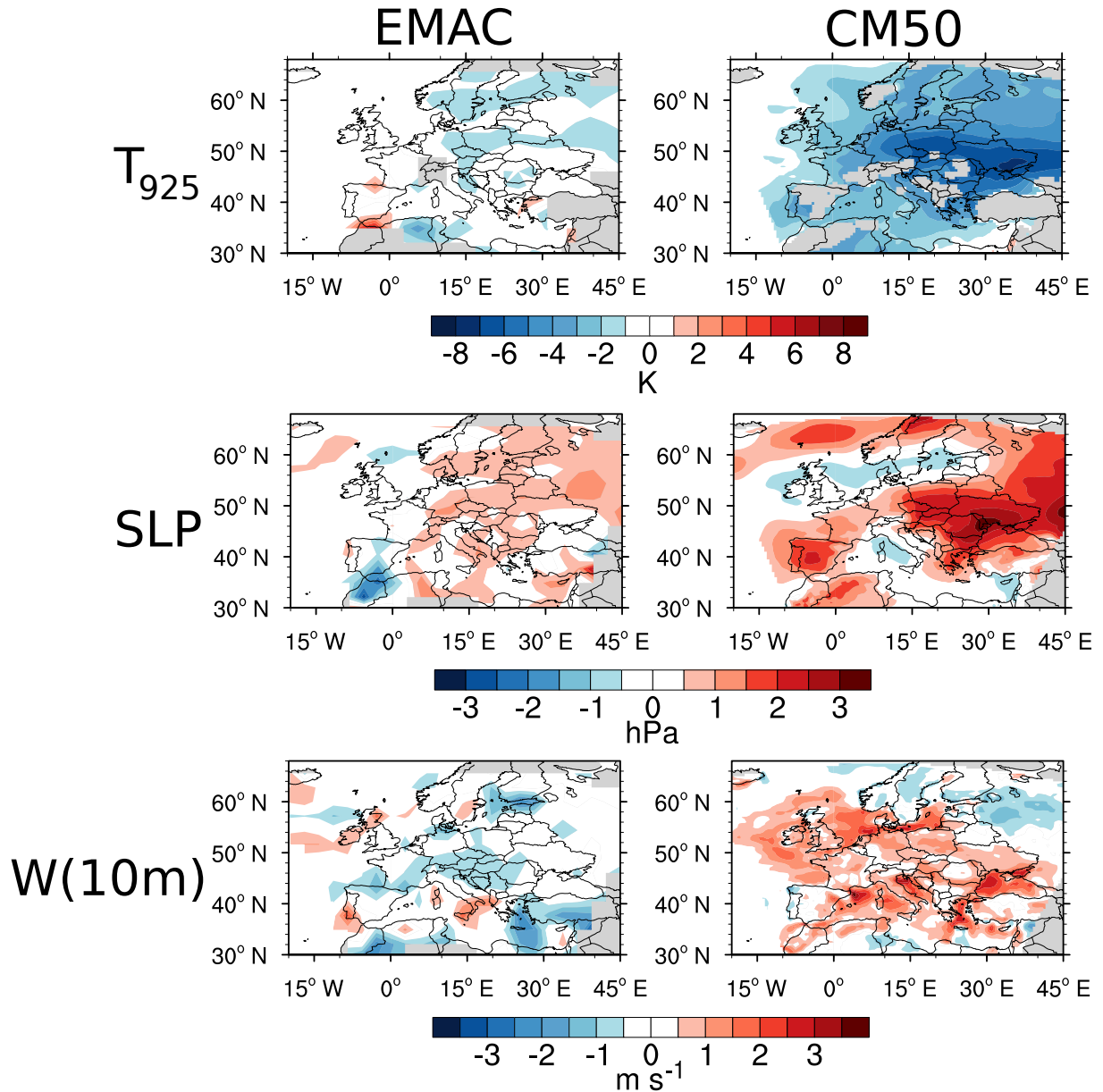


Figure A8: Monthly average difference between EMAC (left) CM50 (right) and ERA-Interim for June 2008. Shown are the differences of the temperature at 925 hPa (T_{925} , in K), the sea level pressure (SLP, in hPa) and the the 10 m wind speed ($W(10m)$), in $m s^{-1}$ (cf. page 51).

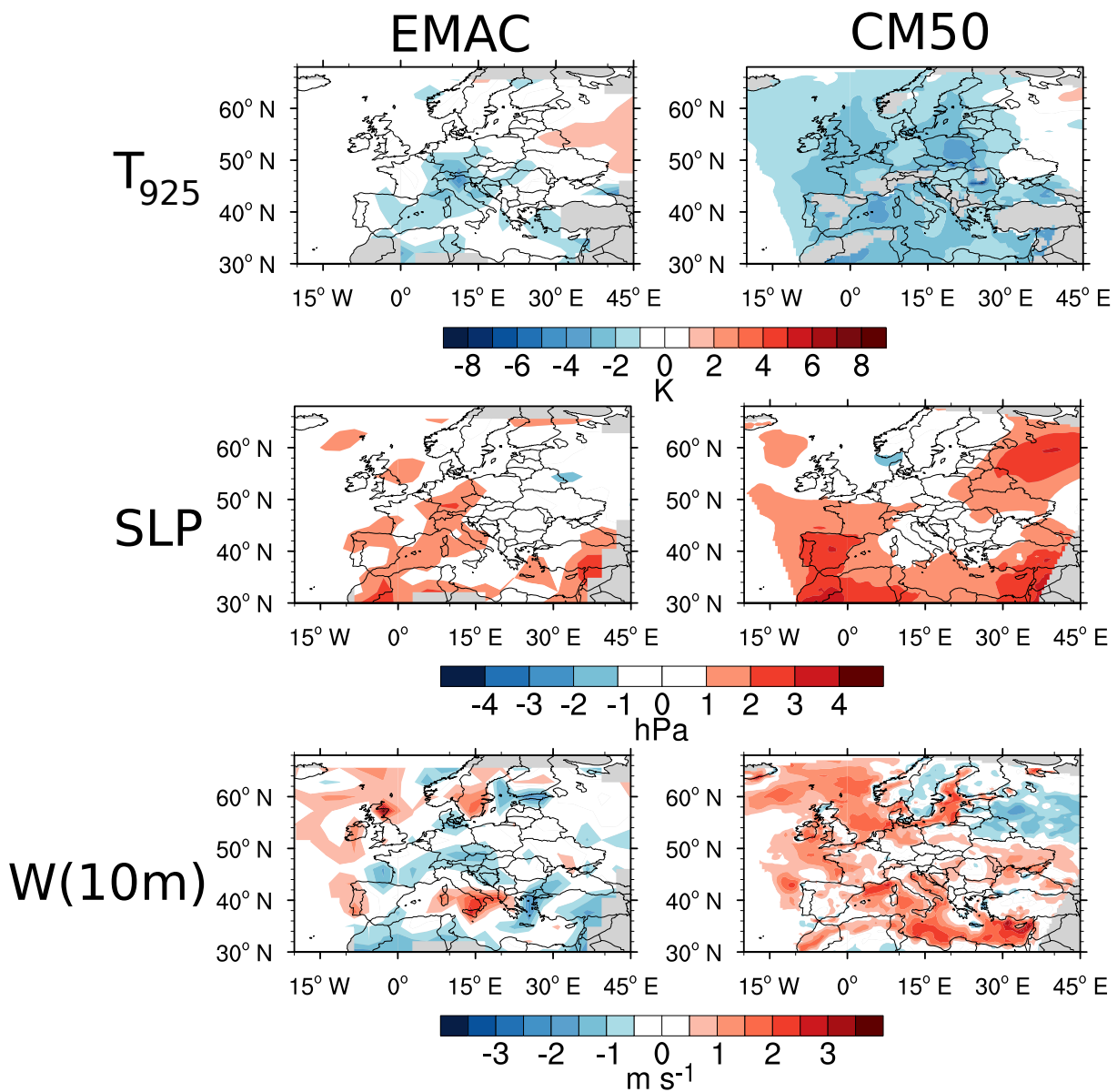


Figure A9: As Fig. A8 but for December 2008 (cf. page 51).

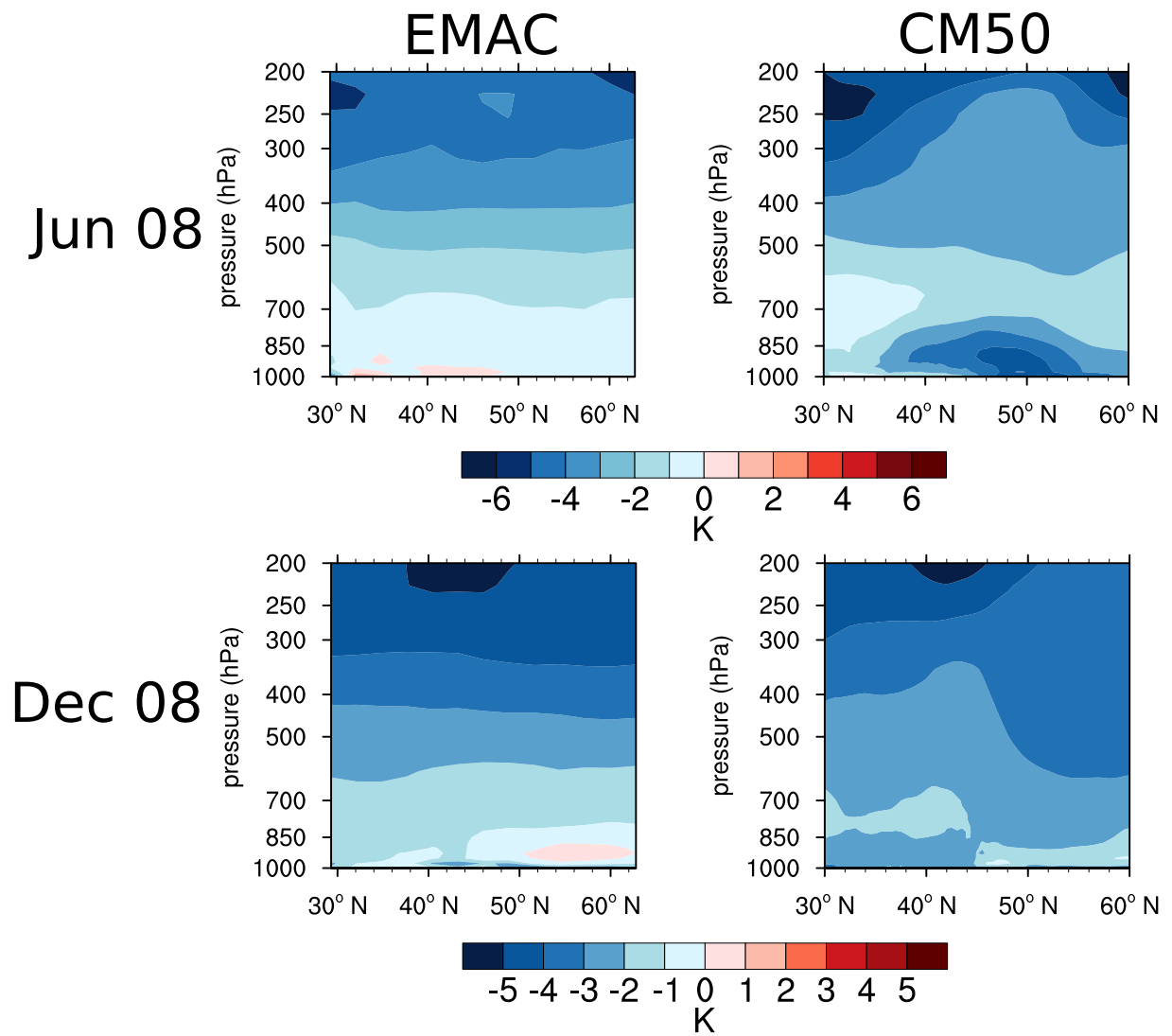


Figure A10: Difference of the zonally averaged temperature (in K) between EMAC and ERA-Interim (left side) and CM50 and ERA-Interim. The shown values are averaged for June 2008 (top) and December 2008 (bottom) (cf. page 51).

The Table A15 and Table A16 give information regarding the subtracted mean values from the diurnal cycles to calculate the amplitudes (cf. page 64).

Table A15: Mean values which were subtracted from the diurnal cycle (in $\mu\text{g m}^{-3}$) for EMAC and CM50. The range indicates on standard deviation with respect to the values at the individual station.

	June non- mountain	June mountain	December non- mountain	December mountain
EMAC	88.8 ± 19.2	103.4 ± 8.5	57.5 ± 11.6	72.6 ± 9.3
CM50	95.3 ± 12.1	95.3 ± 8.7	68.2 ± 9.7	77.1 ± 6.0
Observations	74.2 ± 11.4	95.5 ± 7.2	39.1 ± 13.2	64.2 ± 11.3

Table A16: As Table A15 but only for the stations located in the CM12 domain.

	June non- mountain	June mountain
EMAC	89.6 ± 17.3	99.1 ± 1.6
CM50	87.2 ± 10.3	88.3 ± 8.2
CM12	89.9 ± 7.4	89.4 ± 0.9
Observations	79.2 ± 8.9	94.4 ± 2.2

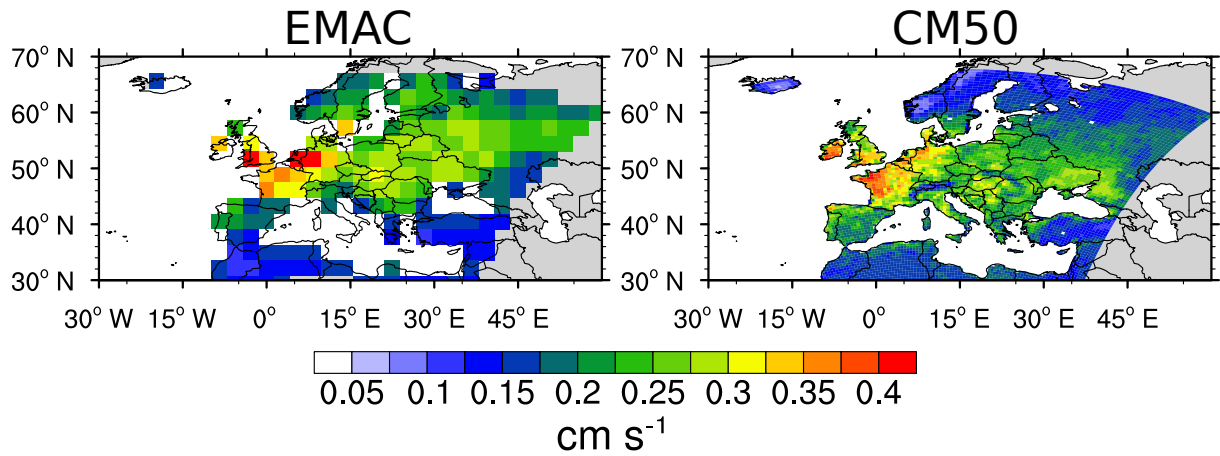


Figure A11: Annual average (2008) dry deposition velocity of O_3 (in $cm\ s^{-1}$) for EMAC (left) and CM50 (right).

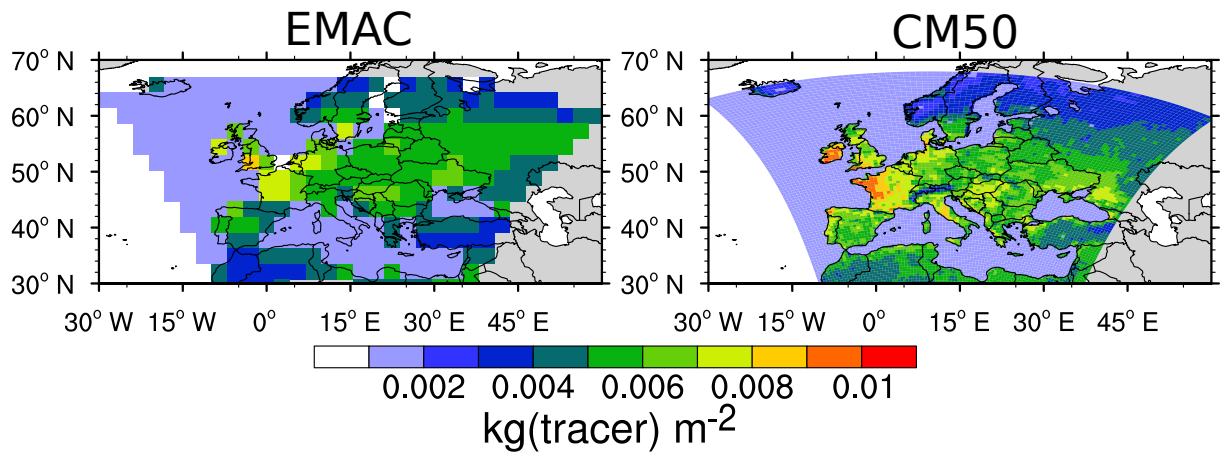


Figure A12: Annual dry deposition sum of O_3 (in $kg\ m^{-2}$) for EMAC (left) and CM50 (right).

Chapter 5

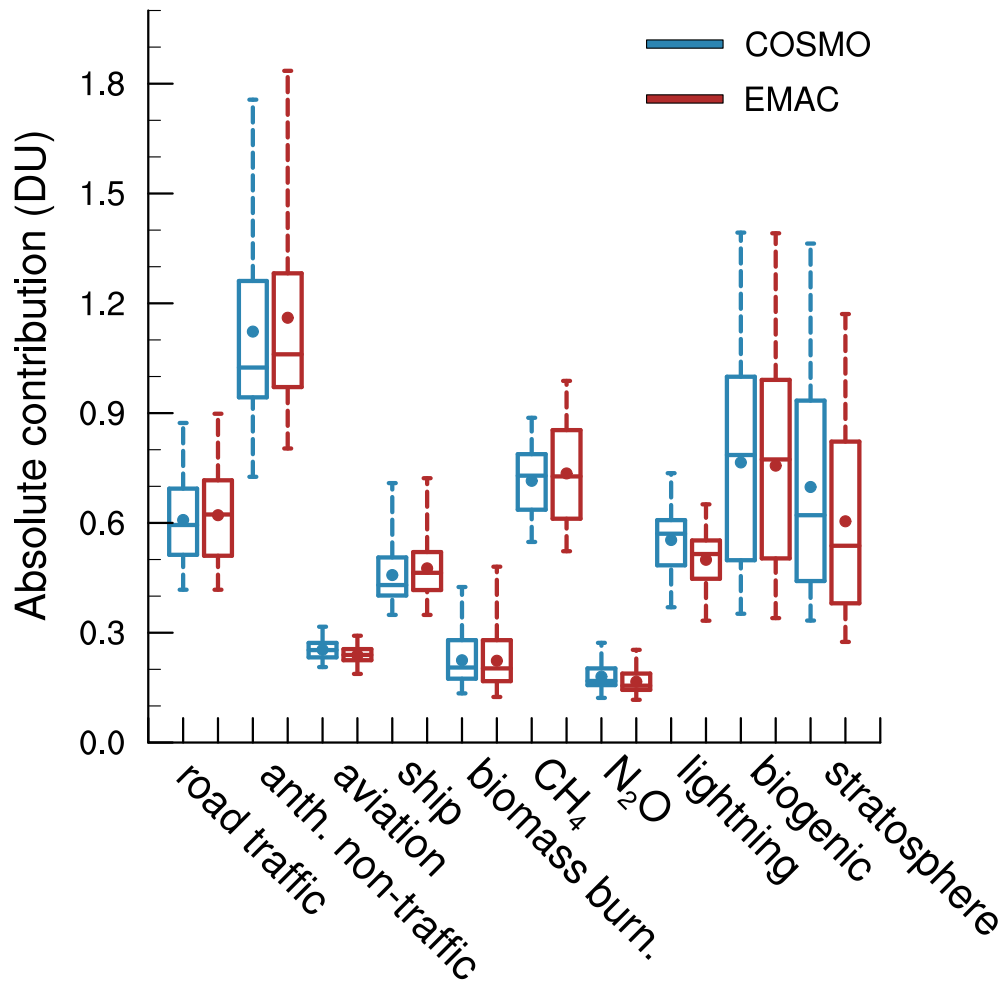


Figure A13: Box and whisker plot for the 850PC of the tagged categories (in DU). The values are area-averaged over the domain of the CM50 domain. The upper and lower end of the box indicate the 75 and 25 percentile, the bar the median, the dot the average and the whiskers the minimum and maximum of the timeseries for the whole year 2008. Compared are the results of the EMAC instance (EMAC) and the CM50 instance (COSMO) of the *REFbio* simulation (cf. page 78).

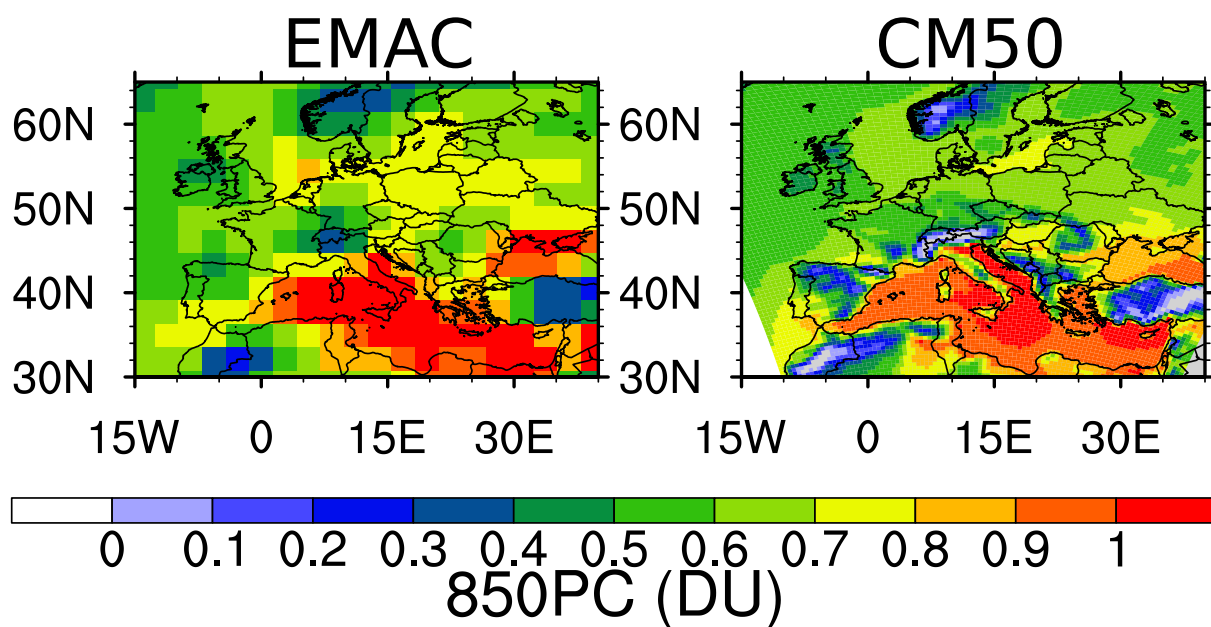


Figure A14: 850 for O_3^{tra} (in DU) averaged over JJA. (a) shows the values for EMAC, (b) for COSMO).

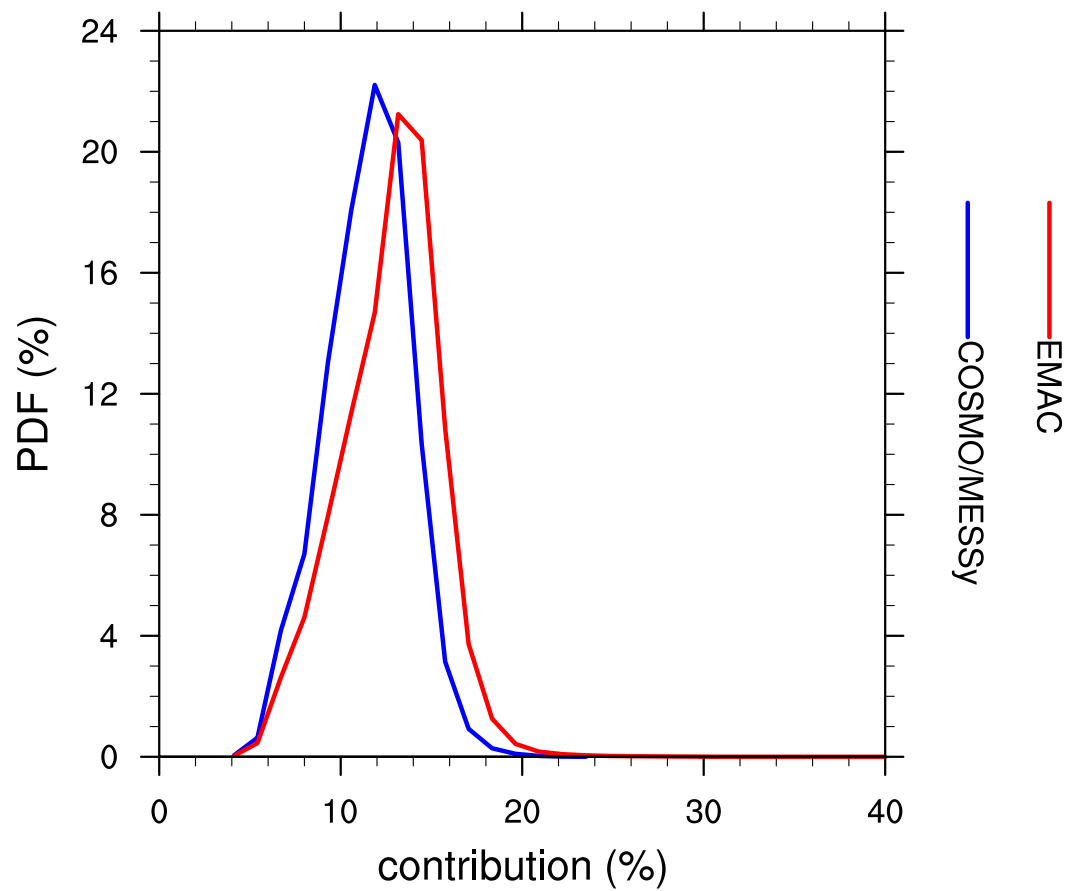


Figure A15: PDF of the contribution of O_3^{tra} to ground-level O_3 values. The PDF is calculated for all grid-boxes covered by the CM50 domain and for all time-steps for the JJA period between 9–18 o'clock. The results of both models were transformed to a regular grid (0.5 x 0.5 resolution).

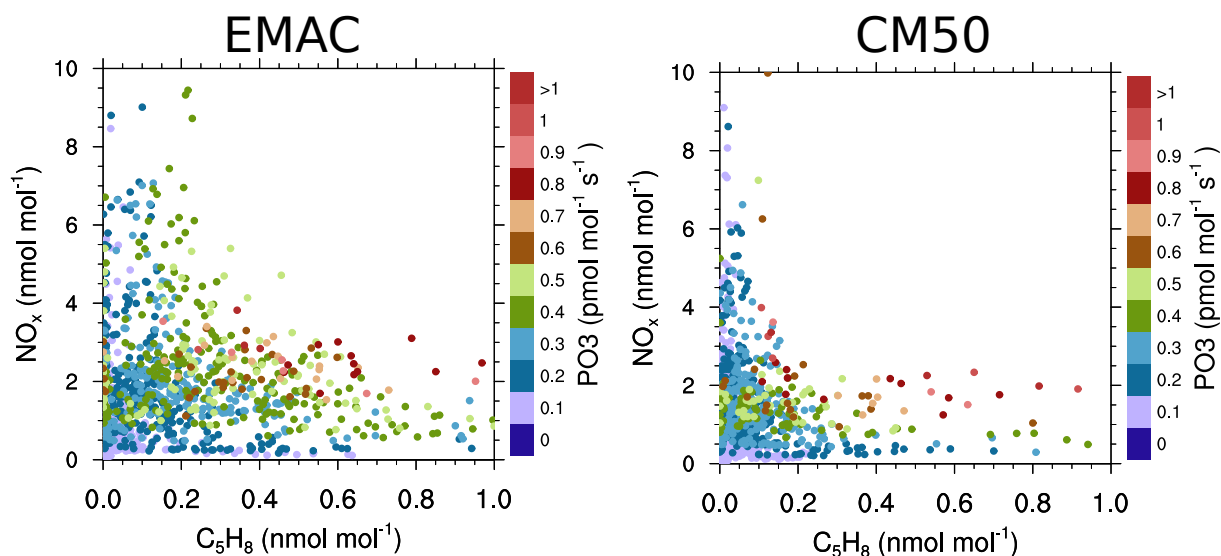


Figure A16: Scatter plot of the the NO_x mixing ratio (in $\text{nmol mol}^{-1} \text{ s}^{-1}$) versus the C_5H_8 mixing ratio (in nmol mol^{-1}). The colour of the dots depict the net O_3 production (in $\text{pmol mol}^{-1} \text{ s}^{-1}$). Shown are monthly averaged values for every ground level grid box for May–September. The results of EAMC and CM50 are shown only for the values for the grid boxes covering the CM50 domain are shown (cf. page 84).

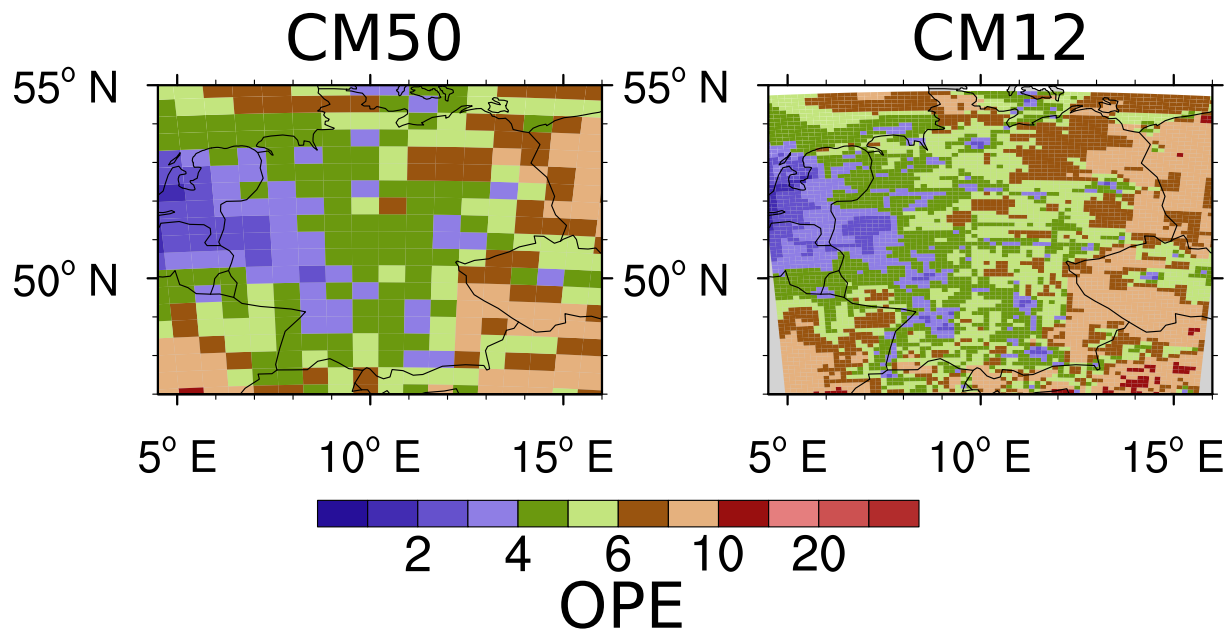


Figure A17: OPE at ground level averaged over JJA for CM50 and CM12 (cf. Sect. 5.2).

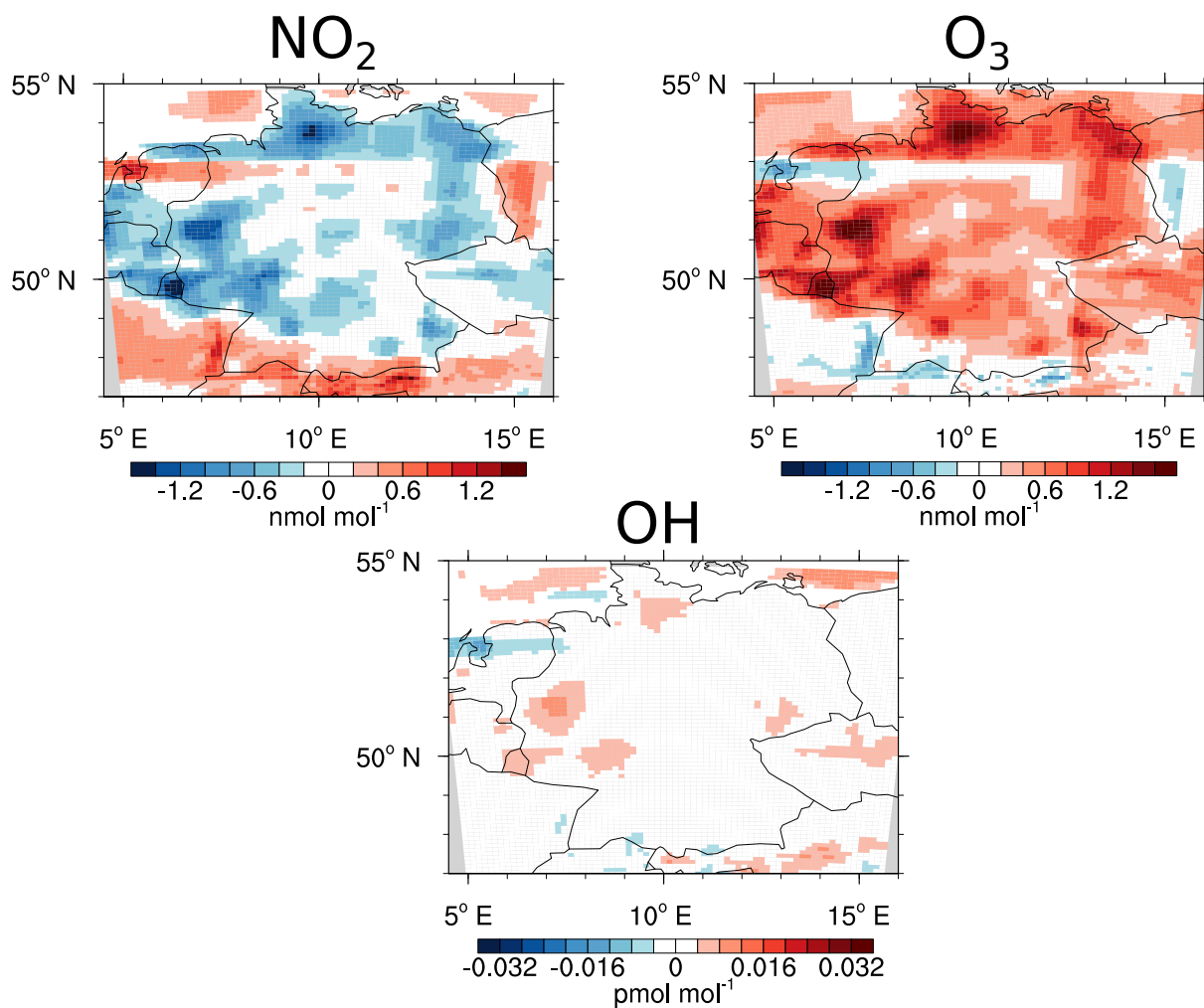


Figure A18: Differences (REF_{T42} minus REF), averaged over JJA for ground level values of NO_2 , O_3 and OH . Please note the different colour scales.

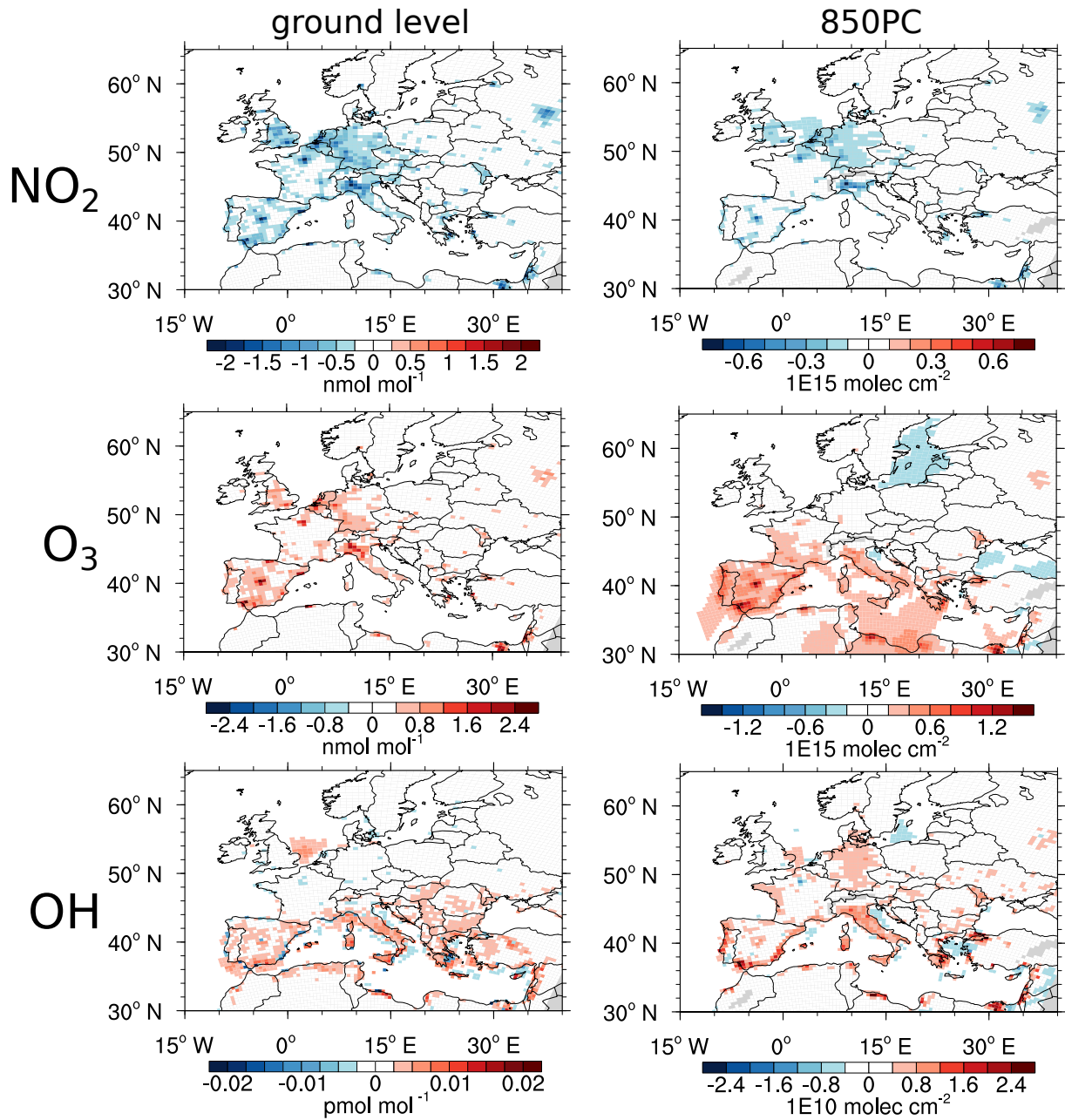


Figure A19: Differences (EU08TE minus EU08), averaged over JJA: Shown are the ground level mixing ratios (left side) and the 850PC (right side) for NO_2 , O_3 , and OH . Please note the different colour scales.

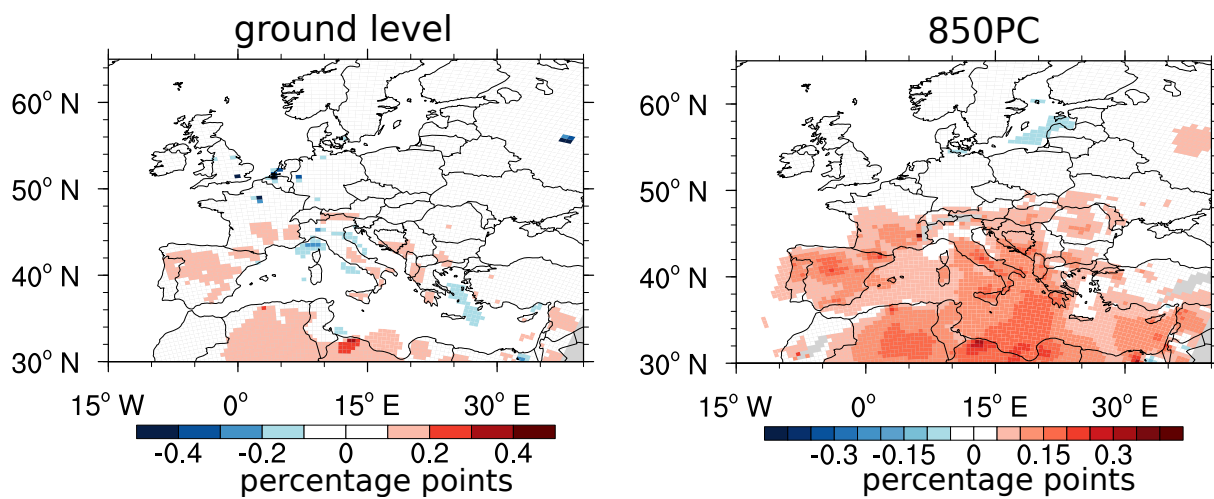


Figure A20: Differences ($EU08TE$ minus $EU08$), averaged over JJA, of the contribution of O_3^{tra} (in ppt) of the road traffic sector for ground level and the 850PC. Please note the different colour scales.

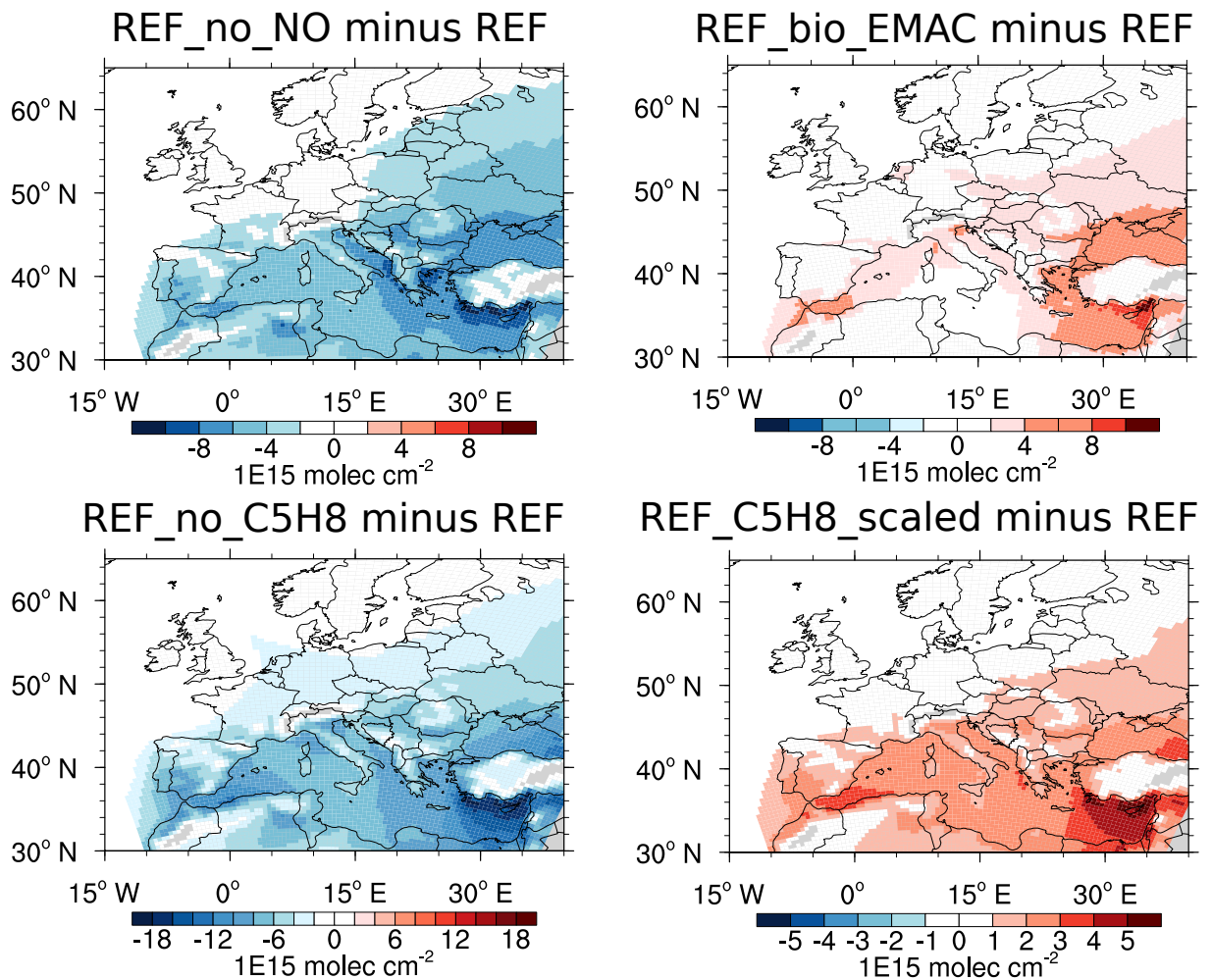


Figure A21: Differences averaged over JJA of the 850PC for O₃. (a) '*REF_no_NO* minus *REF*'; (b) '*REF_bio_EMAC* minus *REF*'; (c) '*REF_no_C5H8* minus *REF*'; (d) '*REF_C5H8_scaled* minus *REF*'. Please note the different colour scales.

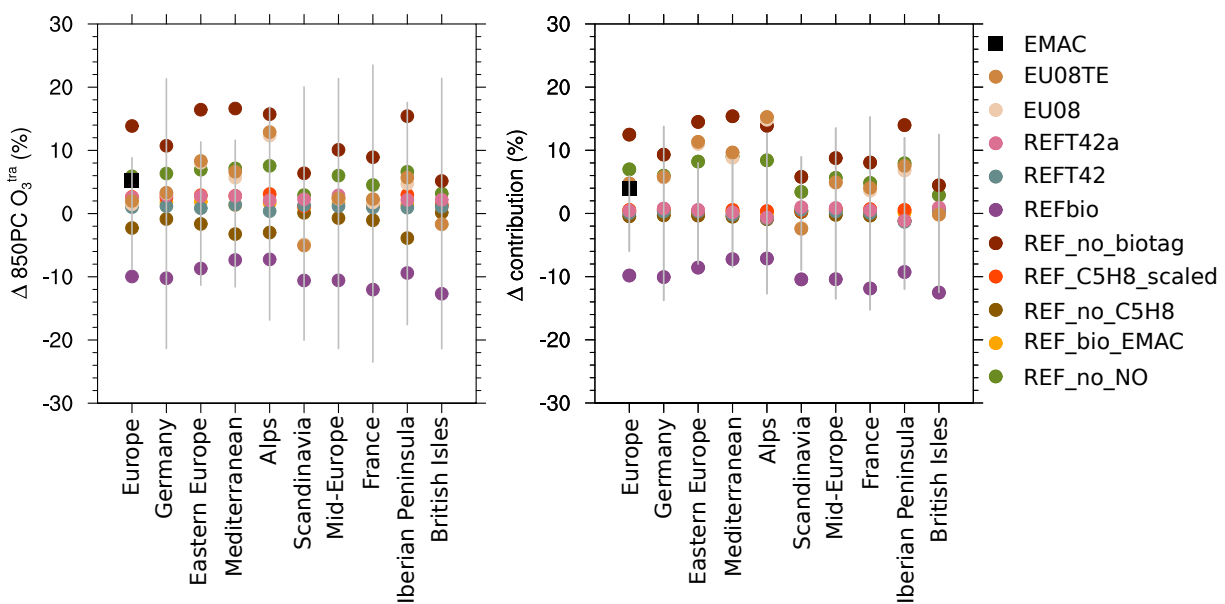


Figure A22: Differences ('SIMULATION - REF') for the individual simulation results compared to the REF simulation, averaged for JJA and over the whole domain (Europe), Germany as well as the different PRUDENCE regions. EMAC indicates in addition the difference ('EMAC-COSMO') between COSMO and EMAC for the REFbio simulation. The grey bars indicate one standard deviation with respect to time for the REF simulation. (a) the difference of the 850PC of O_3^{tra} (in %); (b) the difference for the contribution of O_3^{tra} to the 850PC of O_3 (in %) (cf. page 106).

Chapter 6

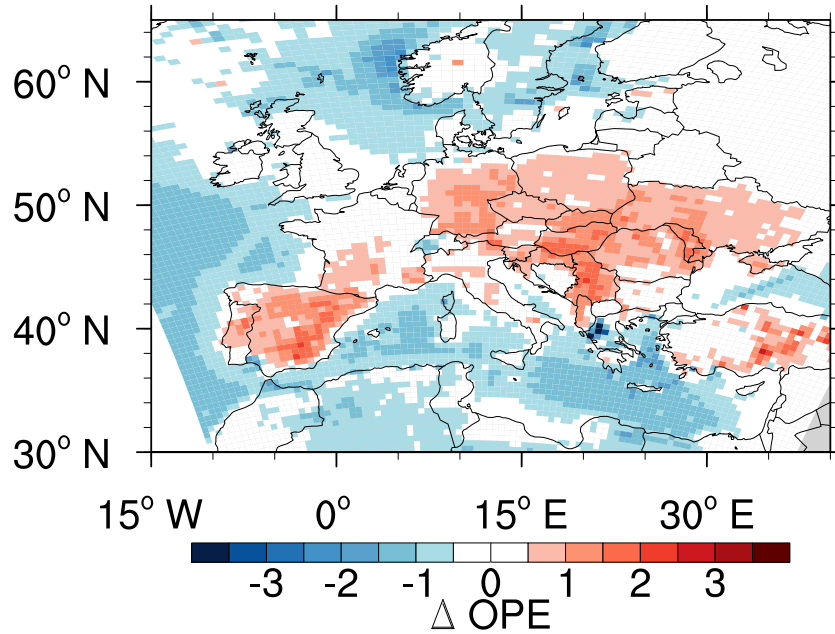


Figure A23: Differences ('*EU30TE* minus *EU08TE*') of the OPE at ground level averaged for the year 2008.

Table A17: Net O₃ production (PO_3 , in Tg a⁻¹), NO_x emissions (E_{NO_x} , in Tg a⁻¹ in a mount of NO) and R_{prod} (PO_3/E_{NO_x}) for the three most important anthropogenic ground level sources. The values are integrated over the CM12 domain up to 200 hPa and for the period JJA.

	PO_3 O_3^{tra} (Tg a ⁻¹)	E_{NO_x} road traffic (Tg a ⁻¹)	R_{prod}	PO_3 $O_3^{anth.}$ (Tg a ⁻¹)	E_{NO_x} anth. non- traffic (Tg a ⁻¹)	R_{prod}	PO_3 O_3^{ship} (Tg a ⁻¹)	E_{NO_x} ship (Tg a ⁻¹)	R_{prod}
<i>EU08TE</i>	0.95	0.33	2.86	0.76	0.20	3.79	0.12	0.02	6.16
<i>EU30TE</i>	0.60	0.19	3.17	0.89	0.24	3.67	0.13	0.02	5.91
<i>EU30RT</i>	0.64	0.19	3.39	0.91	0.24	3.78	0.14	0.02	6.32

Bibliography

- Allen, D. J. and Pickering, K. E.: Evaluation of lightning flash rate parameterizations for use in a global chemical transport model, *J. Geophys. Res. Atmos.*, 107, ACH 15–1–ACH 15–21, doi:10.1029/2002JD002066, 2002.
- Andersson, C. and Engardt, M.: European ozone in a future climate: Importance of changes in dry deposition and isoprene emissions, *J. Geophys. Res. Atmos.*, 115, doi:10.1029/2008JD011690, d02303, 2010.
- Arakawa, A. and Lamb, V.: Computational design of the basic dynamical processes of the UCLA general circulation model, vol. 17 of *Methods in Computational Physics*, Academic Press, New York, general circulation of the atmosphere edn., 1977.
- Asselin, R.: Frequency Filter for Time Integrations, *Mon. Wea. Rev.*, 100, 487–490, doi:10.1175/1520-0493(1972)100<0487:FFFTI>2.3.CO;2, 1972.
- Auvray, M. and Bey, I.: Long-range transport to Europe: Seasonal variations and implications for the European ozone budget, *J. Geophys. Res. Atmos.*, 110, doi:10.1029/2004JD005503, d11303, 2005.
- Bechtold, P., Chaboureaud, J.-P., Beljaars, A., Betts, A. K., Khler, M., Miller, M., and Redelsperger, J.-L.: The simulation of the diurnal cycle of convective precipitation over land in a global model, *Quarterly Journal of the Royal Meteorological Society*, 130, 3119–3137, doi:10.1256/qj.03.103, 2004.
- Bey, I., Jacob, D. J., Yantosca, R. M., Logan, J. A., Field, B. D., Fiore, A. M., Li, Q., Liu, H. Y., Mickley, L. J., and Schultz, M. G.: Global modeling of tropospheric chemistry with assimilated meteorology: Model description and evaluation, *J. Geophys. Res. Atmos.*, 106, 23 073–23 095, doi:10.1029/2001JD000807, 2001.
- Blesl, M., Kober, T., Bruchof, D., and Kuder, R.: Effects of climate and energy policy related measures and targets on the future structure of the European energy system in 2020 and beyond, *Energy Policy*, 38, 6278–6292, doi:http://dx.doi.org/10.1016/j.enpol.2010.06.018, the socio-economic transition towards a hydrogen economy - findings from European research, with regular papers, 2010.
- Blond, N., Boersma, K. F., Eskes, H. J., van der A, R. J., Van Roozendael, M., De Smedt, I., Bergametti, G., and Vautard, R.: Intercomparison of SCIAMACHY nitrogen dioxide observations, in situ measurements and air quality modeling results over Western Europe, *J. Geophys. Res. Atmos.*, 112, doi:10.1029/2006JD007277, d10311, 2007.

- Boersma, K. F., Eskes, H. J., and Brinksma, E. J.: Error analysis for tropospheric NO₂ retrieval from space, *J. Geophys. Res. Atmos.*, 109, doi:10.1029/2003JD003962, 2004.
- Bott, A.: A Positive Definite Advection Scheme Obtained by Nonlinear Renormalization of the Advective Fluxes, *Mon. Wea. Rev.*, 117, 1006–1016., 117, 1006–1016, doi:10.1175/1520-0493(1989)117<1006:APDASO>2.0.CO;2, 1989.
- Brasseur, G., P., Cox, R., A. a. H. D., Wiesen, P., Isaksen, I., Lelieveld, J., Lister, D., H., Sausen, R., Schumann, U., Wahner, A., and Wiesen, P.: European Scientific Assessment of the Atmospheric Effects of Aircraft Emission, *Atmos. Env.*, 32, 2329–2418, doi:10.1016/S1352-2310(97)00486-X, 1998.
- Canty, T. P., Hembeck, L., Vinciguerra, T. P., Anderson, D. C., Goldberg, D. L., Carpenter, S. F., Allen, D. J., Loughner, C. P., Salawitch, R. J., and Dickerson, R. R.: Ozone and NO_x chemistry in the eastern US: evaluation of CMAQ/CB05 with satellite (OMI) data, *Atmos. Chem. Phys.*, 15, 10965–10982, doi:10.5194/acp-15-10965-2015, 2015.
- Carpenter, L., Clemitshaw, K., Burgess, R., Penkett, S., Cape, J., and McFadyen, G.: Investigation and evaluation of the NO_x/O₃ photochemical steady state, *Atmos. Environ.*, 32, 3353–3365, doi:10.1016/S1352-2310(97)00416-0, 1998.
- Chen, S., Ren, X., Mao, J., Chen, Z., Brune, W. H., Lefer, B., Rappenglöck, B., Flynn, J., Olson, J., and Crawford, J. H.: A comparison of chemical mechanisms based on TRAMP-2006 field data, *Atmospheric Environment*, 44, 4116–4125, doi:http://dx.doi.org/10.1016/j.atmosenv.2009.05.027, 2010.
- Christensen, J. H., Carter, T. R., Rummukainen, M., and Amanatidis, G.: Evaluating the performance and utility of regional climate models: the PRUDENCE project, *Climatic Change*, 81, 1–6, doi:10.1007/s10584-006-9211-6, 2007.
- Coates, J. and Butler, T. M.: A comparison of chemical mechanisms using tagged ozone production potential (TOPP) analysis, *Atmos. Chem. Phys.*, 15, 8795–8808, doi:10.5194/acp-15-8795-2015, 2015.
- Cohan, D. S., Hu, Y., and Russell, A. G.: Dependence of ozone sensitivity analysis on grid resolution, *Atmos. Environ.*, 40, 126–135, doi:http://dx.doi.org/10.1016/j.atmosenv.2005.09.031, 2006.
- Collet, S., Minoura, H., Kidokoro, T., Sonoda, Y., Kinugasa, Y., and Karamchandani, P.: Evaluation of light-duty vehicle mobile source regulations on ozone concentration trends in 2018 and 2030 in the western and eastern United States, *Journal of the Air & Waste Management Association*, 64, 175–183, doi:10.1080/10962247.2013.845621, 2014.
- Coyle, M., Nemitz, E., Storeton-West, R., Fowler, D., and Cape, J. N.: Measurements of ozone deposition to a potato canopy, *Agricultural and Forest Meteorology*, 149, 655 – 666, doi:http://dx.doi.org/10.1016/j.agrformet.2008.10.020, 2009.
- Crutzen, Paul, J.: Photochemical reactions initiated by and influencing ozone in unpolluted tropospheric air, *Tellus*, 26, 47–57, doi:10.1111/j.2153-3490.1974.tb01951.x, 1974.

- Crutzen, P. J. and Schmailzl, U.: Chemical budgets of the stratosphere, *Planet. Space Sci.*, 31, 1009 – 1032, doi:[http://dx.doi.org/10.1016/0032-0633\(83\)90092-2](http://dx.doi.org/10.1016/0032-0633(83)90092-2), 1983.
- Dahlmann, K., Grewe, V., Ponater, M., and Matthes, S.: Quantifying the contributions of individual NO_x sources to the trend in ozone radiative forcing, *Atmos. Environ.*, 45, 2860–2868, doi:<http://dx.doi.org/10.1016/j.atmosenv.2011.02.071>, 2011.
- Davies, H. C.: A lateral boundary formulation for multi-level prediction models, *Quart. J. Roy. Meteor. Soc.*, 102, 405–418, doi:10.1002/qj.49710243210, 1976.
- Deckert, R., Jöckel, P., Grewe, V., Gottschaldt, K.-D., and Hoor, P.: A quasi chemistry-transport model mode for EMAC, *Geosci. Model Dev.*, 4, 195–206, doi:10.5194/gmd-4-195-2011, 2011.
- Dee, D. P., Uppala, S. M., Simmons, A. J., Berrisford, P., Poli, P., Kobayashi, S., Andrae, U., Balmaseda, M. A., Balsamo, G., Bauer, P., Bechtold, P., Beljaars, A. C. M., van de Berg, L., Bidlot, J., Bormann, N., Delsol, C., Dragani, R., Fuentes, M., Geer, A. J., Haimberger, L., Healy, S. B., Hersbach, H., Hólm, E. V., Isaksen, I., Kållberg, P., Köhler, M., Matricardi, M., McNally, A. P., Monge-Sanz, B. M., Morcrette, J.-J., Park, B.-K., Peubey, C., de Rosnay, P., Tavolato, C., Thépaut, J.-N., and Vitart, F.: The ERA-Interim reanalysis: configuration and performance of the data assimilation system, *Quart. J. Roy. Meteor. Soc.*, 137, 553–597, doi:10.1002/qj.828, 2011.
- Derwent, R.: New Directions: Prospects for regional ozone in north-west Europe, *Atmos. Environ.*, 42, 1958–1960, doi:<http://dx.doi.org/10.1016/j.atmosenv.2007.11.028>, 2008.
- Derwent, R. G., Utembe, S. R., Jenkin, M. E., and Shallcross, D. E.: Tropospheric ozone production regions and the intercontinental origins of surface ozone over Europe, *Atmos. Environ.*, 112, 216–224, doi:<http://dx.doi.org/10.1016/j.atmosenv.2015.04.049>, 2015.
- Dietmüller, S., Jöckel, P., Tost, H., Kunze, M., Gellhorn, C., Brinkop, S., Frömming, C., Ponater, M., Steil, B., Lauer, A., and Hendricks, J.: A new radiation infrastructure for the Modular Earth Submodel System (MESSy, based on version 2.51), *Geoscientific Model Development*, 9, 2209–2222, doi:10.5194/gmd-9-2209-2016, 2016.
- Doherty, R. M., Wild, O., Shindell, D. T., Zeng, G., MacKenzie, I. A., Collins, W. J., Fiore, A. M., Stevenson, D. S., Dentener, F. J., Schultz, M. G., Hess, P., Derwent, R. G., and Keating, T. J.: Impacts of climate change on surface ozone and intercontinental ozone pollution: A multi-model study, *J. Geophys. Res. Atmos.*, 118, 3744–3763, doi:10.1002/jgrd.50266, 2013.
- Ehlers, C., Klemp, D., Rohrer, F., Mihelcic, D., Wegener, R., Kiendler-Scharr, A., and Wahner, A.: Twenty years of ambient observations of nitrogen oxides and specified hydrocarbons in air masses dominated by traffic emissions in Germany, *Faraday Discuss*, doi:10.1039/C5FD00180C, 2016.
- Emmons, L. K., Walters, S., Hess, P. G., Lamarque, J.-F., Pfister, G. G., Fillmore, D., Granier, C., Guenther, A., Kinnison, D., Laepple, T., Orlando, J., Tie, X., Tyndall, G., Wiedinmyer, C., Baughcum, S. L., and Kloster, S.: Description and evaluation of the

- Model for Ozone and Related chemical Tracers, version 4 (MOZART-4), *Geosci. Model Dev.*, 3, 43–67, doi:10.5194/gmd-3-43-2010, 2010.
- Emmons, L. K., Hess, P. G., Lamarque, J.-F., and Pfister, G. G.: Tagged ozone mechanism for MOZART-4, CAM-chem and other chemical transport models, *Geosci. Model Dev.*, 5, 1531–1542, doi:10.5194/gmd-5-1531-2012, 2012.
- European Environment Agency: EMEP/EEA air pollutant emission inventory guidebook 2009, European Environment Agency, doi:10.2800/23924, 2009.
- Eyring, V., Stevenson, D. S., Lauer, A., Dentener, F. J., Butler, T., Collins, W. J., Ellingsen, K., Gauss, M., Hauglustaine, D. A., Isaksen, I. S. A., Lawrence, M. G., Richter, A., Rodriguez, J. M., Sanderson, M., Strahan, S. E., Sudo, K., Szopa, S., van Noije, T. P. C., and Wild, O.: Multi-model simulations of the impact of international shipping on Atmospheric Chemistry and Climate in 2000 and 2030, *Atmos. Chem. Phys.*, 7, 757–780, doi:10.5194/acp-7-757-2007, 2007.
- Filippidou, E. and Koukoulia, A.: Ozone effects on the respiratory system, *Progress in Health Science*, 2, 144–155, 2011.
- Flagan, R. C. and Seinfeld, J. H.: *Fundamentals of air pollution engineering*, Prentice Hall, 1988.
- Fowler, D., Pilegaard, K., Sutton, M., Ambus, P., Raivonen, M., Duyzer, J., Simpson, D., Fagerli, H., Fuzzi, S., Schjoerring, J., Granier, C., Neftel, A., Isaksen, I., Laj, P., Maione, M., Monks, P., Burkhardt, J., Daemmgen, U., Neiryneck, J., Personne, E., Wichink-Kruit, R., Butterbach-Bahl, K., Flechard, C., Tuovinen, J., Coyle, M., Gerosa, G., Loubet, B., Altimir, N., Gruenhage, L., Ammann, C., Cieslik, S., Paoletti, E., Mikkelsen, T., Ro-Poulsen, H., Cellier, P., Cape, J., Horvath, L., Loreto, F., Niinemets, U., Palmer, P., Rinne, J., Misztal, P., Nemitz, E., Nilsson, D., Pryor, S., Gallagher, M., Vesala, T., Skiba, U., Brüggemann, N., Zechmeister-Boltenstern, S., Williams, J., O'Dowd, C., Facchini, M., de Leeuw, G., Flossman, A., Chaumerliac, N., and Erisman, J.: Atmospheric composition change: Ecosystems-Atmosphere interactions, *Atmospheric Environment*, 43, 5193–5267, doi:http://dx.doi.org/10.1016/j.atmosenv.2009.07.068, ACCENT Synthesis, 2009.
- Galanter, M., Levy, H., and Carmichael, G. R.: Impacts of biomass burning on tropospheric CO, NO_x, and O₃, *Journal of Geophysical Research: Atmospheres*, 105, 6633–6653, doi:10.1029/1999JD901113, 2000.
- Gauss, M., Isaksen, I. S. A., Lee, D. S., and Søvde, O. A.: Impact of aircraft NO_x emissions on the atmosphere – tradeoffs to reduce the impact, *Atmospheric Chemistry and Physics*, 6, 1529–1548, doi:10.5194/acp-6-1529-2006, 2006.
- Giorgetta, M. A. and Bengtsson, L.: Potential role of the quasi-biennial oscillation in the stratosphere-troposphere exchange as found in water vapor in general circulation model experiments, *J. Geophys. Res. Atmos.*, 104, 6003–6019, doi:10.1029/1998JD200112, 1999.

- Granier, C. and Brasseur, G. P.: The impact of road traffic on global tropospheric ozone, *Geophys. Res. Lett.*, 30, doi:10.1029/2002GL015972, 2003.
- Granier, C., Bessagnet, B., Bond, T., D'Angiola, A., van der Gon, H. D., Frost, G., Heil, A., Kaiser, J., Kinne, S., Klimont, Z., Kloster, S., Lamarque, J.-F., Lioussé, C., Masui, T., Meleux, F., Mieville, A., Ohara, T., Raut, J.-C., Riahi, K., Schultz, M., Smith, S., Thompson, A., Aardenne, J., Werf, G., and Vuuren, D.: Evolution of anthropogenic and biomass burning emissions of air pollutants at global and regional scales during the 1980–2010 period, *Clim. Change*, 109, 163–190, 2011.
- Grell, G. A., Peckham, S. E., Schmitz, R., McKeen, S. A., Frost, G., Skamarock, W. C., and Eder, B.: Fully coupled online chemistry within the WRF model, *Atmos. Environ.*, 39, 6957–6975, doi:http://dx.doi.org/10.1016/j.atmosenv.2005.04.027, 2005.
- Grewe, V.: Technical Note: A diagnostic for ozone contributions of various NO_x emissions in multi-decadal chemistry-climate model simulations, *Atmos. Chem. Phys.*, 4, 729–736, doi:10.5194/acp-4-729-2004, 2004.
- Grewe, V.: The origin of ozone, *Atmos. Chem. Phys.*, 6, 1495–1511, doi:10.5194/acp-6-1495-2006, 2006.
- Grewe, V.: Impact of climate variability on tropospheric ozone, *Science of The Total Environment*, 374, 167–181, doi:http://dx.doi.org/10.1016/j.scitotenv.2007.01.032, 2007.
- Grewe, V.: A generalized tagging method, *Geosci. Model Dev.*, 6, 247–4253, doi:10.5194/gmdd-5-3311-2012, 2013.
- Grewe, V., Brunner, D., Dameris, M., Grenfell, J., Hein, R., Shindell, D., and Staehelin, J.: Origin and variability of upper tropospheric nitrogen oxides and ozone at northern mid-latitudes, *Atmos. Environ.*, 35, 3421–3433, 2001.
- Grewe, V., Dameris, M., Fichter, C., and Sausen, R.: Impact of aircraft NO_x emissions. Part 1: Interactively coupled climate-chemistry simulations and sensitivities to climate-chemistry feedback, lightning and model resolution, *Meteorologische Zeitschrift*, 11, 177–186, doi:10.1127/0941-2948/2002/0011-0177, 2002.
- Grewe, V., Tsati, E., and Hoor, P.: On the attribution of contributions of atmospheric trace gases to emissions in atmospheric model applications, *Geosci. Model Dev.*, 3, 487–499, doi:10.5194/gmd-3-487-2010, 2010.
- Grewe, V., Dahmann, K., Matthes, S., and Steinbrecht, W.: Attributing ozone to NO_x emissions: Implications for climate mitigation measures, *Atmos. Environ.*, 59, 102–107, doi:10.1016/j.atmosenv.2012.05.002, 2012.
- Grewe, V., Tsati, E., Mertens, M., Frömming, C., and Jöckel, P.: Contribution of emissions to concentrations: The TAGGING 1.0, *subm. to Geosci. Model Dev. Disc.*, 2016.
- Gromov, S., Jöckel, P., Sander, R., and Brenninkmeijer, C. A. M.: A kinetic chemistry tagging technique and its application to modelling the stable isotopic composition of atmospheric trace gases, *Geosci. Model Dev.*, 3, 337–364, doi:10.5194/gmd-3-337-2010, 2010.

- Guenther, A., Hewitt, C., E., D., Fall, R. G., C., Graedel, T., Harley, P., Klinger, L., Lerdau, M., McKay, W., Pierce, T., S., B., Steinbrecher, R., Tallamraju, R., Taylor, J., and Zimmermann, P.: A global model of natural volatile organic compound emissions, *J. Geophys. Res.*, 100, 8873–8892, 1995.
- Guenther, A., Karl, T., Harley, P., Wiedinmyer, C., Palmer, P. I., and Geron, C.: Estimates of global terrestrial isoprene emissions using MEGAN (Model of Emissions of Gases and Aerosols from Nature), *Atmos. Chem. Phys.*, 6, 3181–3210, doi:10.5194/acp-6-3181-2006, 2006.
- Hall, S. J., Matson, P. A., and Roth, P. M.: NO_x EMISSIONS FROM SOIL: Implications for Air Quality Modeling in Agricultural Regions, *Annu. Rev. Energy Env.*, 21, 311–346, doi:10.1146/annurev.energy.21.1.311, 1996.
- Hardacre, C., Wild, O., and Emberson, L.: An evaluation of ozone dry deposition in global scale chemistry climate models, *Atmospheric Chemistry and Physics*, 15, 6419–6436, doi:10.5194/acp-15-6419-2015, 2015.
- Hauglustaine, D. A., Madronich, S., Ridley, B. A., Flocke, S. J., Cantrell, C. A., Eisele, F. L., Shetter, R. E., Tanner, D. J., Ginoux, P., and Atlas, E. L.: Photochemistry and budget of ozone during the Mauna Loa Observatory Photochemistry Experiment (MLOPEX 2), *J. Geophys. Res. Atmos.*, 104, 30 275–30 307, doi:10.1029/1999JD900441, 1999.
- Hodnebrog, Ø., Berntsen, T. K., Dessens, O., Gauss, M., Grewe, V., Isaksen, I. S. A., Koffi, B., Myhre, G., Olivie, D., Prather, M. J., Stordal, F., Szopa, S., Tang, Q., van Velthoven, P., and Williams, J. E.: Future impact of traffic emissions on atmospheric ozone and OH based on two scenarios, *Atmos. Chem. Phys.*, 12, 12 211–12 225, doi:10.5194/acp-12-12211-2012, 2012.
- Hofmann, C.: Austauschprozesse an Tropopausenfalten extratropischer Zyklonen, Ph.D. thesis, Johannes Gutenberg-Universität, doi:urn:nbn:de:hebis:77-39261, 2014.
- Hofmann, C., Kerkweg, A., Wernli, H., and Jöckel, P.: The 1-way on-line coupled atmospheric chemistry model system MECO(n) Part 3: Meteorological evaluation of the on-line coupled system, *Geosci. Model Dev.*, 5, 129–147, doi:10.5194/gmd-5-129-2012, 2012.
- Hoor, P., Borcken-Kleefeld, J., Caro, D., Dessens, O., Endresen, O., Gauss, M., Grewe, V., Hauglustaine, D., Isaksen, I. S. A., Jöckel, P., Lelieveld, J., Myhre, G., Meijer, E., Olivie, D., Prather, M., Schnadt Poberaj, C., Shine, K. P., Staehelin, J., Tang, Q., van Aardenne, J., van Velthoven, P., and Sausen, R.: The impact of traffic emissions on atmospheric ozone and OH: results from QUANTIFY, *Atmos. Chem. Phys.*, 9, 3113–3136, doi:10.5194/acp-9-3113-2009, 2009.
- Hosaynali Beygi, Z., Fischer, H., Harder, H. D., Martinez, M., Sander, R., Williams, J., Brookes, D. M., Monks, P. S., and Lelieveld, J.: Oxidation photochemistry in the Southern Atlantic boundary layer: unexpected deviations of photochemical steady state, *Atmos. Chem. Phys.*, 11, 8497–8513, doi:10.5194/acp-11-8497-2011, 2011.

- HTAP: Hemispheric Transport of Air Pollution 2007, Geneva, URL <http://www.unece.org/fileadmin/DAM/env/lrtap/ExecutiveBureau/Air.Pollution%20Studies.No.16.Hemispheric%20Transport.pdf>, last access 22.06.2016, 2007.
- HTAP: Hemispheric Transport of Air Pollution 2010, Part A: Ozone and Particulate Matter, Geneva, URL <http://www.unece.org/fileadmin/DAM/env/lrtap/Publications/11-22134-Part-A.pdf>, 2010a.
- HTAP: Hemispheric Transport of Air Pollution 2010 Part D: Answers to Policy-Relevant Science Questions, 2010b.
- Hudman, R. C., Moore, N. E., Mebust, A. K., Martin, R. V., Russell, A. R., Valin, L. C., and Cohen, R. C.: Steps towards a mechanistic model of global soil nitric oxide emissions: implementation and space based-constraints, *Atmospheric Chemistry and Physics*, 12, 7779–7795, doi:10.5194/acp-12-7779-2012, 2012.
- Jacob, D. J.: *Introduction to Atmospheric Chemistry*, Princeton University Press, 1999.
- Jacob, D. J. and Winner, D. A.: Effect of climate change on air quality, *Atmos. Environ.*, 43, 51–63, doi:<http://dx.doi.org/10.1016/j.atmosenv.2008.09.051>, *atmospheric Environment - Fifty Years of Endeavour*, 2009.
- Jang, J.-C. C., Jeffries, H. E., Byun, D., and Pleim, J. E.: Sensitivity of ozone to model grid resolution – I. Application of high-resolution regional acid deposition model, *Atmos. Environ.*, 29, 3085–3100, doi:10.1016/1352-2310(95)00118-I, a and WMA International Specialty Conference on Regional Photochemical Measurements and Modeling, 1995a.
- Jang, J.-C. C., Jeffries, H. E., and Tonnesen, S.: Sensitivity of ozone to model grid resolution – II. Detailed process analysis for ozone chemistry, *Atmos. Environ.*, 29, 3101–3114, doi:10.1016/1352-2310(95)00119-J, a and WMA International Specialty Conference on Regional Photochemical Measurements and Modeling, 1995b.
- Jöckel, P., Sander, R., Kerkweg, A., Tost, H., and Lelieveld, J.: Technical Note: The Modular Earth Submodel System (MESSy) - a new approach towards Earth System Modeling, *Atmos. Chem. Phys.*, 5, 433–444, doi:10.5194/acp-5-433-2005, 2005.
- Jöckel, P., Tost, H., Pozzer, A., Brühl, C., Buchholz, J., Ganzeveld, L., Hoor, P., Kerkweg, A., Lawrence, M., Sander, R., Steil, B., Stiller, G., Tanarhte, M., Taraborrelli, D., van Aardenne, J., and Lelieveld, J.: The atmospheric chemistry general circulation model ECHAM5/MESSy1: consistent simulation of ozone from the surface to the mesosphere, *Atmos. Chem. Phys.*, 6, 5067–5104, doi:10.5194/acp-6-5067-2006, 2006.
- Jöckel, P., Kerkweg, A., Buchholz-Dietsch, J., Tost, H., Sander, R., and Pozzer, A.: Technical Note: Coupling of chemical processes with the Modular Earth Submodel System (MESSy) submodel TRACER, *Atmos. Chem. Phys.*, 8, 1677–1687, doi:10.5194/acp-8-1677-2008, 2008.
- Jöckel, P., Kerkweg, A., Pozzer, A., Sander, R., Tost, H., Riede, H., Baumgaertner, A., Gromov, S., and Kern, B.: Development cycle 2 of the Modular Earth Submodel System (MESSy2), *Geosci. Model Dev.*, 3, 717–752, doi:10.5194/gmd-3-717-2010, 2010.

- Jöckel, P., Tost, H., Pozzer, A., Kunze, M., Kirner, O., Brenninkmeijer, C. A. M., Brinkop, S., Cai, D. S., Dyroff, C., Eckstein, J., Frank, F., Garny, H., Gottschaldt, K.-D., Graf, P., Grewe, V., Kerkweg, A., Kern, B., Matthes, S., Mertens, M., Meul, S., Neumaier, M., Nützel, M., Oberländer-Hayn, S., Ruhnke, R., Runde, T., Sander, R., Scharffe, D., and Zahn, A.: Earth System Chemistry integrated Modelling (ESCiMo) with the Modular Earth Submodel System (MESSy) version 2.51, *Geosci. Model Dev.*, 9, 1153–1200, doi:10.5194/gmd-9-1153-2016, 2016.
- Karl, M., Guenther, A., Köble, R., Leip, A., and Seufert, G.: A new European plant-specific emission inventory of biogenic volatile organic compounds for use in atmospheric transport models, *Biogeosciences*, 6, 1059–1087, doi:10.5194/bg-6-1059-2009, 2009.
- Kerkweg, A. and Jöckel, P.: The 1-way on-line coupled atmospheric chemistry model system MECO(n) Part 1: Description of the limited-area atmospheric chemistry model COSMO/MESSy, *Geosci. Model Dev.*, 5, 87–110, doi:10.5194/gmd-5-87-2012, 2012a.
- Kerkweg, A. and Jöckel, P.: The 1-way on-line coupled atmospheric chemistry model system MECO(n) - Part 2: On-line coupling with the Multi-Model-Driver (MMD), *Geosci. Model Dev.*, 5, 111–128, doi:10.5194/gmd-5-111-2012, 2012b.
- Kerkweg, A., Buchholz, J., Ganzeveld, L., Pozzer, A., Tost, H., and Jöckel, P.: Technical Note: An implementation of the dry removal processes DRY DEPosition and SEDImentation in the Modular Earth Submodel System (MESSy), *Atmos. Chem. Phys.*, 6, 4617–4632, doi:10.5194/acp-6-4617-2006, 2006a.
- Kerkweg, A., Sander, R., Tost, H., and Jöckel, P.: Technical note: Implementation of prescribed (OFFLEM), calculated (ONLEM), and pseudo-emissions (TNUDGE) of chemical species in the Modular Earth Submodel System (MESSy), *Atmos. Chem. Phys.*, 6, 3603–3609, doi:10.5194/acp-6-3603-2006, 2006b.
- Knote, C., Brunner, D., Vogel, H., Allan, J., Asmi, A., Äijälä, M., Carbone, S., van der Gon, H. D., Jimenez, J. L., Kiendler-Scharr, A., Mohr, C., Poulain, L., Prévôt, A. S. H., Swietlicki, E., and Vogel, B.: Towards an online-coupled chemistry-climate model: evaluation of trace gases and aerosols in COSMO-ART, *Geosci. Model Dev.*, 4, 1077–1102, doi:10.5194/gmd-4-1077-2011, 2011.
- Knote, C., Tuccella, P., Curci, G., Emmons, L., Orlando, J. J., Madronich, S., Baró, R., Jiménez-Guerrero, P., Luecken, D., Hogrefe, C., Forkel, R., Werhahn, J., Hirtl, M., Pérez, J. L., Jos, R. S., Giordano, L., Brunner, D., Yahya, K., and Zhang, Y.: Influence of the choice of gas-phase mechanism on predictions of key gaseous pollutants during the AQMEII phase-2 intercomparison, *Atmos. Environ.*, 115, 553–568, doi:http://dx.doi.org/10.1016/j.atmosenv.2014.11.066, 2015.
- Koffi, B., Szopa, S., Cozic, A., Hauglustaine, D., and van Velthoven, P.: Present and future impact of aircraft, road traffic and shipping emissions on global tropospheric ozone, *Atmos. Chem. Phys.*, 10, 11 681–11 705, doi:10.5194/acp-10-11681-2010, 2010.
- Kotlarski, S., Keuler, K., Christensen, O. B., Colette, A., Déqué, M., Gobiet, A., Goergen, K., Jacob, D., Lüthi, D., van Meijgaard, E., Nikulin, G., Schär, C., Teichmann, C.,

- Vautard, R., Warrach-Sagi, K., and Wulfmeyer, V.: Regional climate modeling on European scales: a joint standard evaluation of the EURO-CORDEX RCM ensemble, *Geosci. Model Dev.*, 7, 1297–1333, doi:10.5194/gmd-7-1297-2014, 2014.
- Krol, M., Houweling, S., Bregman, B., van den Broek, M., Segers, A., van Velthoven, P., Peters, W., Dentener, F., and Bergamaschi, P.: The two-way nested global chemistry-transport zoom model TM5: algorithm and applications, *Atmos. Chem. Phys.*, 5, 417–432, doi:10.5194/acp-5-417-2005, 2005.
- Kuenen, J. H. Denier van der Gon, A. V. H. v. d. B.: High resolution European emission inventory for the years 2003–2007, TNO report TNO-060-UT-2011-00588, Utrecht, 201, URL <https://gmes-atmosphere.eu/documents/deliverables/d-emis/>, 2011.
- Kugler, U., Theoloke, J., Thiruchittampalam, B., Friedrich, R., Laufer, S., Knecht, M., Schieberle, C., and Kampffmeyer, T.: Dokumentation der vom IER erarbeiteten Beiträge, projektbericht Projekt 'Verkehrsentwicklung und Umwelt' (VEU), 2013.
- Kwok, R. H. F., Baker, K. R., Napelenok, S. L., and Tonnesen, G. S.: Photochemical grid model implementation and application of VOC, NO_x, and O₃ source apportionment, *Geoscientific Model Development*, 8, 99–114, doi:10.5194/gmd-8-99-2015, 2015.
- Lamarque, J.-F., Bond, T. C., Eyring, V., Granier, C., Heil, A., Klimont, Z., Lee, D., Liousse, C., Mieville, A., Owen, B., Schultz, M. G., Shindell, D., Smith, S. J., Stehfest, E., Van Aardenne, J., Cooper, O. R., Kainuma, M., Mahowald, N., McConnell, J. R., Naik, V., Riahi, K., and van Vuuren, D. P.: Historical (1850–2000) gridded anthropogenic and biomass burning emissions of reactive gases and aerosols: methodology and application, *Atmos. Chem. Phys.*, 10, 7017–7039, doi:10.5194/acp-10-7017-2010, 2010.
- Landgraf, J. and Crutzen, P. J.: An efficient method for online calculations of photolysis and heating rates., *J. Atmos. Sci.*, 55, 863–878, doi:http://dx.doi.org/10.1175/1520-0469, 1998.
- Lathièrre, J., Zhang, L., Adon, M., Ashworth, K., Burkhardt, J., Flechard, C., Forkel, R., Guenther, A., Walker, J., Nemitz, E., Potier, E., and Rumsey, I.: Impact of Leaf Surface and In-canopy Air Chemistry on the Ecosystem/Atmosphere Exchange of Atmospheric Pollutants, pp. 199–206, doi:10.1007/978-94-017-7285-3_11, , 2015.
- Lauer, A., Eyring, V., Hendricks, J., Jöckel, P., and Lohmann, U.: Global model simulations of the impact of ocean-going ships on aerosols, clouds, and the radiation budget, *Atmospheric Chemistry and Physics*, 7, 5061–5079, doi:10.5194/acp-7-5061-2007, 2007.
- Lavoie, G. A., Heywood, J. B., and Keck, J. C.: Experimental and Theoretical Study of Nitric Oxide Formation in Internal Combustion Engines, *Combustion Science and Technology*, 1, 313–326, doi:10.1080/00102206908952211, 1970.
- Lawrence, M. G. and Crutzen, P. J.: Influence of NO_x emissions from ships on tropospheric photochemistry and climate, *Nature*, 402, 167–170, 1999.
- Leighton, P. A.: *Photochemistry of Air Pollution*, Academic, San Diego, Calif., 1961.

- Lelieveld, J. and Dentener, F. J.: What controls tropospheric ozone?, *J. Geophys. Res. Atmos.*, 105, 3531–3551, doi:10.1029/1999JD901011, 2000.
- Levy, H.: Normal Atmosphere: Large Radical and Formaldehyde Concentrations Predicted, *Science*, 173, 141–143, doi:10.1126/science.173.3992.141, 1971.
- LfU: Jahresverläufe der Schadstoffbelastung durch Stickstoffdioxid im Jahr 2014 auf Basis von Tagesmittelwerten an den bayerischen LÜB- Messstationen, Bayerisches Landesamt für Umwelt (LfU), URL http://www.lfu.bayern.de/luft/tagesmittelverlaeufe/doc/no2_tm_2014.pdf, 2015.
- Li, Y., Lau, A. K.-H., Fung, J. C.-H., Zheng, J. Y., Zhong, L. J., and Louie, P. K. K.: Ozone source apportionment (OSAT) to differentiate local regional and super-regional source contributions in the Pearl River Delta region, China, *Journal of Geophysical Research: Atmospheres*, 117, doi:10.1029/2011JD017340, d15305, 2012.
- Lin, S.-J. and Rood, R. B.: Multidimensional Flux-Form Semi-Lagrangian Transport Schemes, *Mon. Wea. Rev.*, 124, 2046–2070, doi:10.1175/1520-0493(1996)124<2046:MFFSLT>2.0.CO;2, 1996.
- Logan, J. A.: Tropospheric ozone: Seasonal behavior, trends, and anthropogenic influence, *J. Geophys. Res. Atmos.*, 90, 10 463–10 482, doi:10.1029/JD090iD06p10463, 1985.
- Logan, J. A., Prather, M. J., Wofsy, S. C., and McElroy, M. B.: Tropospheric chemistry: A global perspective, *J. Geophys. Res. Oceans*, 86, 7210–7254, doi:10.1029/JC086iC08p07210, 1981.
- Lopez, P.: A Lightning Parameterization for the ECMWF Integrated Forecasting System, *Monthly Weather Review*, 144, 3057–3075, doi:10.1175/MWR-D-16-0026.1, 2016.
- Markakis, K., Valari, M., Colette, A., Sanchez, O., Perrussel, O., Honore, C., Vautard, R., Klimont, Z., and Rao, S.: Air quality in the mid-21st century for the city of Paris under two climate scenarios; from the regional to local scale, *Atmos. Chem. Phys.*, 14, 7323–7340, doi:10.5194/acp-14-7323-2014, 2014.
- Matthes, S., Grewe, V., Sausen, R., and Roelofs, G.-J.: Global impact of road traffic emissions on tropospheric ozone, *Atmos. Chem. Phys.*, 7, 1707–1718, doi:10.5194/acp-7-1707-2007, 2007.
- Matthias, V., Aulinger, A., Backes, A., Bieser, J., Geyer, B., Quante, M., and Zeretzke, M.: The impact of shipping emissions on air pollution in the greater North Sea region? Part 2: Scenarios for 2030, *Atmos. Chem. Phys.*, 16, 759–776, doi:10.5194/acp-16-759-2016, 2016.
- Mauzerall, D. L., , and Wang, X.: Protecting agricultural crops from the effects of tropospheric ozone exposure: Reconciling Science and Standard Setting in the United States, Europe, and Asia, *Annu Rev Energ Environ*, 26, 237–268, doi:10.1146/annurev.energy.26.1.237, 2001.

- Menuet, L., Bessagnet, B., Khvorostyanov, D., Beekmann, M., Blond, N., Colette, A., Coll, I., Curci, G., Foret, G., Hodzic, A., Mailler, S., Meleux, F., Monge, J.-L., Pison, I., Siour, G., Turquety, S., Valari, M., Vautard, R., and Vivanco, M. G.: CHIMERE 2013: a model for regional atmospheric composition modelling, *Geosci. Model Dev.*, 6, 981–1028, doi:10.5194/gmd-6-981-2013, 2013.
- Mertens, M., Kerkweg, A., Jöckel, P., Tost, H., and Hofmann, C.: The 1-way on-line coupled model system MECO(n) – Part 4: Chemical evaluation (based on MESSy v2.52), *Geoscientific Model Development*, 9, 3545–3567, doi:10.5194/gmd-9-3545-2016, 2016.
- Milford, J. B., Gao, D., Sillman, S., Blossey, P., and Russell, A. G.: Total reactive nitrogen (NO_y) as an indicator of the sensitivity of ozone to reductions in hydrocarbon and NO_x emissions, *J. Geophys. Res. Atmos.*, 99, 3533–3542, doi:10.1029/93JD03224, 1994.
- Mills, G., Buse, A., Gimeno, B., Bermejo, V., Holland, M., Emberson, L., and Pleijel, H.: A synthesis of AOT40-based response functions and critical levels of ozone for agricultural and horticultural crops, *Atmos. Environ.*, 41, 2630–2643, doi:http://dx.doi.org/10.1016/j.atmosenv.2006.11.016, 2007.
- Minkos, A., Dauert, U., Schütze, G., Feigenspan, S., Himpel, T., and Kessinger, S.: Luftqualität 2015, Vorläufige Auswertung, Umweltbundesamt, URL <https://www.umweltbundesamt.de/publikationen/luftqualitaet-2015>, 2016.
- Monks, P. S.: Gas-phase radical chemistry in the troposphere, *Chem. Soc. Rev.*, 34, 376–395, doi:10.1039/B307982C, 2005.
- Monks, P. S., Archibald, A. T., Colette, A., Cooper, O., Coyle, M., Derwent, R., Fowler, D., Granier, C., Law, K. S., Mills, G. E., Stevenson, D. S., Tarasova, O., Thouret, V., von Schneidmesser, E., Sommariva, R., Wild, O., and Williams, M. L.: Tropospheric ozone and its precursors from the urban to the global scale from air quality to short-lived climate forcer, *Atmos. Chem. Phys.*, 15, 8889–8973, doi:10.5194/acp-15-8889-2015, 2015.
- Myhre, G., Shindell, D., Breón, F.-M., Collins, W., Fuglestvedt, J., Huang, J., Koch, D., Lamarque, J.-F., Lee, D., Mendoza, B., Nakajima, T., Robock, A., Stephens, G., Takemura, T., and Zhang, H.: Anthropogenic and Natural Radiative Forcing, pp. 659–740, doi:10.1017/CBO9781107415324.018, 2013.
- Niemeier, U., Granier, C., Kornbluh, L., Walters, S., and Brasseur, G. P.: Global impact of road traffic on atmospheric chemical composition and on ozone climate forcing, *J. Geophys. Res. Atmos.*, 111, doi:10.1029/2005JD006407, 2006.
- Nordeng, T. E.: Extended versions of the convective parametrization scheme at ECMWF and their impact on the mean and transient activity of the model in the tropics, *Tech. rep.*, ECMWF, 1994.
- Oikawa, P. Y., Ge, C., Wang, J., Eberwein, J. R., Liang, L. L., Allsman, L. A., Grantz, D. A., and Jenerette, G. D.: Unusually high soil nitrogen oxide emissions influence air quality in a high-temperature agricultural region, *Nat Commun*, 6, article, 2015.

- Orville, R. E.: A High-Speed Time-Resolved Spectroscopic Study of the Lightning Return Stroke: Part II. A Quantitative Analysis, *Journal of the Atmospheric Sciences*, 25, 839–851, doi:10.1175/1520-0469(1968)025<0839:AHSTRS>2.0.CO;2, 1968.
- Pacifico, F., Harrison, S. P., Jones, C. D., Arneeth, A., Sitch, S., Weedon, G. P., Barkley, M. P., Palmer, P. I., Serça, D., Potosnak, M., Fu, T.-M., Goldstein, A., Bai, J., and Schurgers, G.: Evaluation of a photosynthesis-based biogenic isoprene emission scheme in JULES and simulation of isoprene emissions under present-day climate conditions, *Atmospheric Chemistry and Physics*, 11, 4371–4389, doi:10.5194/acp-11-4371-2011, 2011.
- Pacifico, F., Folberth, G. A., Jones, C. D., Harrison, S. P., and Collins, W. J.: Sensitivity of biogenic isoprene emissions to past, present, and future environmental conditions and implications for atmospheric chemistry, *J. Geophys. Res. Atmos.*, 117, doi:10.1029/2012JD018276, d22302, 2012.
- Pacifico, F., Folberth, G. A., Sitch, S., Haywood, J. M., Rizzo, L. V., Malavelle, F. F., and Artaxo, P.: Biomass burning related ozone damage on vegetation over the Amazon forest: a model sensitivity study, *Atmospheric Chemistry and Physics*, 15, 2791–2804, doi:10.5194/acp-15-2791-2015, 2015.
- Padro, J.: Summary of ozone dry deposition velocity measurements and model estimates over vineyard, cotton, grass and deciduous forest in summer, *Atmos. Environ.*, 30, 2363–2369, doi:http://dx.doi.org/10.1016/1352-2310(95)00352-5, fourth International Conference on Atmospheric Science and Applications to Air Quality, 1996.
- Palmer, P. I., Abbot, D. S., Fu, T.-M., Jacob, D. J., Chance, K., Kurosu, T. P., Guenther, A., Wiedinmyer, C., Stanton, J. C., Pilling, M. J., Pressley, S. N., Lamb, B., and Sumner, A. L.: Quantifying the seasonal and interannual variability of North American isoprene emissions using satellite observations of the formaldehyde column, *Journal of Geophysical Research: Atmospheres*, 111, doi:10.1029/2005JD006689, d12315, 2006.
- Parrish, D. D., Lamarque, J.-F., Naik, V., Horowitz, L., Shindell, D. T., Staehelin, J., Derwent, R., Cooper, O. R., Tanimoto, H., Volz-Thomas, A., Gilge, S., Scheel, H.-E., Steinbacher, M., and Frhlich, M.: Long-term changes in lower tropospheric baseline ozone concentrations: Comparing chemistry-climate models and observations at northern midlatitudes, *Journal of Geophysical Research: Atmospheres*, 119, 5719–5736, doi:10.1002/2013JD021435, 2013JD021435, 2014.
- Pio, C., Feliciano, M., Vermeulen, A., and Sousa, E.: Seasonal variability of ozone dry deposition under southern European climate conditions, in Portugal, *Atmos. Environ.*, 34, 195–205, doi:http://dx.doi.org/10.1016/S1352-2310(99)00276-9, 2000.
- Plant, R. S. and Craig, G. C.: A Stochastic Parameterization for Deep Convection Based on Equilibrium Statistics, *Journal of the Atmospheric Sciences*, 65, 87–105, doi:10.1175/2007JAS2263.1, 2008.
- Pöschl, U., von Kuhlmann, R., Poisson, N., and Crutzen, P.: Development and Intercomparison of Condensed Isoprene Oxidation Mechanisms for Global Atmospheric Modeling, *J. Atmos. Chem.*, 37, 29–152, doi:10.1023/A:1006391009798, 2000.

- Pour-Biazar, A., Khan, M., Wang, L., Park, Y.-H., Newchurch, M., McNider, R. T., Liu, X., Byun, D. W., and Cameron, R.: Utilization of satellite observation of ozone and aerosols in providing initial and boundary condition for regional air quality studies, *J. Geophys. Res. Atmos.*, 116, doi:10.1029/2010JD015200, d18309, 2011.
- Pozzer, A., Jöckel, P., Sander, R., Williams, J., Ganzeveld, L., and Lelieveld, J.: Technical Note: The MESSy-submodel AIRSEA calculating the air-sea exchange of chemical species, *Atmos. Chem. Phys.*, 6, 5435–5444, doi:10.5194/acp-6-5435-2006, 2006.
- Price, C. and Rind, D.: A simple lightning parameterization for calculating global lightning distributions, *J. Geophys. Res. Atmos.*, 97, 9919–9933, doi:10.1029/92JD00719, 1992.
- Rap, A., Richards, N. A. D., Forster, P. M., Monks, S. A., Arnold, S. R., and Chipperfield, M. P.: Satellite constraint on the tropospheric ozone radiative effect, *Geophys. Res. Lett.*, 42, 5074–5081, doi:10.1002/2015GL064037, 2015GL064037, 2015.
- Reichler, T., Dameris, M., and Sausen, R.: Determining the tropopause height from gridded data, *Geophysical Research Letters*, 30, doi:10.1029/2003GL018240, 2042, 2003.
- Reis, S., Simpson, D., Friedrich, R., Jonson, J., Unger, S., and Obermeier, A.: Road traffic emissions? predictions of future contributions to regional ozone levels in Europe, *Atmospheric Environment*, 34, 4701–4710, doi:http://dx.doi.org/10.1016/S1352-2310(00)00202-8, 2000.
- Riese, M., Ploeger, F., Rap, A., Vogel, B., Konopka, P., Dameris, M., and Forster, P.: Impact of uncertainties in atmospheric mixing on simulated UTLS composition and related radiative effects, *J. Geophys. Res. Atmos.*, 117, doi:10.1029/2012JD017751, 16305, 2012.
- Righi, M., Eyring, V., Gottschaldt, K.-D., Klinger, C., Frank, F., Jöckel, P., and Cionni, I.: Quantitative evaluation of ozone and selected climate parameters in a set of EMAC simulations, *Geosci. Model Dev.*, 8, 733–768, doi:10.5194/gmd-8-733-2015, 2015.
- Rio, C., Hourdin, F., Grandpeix, J.-Y., and Lafore, J.-P.: Shifting the diurnal cycle of parameterized deep convection over land, *Geophysical Research Letters*, 36, doi:10.1029/2008GL036779, 107809, 2009.
- Roeckner, E., Bäuml, G., Bonaventura, L., Brokopf, R., Esch, M., Giorgetta, M., Hagemann, S., Kirchner, I., Kornblueh, L., Manzini, E., Rhodin, A., Schlese, U., Schulzweida, U., and Tompkins, A.: The atmospheric general circulation model ECHAM5. PART I: Model description, MPI-Report 349, Max Planck Institut für Meteorologie in Hamburg, Deutschland, available at: https://www.mpimet.mpg.de/fileadmin/publikationen/Reports/max_scirep_349.pdf (last access: 18 October 2015), 2003.
- Roeckner, E., Brokopf, R., Esch, M., Giorgetta, M., Hagemann, S., Kornblueh, L., Manzini, E., Schlese, U., and Schulzweida, U.: Sensitivity of Simulated Climate to Horizontal and Vertical Resolution in the ECHAM5 Atmosphere Model, *J. Climate*, 19, 3771–3791, doi:10.1175/jcli3824.1, 2006.

- Roustan, Y., Pausader, M., and Seigneur, C.: Estimating the effect of on-road vehicle emission controls on future air quality in Paris, France, *Atmos. Environ.*, 45, 6828–6836, doi:<http://dx.doi.org/10.1016/j.atmosenv.2010.10.010>, 2011.
- Royal Society: Ground-level ozone in the 21st century: future trends, impacts and policy implications, Royal Society, London, 2008.
- Saikawa, E., Kurokawa, J., Takigawa, M., Borcken-Kleefeld, J., Mauzerall, D. L., Horowitz, L. W., and Ohara, T.: The impact of China's vehicle emissions on regional air quality in 2000 and 2020: a scenario analysis, *Atmospheric Chemistry and Physics*, 11, 9465–9484, doi:[10.5194/acp-11-9465-2011](https://doi.org/10.5194/acp-11-9465-2011), 2011.
- Sander, R., Baumgaertner, A., Gromov, S., Harder, H., Jöckel, P., Kerkweg, A., Kubistin, D., Regelin, E., Riede, H., Sandu, A., Taraborrelli, D., Tost, H., and Xie, Z.-Q.: The atmospheric chemistry box model CAABA/MECCA-3.0, *Geosci. Model Dev.*, 4, 373–380, doi:[10.5194/gmd-4-373-2011](https://doi.org/10.5194/gmd-4-373-2011), 2011.
- Schumann, U. and Huntrieser, H.: The global lightning-induced nitrogen oxides source, *Atmos. Chem. Phys.*, 7, 3823–3907, doi:[10.5194/acp-7-3823-2007](https://doi.org/10.5194/acp-7-3823-2007), 2007.
- Seinfeld, J. H. and Pandis, S. N.: *Atmospheric Chemistry and Physics: From Air Pollution to Climate Change*, Wiley, 2006.
- Sharkey, T. D., Wiberley, A. E., and Donohue, A. R.: Isoprene Emission from Plants: Why and How, *Annals of Botany*, 101, 5–18, doi:[10.1093/aob/mcm240](https://doi.org/10.1093/aob/mcm240), 2008.
- Sillman, S.: The use of NO_y, H₂O₂, and HNO₃ as indicators for ozone-NO_x-hydrocarbon sensitivity in urban locations, *J. Geophys. Res. Atmos.*, 100, 14 175–14 188, doi:[10.1029/94JD02953](https://doi.org/10.1029/94JD02953), 1995.
- Sillman, S.: The relation between ozone, NO_x and hydrocarbons in urban and polluted rural environments, *Atmos. Environ.*, 33, 1821–1845, doi:[10.1016/S1352-2310\(98\)00345-8](https://doi.org/10.1016/S1352-2310(98)00345-8), 1999.
- Singh, H. B.: Reactive nitrogen in the troposphere, *Environmental Science & Technology*, 21, 320–327, doi:[10.1021/es00158a001](https://doi.org/10.1021/es00158a001), PMID: 22280168, 1987.
- Squire, O. J., Archibald, A. T., Abraham, N. L., Beerling, D. J., Hewitt, C. N., Lathièrè, J., Pike, R. C., Telford, P. J., and Pyle, J. A.: Influence of future climate and cropland expansion on isoprene emissions and tropospheric ozone, *Atmos. Chem. Phys.*, 14, 1011–1024, doi:[10.5194/acp-14-1011-2014](https://doi.org/10.5194/acp-14-1011-2014), 2014.
- Squire, O. J., Archibald, A. T., Griffiths, P. T., Jenkin, M. E., Smith, D., and Pyle, J. A.: Influence of isoprene chemical mechanism on modelled changes in tropospheric ozone due to climate and land use over the 21st century, *Atmospheric Chemistry and Physics*, 15, 5123–5143, doi:[10.5194/acp-15-5123-2015](https://doi.org/10.5194/acp-15-5123-2015), 2015.
- Stark, M. S., Harrison, J. T. H., and Anastasi, C.: Formation of nitrogen oxides by electrical discharges and implications for atmospheric lightning, *Journal of Geophysical Research: Atmospheres*, 101, 6963–6969, doi:[10.1029/95JD03008](https://doi.org/10.1029/95JD03008), 1996.

- Stock, Z. S., Russo, M. R., Butler, T. M., Archibald, A. T., Lawrence, M. G., Telford, P. J., Abraham, N. L., and Pyle, J. A.: Modelling the impact of megacities on local, regional and global tropospheric ozone and the deposition of nitrogen species, *Atmos. Chem. Phys.*, 13, 12 215–12 231, doi:10.5194/acp-13-12215-2013, 2013.
- Stock, Z. S., Russo, M. R., and Pyle, J. A.: Representing ozone extremes in European megacities: the importance of resolution in a global chemistry climate model, *Atmos. Chem. Phys.*, 14, 3899–3912, doi:10.5194/acp-14-3899-2014, 2014.
- Stockwell, W. R., Lawson, C. V., Saunders, E., and Goliff, W. S.: A Review of Tropospheric Atmospheric Chemistry and Gas-Phase Chemical Mechanisms for Air Quality Modeling, *Atmosphere*, 3, 1, doi:10.3390/atmos3010001, 2012.
- Tagaris, E., Sotiropoulou, R. E. P., Gounaris, N., Andronopoulos, S., and Vlachogiannis, D.: Effect of the Standard Nomenclature for Air Pollution (SNAP) Categories on Air Quality over Europe, *Atmosphere*, 6, 1119, doi:10.3390/atmos6081119, 2015.
- Tai, A. P. K., Mickley, L. J., Heald, C. L., and Wu, S.: Effect of CO₂ inhibition on biogenic isoprene emission: Implications for air quality under 2000 to 2050 changes in climate, vegetation, and land use, *Geophys. Res. Lett.*, 40, 3479–3483, doi:10.1002/grl.50650, 2013.
- Tang, Y., Carmichael, G. R., Thongboonchoo, N., Chai, T., Horowitz, L. W., Pierce, R. B., Al-Saadi, J. A., Pfister, G., Vukovich, J. M., Avery, M. A., Sachse, G. W., Ryerson, T. B., Holloway, J. S., Atlas, E. L., Flocke, F. M., Weber, R. J., Huey, L. G., Dibb, J. E., Streets, D. G., and Brune, W. H.: Influence of lateral and top boundary conditions on regional air quality prediction: A multiscale study coupling regional and global chemical transport models, *J. Geophys. Res. Atmos.*, 112, doi:10.1029/2006JD007515, d10S18, 2007.
- Taylor, K. E.: Summarizing multiple aspects of model performance in a single diagram, *J. Geophys. Res. Atmos.*, 106, 7183–7192, doi:10.1029/2000JD900719, 2001.
- Teixeira, E., Fischer, G., van Velthuizen, H., van Dingenen, R., Dentener, F., Mills, G., Walter, C., and Ewert, F.: Limited potential of crop management for mitigating surface ozone impacts on global food supply, *Atmos. Environ.*, 45, 2569 – 2576, doi: <http://dx.doi.org/10.1016/j.atmosenv.2011.02.002>, 2011.
- Tereszczuk, K. A., Moore, D. P., Harrison, J. J., Boone, C. D., Park, M., Remedios, J. J., Randel, W. J., and Bernath, P. F.: Observations of peroxyacetyl nitrate (PAN) in the upper troposphere by the Atmospheric Chemistry Experiment-Fourier Transform Spectrometer (ACE-FTS), *Atmospheric Chemistry and Physics*, 13, 5601–5613, doi:10.5194/acp-13-5601-2013, 2013.
- Thornton, J. A., Wooldridge, P. J., Cohen, R. C., Martinez, M., Harder, H., Brune, W. H., Williams, E. J., Roberts, J. M., Fehsenfeld, F. C., Hall, S. R., Shetter, R. E., Wert, B. P., and Fried, A.: Ozone production rates as a function of NO_x abundances and HO_x production rates in the Nashville urban plume, *J. Geophys. Res. Atmos.*, 107, ACH 7–1–ACH 7–17, doi:10.1029/2001JD000932, 2002.

- Tie, X., Brasseur, G., and Ying, Z.: Impact of model resolution on chemical ozone formation in Mexico City: application of the WRF-Chem model, *Atmos. Chem. Phys.*, 10, 8983–8995, doi:10.5194/acp-10-8983-2010, 2010.
- Tiedtke, M.: A Comprehensive Mass Flux Scheme for Cumulus Parameterization in Large-Scale Models, *Monthly Weather Review*, 117, 1779–1800, doi:10.1175/1520-0493(1989)117<1779:ACMFSF>2.0.CO;2, 1989.
- Tørseth, K., Aas, W., Breivik, K., Fjæraa, A. M., Fiebig, M., Hjellbrekke, A. G., Lund Myhre, C., Solberg, S., and Yttri, K. E.: Introduction to the European Monitoring and Evaluation Programme (EMEP) and observed atmospheric composition change during 1972 - 2009, *Atmos. Chem. Phys.*, 12, 5447–5481, doi:10.5194/acp-12-5447-2012, 2012.
- Tost, H., Jöckel, P., Kerkweg, A., Sander, R., and Lelieveld, J.: Technical note: A new comprehensive SCAVenging submodel for global atmospheric chemistry modelling, *Atmos. Chem. Phys.*, 6, 565–574, doi:10.5194/acp-6-565-2006, 2006a.
- Tost, H., Jöckel, P., and Lelieveld, J.: Influence of different convection parameterisations in a GCM, *Atmos. Chem. Phys.*, 6, 5475–5493, doi:10.5194/acp-6-5475-2006, 2006b.
- Tost, H., Jöckel, P., Kerkweg, A., Pozzer, A., Sander, R., and Lelieveld, J.: Global cloud and precipitation chemistry and wet deposition: tropospheric model simulations with ECHAM5/MESy1, *Atmos. Chem. Phys.*, 7, 2733–2757, doi:10.5194/acp-7-2733-2007, 2007a.
- Tost, H., Jöckel, P., and Lelieveld, J.: Lightning and convection parameterisations & uncertainties in global modelling, *Atmos. Chem. Phys.*, 7, 4553–4568, doi:10.5194/acp-7-4553-2007, 2007b.
- Tost, H., Lawrence, M. G., Brühl, C., Jöckel, P., Team, T. G., and Team, T. S.-O.-D.: Uncertainties in atmospheric chemistry modelling due to convection parameterisations and subsequent scavenging, *Atmos. Chem. Phys.*, 10, 1931–1951, doi:10.5194/acp-10-1931-2010, 2010.
- Trebs, I., Mayol-Bracero, O. L., Pauliquevis, T., Kuhn, U., Sander, R., Ganzeveld, L., Meixner, F. X., Kesselmeier, J., Artaxo, P., and Andreae, M. O.: Impact of the Manaus urban plume on trace gas mixing ratios near the surface in the Amazon Basin: Implications for the NO-NO₂-O₃ photostationary state and peroxy radical levels, *J. Geophys. Res. Atmos.*, 117, doi:10.1029/2011JD016386, d05307, 2012.
- Tsati, E.-E.: Investigation of the impacts of emissions on the trace gas budgets in the troposphere by using global climate chemistry model simulations, URL <http://nbn-resolving.de/urn:nbn:de:bvb:19-175246>, 2014.
- Valverde, V., Pay, M. T., and Baldasano, J. M.: Ozone attributed to Madrid and Barcelona on-road transport emissions: Characterization of plume dynamics over the Iberian Peninsula, *Science of The Total Environment*, 543, Part A, 670 – 682, doi: <http://dx.doi.org/10.1016/j.scitotenv.2015.11.070>, 2016.

- Vingarzan, R.: A review of surface ozone background levels and trends, *Atmos. Environ.*, 38, 3431–3442, doi:<http://dx.doi.org/10.1016/j.atmosenv.2004.03.030>, 2004.
- Vinken, G. C. M., Boersma, K. F., Maasakkers, J. D., Adon, M., and Martin, R. V.: Worldwide biogenic soil NO_x emissions inferred from OMI NO₂ observations, *Atmos. Chem. Phys.*, 14, 10 363–10 381, doi:10.5194/acp-14-10363-2014, 2014.
- von Kuhlmann, R., Lawrence, M. G., Pöschl, U., and Crutzen, P. J.: Sensitivities in global scale modeling of isoprene, *Atmos. Chem. Phys.*, 4, 1–17, doi:10.5194/acp-4-1-2004, 2004.
- Wesely, M.: Parameterization of surface resistances to gaseous dry deposition in regional-scale numerical models, *Atmospheric Environment (1967)*, 23, 1293–1304, doi:[http://dx.doi.org/10.1016/0004-6981\(89\)90153-4](http://dx.doi.org/10.1016/0004-6981(89)90153-4), 1989.
- Wesely, M. and Hicks, B.: A review of the current status of knowledge on dry deposition, *Atmos. Environ.*, 34, 2261–2282, doi:[http://dx.doi.org/10.1016/S1352-2310\(99\)00467-7](http://dx.doi.org/10.1016/S1352-2310(99)00467-7), 2000.
- Wild, O.: Modelling the global tropospheric ozone budget: exploring the variability in current models, *Atmospheric Chemistry and Physics*, 7, 2643–2660, doi:10.5194/acp-7-2643-2007, 2007.
- Wild, O. and Prather, M. J.: Global tropospheric ozone modeling: Quantifying errors due to grid resolution, *J. Geophys. Res. Atmos.*, 111, doi:10.1029/2005JD006605, d11305, 2006.
- Worden, H. M., Bowman, K. W., Kulawik, S. S., and Aghedo, A. M.: Sensitivity of outgoing longwave radiative flux to the global vertical distribution of ozone characterized by instantaneous radiative kernels from Aura-TES, *J. Geophys. Res. Atmos.*, 116, doi:10.1029/2010JD015101, URL <http://dx.doi.org/10.1029/2010JD015101>, d14115, 2011.
- World Health Organization: Health aspect of air pollution with particulate matter, ozone and nitrogen dioxide, World Health Organization, Bonn, 2003.
- World Health Organization: Air quality guidelines for particulate matter, ozone, nitrogen dioxide and sulfur dioxide Global update 2005, Copenhagen, URL http://whqlibdoc.who.int/hq/2006/WHO_SDE_PHE_OEH_06.02_eng.pdf, 2006.
- Wu, S., Duncan, B. N., Jacob, D. J., Fiore, A. M., and Wild, O.: Chemical nonlinearities in relating intercontinental ozone pollution to anthropogenic emissions, *Geophys. Res. Lett.*, 36, doi:10.1029/2008GL036607, l05806, 2009.
- Xie, Y., Elleman, R., Jobson, T., and Lamb, B.: Evaluation of O₃-NO_x-VOC sensitivities predicted with the CMAQ photochemical model using Pacific Northwest 2001 field observations, *Journal of Geophysical Research: Atmospheres*, 116, doi:10.1029/2011JD015801, d20303, 2011.
- Yienger, J. J. and Levy, H.: Global inventory of soil-biogenic NO_x emissions, *J. Geophys. Res.*, 100, 11,447–11,464, 1995.

- Young, P. J., Archibald, A. T., Bowman, K. W., Lamarque, J.-F., Naik, V., Stevenson, D. S., Tilmes, S., Voulgarakis, A., Wild, O., Bergmann, D., Cameron-Smith, P., Cionni, I., Collins, W. J., Dalsøren, S. B., Doherty, R. M., Eyring, V., Faluvegi, G., Horowitz, L. W., Josse, B., Lee, Y. H., MacKenzie, I. A., Nagashima, T., Plummer, D. A., Righi, M., Rumbold, S. T., Skeie, R. B., Shindell, D. T., Strode, S. A., Sudo, K., Szopa, S., and Zeng, G.: Pre-industrial to end 21st century projections of tropospheric ozone from the Atmospheric Chemistry and Climate Model Intercomparison Project (ACCMIP), *Atmos. Chem. Phys.*, 13, 2063–2090, doi:10.5194/acp-13-2063-2013, 2013.
- Zare, A., Christensen, J. H., Irannejad, P., and Brandt, J.: Evaluation of two isoprene emission models for use in a long-range air pollution model, *Atmospheric Chemistry and Physics*, 12, 7399–7412, doi:10.5194/acp-12-7399-2012, 2012.
- Zeldovich, Y.: The Oxidation of Nitrogen in Combustion and Explosions, *Acta Physico-chimica URSS*, 21, 577–628, 1946.
- Zellner, R., ed.: *Global Aspects of Atmospheric Chemistry*, Topics in Physical Chemistry, Steinkopff, 1999.
- Zhang, L., Brook, J. R., and Vet, R.: A revised parameterization for gaseous dry deposition in air-quality models, *Atmospheric Chemistry and Physics*, 3, 2067–2082, doi:10.5194/acp-3-2067-2003, 2003.
- Ziemke, J. R., Chandra, S., Duncan, B. N., Froidevaux, L., Bhartia, P. K., Levelt, P. F., and Waters, J. W.: Tropospheric ozone determined from Aura OMI and MLS: Evaluation of measurements and comparison with the Global Modeling Initiative's Chemical Transport Model, *J. Geophys. Res. Atmos.*, 111, doi:10.1029/2006JD007089, 2006.
- Ziemke, J. R., Chandra, S., Labow, G. J., Bhartia, P. K., Froidevaux, L., and Witte, J. C.: A global climatology of tropospheric and stratospheric ozone derived from Aura OMI and MLS measurements, *Atmos. Chem. Phys.*, 11, 9237–9251, doi:10.5194/acp-11-9237-2011, 2011.

Acronyms and specie names

List of used acronyms

850PC	partical column up to 850 hPa
AR5	assessment report 5
AWB	agricultural waste burning
BML	base model layer
BMIL	base model interface layer
CCM	chemistry-climate model
CLRTAP	Convention on Long-range Transboundary Air Pollution
CM50	COSMO(50km)/MESSy
CM12	COSMO(12km)/MESSy
CTM	chemistry-transport model
DWD	Deutscher Wetterdienst
ESM	earth system model
ECMWF	European-Centre for medium-Range Forecast
GCM	global circulation model
IER	Institut für Energiewirtschaft und Rationelle Energieanwendung
IPCC	Intergovernmental Panel on Climate Change
LTO	landing and take-off
MAC08	MACCity emissions inventory (Granier et al., 2011) for the year 2008
MBE	normalised mean bias error
MESSy	Modular Earth Submodel System
MECO(n)	MESSy-fied ECHAM and COSMO models nested n-times

NA	North America
MIM	Mainz Isoprene Mechanism
MLS	Microwave Limb Sounder
MMD	Multi Model DriverMMD
MPI	Message Passing Interface
OMI	Ozone Monitoring Instrument
OPE	O ₃ production efficiency
ppts	percentage points
PBL	planetary boundary layer
QCTM	Quasi Chemistry Transport Model
RCP	Representative Concentration Pathways
RF	radiative forcing
RMSE	root mean square error
SCIAMACHY	SCanning Imaging Absorption spectroMeter for Atmospheric CHartography
SLP	sea level pressure
SMCL	submodel core layer
SMIL	submodel interface layer
SNAP	significant new alternatives policy
STE	stratosphere-troposphere-exchange
TOC	tropospheric O ₃ column
TF HTAP	Task Force on Hemispheric Transport of Air Pollution
UTLS	upper troposphere/lower stratosphere
UNECE	United Nations Economic Commission for Europe
VEU	'Verkehrsentwicklung und Umwelt'
VEU08	VEU emission inventory for the year 2008
VEU30	VEU emission inventory for the year 2030
WHO	World Health Organisation
WMO	World Meteorological Organisation

List of chemical species

The following gives an overview about the chemical species and additional tracers (mainly for TAGGING) used in the present study.

Table B1: Alphabetical list of chemical species and tracers used in the present study.

C_5H_8	isoprene
CH_3	methyl radical
CH_3I	iodmethane
$CHBr_3$	bromoform
CH_3Br	bromomethane
CH_3O	methoxy radical
CH_3CO	acetyl
CH_3CHO	acetaldehyde
$CH_3C(O)O_2NO_2$	peroxyacetyl nitrate
CH_3O_2	methyl peroxy radical
CH_3OOH	methyl hydroperoxide
$CH_3C(O)O_2$	peroxyacetyl radical
CH_4	methane
CO	carbon monoxide
CO_2	carbon dioxide
H	hydrogen atom
H_2	hydrogen molecule
H_2O	water
H_2O_2	hydrogen peroxide
$HCHO$	formaldehyde
HNO_3	nitric acid
HO_x	family of OH and HO_2
HO_2	hydroperoxyl radical
N_2O	nitrous oxide
NH_4	ammonium
NMHC	non methane hydro carbon
$NMHC^{tra}$	non methane hydro carbon from road traffic
N_2	molecular nitrogen
N_2O_5	dinitrogen pentoxide
NO	nitrogen oxide
NO_2	nitrogen dioxide
NO_3	nitrate
NO_3^-	nitrate ion
NO_x	family of NO and NO_2
NO_y	family of reactive nitrogen compounds
NO_y^{tra}	NO_y^{tra} from the road traffic category

Continued on next page

Table B1 – *Continued from previous page*

name	description
NO ₃	nitrate
PAN	short form peroxyacetyl nitrate
RO ₂	alkyl peroxy radical
RH	generalised form of hydrocarbons (e.g. alkanes)
RO	alkoxy radical
R'CHO	higher carbonyl
O	oxygen
O(¹ D)	excited singlet state oxygen atom
O ₂	molecular oxygen
O ₃	ozone
O ₃ ^{air}	O ₃ of the aviation category
O ₃ ^{anth}	O ₃ of the anthropogenic non-traffic category
O ₃ ^{bio}	O ₃ of the biomass burning category
O ₃ ^{biog}	O ₃ of the biogenic category
O ₃ ^{ch4}	O ₃ of the CH ₄ category
O ₃ ^{lig}	O ₃ of the lightning category
O ₃ ^{n2o}	O ₃ of the N ₂ O category
O ₃ ^{ship}	O ₃ of the shipping category
O ₃ ^{str}	O ₃ of the stratosphere category
O ₃ ^{tra}	O ₃ of the road traffic category
OH	hydroxyl radical
VOC	volatile organic compound

Danksagung

Bedanken möchte ich mich bei meinem Doktorvater Prof. Dr. Robert Sausen für die Möglichkeit zu dieser Arbeit, für seine Unterstützung und die wertvollen Kommentare während der gesamten Zeit. Danken möchte ich ebenfalls Prof. Dr. George Craig für die Übernahme des Zweitgutachtens sowie den sehr hilfreichen Kommentaren zu meiner Arbeit. Ein Dank geht außerdem an den Institutsleiter Prof. Dr. Markus Rapp für die Möglichkeit diese Arbeit anfertigen zu können und den wertvollen Kommentaren zu dieser.

Ein ganz besonderer Dank gilt Dr. Patrick Jöckel für seine hervorragende Betreuung, den Einsatz und all die Unterstützung. Bei jeder Frage und bei jedem Problem stand er stets mit Rat und Tat zur Verfügung. Des Weiteren möchte ich mich bei Dr. Astrid Kerkweg für all die Hilfe mit dem Modellsystem sowie den vielen Tipps, Diskussionen und Bugfixes bedanken. Ein weiteres Dankeschön geht an Prof. Dr. Volker Grewe für wertvolle Kommentare und Diskussionen sowie die Hilfe mit der Tagging Methode.

Ein riesengroßes Dankeschön geht an alle aktuellen und ehemaligen 'Bewohner' der Chili-Aufzuchtstation 102. Ihr habt stets für eine sehr angenehme Arbeitsatmosphäre, viel Spaß aber auch für die nötige Ablenkung gesorgt. Für wertvolle Diskussionen standet ihr zur Seite und habt mich unterstützt wenn es nötig war. Ebenfalls bedanken möchte ich mich bei der ganze Abteilung 1 für den Spaß, den Kuchen aber auch die vielen hilfreichen und kritischen Kommentare während der gesamten Zeit.

Nicht zuletzt geht ein großer Dank an meine Familie und Freunde die immer für die notwendige Ablenkung und Spaß gesorgt und mich stets unterstützt haben.